Report Prepared by :

Alberto. A. Sagüés
S.C. Kranc
with:
Francisco Presuel-Moreno
David Rey
Andres Torres-Acosta
Lan Yao

CORROSION FORECASTING FOR 75-YEAR DURABILITY

DESIGN OF REINFORCED CONCRETE

State Job 99700-3515-020, WPI 0510805

Contract No. BA502

Final Report to Florida Department of Transportation

Alberto A. Sagüés and S.C. Kranc
Principal Investigators
Department of Civil and Environmental Engineering

University of South Florida
Tampa, FL, 33620
December 31, 2001

1. Report No. BA502	2. Government Accession No.	3. Recipient's Catalog No.		
4. Title and Subtitle CORROSION FORECASTING FOR 75-YEAR DURABILITY DESIGN OF REINFORCED CONCRETE		5. Report Date December 31, 2001		
		6. Performing Organization Code		
		8. Performing Organization Report No.		
7. Author's Alberto. A. Sagüés, S.C. Kranc, Francisco Presuel-Moreno, David Rey, Andres Torres-Acosta, Lan Yao				
9. Performing Organization Name and Address Department of Civil and Environmental Engineering University of South Florida Tampa, FL 33620		10. Work Unit No. (TRAIS)		
		11. Contract or Grant No. BA502		
		13. Type of Report and Period Covered Final Report August 1996-May 2001		
12. Sponsoring Agency Name and Address Florida Department of Transportation 605 Suwannee Street Tallahassee, FL 32399-0450				
		14. Sponsoring Agency Code		
15. Supplementary Notes Prepared in cooperation with the U.S. Department of Transportation and the Federal Highway Administration				

16. Abstract This investigation addressed the prognosis for 75-year durability of the substructure of Florida D.O.T. marine bridges constructed with promising concrete formulations. Thirteen bridges, most built with improved concrete formulations, were investigated to determine rate of chloride ion penetration and how it may be affected by preexisting stress cracks. Sound concrete made per recent FDOT specifications for high cement factor, low w/c and pozzolanic cement replacement exhibited very slow chloride penetration in aggressive marine bridge substructure service. The best performing concrete, having >752 lb/yd^3 (446 kg/m^3) cementitious content, 20% fly ash cement replacement, and w/c~ 0.32 showed an average chloride diffusivity ~0.01 in^2/y (~2 10^{-9} cm^2/sec) at age 11 years in the tidal and low elevation region. Thin (typical ~0.15 mm) stress cracks were found in many of the substructures examined. Many of these cracks in footers or piles reached down to the waterline and extended to at least the rebar depth. Crack incidences in the order of one crack every several meters of waterline perimeter were not uncommon. Even though the cracks were thin, there was substantial preferential chloride penetration immediately around the crack compared with the surrounding sound concrete in the splash evaporation zone. However, no clear indications of corrosion were observed in any of the crack locations examined. Numerical modeling indicates that even very thin preexisting cracks could substantially increase chloride penetration in the immediately surrounding concrete, and that corrosion if initiated could be locally severe. Experiments revealed that the amount of critical corrosion penetration needed to cause damage was greater when corrosion was localized than when corrosion was more uniform. An integrated corrosion initiation and propagation model for sound concrete was created that takes into account the concrete mixture proportions, rebar cover and size, and system geometry. Additional modeling revealed that rebar itself can act as an obstruction to the diffusional chloride flow, causing a local increase in concentration and considerable relative reduction in the projected time to corrosion initiation when the rebar cover is low or the critical chloride concentration high. Derating factors to account for this effect were computed and proposed for use. Further modeling indicated that the region immediately above high tide may be amenable to cathodic prevention of the passive steel with sacrificial anodes.

17. Key Words Reinforcing Steel, Corrosion, Chlorides, Concrete, Cracks, Cathodic, Durability, Forecast	18. Distribution Statement No restrictions. This document is available to the public through the National Technical Information Service, Springfield, VA 22161		
19. Security Classif.(of this report) Unclassified	20. Security Classif. (of this page) Unclassified	21. No. of Pages 174	22. Price

TABLE OF CONTENTS

NOTICE

EXECUTIVE SUMMARY

About two thirds of the 5,500 bridges in the Florida Department of Transportation (FDOT) inventory are exposed to salt water. The resulting corrosion of reinforcement has in the past created serious limitations to the durability of the substructure of those bridges, resulting in continuing need for costly repairs or early replacement of the structure. The nationwide mandate for 75-year durability construction represents therefore an especially difficult challenge when designing new bridges for these aggressive service marine applications.

Previous work has quantified the chloride ion penetration into the concrete of the substructure of FDOT bridges by an effective diffusion coefficient "D" particular to the structure location and the type of concrete used. The value of D is obtained from analysis of drilled cores. This value, combined with other chemical and structural information, can be used with computational models created for FDOT to produce a quantitative estimate of the length of the corrosion initiation stage, as is called the service time before external signs of corrosion are observed. Initial surveys have shown that concrete formulations such as those intended for highest performance in Section 346 of the FDOT Standard Specifications for Road and Bridge Construction yield extremely low values of D, with consequently long projected durability. Those concrete formulations include a high cement factor; a significant amount of pozzolanic cement replacement, usually by type F fly ash (FA) and occasionally by micro silica (MS); and a low water-to-cementitious content ratio (w/c). This initial information was limited to a few structures. The extent to which narrow preexisting stress cracks may facilitate chloride penetration in otherwise sound high quality concrete was not known.

The present investigation was conducted with the main objective of improving forecasting ability by updating information on the rate of chloride ion penetration, with special attention to the effect of cracks, in the substructure of FDOT marine bridges constructed with the most promising concrete formulations. The resulting information was applied to improving methods of predicting the length of the corrosion initiation and the corrosion propagation stages, which was then integrated as a comprehensive forecasting model. Finally, part of the information and methods developed were applied in an exploratory manner to evaluate the feasibility of electrochemical corrosion protection methods for extending the durability of new and existing structures. In executing this investigation, thirteen FDOT bridges were examined and samples were analyzed to assess chloride penetration and extent as well as consequences of stress cracks.   Laboratory experiments and computer calculations were conducted to supplement the information from the field and address the other issues.

Analysis of the bridge samples confirmed that sound concrete made per Section 346 of the FDOT Standard Specifications for Road and Bridge Construction with high cement factor, low w/c and pozzolanic cement replacement exhibits very slow chloride penetration in aggressive marine bridge substructure service. The best performing concrete, comparable to a Class V formulation and with w/c~0.32, showed an average

value of D of about 0.01 in^2/y (2 10^{-9} cm^2/sec) at age 11 years in the Tidal to 6 ft (1.8 m) above high tide region. Results from the Sunshine Skyway Bridge suggest that D decreases with age of the structure, in agreement with reports from other investigations of aging concrete with pozzolanic additions. The surface chloride concentration (C$_S$) appeared to reach relatively steady values early in the life of the substructures examined. A value of C$_S$ of about 30 pcy (18 kg/m^3) may be considered to be typical in the Tidal to 6 ft (1.8 m) AHT region. The surface concentration was not found to be a strong function of the salt content of the surrounding seawater.

Thin (typical width ~0.15 mm) stress cracks were found in many of the substructures examined. Many of these cracks in footers or piles reached down to the waterline and extended to at least the rebar depth. Crack incidences in the order of one crack every several meters of waterline perimeter were not uncommon. Even though the cracks were thin, there was substantial preferential chloride penetration immediately around the crack compared with the surrounding sound concrete, to levels exceeding commonly assumed values of the chloride initiation threshold. The effect was most marked in the splash evaporation zone. In spite of this enhanced chloride penetration, conspicuous indications of corrosion were not observed in any of the crack locations examined (the use of epoxy-coated rebar in some of the bridges may have masked or mitigated corrosion development there). Numerical models of chloride transport in the cracks reproduced the observed chloride penetration behavior. The analysis predicts that under moist substructure conditions significant chloride penetration can occur even in extremely thin cracks, and that chloride buildup could be more severe when a crack terminates at a short distance from the surface instead of extending deep into the concrete.

Calculations of the penetration of chloride in sound concrete revealed that the rebar acts as an obstruction to the diffusional chloride flow, causing a local increase in concentration. That increase shortens the projected time for corrosion initiation (t$_i$) compared to that evaluated assuming unrestricted diffusion. The effect can be strong (e.g. reductions in t$_i$ by as much as 40%) depending on the concrete cover, rebar diameter, and chloride threshold value. Derating factors to account for this effect were computed. and proposed for use in durability estimates. An integrated corrosion initiation model for sound concrete was created that takes into account the concrete mixture proportions, rebar cover and size, and system geometry (flat wall, 2- and 3- way corners, or cylindrical columns). Software for rapid calculation of t$_i$ incorporating the initiation model and input values based on the field findings has been created.

Experiments revealed that the amount of critical corrosion penetration needed to cause cover cracking was greater when corrosion was localized (as it may happen in an area of preferential chloride penetration) than when corrosion was more uniform (as in sound concrete). A quantitative relationship between critical corrosion penetration, rebar cover and diameter, and length of the corroding region was established.

A theoretical analysis of localized corrosion at preexisting concrete cracks indicated that local corrosion rates could be about one order of magnitude greater than under more uniform conditions. The results agreed with independent experimental observations. The above findings indicated that corrosion at localized active spots could result in significant damage after relatively short times following corrosion initiation.

An overall corrosion process forecast approach was formulated based on the findings described above. The durability projections obtained when applying this procedure to substructure built under present FDOT guidelines with the highest concrete grades indicate a generally good prognosis of achieving the 75-year goal, as long as concrete away from stress cracks is considered. For locations where preexisting cracks are present the forecast, although inherently conservative, indicates that a small but noticeable fraction of the substructure built using present design could encounter localized corrosion damage in the near future.   Specialized corrosion control procedures need to be developed in anticipation of this problem.

A next-generation computational approach for forecasting durability of marine substructure was formulated, integrating both the corrosion initiation and propagation stages with evaluation of damage distribution over the entire elevation range of the substructure element. A detailed (rebar scale) predictive model to compute corrosion distribution was also developed. The model successfully reproduced the throwing power of a galvanic system for cathodic prevention in a laboratory system. Application of variations of the model to typical marine substructure conditions indicate that polarization levels in the order of 100 mV may be attained on passive steel in the area immediately above high tide with an immersed galvanic anode.

INTRODUCTION

About two thirds of the 5,500 bridges in the Florida Department of Transportation (FDOT) inventory are exposed to salt water. The resulting corrosion of reinforcement has in the past created serious limitations to the durability of the substructure of those bridges, resulting in continuing need for costly repairs or early replacement of the structure. The nationwide mandate for 75-year durability construction represents therefore an especially difficult challenge when designing new bridges for these aggressive service marine applications.

The 75-year durability goal presumes the adoption of design strategies such as those outlined in the AASHTO-AGC-ARTBA Joint Committee Report on Corrosion Protection [1]. Possible strategies address concrete quality, steel coatings, concrete admixtures, cathodic protection, membranes, overlays and concrete surface coatings. Those are general approaches that need to be selected and tailored to the specific needs of each State.

Implementation of a 75-year design service life (DSL) is in progress and FDOT needs to establish a 75-year DSL policy that fits the unique service conditions encountered in our State. These conditions include a highly aggressive marine environment with consistently high temperatures and humidity, with corrosion severity greatest in the seawater splash-evaporation portion of the substructure. Materials choices and construction practices have also aspects unique to Florida. Corrosion prevention measures that appear to be adequate in other service regimes may not suffice in our environment, as illustrated by the failure of epoxy-coated rebar installed to prevent corrosion in several major bridges in the Florida Keys [2].

FDOT has long recognized special needs for corrosion control and has implemented design practices [3,4] and sponsored continuing research to achieve increasing levels of corrosion protection in new structures. Significant progress towards this goal has been made as a result, and preliminary methods for long-term corrosion forecasting and design are now available to the FDOT. For example, previous research has quantified the rate of chloride ion penetration into the concrete of the substructure of FDOT bridges with an effective diffusion coefficient "D" particular to the structure location and the type of concrete used [2]. The value of D is obtained from analysis of drilled cores. This value, combined with other chemical and structural information, can be used with computational models created for FDOT [2,5,6] to produce a quantitative estimate of the length of the corrosion initiation stage, as is called the service time before external signs of corrosion are observed [2]. Initial surveys have shown that concrete formulations such as those intended for highest performance in Section 346 of the FDOT Standard Specifications for Road and Bridge Construction [4] yield extremely low values of D with consequently long projected durability [2,7]. Those concrete formulations include a high cement factor; a significant amount of pozzolanic cement replacement, usually by type F fly ash (FA) and occasionally by micro silica (MS); and a low water-to-cementitious content ratio (w/c).

Existing preliminary methods of corrosion forecasting are promising as a basis for forecasting durability in an effective 75-year DSL policy. However, at the beginning of this project the FDOT field database on chloride ion penetration was very limited for new concrete formulations that may become the standards of new design. The durability estimation models considered only some of the variables of importance. For example there were as yet no provisions to address the presence of localized chloride penetration paths such as structural cracks, and furthermore, the incidence in the field of defects of this type was not known in sufficient detail for the FDOT structures of interest. Moreover, the earlier forecasting models assumed only a nominal corrosion propagation stage length (after chloride contamination has reached the corrosion threshold) for the formation of cracks in the concrete cover. The actual time may vary considerably from the current assumptions, especially in new FDOT concrete classes.

The present investigation was conducted with the objective of improving forecasting ability by first updating information on the rate of chloride ion penetration, with special attention to the effect of cracks, in the substructure of FDOT marine bridges constructed with the most promising concrete formulations. The resulting information was then applied to improving methods of predicting the length of the corrosion initiation and the corrosion propagation stages, which was then integrated as a comprehensive forecasting model. Finally, part of the information and methods developed were applied in an exploratory manner to evaluate the feasibility of electrochemical corrosion protection methods for extending the durability of new and existing structures. The following tasks were conducted toward achieving those objectives:

1. *Field survey of chloride penetration of concrete in FDOT bridge structures.* In this task 13 bridges in Florida, mostly built recently using the most promising concrete formulations and construction techniques, were examined for the extent of chloride penetration in both sound concrete and at preexisting crack locations. The extent of preexisting cracking was characterized. Parameters descriptive of the rate of chloride penetration (e.g. D) were abstracted from the results and correlated with the concrete formulation and construction properties.

2. *Predictive methods - Corrosion initiation stage.* The mechanisms and data available from the literature and the field survey were used to formulate models for forecasting the penetration of chloride in both sound and cracked concrete under the conditions of interest. The results were considered together with appropriate assumptions on the chloride concentration threshold to formulate an integrated initiation model and a working calculation package was tailored to FDOT applications of interest.

3. *Predictive methods - Corrosion propagation stage.* In this task the extent of steel corrosion needed to cause external cracking was evaluated experimentally, with emphasis on the presence of corrosion localization as may take place when corrosion starts at a preexisting crack. Computer models of corrosion evolution at the rebar size scale were also developed in preparation for future development. The results were

7

used to formulate an integrated propagation stage model for FDOT marine substructures.

4. *Overall corrosion process forecast.* As the main product of this investigation, an integrated initiation-propagation model for FDOT marine substructure elements was formulated with input from the outcome of the previous tasks. In addition, computational methods for the next generation of forecasting tools were formulated and demonstrated.

5. *Evaluation of electrochemical corrosion prevention.* The computational procedures developed in the previous tasks were applied to evaluate the ability of implementing cathodic prevention to extend durability of new or existing marine substructure.

The activities and findings for each of the above tasks are described in the following sections.

1. FIELD SURVEY OF CHLORIDE PENETRATION OF CONCRETE IN FDOT BRIDGE SUBSTRUCTURES

1.1 Structures Investigated

Table 1 lists the bridges investigated with abbreviation identifiers, building date, locations and water chloride content. The bridges were for the most part recently built structures with concrete mixture proportions representative of the current FDOT strategies to reduce chloride penetration and damage from reinforcement corrosion. Some older structures were included for comparison. Table 2 lists information on the type of substructure and concrete present in each bridge, and whether pre-cast (PC) or cast-in-place (CIP) concrete was being sampled. The detailed information in the table originated from direct sources for the particular structure, or was inferred from generic construction information for the class of structures considered if specific information was not available, or as result of tests conducted in the field-extracted cores. Therefore, the listings in Table 2 are subject to revision pending new information. The details on the information and assumptions for each bridge are summarized in Appendix 1.

1.2 Methodology

Note on units: In this and the following sections customary English units are used for most of the reporting, with Metric equivalent usually indicated next in parenthesis with comparable numeric resolution. For convenience and sometimes because the measurements were so performed, the English or Metric units are given only by themselves in Tables and at selected places. A unit conversion table is presented at the end of the report. For conversions from pounds per cubic yard (pcy) to kg/m^3 a rounded-off exact multiplier of 0.593 was used. For conversion from in/y^2 to cm^2/sec a rounded-off exact multiplier of $2.046\ 10^{-7}$ was used.

Field activities were conducted in cooperation with personnel from the Corrosion laboratory of the Materials Office, FDOT. In each structure concrete cores were extracted at the tidal and splash-evaporation zones, as well as the atmospheric exposure zone of one of the bridges. The cores were extracted with a cylindrical 2-in (5 cm) core drill core bit operating at ~200 turns/min, resulting in a core diameter of 1-3/4 in (~4.5 cm). Table 3 is a comprehensive listing of cores extracted and selected associated properties. The core elevations ranged from -2 ft (-0.6 m) to + 120 ft (+37 m) above the high tide (AHT) line. The structures were also examined for incidence of substructure concrete cracking (see below). At several positions in bridges that had cracks, double cores were extracted at the same elevation with one core centered on the crack and the other 6 in (15 cm) to one side. Figures A2-1 to A2-13 in Appendix 2 show sketches of the core extraction spots and relationship to crack surface positions. Extra samples were extracted at most locations and kept for archival purposes. Most cores were extracted using fresh water bit cooling, flowing at a rate of ~1 liter/min. Initially in some cores on cracks the cooling was applied only intermittently, by withdrawing the bit every few seconds while still turning, and briefly pressing against it a sponge soaked in fresh water. Subsequent testing with adjacent cores on cracks, but

9

using continuous cooling, revealed that the chloride concentration profiles obtained with either cooling procedure were similar. Consequently, continuous cooling was used afterwards as the normal procedure.

Cores selected for chloride analysis were dry sliced with a fine-bladed tile saw to obtain sections corresponding to various distances from the external concrete surface. The slicing schemes used (Table 4) sought to obtain thinner but more frequent slices near the external concrete surface where chloride concentration varied rapidly. Each solid slice was ground to a powder separately. In selected cores (slicing schemes 3-6, Table 4) an ~0.08 in - ~0.16 in (~2 mm – ~4 mm) thick region at the external concrete surface was sampled for future analysis (before slicing the rest of the core) by shaving with a hardened steel tool in a lathe and collecting the resulting powder. The concrete powders were chemically analyzed for acid-soluble chloride ("total chloride") content following an adaptation of the corresponding FDOT procedure [8]. The as-ground (no oven-dried) powder mass was used to calculate the chloride content per unit mass of sample. Control tests showed that oven-drying would have typically reduced the powder mass by ~2% to 3%. The results were reported as chloride mass per unit volume, using an assumed unit weight of 4,000 pounds per cubic yard (pcy) (2,374 kg/m^3). Some cores (No. 521-523, 525, 527-533 and 611-616) were extracted and analyzed separately by FDOT supplementary to this study. Entries for those cores in Table 3 contain only partial information. For cores in sound concrete the resulting chloride concentration vs. depth profile was mathematically processed to determine the combination of surface chloride concentration (C_S), background chloride concentration (C_0) and apparent chloride diffusion coefficient (D) that provided a satisfactory numerical fit to a simple diffusion concentration profile per Eq.1.

$$C(x,t)= C_S-(C_S-C_0)\text{erf}\frac{x}{2\sqrt{Dt}}\qquad\qquad(1)$$

where t=bridge age at the time of core extraction and x= distance from concrete surface. Results are reported in Table 5. Because of phenomena that include leaching and shallow surface carbonation, the total chloride concentration immediately below the surface can be significantly less than deeper into the concrete. Thus, for cores with slicing schemes 3-6 (Table 4) the data for slice A was not included in the present calculations but archived for future analysis as indicated in Section 1.3.1 below.

Other selected sound concrete cores were placed in a 100 % relative humidity chamber and exposed until reaching constant weight. The electrical resistivity of the concrete was then determined nondestructively using a 4-point Wenner array probe, correcting for specimen size [9] and reported as the wet electric resistivity (ρ_{WET}) in Table 3. Normally cores were examined for type and size of coarse aggregate, and tested for magnetic attraction [2,10] as a possible indicator of the presence of FA or other magnetic species [10]. The magnetic attraction results, expressed in mg-force, are listed in Table 3 and summarized in Table 2.

Part or all of the substructure of each bridge was normally visually inspected for cracks in the tidal area and elevations up to ~10 ft (~3 m) above high tide (AHT). Cracks on pier caps or superstructure were not included. The cracks were classified per appearance as either shrinkage cracks or stress cracks. Crack widths near extracted cores at the point where the surface was intersected were estimated using a CTL Crack Comparator visual gage and the results are indicated in Table 3. A crack index was calculated as the ratio of the number of stress cracks observed to the perimeter of substructure in contact with the waterline examined. Table 7 presents a summary of the crack survey results.

1.3   Findings on sound concrete

1.3.1   Diffusion parameters

In the following analysis it must be noted that the diffusion parameters estimated by fit to Eq. (1) represent only a highly simplified description of the complex process of chloride transport in concrete. Numerous factors have been ignored, such as the effect of chloride ion binding on the shape of concentration profiles, local characteristics of the concrete immediately next to the external surface, effect of concrete aging on the diffusion rate, and variations in effective surface concentration with time. In addition to model uncertainty, there is also sampling variability from systematic and random aggregate distribution along the core, and the usual experimental scatter associated with chemical determinations plus uncertainty on the actual age of the substructure element examined. Therefore, the values of C_S, D and C_0 listed in Table 5 should be viewed as nominal descriptors of the chloride profiles encountered rather than as parameters with precise mechanistic significance.   A more detailed analysis of the factors at play in chloride transport and the interpretation of experimental profiles from field samples is being addressed in FDOT project BB-880 "Advanced Analysis of Chloride Ion Penetration Profiles in Marine Substructure Concrete" , A.A. Sagüés and S.C. Kranc, P.I.'s, which will be reported at a later date.   Further analysis of selected data from the present investigation will be conducted under project BB-880. Such analysis will include data for near-surface Slice "A" which were not used here.   Further processing of the data in Table 5, with possible reevaluation of diffusion parameters, is anticipated as improved assessment methods become available.

Figures 1 and 2 show composite plots of all the C_S and D values respectively obtained from analysis of the sound concrete cores in all 13 bridges examined. The results are shown as function of elevation AHT. A log-log scale is used to accommodate variability in the results and to reveal broad trends. Data from cores at or below the high tide line have been plotted at the left edge of the graph and the elevation was designated as Tidal.

The results include scatter from the uncertainty sources indicated above, and from actual variability due to different materials and service conditions. A general tendency is nevertheless evident in Figure 2 toward lower values of D as elevation increases. This trend was as expected, as concrete water content near the surface

11

decreases with elevation with consequently slower transport of ionic species such as chloride (although the decrease of D with elevation may also reflect in part ignoring chloride binding in the model used here to analyze the profiles, an effect being addressed under FDOT project BB-880). There is no clearly discernable decay trend of Cs with increasing elevation except when exceeding ~6 ft (~1.8m). To reveal other possible effects of materials and exposure conditions, the results were examined in alternative groupings, focusing on the tidal and splash-evaporation zones where the environment is most aggressive. To that end, the values of D and C_S in the tidal to 6 ft (~1.8 m) elevation range have been plotted in Figures 3-8 for each bridge (and for PC and CIP construction) as cumulative fraction graphs [1]. For several of those structures enough cores were analyzed so that statistical distributions of C_S and D could be roughly evaluated and discussed in the following. The data for structures for which very few cores are available are shown in the graphs for comparative purposes but with no claim of statistical relevance. Median and percentile values mentioned below should be taken in the context of these limitations. The BCB structure was an older bridge with a later expansion using materials of uncertain origin. Data for this bridge are presented only for completeness but generally not considered in the trends discussed next.

Figure 3 shows the cumulative fraction of C_S values in the Tidal to 6 ft (~1.8 m) AHT elevation range for the 8 bridges for which PC components were examined. Not considering BCB, those components show apparent median C_S values between ~20 pcy and ~40 pcy. The high end C_S values (corresponding to elevations close to the high tide level) are in the range of 25 pcy (15 kg/m³) to 70 pcy (42 kg/m³). Comparable trends are observed in Figure 4 for the bridges with CIP components, with some of the distributions starting at and extending to lower values than in the CP components possibly because in CIP structures higher elevation spots in columns on top of footers were routinely sampled. Estimated concentrations much in excess of 50 pcy (30 kg/m³) are probably the result of scatter in the concentration profile data and model uncertainty inherent to the use of Eq.(1). As indicated above, the listed value of C_S is only a projection resulting from the simplifying assumptions used. Consequently, C_S can and often does differ substantially from the value encountered in near-surface samplings such as Slice A. With those qualifications, it was determined that the upper 10th percentile of C_S values for Tidal to 6 ft AHT in all the substructures investigated is about 40 pcy (24 kg/m³) or higher.

The results in Figures 3 and 4 also show that considerably high values of C_S have been reached after as little as 2 years of service. Figure 5 shows C_S data for SSK obtained at ages 7 y [2] and 9 y [11], together with the present results for 11 y, indicating that the median value of C_S did not change significantly (considering the small size of the data set for 9 y) over that age range. Thus, the results support the use of a

---

[1] A cumulative fraction is obtained by the procedure shown in the following example: If a group of 8 cores was extracted from a bridge and 2 of the cores had values of D equal or less than 0.3 in²/y, then the cumulative fraction for D=0.3 in²/y was assigned the value 2/8 = 0.25. For uniformity of presentation, the procedure was used even if the group consisted of very few cores recognizing that the statistical significance in those cases is very limited. The median value of a distribution was defined as the value corresponding to a cumulative fraction of 0.5.

time-independent nominal value of C_S (implicit in Eq.(1)) for approximate evaluation of chloride penetration.

Figure 6 shows the average and range of Cs values for each of the structures as function of chloride content in the water, C_W. There is no discernible trend of C_S as function of C_W in the range examined. High values of Cs could develop even when C_W is quite small, as exemplified by a range of surface concentrations evaluated from reported measurements from the Rafael Urdaneta bridge in Lake Maracaibo, Venezuela [12], and included in the same figure for comparison. That structure was ~40 years old when tested, over which time the chloride content in the lake had increased slowly from 400 ppm to about 3,000 ppm. These findings agree with the expectation that significant evaporative accumulation of chlorides will take place in the splash-evaporation zone. The development of an upper limit of chloride concentration at about 30 to 50 pcy (18 to 30 kg/m^3) can be explained by assuming that the capillary pores of concrete at the surface eventually become filled with a solution much like saturated sodium chloride (containing ~200 g Cl$^-$/liter). If the typical capillary volume porosity ε and concrete Cl-binding capacity are assumed to be ε ~0.1 and C_B ~ 8.4 pcy (~5 kg/ m^3) of concrete respectively [6], the resulting limit value for Cs becomes ~42 pcy (~25 kg/m^3), which is consistent with the typical highest values observed here.

The estimated values of C_0 are as expected typically negligible or on the order of a small fraction of a pcy (kg/m^3), consistent with FDOT specifications for background chloride levels in concrete materials. In a few instances, because the chloride content of Slice G was still quite high, the best fit to Eq.(1) consistent with the data yielded a relatively high value of C_0. Such value is not necessarily representative of the background chloride content of the concrete, and a longer core would have been needed to obtain more accurate results.

Figures 7 and 8 show the cumulative distribution of D values for PC and CIP components respectively of each bridge, for the Tidal to 6 ft (1.8 m) elevation range. Table 6 summarizes the average, minimum and maximum values of D for the same elevation range. The estimated median D values ranged from ~ 0.008 in^2/y (~1.6 10^{-9} cm^2/sec) for SSK to ~ 0.1 in^2/y (~2 10^{-8} cm^2/sec) for NSB, the latter being the only one (except for BCB) showing no magnetic indication of FA presence. Concrete with FA has been reported to show significant decrease of D with time [13]. Such shift is suggested, within the limits of available data, by the results for SSK at 7 y [2], 9 y [11], and 11 y shown in Figure 9.

Despite the natural data scatter and any systematic variations with elevation, the spread of results within each bridge tended with some exceptions (notably DPE) to be moderate. For example, for the Tidal to 6ft (1.8 m) AHT elevation range of SSK, HF and CCC, about 90% of the D values in each bridge were less than twice the median for the same bridge. Median and average D values for each bridge tended to be comparable. The median values for each bridge followed trends expected from the bridge age and concrete mixture proportions used. The lowest median value of D (~0.08 in^2/y) was obtained for SSK, which had a mixture with a cement factor > 752 pcy (446

13

kg/m^3), 20% FA replacement, typical w/c ~ 0.32 and the oldest age (11 years) of the PC group excepting the special case of BCB. Other PC substructures (CCC, BSB, BPB) with age approaching that of SSK, high cement factors and pozzolanic addition also had very low median D values. Younger PC structures (BLP, MIB), with concrete design comparable to the others just mentioned, showed larger D values as expected from aging effects [13].   Comparing bridges of similar ages, the CIP structures with admixed FA tended to show as a group greater D values than the PC structures with admixed FA or Blast Furnace Slag (BFS). This difference likely reflects the use in the CIP structures of Class IV concrete (normally min CF =658 pcy (390 kg/m^3), 0.41 max. w/c) compared with Class V (Special) concrete (normally min CF =752 pcy (446 kg/m^3), 0.37 max. w/c) for PC structures.   The available results showed no clear effect of incorporating MS in addition to FA; but no structures were examined where only MS was used as a pozzolanic addition. No clear conclusion could be derived from the available results on the effect on chloride diffusivity, if any, of using granite instead limestone coarse aggregate, or of the presence of calcium nitrite inhibitor.

Aside from BCB, for which makeup of the piles examined is uncertain, the typical D values of all the bridges examined containing concrete admixed with pozzolans or BFS were quite low compared with the typical D values of mature substructures overall in Florida (median value ~0.1 in^2/y (~2 10^{-8} cm^2/sec)) obtained in a previous FDOT investigation completed in 1993 [2]. Many of the structures examined then were constructed with concrete formulations representative of those used before the introduction of the 346 specifications and concurrent emphasis on high CF, low w/c and pozzolanic admixtures.

1.3.2 Correlation of D with material properties and exposure parameters

The value of the effective diffusion coefficient is affected by many poorly known concrete properties and exposure conditions, limiting the development of an accurate universal relationship between D and these parameters.   However, a practical correlation between D and some of the most important mix design factors may be made, by narrowing the analysis to the type of materials and conditions applying to the low elevation portion of the substructures examined here.   This correlation can then be used to estimate the value of D that may be expected in structures using comparable materials.

The data from SSK indicates that an average value of D ~ 0.01 in^2/y (~2 10^{-9} cm^2/sec)was achieved at low elevations at age 11 years with CF >752 pcy (8 bags), 20% FA replacement and w/c ~0.32.   The available data from the CIP structures of comparable ages indicated that the combined effect of lowering the cement factor to 658 pcy (while still keeping at least 20% FA replacement) and relaxing the w/c to a maximum of 0.41 substantially increased the average value of D, to about 0.04 in^2/y (~8 10^{-9} cm^2/sec).   The average D further increased by a factor of ~3 when no FA replacement was used (NSB).

Based on the above, an approximate relationship is proposed for estimating the value of D (for structures about one decade old) for concrete with mixture proportions likely to be used in future FDOT marine substructures. Mixtures with >752 pcy (446 kg/m^3) cement factor, 18%-30% FA replacement and w/c = 0.32 or less are designated as a base case and assigned a nominal value of D=0.01 in^2/y. Mixtures with w/c between 0.32 and 0.41 and CF between 658 (390 kg/m^3) and 752 pcy (446 kg/m^3) are assigned a value of D greater than the base case multiplied by a factor equal to [1+(w/c - 0.32)/ (0.41-0.32)]*[1+(752 pcy -CF)/(752-658)], where the CF is in pcy. This corresponds to a factor of 2 derating in performance for either increasing w/c to 0.41 or reducing CF to 658 pcy. Use of mixture proportions as those for the Class IV limits (with FA) would therefore result in a nominal D value of 0.04 in^2/y (~8 10^{-9} cm^2/sec), typical of what was observed. Based also on the limited available observations, no nominal benefit is assigned for including MS when FA replacement is already used. However, it is proposed based on evidence from the technical literature [14] that the use of MS alone (to 8%-10% cement replacement) be considered equivalent to using 18%-30% FA cement replacement. Based on the data from NSB, it is proposed that D for mixtures without any pozzolanic or BFS addition be assigned an additional X3 performance derating factor.

Therefore, the following estimating formula is proposed for decade-old structures:

$$D_{estimated} = 0.01 \bullet \left(1 + \frac{\text{w/c} - 0.32}{0.41 - 0.32}\right) \bullet \left(1 + \frac{752 - CF}{752 - 658}\right) \bullet F1 \bullet in^2/y \qquad (2)$$

where   CF is in pcy
        $0.32 \le$ w/c ≤ 0.41 (use 0.32 if w/c<0.32)
        $658 \le CF \le 752$ (use 752 if CF> 752)
        F1 = 1 if $18\% \le FA\% \le 30\%$, or $8\% \le MS\% \le 10\%$, or BFS%=70%
        F1 = 3 if no pozzolanic or BFS replacement is used.

As a test of the applicability of Eq. (2), the concrete data listed in Table 2 for the structures examined here (excepting BCB) was used as input and the result contrasted with the actual average D measurements listed in Table 6. However, since Eq. 2 was developed using as a baseline the behavior of SSK at age 11 y, direct comparison of results from much younger bridges was not expected to be very meaningful. Thus for the purposes of this comparison, the D value given by Eq.(2) was multiplied by a factor F2 = (Age / 11 y)$^{-0.7}$ *(a)*, which represents the estimated age dependence of D reported elsewhere [13,15] for FA containing concretes. The comparison, including the age correction, is shown in Figure 10 which indicates that Eq.(2) gives plausible estimates considering the uncertainty and variability inherent to data extracted from field behavior.

(a) Modified to include minus sign missing in original printed version

1.3.3 Concrete resistivity trends.

Figure 11 shows the average value of D for PC or CIP components of each bridge as function of average resistivity of available cores for the same type of components in the same bridge. The resistivity average was obtained as the inverse of the average conductivity of the cores. As expected, the concretes with the lowest values of D tended to show the highest wet resistivity, which for a given pore water composition increases as the openness of the pore network decreases. The correlation observed by Berke [14] between chloride diffusivity and wet resistivity of laboratory concrete specimens is shown by comparison. While the present results are offset by a factor of ~ 2 from that correlation, the overall trend indicative of a nearly inverse relationship is essentially the same in both cases.   These results suggest that for the type of concretes examined here the wet resistivity may serve through a calibration factor as a rough, supplementary indicator of chloride diffusivity. Another correlation between D and concrete resistivity, matching the general trend and values observed here, has been presented by Bamforth [13].

1.4 Findings on cracked concrete

1.4.1 Incidence and characteristics of cracking

Appendix 2 shows sketches of the surface traces of the cracks present in substructure elements from which cores were extracted and Table 3 lists the observed crack widths. Many stress cracks in footers or piles reached down to the waterline. Table 7 summarizes the overall observations of cracks encountered in the substructure of the bridges examined. Shrinkage cracks are noted but counts are not presented; only a few cores have been extracted centered on shrinkage cracks (Table 3). Stress crack detection was primarily by visual observation from a moving boat at a distance of about 6 –15 ft (2 - 5 m), so the survey could not be exhaustive and the results are only semi-quantitative. Besides, the distinction between stress and shrinkage cracks depended strongly on observer judgment. Nevertheless, the results suggest that incidences in the order of one stress crack every several meters of waterline perimeter are not uncommon. Shrinkage cracks were deemed to be normally superficial; stress cracks often penetrated down to the rebar level and beyond, as shown by the crack trace on extracted cores. There was no evidence of any of the cracks being originated by prior corrosion, and no obvious signs of steel corrosion were observed in any of the sampling coring places on cracks. However, the use of epoxy-coated rebar in some of the bridges may have masked or mitigated corrosion development there so continuing monitoring of those locations is important.

Some of the stress cracks tended to show white efflorescence, but even in those cases the crack width was small, rarely reaching 0.3 mm. The cumulative distribution of the width of the stress cracks documented in Table 3 is shown in Figure 12, indicating a median of ~0.15 mm (some very wide cracks were found in NSB, but those had been epoxy-injected at an earlier date).   The survey confirms that a modest incidence of

stress cracks penetrating to the rebar depth is a regular feature of present FDOT construction methods. Therefore, the effect of crack presence needs to be considered in any realistic service life estimate.

1.4.2 Preferential penetration phenomenology

Appendix 3 shows chloride concentration profiles of pairs of cores (on crack and on sound concrete on the side) extracted at elevations from Tidal to 6 ft (1.8m) AHT, for the bridges that exhibited stress cracks. In most bridges (SSK, HFB, DPE, BSB, SHB, NSB, BCB) there was a marked difference between the chloride concentration profiles of the core on the crack and the core on sound concrete in the same pair. A few cm into the concrete, the core on the crack tended to show significantly higher chloride contents than the core on sound concrete. In most cases the chloride concentration in sound concrete, measured or extrapolated to typical steel depths ($\geqslant$ 3 in (7.5 cm)), was well below values commonly assumed as the threshold levels for corrosion initiation (on the order of one to a few pcy (kg/m^3)). In contrast, in several cases the chloride profiles for cracked concrete suggest that the threshold may have been already exceeded, especially when considering that the concentration reported is an average over the core slice. As it is shown below (and discussed in Section 2.2.1), chloride content immediately next to the crack is expected to be even higher.

One of the cores from SSK (No. 543, 3 ft (0.9 m) AHT) was fragmented by chiseling to obtain concrete samples at various distances both from the external concrete surface and from the crack plane, which was on a vertical and ran approximately along the axis of the core. Each fragment was analyzed for chlorides in the usual manner and the results are shown in Figure 13 as a two-dimensional bar graph. The results illustrate the combination of preferential transport of chlorides along the crack with matrix diffusion from the crack face into the adjacent concrete. The chloride concentration in the concrete immediately adjacent to the sides of the crack was greater than elsewhere at the same depth. This observation should be kept in mind when viewing the chloride concentration profiles for cracked concrete reported in Figures A3-1 to A3-11 , since the chloride contents immediately next to the crack plane can be considerably higher than the average reported for the slice.

The observed enhanced chloride penetration at cracks is notable in that many of the cracks associated with this behavior where significantly narrower than the value of 0.3 mm sometimes quoted as the minimum for concern. As it will be shown in Section 2.2.1, even extremely narrow cracks appear to have the potential for significant chloride penetration under high moisture conditions.

1.4.3 Correlation with material properties and exposure parameters

Core sampling of sound and cracked concrete at SSK involved a large elevation range. The results (Table 5) suggest that the difference between sound and cracked concrete becomes much less pronounced at elevations of 18 ft (6 m) and higher.

Results from DPE, where the elevation range was small, nevertheless indicate preferential chloride penetration only at the cores at the lowest elevations. These findings suggest that narrow cracks act as effective channels for preferential chloride transport only when substantial moisture is available, presumably enough to create a continuous film of water nearly filling the crack. Such behavior may explain why preferential chloride penetration is not so severe for narrow cracks in service with much less wet conditions, such as bridge decks exposed to deicing salts [17]. A model based on the above for preferential chloride penetration in cracked, wet concrete has been formulated and is presented in Section 2.2.1.

2. PREDICTIVE METHODS - CORROSION INITIATION STAGE

2.1 Sound concrete

2.1.1 Fundamental assumptions

The information developed in the field survey can be used for durability forecasting purposes by considering the corrosion initiation and propagation phases mentioned in the Introduction. The length of the initiation stage, addressed in this section, has been approximated with a corrosion initiation model that uses the following simplifying assumptions:

a.   The steel is initially protected from corrosion by the surrounding concrete, which is nearly chloride-free (i.e., $C_0 \sim 0$). Corrosion is triggered only when the concrete in contact with the steel becomes contaminated with chloride ions to a value C_T (expressed as mass of chloride per unit volume of concrete) called the threshold concentration.

b.   Chloride contamination progresses inward from the external surface of the concrete, which is covered by an enriched brine resulting from seawater splash and evaporation. The concrete immediately below the surface has consequently acquired a surface chloride concentration C_S of chloride ions, also expressed as mass of chloride per unit volume of concrete. The value of C_S is constant from the moment in which the structural element is placed in service.

c.   Chloride contamination progresses inward by simple diffusion, driven by the gradient of the concentration of chloride ions in the concrete, with an apparent diffusion coefficient D. The value of D is constant with time and space, and is a property of the concrete between the surface and the steel.

d.   The reinforcing steel is placed with a clear concrete cover x_C, and the structural element is configured either as a flat wall, a two-way corner (convex, as in the edge of a square pile), a three-way corner (convex, as in the corner of a cube), or a round column with a diameter W.

e.　　Given C_T, C_S, D, x_C and the element geometry, the time to corrosion initiation t_i can be calculated based on the model assumptions by application of standard transport equations. These procedures are described in detail in Reference [5] with the exception of the newly introduced geometric rebar effect which is detailed in Section 2.1.3. Corrections can easily be implemented for cases where C_0 could not be neglected.

Specific issues concerning some of the assumptions described above are considered in the following subsections.

2.1.2　Chloride diffusivity values

In the treatment considered here the transport of chloride through concrete is assumed to proceed as in a simple diffusional case, incorporating any complicating phenomena such as chloride binding, moisture transport, and aging of the concrete into adopting a simple time-invariant apparent diffusion coefficient.　The D values obtained in the present survey for modern FDOT concrete formulations, which can be approximately described using Eq.(2), correspond to a typical bridge age of about one decade which is early compared to the 75-year time frame of interest. As mentioned above the literature evidence [13,15,16] and the results in Figure 9 for SSK suggest that the D value of concrete containing FA tends to decrease significantly with time. However, most evidence available at present concerns relatively young concrete and few data exist for structures more than about 15 years old [13,15,16]. It is recommended therefore that the D values estimated using Eq.(2) be used for conservative durability estimates, and that lower long-term values (e.g., half as much as those estimated Eq.(2)) be considered as a less conservative alternative pending the development of confirming evidence as structures age. This issue is considered further in Section 2.3.

2.1.3　Geometric rebar effect

This portion of the work identified an important factor, not previously recognized, in estimating chloride penetration during the corrosion initiation stage. When chlorides migrate into concrete by diffusion, rebars act as a barrier to transport, causing a more rapid increase in concentration at the leading face of the rebar than would be expected from simple one dimensional predictions. The time interval to reach the critical concentration to initiate corrosion can be significantly shortened, reducing the effectiveness of the concrete cover in protecting the steel reinforcing. The purpose of the present effort was to assess the importance of the rebar, acting as a local barrier to diffusive transport, on the development of critical concentration ratios. Estimates of the magnitude of this effect are presented.

Investigations into the importance of rebar size and location on the time to initiation of corrosion of steel rebar in concrete (due to chloride buildup) have been treated for the simple case of rebar imbedded in a semi-infinite concrete specimen.

Results of this investigation can be summarized in terms of a derating factor $T_f < 1$ that can be used to estimate the reduction in time to initiation of corrosion due the presence of rebar. Thus the actual time to initiation is equal to $T_f \bullet t_i^*$, where t_i^* is the time to initiation calculated when ignoring the effect from the presence of the rebar. This work is summarized in Reference [18] and attached as Appendix 4. The principal design information has been extracted and presented here as Figure 14 where T_f is given as function of Φ/x_C , where Φ is the rebar diameter and x_C is the clear rebar cover, and of C_T/C_S.

The results show that ignoring the effect of rebar presence can sometimes lead to substantial overestimation of corrosion-related durability in reinforced concrete. The derating factor is relatively unimportant (e.g. 0.9) for cases of relatively large concrete cover and moderate rebar diameter, but can be substantial (e.g. 0.6) when the ratio of rebar diameter to cover is large or when C_T is large compared to C_S. Thus, the effect can be especially important when corrosion control relies on elevating the chloride concentration threshold for corrosion initiation.

The present work has produced preliminary calculations that will be used to evaluate derating factors for these geometries in future investigations. Since the completion of the paper in Appendix 4, further efforts have been made to understand the influence of the following factors: rebar positioned near an exterior corner, rebar in slabs of finite thickness, rebar lap joints, and rebar crossings. In the case of a rebar located along a 45° line from an exterior corner, the acceleration of chloride penetration due to the rebar presence does not add much over the already strong adverse effect of the presence of the two sided corner (already accounted for in the existing models). For rebars located in close proximity to one another (parallel to the external concrete surface), numerical experiments show that the rebar must be spaced closer than about one diameter for a substantial effect. Significantly stronger derating than for a single rebar is found at low cover-to-diameter values for the limit case of a lap joint of two rebar. The case of rebar crossing was also investigated numerically. The magnitude of additional buildup was found to be relatively small and this case will not be considered further at this time.

2.1.4 Chloride threshold concentration values for sound concrete

Choosing an adequate value for C_T is a difficult challenge as this parameter varies over a wide range of reported values [19]. A detailed review of this issue has been conducted under FDOT Contract BA501 "Metallurgical effects on chloride ion corrosion threshold of steel in concrete", and is described in the Final Report by L. Li and A. Sagüés (P.I.) for that project. The often-quoted value of 1.2 pcy (0.7 kg/m^3) [19,20] seems to be conservative for the concretes considered here, as it corresponds to only <0.2% of the CF. Field evidence for marine substructure suggests that ~0.5% of the CF may be more descriptive of the low end of concentrations associated with the development of sustained corrosion [13]. It is proposed therefore that a value of 1.2 pcy (0.7 kg/m^3) be used for conservative estimates of t_i and that a value equal to 0.5% of CF

(e.g. 3.76 pcy (2.23 kg/m^3) for CF= 752 pcy (446 kg/m^3); 3.29 pcy (1.95 kg/m^3) for CF = 658 pcy (390 kg/m^3)) be used when considering a less conservative approach.

2.2   Cracked concrete

2.2.1 Model and application

The time interval between the creation of a reinforced concrete structural element and the first development of steel corrosion is usually quite long in sound concrete because the aggressive agents such as chloride ions must travel by slow transport mechanisms such as diffusion. As shown earlier, circumstances may be radically different if early cracks develop in the concrete covering the reinforcing steel, since more direct channels to the steel are opened. Such cracks occur as the result of mechanical stresses during the curing process, or structural loads. The purpose of this phase of the investigation (performed partially in conjunction with the execution of FDOT Contract BB-880) was to model the consequences of crack development on the transport of aggressive agents to the reinforcing steel. Here cracks in the concrete are treated in an idealized fashion, in order to construct a simple model amenable to numerical solution.   This work has been summarized in a paper attached in Appendix 5 and to be submitted for publication in the future.

Results of modeling project a rapid build up of chloride ions due to cracks. Incidentally it is noted that in higher quality concrete the chlorides are projected to remain closer to the crack rather than diffusing further away as in lower quality concrete. Repair of the surface may not accomplish the desired result if the concentration remains high around the crack. Efforts were made to compare the results obtained numerically with the physical manifestations of cracks in field extracted core samples. Reasonable agreement was obtained, indicating that the model may account for the chloride content observed in cracked cores. An important finding was that large relative reductions in the crack width (for example from 0.1 mm to 0.01 mm) were not likely to dramatically reduce the overall amount of chloride penetration. In addition, calculations of effective diffusion coefficients for cores extracted on cracks are not likely to be meaningful or useful as these calculations and the evidence presented earlier indicate that the actual chloride concentration in the concrete next to the crack can be much higher than that in the average for the slice.   Consequently, values of the diffusion parameters were not computed (and the corresponding entries in Table 3 were left blank) for the cores extracted from cracked concrete.

The amount of chloride needed to initiate and sustain corrosion at the point of intersection of a crack with the rebar cannot be established with certainty. On first approximation, it may be assumed that corrosion will be initiated if the concrete at the rebar surface immediately adjacent to the crack has a concentration equal to that of the threshold value for sound concrete. This issue requires further investigation.

2.3 Integrated initiation stage model

In the integrated initiation stage model the chloride transport findings addressed above are used to assess when the chloride concentration threshold is reached at the surface of the steel.

2.3.1 Sound Concrete

As part of the scope of the present investigation, a software package ("Time to Corrosion Initiation - Version 1.1") implementing the initiation model assumptions listed in Section 2.1 has been developed. A CD-ROM has been separately delivered as part of an interim report on this project to FDOT in 1999. The program requires input of C_T, C_S, D, x_C and the element geometry, and operates in a prompting mode. Computations are made continually as soon as the required information is complete, and are available in English or Metric units. The program is intended for rapid evaluation of the effect on the time to corrosion of changing values of the input variables, thus facilitating the evaluation of alternative scenarios. If desired, the program will supply default information on C_T, C_S, and D in lieu of user input[2]. The program assumes C_0=0 , but evaluation of cases where C_0 is not negligible can be made easily by subtracting C_0 from both the assumed C_T and C_S values.

To date this program has been tested and utilized by FDOT. It is suggested that updating and expanding this program be considered as part of future investigations. At present the effect of rebar obstruction (Section 2.1.3) must be introduced manually using the derating factor per Figure 14. This and any other newly developed information could be included as an automatic feature in a more advanced version of the program.

Application of the integrated initiation model for sound concrete, based on the field data and suitable threshold assumptions, has yielded generally encouraging projections for the performance of substructure built with the current specifications for aggressive corrosive service in the FDOT Standard Specifications for Road and Bridge Construction. Table 8 shows examples of the resulting projected values of t_i using as conservative assumptions C_T= 1.2 pcy (0.7 kg/m^3) and the value of D from Eq. (2) reflecting data from young structures (C_0 was assumed to be negligible). Less conservative but still reasonable assumptions are also considered by adopting a threshold concentration equal to 0.5% of CF, and assuming that for the long term the value of D will become at most half of what was observed in the present survey of decade-old bridges.   In both cases a typical situation is considered, with D reflecting average conditions and C_S = 30 pcy (18 kg/m^3), and an extreme situation with twice the

---

[2] The default values for D in Version 1.1 were obtained as indicated in Section 1.3 except that the derating for w/c was between 0.37 and 0.41; future versions will include the 0.32-0.41 derating indicated in Eq.(2). The default value of C_S and C_T in Version 1.1 were 40 pcy (24 kg/m^3) and 1.2 pcy (0.7 kg/m^3) respectively. These values will also be updated in future versions to address different scenarios.

average D and C_S = 40 pcy (24 kg/m^3). The extreme situation roughly represents the upper 90th percentile of values obtained in individual bridges during the survey. Both a high performance concrete comparable to that used in SSK (effectively a Class V with low w/c) with 3 in (7.5 cm) cover, and a concrete just meeting the requirements for Class IV with 4 in (10 cm) cover are examined. The flat wall and the more severe 2-way corner cases are illustrated in each example.

Except for the conservative-extreme combined scenario, projected times to corrosion initiation were always longer than 75 years for the high-end concrete and about 40 years or longer for the Class IV concrete just meeting specification.   Under the less conservative, possibly more realistic scenarios the projections for typical conditions amply exceeded 75 years. The conservative-extreme conditions are likely to be overly pessimistic, but serve as a reminder of the sensitivity of the projections to variations in the key predictive parameters. The projections suggest also that stringent concrete and construction quality implementation is important. Previous analysis of the consequences of Eq.(1) [5] indicated that t_i increases with the square of the concrete cover, decreases inversely with the value of D, and varies roughly with only a fractional power of the ratio C_T/C_S. Thus increasing cover in the Class V concrete case from 3 in (7.5 cm) to 4 in (10 cm) would have increased t_i projections by almost 80%. Likewise, if the w/c in the Class IV case would have been 0.37 instead of 0.41, the base value for D per Eq.(2) would have been about ~25% lower with consequent ~25% increase in all the projected t_i values for that concrete.

It must be emphasized that the projections such as those in Table 8 are only nominal estimates subject to considerable model and parameter uncertainty. Additional conservatisms may exist, for example due to ignoring the effect of chloride binding on the concentration profile shape, which tends to cause overestimation of how much chloride will be present at the rebar depth. In addition, as some of the variability in D and C_S may have simply reflected measurement uncertainty, extreme values of those parameters may actually be less severe than they appear to be. Further discussion of the sensitivity of results to the input assumptions, and a statistical approach to predict deterioration when corrosion conditions vary from point to point in a bridge, are available in other publications [21,22].

2.3.2 Cracked concrete

The findings from the field survey in Section 1.4 and the theoretical treatment in Appendix 5 indicate that in the tidal and splash zones preferential chloride penetration at cracks is severe. Even though no clear indications of corrosion were seen at the core-on-crack locations sampled during the present survey, it may be assumed that in the context of a 75 year service life the length of the corrosion initiation stage at a preexisting crack could be greatly reduced compared to that in sound concrete.   In the case of uncoated reinforcing steel the length of the initiation stage at the point where the rebar intersects the crack may be, as a conservative limit, considered to be zero. Corrosion related damage, however, should affect only the very small fraction of the rebar assembly that is immediately around the locations where it is intersected by a

crack. Furthermore, several of the bridges showing stress cracks (e.g. SSK, HFB) were built with epoxy coated rebar. In those cases the situation at the cracks may be much less severe if the rebar coating is generally in very good condition. In such case the probability of a significant coating break being present very near the crack-rebar intersection would be small. In any event, the development of corrosion damage at a crack is expected to be dominated by the propagation stage which is analyzed in the next section.

3. PREDICTIVE METHODS - CORROSION PROPAGATION STAGE

3.1 Sound concrete - nearly uniform corrosion.

The length of the corrosion propagation stage in sound concrete when corrosion acts approximately uniformly over the length of the rebar is usually found to be relatively small (typically only a few years [23]), and as a result much of the emphasis on achieving durability of 75 years or longer is on achieving a long initiation stage. The findings of the previous sections indicate that the advanced concrete formulations presently used in Florida have a good prognosis for achieving that goal. For durability estimates in such cases the total service life could be conservatively estimated as being equal to the length t_i of the initiation stage, or by simple addition of a nominal amount (e.g. 3.5 years [2]) to t_i. This last addition can be further refined by multiplying the nominal amount by the ratio x / 5 Φ (see Section 3.2.2) to account for the effect of the cover to rebar diameter ratio on tp.

If the structure is built with epoxy coated rebar corrosion damage development could be significantly slower, compared to the case of plain rebar construction, depending on the extent of coating distress [2,22]. However, because distress can vary widely, it is recommended that no additional credit for the use of ECR l be taken as a conservative approach in evaluating the length of the propagation stage in sound concrete.

3.2 Strongly localized corrosion

3.2.1 Extent of corrosion localization

When corrosion is localized to a small anodic spot, electrochemical coupling with the surrounding passive steel area forms a macrocell that aggravates corrosion at the anode. In this project, the extent of possible local corrosion intensity was investigated by modeling and comparison with published data.

A detailed description of the work conducted under this contract is presented in Appendix 6, which has also been published in the open literature [24]. The results, obtained for a system with a concrete cover of only 15 mm (0.6 in), indicate that for a variety of plausible concrete conditions the calculated total corrosion current changed relatively little with the size of the corroding region. Thus the corrosion intensity

increased as the size of the corroding spot decreased, and a corroding spot ~2 cm (0.75 in) long, as it may be encountered at the intersection of rebar with a preexisting crack, was projected to experience a local corrosion rate about one order of magnitude larger than corrosion rate experienced by a nearly uniformly corroding rebar under otherwise similar conditions. The calculations indicated also that oxygen transport along the preexisting crack was only a small aggravating factor in determining the local corrosion rate. While calculations for other system dimensions should be conducted for confirmation, these general conclusions are expected to apply also to systems with larger cover over bare rebar where localized corrosion had initiated and was sustained.

It must be cautioned that potential beneficial effects in deeper cracks, such as plugging of the crack by corrosion products, or possible autogenous crack filling processes, are not considered in these calculations which should be viewed as representing a severe limiting case. The absence of observations of severe corrosion in the field examinations suggests that mitigating factors may be operative, which should be carefully investigated in continuing work.

3.2.2 Amount of corrosion needed to crack the concrete cover

If strongly localized corrosion were to develop early in the life of the structure where preexisting cracks intersect a plain steel rebar assembly, the length of the propagation stage may become dominant. This portion of the investigation was conducted experimentally to determine the length of the propagation stage in cases where corrosion was limited to a short portion of a rebar.

A detailed description of the work conducted under this contract has been published in the open literature [25]. Reinforced concrete specimens were prepared containing, under a concrete cover x_C, rebar of diameter Φ of which only a segment of length L was made to corrode. The corrosion was allowed to proceed until a crack appeared at the external concrete surface. The average steel depth loss from corrosion at that moment was measured and called x_{CRIT}. Results (including those from other sources) are summarized in Figure 15. It was found that for concrete exposed to ~85% relative humidity x_{CRIT} was a function of Φ, x_C and L as follows:

$$x_{CRIT} \text{ (mm)} \sim 0.011 \, (x_C/\Phi) \, (x_C/L + 1)^{1.8} \qquad (3)$$

that is, as the corrosion became more localized (x_C/L increasing) the corrosion loss in the localized region needed to be greater to achieve cracking of the concrete cover. Eq. (3) was derived from the data in Figure 15 which apply to the ranges $1 \leqslant x_C/\Phi \leqslant 7$ and $0 \leqslant x_C/L \leqslant 3$, so extrapolation outside those ranges is speculative.

Eq.(3) indicates that a depth of steel corrosion that would have caused cracking under nearly uniform conditions ($x_C/L \sim 0$) would not have been enough to crack the cover when corrosion was localized, indicating some mitigating effect in corrosion induced cracking when corrosion is localized. However, as discussed next, that effect

could be counteracted by faster corrosion at the small corroding region than in the uniform corrosion case, because of the aggravating effect of a corrosion macrocell addressed in section 3.2.l.

3.2.3 Length of the corrosion propagation stage

If the corrosion rate C.R. of the corroding region is constant with time, the length t_P of the propagation stage is given by

$$t_P = C.R. / x_{CRIT}.$$ (4)

When corrosion is uniform, corrosion rates measured in actively corroding steel concrete are on the order of 10 μm/y [2,26]. In a typical substructure application $x_C/\Phi \sim$ 5, so per Eqs.(3) and (4) $t_P \sim$ 5 y which is on the order of the propagation period lengths commonly assumed [2].   If corrosion were localized, for example with x_C/L =3, x_{CRIT} would become about an order of magnitude higher than in the uniform corrosion case. However, the work in Appendix 6 indicates that the localized C.R. is also expected to be about one order of magnitude higher than in the generalized corrosion case, so the length of the corrosion propagation stage for corrosion induced cracking to develop around a small corroding spot may be again on the order of only a few years. Associated spall damage may not be as severe as if corrosion were generalized, as the concrete spall associated with the localized corrosion is expected to be limited to the region immediately around the preexisting crack. On the other hand, corrosion localization could later result in concentrated severe loss of rebar cross section with consequent failure of the bar by mechanical overload, a case less often encountered when corrosion is more uniform.

If the structure is built with epoxy coated rebar with minimal coating distress, localized damage at a preexisting crack is not likely to proceed rapidly unless the crack intersects near one of the few coating distress regions.   A nominal propagation time t_p = 20 years is tentatively proposed for cases of localized chloride exposure of bar with minimal coating distress. This value of t_p is based in part on provisional interpretation of spall data of Florida Keys bridges built with epoxy coated rebar, where it appears that most of the corrosion damage involves a fraction of the rebar assembly with extensive coating distress, while the rest with coating in better condition would have a corrosion propagation period > 20 years [22]. Continuing monitoring of those structures as well as of cracked locations in the bridges examined here will be needed to substantiate this interpretation.

3.3   Supplemental work on characterization of the corrosion propagation stage

3.3.1 Development of a detailed model at rebar scale

As part of the present investigation, work continued on the development of advanced computational modeling, which serves as a basis for examining many issues

related to durability concerns, including estimation of the length of time from initiation to the end of service life and also repair and renovation considerations. Numerical modeling of the distribution corrosion of rebar in concrete structures is complicated by the spatial distribution of the rebar in the volume of concrete, by nonlinear boundary conditions associated with the polarization of the corrosion reactions at the steel surface, and by mass transfer processes of the reactants in the bulk of the concrete. A computational method for solving the governing equations has been developed from finite difference representations and a solution procedure that retains the nonlinear character of the boundary conditions. A strategy was successfully devised to compute the local potential and current density at the rebar surface with a minimum of computational effort. This phase of the overall investigation has been published [27] in a paper where both the problem of free corrosion and cathodic protection are discussed for the example of a square slab, reinforced with a double mat of crossing rebar (Figure 16). Although ultimately it is expected that this effort will be integrated with the development of damage function predictions, it appears that at present computational limitations prevent application to large scale problems. This model has however produced useful results in analyzing cathodic prevention scenarios, as discussed in section 5.

4.   OVERALL CORROSION PROCESS FORECAST

4.1   Integrated Initiation-Propagation model for FDOT marine substructure elements.

The findings from Sections 1 to 3 can be integrated into an overall approach to anticipate durability of FDOT marine substructure elements. This approach addresses the region most at-risk, which is the combined tidal and splash-evaporation zone, extending roughly from just AHT to about 6 ft (1.8 m) AHT, and concentrates on the worst-case elevation within that range.

4.1.1 Sound concrete

For portions of the substructure away from preexisting cracks the following parameters are used as final inputs for estimating the combined length of the initiation and propagations stages: C_S, C_T, concrete cover x_C, D, geometric configuration (flat wall, 2- or 3-way corners, round column) and rebar diameter Φ. The following recommended procedure applies:

1)   Assume C_S to be 30 pcy (18 kg/m^3), per the findings in Section 1.3.

2)   Conservatively estimate D as function of the following concrete property inputs: CF, w/c, presence of FA (18%-30%), presence of MS (8%-10%), or presence of BFS using Eq.(2) in Section 1.3.2 . As a less conservative alternative, assume D for FA concrete to decay over the long term to ½ the value estimated using Eq.(2).

3)   Assume C_T to be equal to 1.2 pcy (0.7 kg/m^3) as a conservative estimate, or

compute $C_T = 0.005$ CF (i.e. 0.5%) as a less conservative alternative.

4) Depending on structure geometry select Flat Wall, 2- or 3- corner, or round column configuration.

5) Select clear concrete cover depth x_C.

6) Obtain interim estimate of time to corrosion initiation, t_i^*, by inputting the parameters determined in Steps (1) to (5) in the program "Time to Corrosion Initiation"

7) For a flat wall case (and also conservatively for round columns) calculate the ratios Φ/x_C and C_T/C_S , and obtain the rebar obstruction derating factor T_f using Figure 14. Obtain final value of time to corrosion initiation using $t_i = T_f t_i^*$. For 2- or 3- way corners, use $t_i = t_i^*$.

8) Calculate the propagation time $t_p = (x / 5 \Phi) \bullet 3.5$ y (conservatively assume no credit for epoxy coated rebar in sound concrete).

9) Time for development of observable corrosion damage is given by $t_c = t_i + t_p$.

The examples in Table 8 can serve as illustration of the outcome of this procedure, by addition of the corresponding value of t_p, which in most of those examples represents a relatively small additional period.

4.1.2 At preexisting crack locations

For locations where preexisting cracks intersect the rebar it is conservatively assumed that ti = 0 y for both plain rebar and epoxy coated rebar. Therefore the estimated time for local development of corrosion damage is $t_c = t_p$ per Step 8 above for plain steel rebar.

Based on the assumptions indicated in Section 3, for epoxy coated rebar with minimal coating distress tentatively assume $t_c = 20$ y. In either rebar case the estimated t_c for cracked concrete is usually substantially less than for sound concrete. Although inherently conservative, these estimates project that a small but noticeable fraction of the substructure in FDOT marine bridges is likely to encounter localized corrosion damage in the near future. Specialized corrosion control procedures need to be developed in anticipation of this problem.

4.2 Supplemental work on overall corrosion process forecast

This portion of the work addressed development of a next generation of forecasting tools for marine substructure, integrating both the corrosion initiation and propagation stages with evaluation of damage distribution over the entire elevation range of the substructural element. This work has been presented in the open literature

and is detailed in Appendix 7. The work is preliminary in nature and does not take into account potentially important issues such as the effect of chloride concentration gradients on transport of ionic species, to be treated in future work.

5.   EVALUATION OF ELECTROCHEMICAL CORROSION PREVENTION

The computational procedures developed in the previous tasks were applied to evaluating the ability of cathodic prevention to extend durability of new or existing marine substructure.

5.1   Cathodic prevention in footers/piles

Cathodic protection (CP), implemented either as an impressed current or as a sacrificial anode system, has been successfully used to mitigate corrosion on reinforced concrete structures. One relatively recent variation of the CP technique is cathodic prevention (CPrev) [28-34] for new reinforced concrete structures. To date, CPrev has been principally used to protect atmospherically exposed structures (e.g., bridge decks), by means of impressed current systems [28-33]

CPrev delays the onset of corrosion by polarizing the still passive steel reinforcement to a more negative potential at which corrosion is less likely to initiate. Additional benefits may accrue by slowing the migration of chloride ions toward the rebar and by increasing OH^- concentration at the rebar surface. Although this technique requires a system similar to that used for CP, in contrast to CP, CPrev is usually applied early in the service life of the structure, before the initiation of corrosion. Thus, the system is usually installed during the construction of a structure, and energized a short time later. Since the rebars are in a passive state, the required applied current is much smaller than that normally needed for CP. Cathodic polarization by approximately 100 mV is said to increase the chloride threshold for initiation of corrosion by as much as an order of magnitude [28-29]. More recent publications [35-39], based on experiments conducted in reinforced concrete or mortar cells, suggest that cathodically polarizing the steel from   −100 to -200 mV (SCE) increases the chloride threshold by at least 1.5 to 3 times.

CPrev may be an attractive method to protect new marine reinforced concrete substructures (MRCS) using simple sacrificial submerged anodes, which are economical and easy to replace. The portion above water (AW) may be more protected than in conventional CP because of the lower current demand. It is therefore of interest to find how high above water sacrificial submerged anodes may be able to provide CPrev in these systems.

A literature search found only one published work to date reporting the use of CPrev on a partially submerged structure with sacrificial submerged anodes [29]. In that investigation, only the bottom fifth of a 1 m high laboratory specimen was submerged in artificial seawater, but the whole specimen was found to be cathodically polarized 100

mV or more. These results were encouraging but the test system had not been thoroughly characterized. Additional investigation beyond this limited experiment is needed, and computer modeling offers a powerful means for this evaluation.

In the present investigation, both a CPrev experimental installation and computer models of corrosion distribution in reinforced concrete were utilized to evaluate the extent of CPrev for partially submerged piles provided by a bulk sacrificial anode placed below water. The experiments were made on laboratory columns that were available from an ongoing investigation. For the computational models, a pile was assumed to be at the beginning of its service life, with passive rebar. The models used as input parameters the concrete electrical resistivity, oxygen diffusivity (one model version only), and the cathodic polarization parameters and iron dissolution rate at the passive rebar, obtained from experimental measurements or from values reported in the literature. The experimental and model results describe the state of the system after connection of a zinc sacrificial anode. These results are used to gain insight as to what throwing power above water can be achieved.

5.2   Experimental Arrangement

Four existing reinforced concrete columns were tested (Figure 17) [40]. Each column had 11 horizontal rebar segments, each segment with an exposed surface area of 166 cm^2. The segments were numbered starting from #1 at the top of the column. Only segments #1 to #8 (or #1 to #9 depending on the column), which were in the passive condition, were used for these experiments. The remaining lower segments were in the active condition and were kept isolated. Electrical connections to all segments and embedded reference electrodes [41] were routed to a switch box. The switches kept the segments to be used normally interconnected. During the experiments sacrificial zinc bulk anodes were connected to the passive rebar segment assembly and the extent of cathodic polarization of those segments was determined.

The rebars were commercial #7 stock made of plain carbon steel (0.23 % C) and as-received had a high temperature mill scale. The rebars were intentionally pre-rusted by dipping in a 3.5% NaCl solution. The concrete had a water-cement ratio of 0.45, 360 kg/m^3 Type I Portland cement, and sand as fine aggregate. The coarse aggregate was limestone with maximum size of 1 cm. The concrete mix for the lower 25.4 cm of each column had 11.9 kg/m^3 Cl$^-$ added, by including the appropiate amount of NaCl. Since construction, 9 ½ years before these tests, the columns were placed in a tank with the lower 12.6 cm submerged in salt water (5% NaCl solution). The average temperature and relative humidity (RH) were 21.5°C ± 2°C and 60 % ± 15% respectively in the laboratory during the time that the CPrev system was in place. Two of the columns (named Set W) had been subject to periods of fresh water wetting in the past and retained overall lower resistivity than the other two columns (named Set D). Figure 18 shows typical concrete resistivities as a function of elevation, obtained with a.c. measurements described elsewhere [42].

The rebar static potential measured against the embedded reference electrodes, inter-rebar segment current and inter-rebar segment concrete resistivity were monitored before and during the application of CPrev. The rebar static potential was converted to the saturated calomel electrode (SCE) scale by periodically calibrating the embedded reference electrodes vs. a SCE. All reported potential values are referred to SCE scale. Also, all potentials are presented corrected for ohmic potential drop (obtained using information from periodic instant-off measurements). The current density delivered by the anode to each of the rebars segments was calculated from the inter-rebar segment current measurements and accounting for the rebar surface area. A depolarization test was conducted after CPrev had been applied for 120 days. The depolarization test consisted of disconnecting the anode and opening all switches at the same time then registering the subsequent evolution with time (up to ~22 hrs) of each rebar segment potential with respect to its corresponding embedded reference electrode. Net depolarization values were reported as the difference between the instant-off potential (just after disconnection) and the potentials measured subsequently during the rest of the test.

The CPrev test was preceded by a conditioning period, in which it was determined that the top 8 and 9 segments were passive on column sets W and D respectively [42]. Also during the conditioning period the interconnected passive segments were allowed to develop steady conditions for at least 100 days after isolation of the active segments. Just before the beginning of CPrev the potentials of the passive rebar segments ranged from –35 mV to 10 mV. There was less than 10 mV difference from the top to the bottom passive rebar segment in any given column, and on all these segments the net current density was less than 0.001 $\mu A/cm^2$. To start CPrev application four commercial Zn bulk anodes (one per column) were placed in the water and then separately connected to the passive rebar assembly of each column.

5.3   Experimental Results

Upon connection of the anode to the passive rebar segments (Day 0), there was a brief (~1 day) transient period after which relatively steady conditions developed. The anode connection resulted in cathodic polarization of the rebar segments (especially pronounced at the lower rebar segments). The potential and current densities measured at each rebar segment varied moderately with time, likely reflecting variations in the concrete resistivity due to changes on the degree of water saturation of the concrete as the room RH varied.

Potential and Current Delivery of Anodes. Figure 19 shows the average instant off potential values and the average current delivered by the anodes over time, grouped by column type over time. The average anode potential values were ~ –1020 mV with currents on the order of 1 mA, as expected from commercial Zn anodes of this type.

Currents Density Delivered by the Anodes to each Rebar Segment. Figure 20 shows the cathodic current densities delivered to each rebar segment during the first 305 days of CPrev aplication on column W1. Similar trends with time were observed in the other

three columns. The bottom three rebar segments in all columns received at least 0.1 $\mu A/cm^2$, and the lower segment as much as ~5 $\mu A/cm^2$. The five upper rebar segments on columns of Set W received about one order of magnitude larger current density than the corresponding rebar segments in Set D. Average values for both sets are shown later in Figure 26.

Potential Values of Rebar Segments During Cprev. The average and range of potentials for each rebar segment are shown in Figure 24 (grouped per column set). Pairs of corresponding rebar segments (e.g. #1 segments in Set W) had very similar average potentials, typically within 15 mV of each other.

Polarization. Polarization is defined here as the downward steady state potential shift of each rebar segment, corrected for ohmic potential drop, resulting from anode connection. Table 1 shows the results for each of the four columns obtained by averaging over the first 305 days of CPrev application, but excluding the first day transient. All the rebar segments in the W columns were polarized by at least 100 mV by the Zn bulk anode. This performance is significant considering that concrete resistivity measured was substantial (>70 kΩ-cm above 60 cm elevation) at the upper levels. Polarization > 100 mV in columns of Set D only reached up to rebar segment #6 (60 cm elevation), but concrete resistivity was already 500 kΩ-cm at that elevation. From Figures 25 and 26 it can be observed that the current density required to obtain 100 mV polarization was ~ 0.01 $\mu A/cm^2$, confirming the very low current demand for CPrev. This also agrees with the results presented in the following section.

Polarization Curve – E-log i Curve. The rebar potentials and the net current densitiy values for all the rebar segments measured at day 80 with CPrev were used to build an E-log i graph, Figure 21. The shape of the plot suggests that most of the segments were under cathodic activation polarization, and cathodic polarization parameters can be calculated from the data shown on this figure. The line fitted through the straight portion of the plotted data by regression analysis, indicates a cathodic Tafel slope β_c ~ 145 mV/decade. The magnitude of the passive rate of dissolution i_p was estimated by assuming that the plateau apparent near   ~-45 mV in Figure 21 corresponds to a condition approaching zero net current, i.e. where the passive current density i_p equals that for oxygen reduction at that potential. This assumption is supported by the observation that the open circuit potential (OCP) of steel in concrete is typically ~0 mV to -100 mV [43,44], roughly the same as that of the upper segments of the columns examined here. Thus simple Tafel extrapolation of the cathodic current to the point where potential ~-45 mV in Figure 21 indicates i_p ~ 2.5x 10^{-3} $\mu A/cm^2$. The values of the oxygen reduction exchange current density and effective equilibrium potential (i_{OC} and E_{OC} respectively) are not known individually, but if one of them is arbitrarily chosen the other can be defined so that any resulting segment potential-current density pair falls along the Tafel line. For convenience a nominal value of E_{OC} = 100 mV was chosen, which resulted in a nominal value of i_{OC}=2.5x10^{-4} $\mu A/cm^2$.

Depolarization Test. Figure 22 and 23 show net depolarization curves for the rebar segments of columns W1 and D1. Very similar curves were observed on columns W2

32

and D2 respectively.   The lowest segment in the D columns (#9) was in a zone of very moist concrete. The initial depolarization of segment #9 was much slower than for segment #8 in the same columns, likely as a result of slow oxygen transport through the wet concrete. This observation suggests that there was a significant component of concentration polarization in segment # 9, also supported by the large deviation from apparent Tafel behavior observed for that segment in Figure 21.

Polarization vs Net Depolarization. The observed net depolarization after 22 hours was in average 53% of the separately determined polarization. This behavior is not surprising in view of previous reports [45] that the depolarization of steel in concrete obtained after 4 hours can be as little as 25% of the total polarization.

5.4   Modeling

Two modeling approaches were implemented: a three-dimensional (3-D) model, which handled combined activation concentration polarization cathodic behavior and a simplified one-dimensional (1-D) model. The 3-D model replicated the geometry of the laboratory column and was computationally demanding, whereas the 1-D model required less resources.

5.4.1   3-D Model Description

A brief description of the 3-D model is presented in this section and includes the model governing equations, boundary conditions, model inputs and outputs, and the solution strategy. This model is a modification of previous work described in detail elsewhere [27,46].

a) Governing equations. The concrete was treated as a homogeneous medium, but with both concrete resisitivity and oxygen diffusivity varying on the vertical direction.

The current density in the bulk of the concrete (termed i) was calculated by

$$i = \rho^{-1} \nabla E \tag{5}$$

where ρ concrete resistivity, E=potential in concrete. The potential and the concentration of oxygen in the bulk of the concrete obeyed charge and mass concentration requirements:

$$\nabla(\rho^{-1}\nabla E)=0 \tag{6}$$

$$\nabla(D_o\nabla C)=0 \tag{7}$$

where D_o=Oxygen diffusivity, C=Oxygen concentration

b) Boundary conditions. The oxygen flow on the steel surface was related to the cathodic current density by Faraday's Law:

$$i_c = 4FD_o \frac{\partial C}{\partial n} \qquad (8)$$

where n=normal direction to the rebar surface, F=Faraday constant. On the surface of the concrete the oxygen concentration was assumed to be constant. It was assumed that at the ends of the column there was no oxygen transport. At the rebar, the iron dissolution reaction was assumed to proceed at a small and constant rate described by the anodic passive current density i_p. Oxygen reduction was assumed to follow Butler-Volmer kinetics:

$$i_c = i_{oc} \frac{C}{Co} e^{(E-E_{OC})/\beta_c} \qquad (9)$$

where Co=effective oxygen concentration of concrete in direct contact and equilibrium with air, β_c = cathodic Tafel slope. The reverse reaction is ignored.
Above the water line the current flow through the outer concrete surface was set to zero. The surface of the concrete submerged in 5% NaCl solution was assumed to be equipotential. As the resistivity value of 5% NaCl solution ($\rho \sim 20$ Ω-cm) is much smaller than those assumed for the concrete, the assumption of an equipotential concrete-solution interface was considered to be a justifiable approximation.

c) Model inputs. The model inputs are: concrete properties (resistivity and an oxygen diffusivity as function of elevation), values for the electrochemical polarization parameters, and values for the constant boundary conditions (oxygen concentration at the surface of the concrete and the equipotential value for the submerged portion of the column). The resistivity profiles used for the model were based on the measured resistivities presented in Figure 18.

The values for polarization parameters used in the model were based on the experiment results (E-log i analysis): i_{OC} = 2.5x10^{-4} μA/cm^2, E_{OC}=100 mV, β_c =145 mV/decade and i_p = 2.5x 10^{-3} μA/cm^2. A value of –1020 mV was used as a nominal working anode potential. The effective concentration of O_2 was expressed in moles of O_2 per cm^3 of pore water in concrete. Thus, the concentration of O_2 (Cs) at the concrete surface was set to Cs=3x10^{-7} moles/cm^3 (atmospheric conditions [47]). The values of D_o were chosen as indicated in reference [46], modified as follows: For regions below the water line D_o=6x10^{-6} cm^2/sec. When ρ > 60 kΩ-cm, D_o = 6x10^{-4} cm^2/sec. For portions in between, D_o was obtained by interpolating over log (ρ). These values are also consistent with the units used to represent the oxygen concentration.

d) Solution strategy. The calculations were made using finite difference approximations. The columns and rebar were represented on a three dimensional grid system, with a

grid spacing of 0.9 cm in all directions. The No. 7 rebar was simulated by a square section 1.8 cm per side, which resulted from combining 4 square grid elements. The Jacobi [48] iterative method was used to obtain the numerical solutions.

e) Model outputs. The immediate model outputs are the concentration of oxygen and potential everywhere in the concrete. The following information was extracted from the immediate outputs:
- The current delivered by the anode to each rebar segment, (Sum of the current values corresponding to each discrete element forming the segment)
- The potential of each rebar segment, (Average of the potential values corresponding to each discrete element forming the segment)
- The polarization at each rebar segment (Segment potential before, minus segment potential after CPrev application).

5.4.2 3-D Model Results vs. Experimental Values

Figure 24 shows a comparison of the computed and experimentally determined potential of the rebar segments at different elevations. Figure 25 shows a comparison of the computed and experimental polarization of the rebar segments in each column set as function of elevation. In both cases, reasonable agreement between the experimental measurements and computational model was observed.

Figure 26 shows the calculated and measured cathodic current density delivered by the anode to each of the rebar segments. The calculated current density delivered to each segment and trends with elevation compared well with the measured behavior in most instances. However, it is important to note that in the few cases where a larger relative difference in current density occurred, the measured current densities were very small (e.g. upper segments of Set D, experimental current density < 0.001 μA/cm^2).

5.4.3 1-D Model Description and Implementation

A simpler 1-D model was developed, that retained most of the properties of the 3-D model, but requiring a small fraction of the computational resources. This 1-D model is a modified version of one developed previously [49], implemented for conditions similar to those modeled with the detailed 3-D model. A major difference between both models was that the 1-D model did not include provisions for oxygen transport.

A brief description of the 1-D model is as follows. The column was assumed to consist of a stack of discrete steel segments in concrete, all segments considered to be net cathodes. A constant potential source simulated the Zn anode. Figure 27 shows an idealized column with interconnected segments and the corresponding large-signal electrical equivalent circuit, for the case where segments 1 to 9 (or 8 if from set W) are net cathodes. Rc_i is the effective concrete resistance between consecutive rebar

35

segments j and j+1. Is_j is the current associated with rebar segment j. E_1 to E_9 (or E_8) are current-dependent voltage sources representing the potential difference across the metal-concrete interface of the corresponding regions. All segments were considered to be subject only to activation polarization, so that for rebar segment j:

$$E_j = E_{OC} + \beta_C \log \frac{\left|Is_j\right| - I_p}{I_{OC}} \qquad (10)$$

where β_c is the Tafel slope for the cathodic reaction, the passive current I_p was used as a constraint to bound the results to the observed OCP, and I_{OC} is the exchange current for the cathodic reactions at the equilibrium potential E_{OC}. The polarization parameter values were as in the 3-D model. Since all cathodic rebar segments within a column have the same amount of effective surface area A_C, then $I_{OC}=i_{OC}*(A_C)$, similarly $I_p=i_p*(A_C)$.

The effective resistance of the concrete joining consecutive segments j and j+1 was approximated by $Rc_j= \rho_j * d / A_{CS}$, where ρ_j is the measured resistivity of the concrete between the two segments, A_{CS} is the cross-sectional area of the column expressed in cm^2, and d is the vertical distance between segments.

Independent equations were formulated, establishing a zero-potential sum for each of the 9 (or 8 if set W) closed loops in the ladder circuit in Figure 27. An additional equation was provided by the requirement that the sum of all the cathodic currents needs to be equal to current of the anode. The resulting system of 10 (or 9) equations was solved numerically to obtain the 10 (or 9) values of Is, using as input the resistivity profile of the column, the polarization parameters of the cathodic reaction, and the Zn anode potential.

The results from both models were in reasonable agreement for comparable calculations, as presented in Figure 28, which reproduces Figure 25 but with the addition of the 1-D model results. The major discrepancy between the 1-D model and the 3-D model is at the lower segment of Set D, as expected since this segment is likely under partial concentration control. These results suggest that the simple 1-D model can be used to do exploratory calculations of field size structures for the portion above high tide (little oxygen diffusional limitation) at a fraction of the computational time needed by the more detailed 3-D model.

5.5   Estimation of the Throwing Power on Field Size Structures using 1-D Model.

Having established reasonable confidence in the 1-D model, modifications to represent cases replicating field size structures were implemented. The throwing power on field size structures provided by a Zn bulk anode was quantified with this 1-D model to evaluate the applicability of this approach to obtain CPrev. The model calculations

focus on the portion above high tide where little oxygen diffusional limitation is expected.

5.5.1 Assumptions Made to Represent Field Size Structures.

Columns of two different lengths were modeled: one was 5 m long, typical of field size structures and the other 120 m simulating an infinite length limiting case for conservative evaluation. The column, of selectable diameter ϕ_{col}, was divided into a stack of discrete elements. Fourty-eight segments were used with a segmented thickness dx =0.104 m to discretize the 5 m column. The first 1.25 m of the 120 m column were divided into slices of thickness of dx=0.104 m, above this coarser segments were used. Figure 29 shows how the columns were discretized and also the corresponding equivalent circuit.

The current and potential distribution in the column was modeled by assuming a constant anodic passive current (i_p= 2.5x10^{-9} A/cm^2 as in the experiment or i_p= 1.x10^{-8} A/cm^2 as a more conservative value [50]), accounting for the polarization behavior of the cathodic reaction, and for simplicity a constant electrical resistivity (ρ) of the intervening concrete. When calculating the I_{OC} and I_p (per Eq. (10)) of each slice, appropriate account was made for the steel surface area of that slice.

The resistance of each slice was $R_j=dx_j*\rho/A_c$, where A_c is the column cross-section area ($\pi\phi_{col}^2/4$) and dx_j is the length of slice j. The current is proportional to the steel area (A_s) per unit length. The ratio of A_s to the external surface area per unit length of the concrete (A_{con}) is termed the steel factor (SF). In typical marine substructures applications SF is often in the order of unity [51].

Either β_c=145 mV/decade (similar to the value derived from Figure 21) or β_c=100 mV/decade (as a more conservative alternative) were used as parameters. i_{OC}= 2.5x10^{-11} A/cm^2 was used in combination with appropriate E_{OC} values from 235 mV to 113 mV so as to have an open circuit potential of ~−100 mV, representative of typical passive steel values observed when CPrev is not in place.

The presence of the Zn anode was simulated by connecting a constant potential source (-1 V in this case) beneath the lowest column slice component. The appropriate intervening concrete resistance between the lower slice and the anode was used. Similarly to the 1-D modeling of the laboratory columns appropriate equations were written and solved numerically. From the calculated polarization values, the elevation in the column where the polarization reached 100 mV or 200 mV was determined and designated as the throwing power h_{throw} for that polarization level. The 100 mV was chosen because, as indicated in the introduction, a substantial increase in the chloride threshold has been reported for that polarization level. The 200 mV value explores a more conservative condition.

5.5.2 1-D Model Field Size Structures. Results and Discussion.

For a given column length and polarization level, the value of h_{throw} depends on the values of ρ, ϕ_{col} and SF. The equivalent circuit in Figure 29.b is that of a uniform transmission line [52], which permits combining these three parameters into a single normalizing parameter: $P = SF\rho/\phi_{col}$, having the dimension of resistance (Ω). This parameter was used in the generation of the performance curves shown in Figures 30 and 31. In these figures the dotted lines correspond to columns 5 m long, and the continuous lines to unlimited height columns. The i_p and β_c value choices discussed above were used.

The significance of the results presented in Figure 30 may be understood by considering the case of a tall substructure column of typical size and steel density, for example ϕ_{col} =100 cm and SF=1. When the concrete resistivity is 10 kΩ cm (a value typical of medium quality concrete [53-55]) P is equal to 100 Ω, in the middle of the x axis. For such case and with steel having polarization characteristics similar to those encountered in the laboratory columns (β_c=145 mV/decade, $i_p = 2.5 \times 10^{-9}$ A/cm^2), h_{throw} was approximately 2 m. This projection indicates that cathodic prevention (polarization > 100 mV in Figure 30) by a submerged zinc anode may be achieved under these conditions typical of much of the tidal and splash evaporation zone. However, if all else were to remain the same but ρ was instead 100 kΩ–cm (e.g. very low permeability concrete, or drier overall conditions than in the previous case), h_{throw} would become only ~ 1m and the >100 mV prevention levels would be limited to the lower splash zone.   If the cathodic reaction were less polarizable than assumed above, for example having β_c = 100 mV/decade and $i_p = 10^{-8}$ A/cm^2, h_{throw} would become only ~0.5 m or ~0.3 m for the 10 kΩ–cm or 100 kΩ–cm cases respectively. Again, under these circumstances polarization levels > 100 mV would be achieved only in a fraction of the lower splash zone. Intermediate cases can be evaluated by reference to the appropriate curves. Except for combinations of highly conductive concrete with large column diameter / low steel density, the 5 m long columns behaved similar to the unlimited height cases. It should be noted that polarization may reach further than indicated in Figure 30 if significant concentration polarization were to exist at the lower elevations.

Figure 31 shows curves for polarization levels > 200 mV. For P equal to 100 Ω (as in the previous paragraph) and with steel having polarization characteristics similar to those encountered in the laboratory columns, h_{throw} ~0.8 m, protecting only the lower splash zone. This distance is only 40 % of the distance observed when considering 100 mV polarization. With ρ equal to 100 kΩ-cm and all else the same, h_{throw} becomes only 0.3 m and only a portion of the lower splash zone would be protected. If the cathodic reaction were less polarizable, for example having β_c = 100 mV/decade and $i_p = 10^{-8}$ A/cm^2, h_{throw} would become only ~0.23 m or ~0.12 m for the 10 kΩ–cm or 100 kΩ–cm cases respectively. Under these circumstances polarization levels > 200 mV would be marginal and achieved only in a small fraction of the lower splash zone.

The estimates obtained with the 1-D model adapted to field size structures suggest that with an immersed anode potentially useful levels of cathodic prevention

may be reasonably expected, even under conservative assumptions, in the area immediately above high tide where conditions are otherwise very severe. The use of sacrificial CPrev anodes then appears to be promising in controlling corrosion in a region where early damage is often observed.   These estimates suggest also that Cprev implemented using bulk anodes may not be effective at higher elevations unless a favorable combination of system dimensions and electrochemical properties is present. A more pessimistic overall outlook results if at least 200 mV polarization is needed for adequate CPrev. Further testing should be conducted to reduce uncertainty in the expected range of concrete and steel polarization properties. Such information would allow removing some conservatism in the projections and refine the prognosis for CPrev at higher elevations on substructural elements.

The 1-D model used to evaluate CPrev application could be easily adapted in future work to evaluate the ability of immersed anodes to provide conventional cathodic prevention to substructural elements with small anodic regions, as may be present where preexisting cracks intersect rebar. Another alternative future application could address similar implementation of CPrev to substructural elements with epoxy coated rebar with various levels of coating distress.

5.6   Summary of findings on evaluation of electrochemical corrosion prevention.

CPrev using sacrificial zinc bulk anodes was investigated on aged laboratory columns simulating partially submerged piles. It was observed that rebar segments receiving a current density >0.01 $\mu A/cm^2$ were polarized by >100 mV.

The 3-D model and the 1-D model simulations were compared with the experimental results. Both models successfully represented the reduction in throwing power resulting from an increase in concrete resistivity. The results of both models were generally similar to the measured values except that the 1-D model (which did not include combined cathodic polarization provisions) did not match well the behavior of a segment low in the column subject to partial oxygen concentration polarization. Since the 1-D model required a fraction of the computational time of the 3-D model, the 1-D model was used for exploratory calculations of field size structures for the portion above high tide

The estimates obtained with the 1-D model adapted to field size structures suggest that with an immersed anode polarization > 100 mV may be reasonably expected, even under conservative assumptions, in the area immediately above high tide where conditions are otherwise very severe. These estimates suggest also that Cprev implemented using bulk anodes may not be effective at higher elevations unless a favorable combination of system dimensions and electrochemical properties is present. The 1-D model used to evaluate CPrev application could be easily adapted in future work to evaluate the ability of immersed anodes to provide conventional cathodic prevention to substructural elements with small anodic regions, as may be present where preexisting cracks intersect rebar.

6.   CONCLUSIONS

1.   Sound concrete made per Section 2 of the FDOT Structures Design Guidelines with high cement factor, low w/c and pozzolanic cement replacement exhibits very slow chloride penetration in aggressive marine bridge substructure service. The best performing concrete (>752 lb/yd^3 (446 kg/m^3) cementitious content, FA cement replacement, and w/c~ 0.32), comparable to a Class V formulation, showed an average value of the apparent diffusion coefficient (D) of about 0.01 in^2/y (~2 10^{-9} cm^2/sec) at age 11 years in the Tidal to 6 ft (1.8 m) above high tide (AHT) region. A simplified relationship was proposed to obtain the expected value of D for the type of conditions examined here, as function of cement factor, w/c ratio, and presence of pozzolanic admixture or BFS.

2.   It is recognized that numerous sources of data and model uncertainty affect the determination of chloride diffusion parameters obtained from field-extracted cores. Nevertheless, values of D could be estimated even for cores from structures as young as 2 years by using core slicing schemes that sampled concrete close to the external surface. Results from the Sunshine Skyway Bridge suggest that D decreases with age of the structure, in agreement with reports from other investigations of aging concrete with pozzolanic additions.

3.   The apparent surface chloride concentration (C$_S$) tended to reach relatively steady values early in the life of the substructures examined. A value of C$_S$ of about 30 pcy (18 kg/m^3) may be considered to be typical in the Tidal to 6 ft (1.8 m) AHT region. The surface concentration was not found to be a strong function of the salt content of the surrounding seawater.

4.   Thin (typical width ~0.15 mm) stress cracks were found in many of the substructures examined. Many of these cracks in footers or piles reached down to the waterline and extended to at least the rebar depth. Crack incidences in the order of one crack every several meters of waterline perimeter were not uncommon.

5.   Even though the cracks were thin, there was substantial preferential chloride penetration immediately around the crack compared with the surrounding sound concrete, to levels exceeding typically assumed values of the chloride initiation threshold. The effect was most marked in the splash evaporation zone. Chloride enrichment was closest to the crack face. In spite of this enhanced chloride penetration, indications of corrosion were not observed in any of the crack locations examined (the use of epoxy-coated rebar in some of the bridges may have masked or mitigated corrosion development there).

6.   Numerical models of chloride transport in the cracks reproduced the observed chloride penetration behavior. The analysis predicts that under moist substructure conditions significant chloride penetration can occur even in extremely thin cracks, and

that chloride buildup could be more severe when a crack terminates at a short distance from the surface instead of extending deep into the concrete.

7.   Calculations of the penetration of chloride in sound concrete revealed that the rebar acts as an obstruction to the diffusional chloride flow, causing a local increase in concentration. That increase shortens the projected time for corrosion initiation (t_i) compared to that evaluated assuming unrestricted diffusion. The effect can be strong (e.g. reductions in t_i by as much as 40%) depending on the concrete cover, rebar diameter, and chloride threshold value. Derating factors to account for this effect were computed and proposed for use in durability estimates.

8.   An integrated corrosion initiation model for sound concrete was created that takes into account the concrete mixture proportions, rebar cover and size, and system geometry (flat wall, 2- and 3- way corners, or cylindrical columns). Software for rapid calculation of t_i incorporating the initiation model and input values based on the field findings has been created.

9.   Experiments revealed that the amount of critical corrosion penetration needed to cause cover cracking was greater when corrosion was localized (as it may happen in an area of preferential chloride penetration) than when corrosion was more uniform (as in sound concrete). A quantitative relationship between critical corrosion penetration, rebar cover and diameter, and length of the corroding region was established.

10.   A theoretical analysis of localized corrosion at preexisting concrete cracks indicated that local corrosion rates could be about one order of magnitude greater than under more uniform conditions. The results agreed with independent experimental observations.

11.   The above findings indicated that corrosion at localized active spots could result in significant damage after relatively short times following corrosion initiation.

12.   An overall corrosion process forecast approach was formulated based on the findings described above. The durability projections obtained when applying this procedure to substructure built under present FDOT guidelines with the highest concrete grades indicate a generally good prognosis of achieving the 75-year goal, as long as concrete away from stress cracks is considered.

13.   For locations where preexisting cracks are present the forecast, although inherently conservative, indicates that a small but noticeable fraction of the substructure built using present design could encounter localized corrosion damage in the near future.   Specialized corrosion control methods need to be developed in anticipation of this problem.

14.   A next-generation computational approach for forecasting durability of marine substructure was formulated, integrating both the corrosion initiation and propagation

stages with evaluation of damage distribution over the entire elevation range of the substructure element.

15   A detailed (rebar scale) predictive model to compute corrosion distribution was developed. The model successfully reproduced the throwing power of a galvanic system for cathodic prevention in a laboratory system. Application of variations of the model to typical marine substructure conditions indicate that polarization levels in the order of 100 mV may be attained on passive steel in the area immediately above high tide with an immersed galvanic anode.

7. REFERENCES

[1]   "Manual for Corrosion Protection of Concrete Components in Bridges", Task Force 32 Report, AASHTO-AGC-ARTBA Joint Committee, Subcommittee on New Highway Materials, Nov. 1992.

[2]   Sagüés A., "Corrosion of Epoxy Coated Rebar in Florida Bridges", Final Report to FDOT, State Job. No. 99700-7556-010, WPI 0510603, 1994.

[3]   Kessler R., "Highlights of the Revisions to Structures Design Guidelines, Chapter 7, "Florida Concrete Design, Environmental Classification and Construction Criteria", presented at the FDOT/FTBA Construction Conference, Jan. 1995, Orlando, Fl, 7 pp.

[4]   FDOT Standard Specifications for Road and Bridge Construction, FDOT, Tallahasee, FL, 1996 and subsequent versions.

[5]   Sagüés A., Kranc S.C., F.J. Presuel-Moreno, "Applied Modelling for Corrosion Protection Design for Marine Bridge Substructures", Final Report to FDOT, State Job No.99700-7622-119, WPI 0510718, June1997.

[6]   Sagüés, A.A. and Kranc, S.C. "Effect of Structural Shape and Chloride Binding on Time to Corrosion of Steel in Concrete in Marine Service", p. 105-114 in Corrosion of Reinforcement in Concrete Construction, C.L. Page, P.B. Bamforth and J.W. Figg, Eds, The Royal Society of Chemistry, Cambridge, 1996.

[7]   Sagüés, A.A., Powers, R. G. "Corrosion and Corrosion Control of Concrete Structures in Florida-What Can Be Learned?" p. 49-58 in Repair of Concrete Structures-From Theory to Practice in a Marine Environment, Blankvoll, A., Ed., Norwegian Road Research Laboratory, Oslo, Norway (1997).

[8]   FDOT, "Florida Method of Test for Determining Low-Levels of Chloride in Concrete and Raw Materials", FM 5-516, Florida Department of Transportation, September 1994.

[9]   Morris, W., Moreno, E. I., Sagüés, "Practical Evaluation of Resistivity of Concrete in Test Cylinders using a Wenner Array Probe", Cement and Concrete Research, Vol. 26, p.p. 1779-1787 (1996).

[10]   Presuel F.J. & Sagüés A.A., to be published.

[11]   1995 Sunshine Skyway Bridge Core Analyses, Archived Results, W. Morris and A. Sagüés, University of South Florida, Tampa, FL.

[12]   de Rincon O.T. et. al. "PGRU Bridge: Based on an Electrochemical Diagnosis" p. 60 in Repair and Rehabilitation of Reinforced Concrete Structures: The State of the Art, W.P. Silva-Araya, O. T. de Rincon, and L. Pumarada O'Neill, Eds., American Society of Civil Engineers, Reston, VA, 1998. See also "Manual for inspecting, evaluation and diagnosing corrosion in reinforced concrete structures", DURAR/CYTED, ISBN 980-296-541-3, August 2000.

[13]   Bamforth, P. B., "The Derivation Of Input Data For Modelling Chloride Ingress From Eight-Year UK Coastal Exposure Trials", Magazine of Concrete Research, Vol. 51, p.87-96 (1999).

[14]   Berke, N.S. and Hicks, M.C., "Estimating the Life Cycle of Reinforced Concrete Decks and Marine Piles using Laboratory Diffusion and Corrosion Data", p. 207 in Corrosion Forms and Control for Infrastructure, ASTM STP 1137, Victor Chaker, Ed., ASTM, Philadelphia, 1992.

[15]   "Life 365 – Computer Program For Predicting The Service Life And Life-Cycle Costs Of Reinforced Concrete Exposed To Chlorides", M.D.A. Thomas and E.C. Bentz, 2000.

[16]   Thomas, M.D.A. and Bamforth, P.B., "Modelling Chloride Diffusion In Concrete, Effect Of Fly Ash And Slag", Cement and Concrete Research, Vol. 29, p. 487-495 (1999).

[17]   Weyers R., to be published.

[18]   Kranc S.C., Sagüés A.A. and Presuel-Moreno F.J., "Decreased Corrosion Initiation Time of Steel in Concrete due to Rebar Obstruction of Diffusional Flow" accepted for publication, ACI Materials Journal, (2002).

[19]   Li, L. and Sagüés, A.A., Corrosion, Vol. 57, pp.19-28 (2001).

[20]   Glass, G.K. and Buenfeld, N.R., Corrosion Science Vol. 39, p. 1001-1013 (1997).

[21]   Sagüés, A.A., Scannel, W. and Soh, F.W., "Development of a Deterioration Model to Project Future Concrete Reinforcement Corrosion in a Dual Marine Bridge", in Proc. International Conference on Corrosion and Rehabilitation of Reinforced Concrete Structures, Orlando, FL, Dec. 7-11, 1998, CD ROM Publication No. FHWA-SA-99-014, Federal Highway Administration, 1998.

[22]   Sagüés A.A., Powers R.G. Kessler R. "Corrosion Performance of Epoxy-Coated Rebar in Florida Keys Bridges", Paper 06142, 13 pp., Corrosion/2001, NACE International, Houston, TX, 2001.

[23]   Weyers R.E. "Corrosion Service Life Model", in <u>Repair and Rehabilitation of</u> <u>Reinforced Concrete Structures: The State of the Art</u>, p. 105, W.P. Silva-Araya, O. T. de Rincon, and L. Pumarada O'Neill, Eds., American Society of Civil Engineers, Reston, VA, 1998.

[24]   Kranc S.C., Sagüés A.A., "Computation of Corrosion Distribution of Reinforcing Steel in Cracked Concrete" in <u>Proceedings, International Conference on</u> <u>Corrosion and Rehabilitation of Reinforced Concrete Structures</u>, US Department of Transportation, Federal Highway Administration, CD-ROM Publication No. FHWA-SA-99-014, Washington, DC, 1998.

[25]   Torres-Acosta A.A., Sagüés A.A., "Concrete Cover Cracking with Localized Corrosion of Reinforcing Steel", pp. 363-378 in <u>Proc. of the Fifth CANMET/ACI</u> <u>Int. Conf. On Durability of Concrete</u>, ACI SP 192, 1997.

[26]   Andrade C., Alonso M.C., "Values of corrosion rate of steel in concrete to predict service life of concrete structures", p.282 in <u>Application of Accelerated Corrosion</u> <u>Tests to Service Life Prediction of Materials</u>, ASTM STP 1194, Eds. G. Cragnolino, N. Sridhar, ASTM, Philadelphia, PA, 1994.

[27]   Kranc C., Sagüés A.A., "Detailed Modeling Of Corrosion Macrocells On Steel Reinforcing In Concrete", *Corrosion science.* Vol. 43, 1355-1372 (2001).

[28]   Pedeferri P., "Cathodic Protection and Cathodic Prevention", Construction and Building Materials, Vol 10, p. 391-402 (1996).

[29]   Bertolini L., Bolzoni F., Lazzari L., Pastore T. and Pedeferri P., "Cathodic protection principles and applications", Journal of Applied Electrochemistry, Vol 28, p. 1321-1331 (1998).

[30]   Bertolini L., Bolzoni F., Lazzari L., and Pedeferri P., "Applications of Cathodic Protection to Steel in Concrete", Internationale Zeitschrift für Bauinstandsetzen und Baudenkmalpflege, Vol 6, p.655-668 (2000).

[31]   Daily S.F., Kendell K., "Cathodic Protection of New Reinforced Concrete Structures in Aggressive Environments", Materials Performance Vol 37, p.19-25 (1998).

[32]   Tettamanti M., Rossini A., Cheatani A., "Cathodic Prevention and Protection of Concrete Elements at the Sydney Opera House", Materials Performance V 36, p.21-25 (1997).

[33]   Manian L., Surkein M., "Remediation of a New Reinforcing Steel Cathodic Protection System During Construction", Materials Performance Vol 38, p. 30-35 (1999).

[34] Page C.L., Sergi G., "Developments in Cathodic Protection Applied to Reinforced Concrete", Journal of Materials in Civil Engineering, Vlo 12, p.8-15, (2000).

[35] Alonso C., Andrade C., Castellote M., "The Influence of the Electrical Potential in the Chloride Threshold for Rebar Depassivation", Paper No. 4iv082 In Proc. 10th International Congress on the Chemistry of Cement, vol 4, H. Justnes, Ed., Gothenburg, Sweden, 1997.

[36] Alonso C., Castellote M., Andrade C., "Dependance of Chloride Threshold with the Electrical Potential of Reinforcements", p415-428 in Second International RILEM Workshop on Testing and Modeling the Chloride Ingress into Concrete, PRO 19, RILEM Publications, Cachan France, 2000.

[37] Arup H., "A New Method for Determining Chloride Thresholds as a Function of Potential in Field Exposure Tests", p. 107-112 In Durability of Concrete in Saline Environment, Cementa AB, Lund, Sweden, 1996.

[38] Sandberg P., "The effect of defects at the steel – concrete interface, exposure regime and cement type on pitting corrosion in concrete", Report TVBM-3081, Lund, Sweden, 1998.

[39] Sandberg P., "Chloride initiated reinforcement corrosion in marine concrete", Report TVBM-1015, Lund, Sweden, 1998.

[40] Sagüés A.A., Pech-Canul M.A., Al-Mansur A.K.M., "Corrosion Macrocell Behavior of Reinforcing Steel in Partially Submerged Concrete Columns", submitted for publication (2000).

[41] Castro, P., Sagüés, A.A., Moreno, E.I., Maldonado, L. and Genescá J., "Characterization of Activated Titanium Solid Reference Electrodes for Corrosion Testing of Steel in Concrete", Corrosion, Vol. 52, 609-617 (1996).

[42] Presuel F.J., Sagüés A. A., Kranc S.C., "Steel Activation in Concrete Following Interruption of Long Term Cathodic Polarization", CORROSION/2002, paper 02259 , NACE International, Houston, TX, 2002.

[43] Page C.L. in Corrosion of Steel in Concrete, Report of the Technical Committee 60-SCS, p 17 Editor P. Schiessl, 1988.

[44] Bromfield J.P., Corrosion of Steel in Concrete, E&FN Spon, London, p40, (1997).

[45] Pruckner F., "Corrosion and Protection of Reinforcement in Concrete Measurements and interpretation", Ph.D. Dissertation, University of Vienna. (2001).

[46] Kranc S.C., Sagüés A.A., Presuel-Moreno F.J., "Computational and Experimental Investigation of Cathodic Protection Distribution in Reinforced Concrete Marine Piling", CORROSION/1997, paper No 231., NACE International, Houston, TX, 1997.

[47] CRC. Handbook of Chemistry and Physics, R.C. Weast Editor, CRC Press, Cleveland, (1973).

[48] Burden R., Faires J., Numerical Analysis, PWS-KENT Pub, Boston, p.402-403 (1985).

[49] Sagüés A.A., Perez-Duran H.M., Powers R.G., "Corrosion Performance of Epoxy-Coated Reinforcing Steel in Marine Substructure Service", Corrosion, Vol 47, p. 884-893 (1991).

[50] Li, L.; Sagüés, A., "Effect Of Metal Surface Condition On The Chloride Corrosion Threshold Of Reinforcing Steel In Alkaline Solutions", Paper 801, CORROSION/2000, NACE International, Houston, TX, 2000.

[51] Sagüés A.A., Powers R.G., "Sprayed-Zinc Sacrificial Anodes for Reinforced Concrete in Marine Service", Corrosion, Vol 52, p. 508-522 (1996).

[52] Goldman S., Transformation Calculus and Electrical Transients, Prentice-Hall, New York, p.285-315,(1949).

[53] Feliu S., Gonzalez J.A., and Andrade C., "Electrochemical methods for on-site determination of corrosion rates of rebars", p.107-118 in Techniques to asses the corrosion activity of steel reinforced concrete structures, ASTM STP 1276, N. Berke, E. Escalante, C Nmai, and D Whiting, Eds, ASTM, West Conshohocken, Pa., 1996.

[54] Polder R., "Test methods for on site measurement of resistivity of concrete – a RILEM TC-154 technical recommendation", Construction and Building Materials, Vol. 15, p.125-131, (2001).

[55] Andrade C., Alonso C., "On-site Measurement of Corrosion Rate of Reinforcements", Construction and Building Materials, Vol. 15, p.141-145, (2001).

8. TABLES

Table 1. Bridges Investigated

Name	Abbr.	County	Location	Bridge #	Project #	Year Built	Water Cl Content [a] (ppm)
Sunshine Skyway	SSK	Pinellas	I - 275 / Tampa Bay	150189	15170-3415	1985	18504
Howard Frankland	HFB	Pinellas	I - 275 / Tampa Bay	150210	15190-3479	1990	17143
Courtney Campbell Causeway	CCC	Pinellas	SR 60 / Tampa Bay	150138	15040-3524	1992	14181
Blind Pass	BLP	Pinellas	SR 699 / Blind Pass	150221	15100-3546	1996	19356
McArthur Causeway	MAC	Dade	A-1-A / ICW (McArthur Causeway)	870772		1995	20306
Dame Point Expressway	DPE	Duval	Dame Point Expressway / Jacksonville	720518	72002-3515	1989	16540
BaySide Bridge	BSB	Pinellas	49th Street / Tampa Bay	154259		1993	19850
Safety Harbor Bay	SHB	Pinellas	SR 580 / Safety Harbor Bay	150202	15030-3511	1990	10990
New Smyrna	NSB	Volusia	A-I-A / IWW Indian River, New Smyrna.	790152	79130-3517	1990	17700
Matanzas Inlet	MIB	St. Johns	A-1-A / Matanzas Inlet	780097	78040-3542	1993	18855
Boca Ciega Bay	BCB	Pinellas	SR 692 / Boca Ciega Bay.	150052	15200-3601	1962/86 [b]	19356
Bunces Pass	BPB	Pinellas	I-275 / Bunces Pass.	150211	15170-3427	1991	25902
New Pass	NPB	Sarasota	SR 789 / New Pass.	170158	17030-3506	1986	20915

a. Information provided by FDOT (L. Sessions, I. Lasa).

b. Built 1962 / Modified 1986.

Table 2 Bridge Information
Based on limited records. See Appendix 1 for estimates and assumptions. Entries subject to revision.

Bridge	Number	Pile	Footer	Column	Placed in Service	Examined	Age Years	Concrete Class[f]	Coarse Aggregate	Cement Factor[a] (pcy)	W/C	Fly Ash[b] %	Magnetic Signal	Fly Ash Type	BFS[b] %	Micro Silica[b] %	Calcium Nitrite Specified	Calcium Nitrite Detected
		Elements Examined																
SSK	150189	-	-	PC	1985	02-97	11	V	Limestone	>752	0.32	20	Positive (High)	F	-	-	-	NT
HFB	150210	-	CIP	CIP	1990	04-98	8	IV	Granite	658[d]	0.41[e]	<35	Positive (Low to High)	C	-	-	-	NT
CCC	150138	PC	-	-	1992	04-98	6	V	Limestone	752	0.35	20	Positive (High)	F	-	8	Yes	All positive
BLP	150221	PC	-	-	1996	04-98	2	V	Limestone	752[d]	0.37[e]	20	Positive (Low)	F	-	8	Yes	Negative in one pile
MAC	870772	-	CIP	-	1995	06-98	2.5	IV	Limestone	732	0.33	20	-	F	-	-	-	NT
DPE	720518	-	CIP	-	1989	08-99	11	IV	Granite	658[d]	0.38	-	Positive (Low to high)	-	70	-	-	NT
BSB	154259	PC	-	-	1993	12-99	7	V	Limestone	≥752[c]	0.35[e]	20	Positive	F	-	10	-	NT
		-	CIP	CIP				IV		658[d]	0.41[e]					-		
SHB	150202	PC	-	-	1990	02-00	10	V	Limestone	752[d]	0.37[e]	20	Positive (High)	F	-	-	-	NT
NSB	790152	-	CIP	CIP	1990	06-00	10	IV	Limestone	658[d]	0.41[e]	-	None	-	-	-	-	NT
MIB	780097	PC	-	-	1993	06-00	7	V	Limestone	752[d]	0.37[e]	20	Positive (Low)	F	-	-	-	NT
BCB	150200	PC	-	-	1962	07-00	38	P	Limestone	611	0.42[e]	-	None	-	-			NT
		-	CIP	-	1962		38	U	Limestone	U	U	-	None	-	-			
		PC	-	-	1986		14	U	Limestone	U	U	-	None	-	-			NT
		-	CIP	-	1986		14	U	Limestone	U	U		Positive (High)	U	-			
BPB	150211	PC	-	-	1991	07-00	9	V	Limestone	752[d]	0.37[e]	20	Positive (Low)	U	-	-	-	NT
NPB	170158	-	CIP	CIP	1986	07-00	14	IV	Limestone	658[d]	0.41[e]		Positive (Low)	U	-	-	-	NT

SSK Sunshine Skyway
HFB Howard Frankland
CCC Courtney Campell Causeway
BLP Blind Pass
MAC Mac Arthur

DPE Dame Point Expressway
BSB Bay Side / 49 St
SHB Safety Harbor
NSB New Smyrna
MIB Matanzas Inlet

BCB Boca Ciega Bay
BPB Bunces Pass
NPB New Pass

PC Precast
CIP Cast in Place

U: Unkown
NT: Not Tested

a) Total Cementitious Content
b) As Cement Replacement
c) Piles at S End of Bridge Have Greater CF (Appendix 1)
d) Minimum   e) Maximum   f) Actual or comparable.

Table 3. Cores Extracted

GENERAL CORE NUMBER	LOCAL CORE No.	DATE EXTRACTED	BRIDGE	BRIDGE No.	PIER No.	COLUMN / PILE No.	COLUMN OR PIER SIDE [a]	TYPE	ELEVATION (ft) ABOVE FOOTER	ELEVATION (ft) Above High Tide	CRACK [b]	CRACK WIDTH (mm)	AGGREGATE TYPE	AGGREGATE MAX. SIZE (in)	STEEL EXPOSURE	CONCRETE COVER (cm)	CORE LENGTH (cm)	CORE MASS (gr) AS-RECEIVED	CONCRETE FACE [c]	CHLORIDE PROFILE	AS-RECEIVED RESISTIVITY (Kohm-cm)	WET RESISTIVITY (Kohm-cm)	MAGNETIC READING (mg-force)
541	1 at 6'	02-04-97	SSK	150189	117-2		N	PC		6.0	Y	0.15	Lime Stone	5/8									
542	2 at 6'	02-04-97	SSK	150189	117-2		N	PC		6.0	N		Lime Stone	5/8			6.4						
524	03 at 6'	02-04-97	SSK	150189	117-2	2		PC		6.0	Y		Lime Stone							x			
526	04 at 6'	02-04-97	SSK	150189	117-2	2		PC		6.0	N		Lime Stone							x			
543	5 at 3'	02-04-97	SSK	150189	117-1			PC		3.0	Y	0.08-0.15	Lime Stone	1/2						special			
544	6 at 3'	02-04-97	SSK	150189	117-1		W	PC		3.0	N		Lime Stone	1/2			5.7						
545	7 at 3'	02-04-97	SSK	150189	117-1		W	PC		3.0	Y	0.08-0.15	Lime Stone	3/4			7.5		clean				
546	8 at 3'	02-04-97	SSK	150189	117-1		W	PC		3.0	N		Lime Stone	5/8			9.0		clean				
548	12 at 3'	02-04-97	SSK	150189	106-1		NW	PC		3.0	Y		Lime Stone	2/3			10.0		clean				
549	13 at 3'	02-04-97	SSK	150189	106-1		NW	PC		3.0	N		Lime Stone	2/3					clean				
531	09 at 3'	02-05-97	SSK	150189	106-1	1	SW	PC		3.0	Y		Lime Stone		N		8.0			x			
534	10 at 3'	02-05-97	SSK	150189	106-1	1	SW	PC		3.0	N		Lime Stone		N		8.0			x			
535	11 at 3'	02-05-97	SSK	150189	106-1	1	SW	PC		3.0	N		Lime Stone		N		11.0			x			
536	14 at 3'	02-05-97	SSK	150189	116		N	PC		3.0	Y		Lime Stone		N		9.0			x			
537	15 at 3'	02-05-97	SSK	150189	116		N	PC		3.0	N		Lime Stone		Y		10.0			x			
538	16 at 3'	02-05-97	SSK	150189	116		N	PC		3.0	N		Lime Stone		Y		10.0			x			
539	17 at 3'	02-05-97	SSK	150189	116		N	PC		3.0	N		Lime Stone		Y		10.5			x			
521	01 at 18'	04-03-97	SSK	150189	155			PC		18.0	Y									x			
522	02 at 18'	04-03-97	SSK	150189	155			PC		18.0	N									x			
523	03 at 18'	04-03-97	SSK	150189	155			PC		18.0	Y									x			
525	04 at 19'	04-03-97	SSK	150189	151			PC		19.0	Y									x			
527	05 at 19'	04-03-97	SSK	150189	151			PC		19.0	N									x			
528	06 at 19'	04-03-97	SSK	150189	151			PC		19.0	Y									x			
529	07 at 60'	04-03-97	SSK	150189	126-1	1		PC		60.0	Y									x			
530	08 at 60'	04-03-97	SSK	150189	126-1	1		PC		60.0	N									x			

a) Direction (NSEW) faced by concrete surface.
b) Y: core on stress crack; SHR: shrinkage crack; N: no crack.
c) Appearance of external concrete surface at the core face.
d) Blank entries indicate not applicable or no available data.

Table 3. Cores Extracted (Continued)

GENERAL CORE NUMBER	LOCAL CORE No.	DATE EXTRACTED	BRIDGE	BRIDGE No.	PIER No.	COLUMN / PILE No.	COLUMN OR PIER SIDE [a]	TYPE	ELEVATION (ft) ABOVE FOOTER	ELEVATION (ft) Above High Tide	CRACK [b]	CRACK WIDTH (mm)	AGGREGATE TYPE	AGGREGATE MAX. SIZE (in)	STEEL EXPOSURE	CONCRETE COVER (cm)	CORE LENGTH (cm)	CORE MASS (gr) AS-RECEIVED	CONCRETE FACE [c]	CHLORIDE PROFILE	AS-RECEIVED RESISTIVITY (Kohm-cm)	WET RESISTIVITY (Kohm-cm)	MAGNETIC READING (mg-force)
532	09 at 60'	04-03-97	SSK	150189	126-1	1		PC		60.0	Y									x			
533	10 at 120'	04-03-97	SSK	150189	117-1	1		PC		120.0	Y									x			
550	1	04-16-98	CCC	150138	7	1	S	PC		3.3	N		Lime Stone	1/2	Y	8.9	8.9	331.4	Clean	x	159		192
551	2	04-16-98	CCC	150138	7	1	S	PC		3.3	SHR	<0.08	Lime Stone	1/2	Y	8.3	8.3	307.4	Clean	x	130		197
552	3	04-16-98	CCC	150138	7	1	S	PC		2.2	N		Lime Stone	5/8	Y	8.9	8.9	322.4	Clean	x	166		210
553	4	04-16-98	CCC	150138	7	1	S	PC		2.2	SHR	<0.08	Lime Stone	1/2	Y	8.6	8.6	314.2	Clean	x	126		208
554	5	04-16-98	CCC	150138	7	2	S	PC		0.0	N		Lime Stone	5/8	Y	7.9	7.9	284.0	Barnacle		128	74	227
555	6	04-16-98	CCC	150138	7	2	S	PC		0.0	N		Lime Stone	3/4	Y	8.6	8.6	301.8	Barnacle	x	111		206
556	7	04-16-98	CCC	150138	7	2	S	PC		1.0	N		Lime Stone	5/8	N		15.9	575.9	Clean	x	142		189
557	8	04-16-98	CCC	150138	7	2	S	PC		1.0	N		Lime Stone	1/2	Y	7.3	7.3	264.2	Clean		188	63	206
558	9	04-16-98	CCC	150138	4	1	S	PC		0.0	N		Lime Stone	1/2	Y	7.3	7.3	267.0	Barnacle		155	65	135
559	10	04-16-98	CCC	150138	4	1	S	PC		0.0	N		Lime Stone	1/2	Y	7.6	7.6	295.8	Barnacle		97		142
560	11	04-16-98	CCC	150138	4	1	S	PC		1.0	N		Lime Stone	5/8	N		15.9	571.3	Clean	x	123		134
561	12	04-16-98	CCC	150138	4	1	S	PC		1.0	N		Lime Stone	5/8	N		14.9	541.1	Clean		142	61	147
576	27	06-08-98	CCC	150138	7	1	S	PC		-0.5	N		Lime Stone	5/8	N		9.2	313.7		x	112		204
577	28	06-08-98	CCC	150138	7	1	S	PC		-0.5	N		Lime Stone	1/2	Y	8.9	8.9	323.5		x	139		206
562	13	04-16-98	HFB	150210	12	E	E	CIP	-0.8	1.7	Y	0.42	Granite	1	Y	11.1	11.1	409.8	Clean	x	79		75
563	14	04-16-98	HFB	150210	12	E	E	CIP	-0.8	1.7	SHR	0.08	Granite	7/8	N		14.6	558.1	Clean	x	130		134
564	15	04-16-98	HFB	150210	44		W	CIP	-0.7	1.3	Y	0.28	Granite	1 1/8	N		15.9	602.3	Clean	x	97		178
565	16	04-16-98	HFB	150210	44		W	CIP	-0.7	1.3	N		Granite	3/4	Y	15.2	15.2	579.8	Clean	x	132		254
566	17	04-16-98	HFB	150210	49		N	CIP	1.0	3.5	Y	0.30	Granite	5/8	N		12.7	511.5	Clean	x	110		183
567	18	04-16-98	HFB	150210	49		N	CIP	1.0	3.5	N		Granite	3/4	N		14.0	549.7	Clean	x	154		263
578	29	06-10-98	HFB	150210	12		E	CIP	-1.3	-0.2	Y	0.12	Granite	1/2	Y	10.2	10.2	365.4		x	78		141
579	30	06-10-98	HFB	150210	12		E	CIP	-1.3	-0.2	N		Granite	7/8	N		11.7	449.1		x	99		88
580	31	06-09-98	HFB	150210	12		E	CIP	-1.1	1.4	Y	0.35	Granite	5/8	Y	11.1	11.1	418.4	Clean		76		123

a)   Direction (NSEW) faced by concrete surface.
b)   Y: core on stress crack; SHR: shrinkage crack; N: no crack.
c)   Appearance of external concrete surface at the core face.
d)   Blank entries indicate not applicable or no available data.

Table 3. Cores Extracted (Continued)

GENERAL CORE NUMBER	LOCAL CORE No.	DATE EXTRACTED	BRIDGE	BRIDGE No.	PIER No.	COLUMN / PILE No.	COLUMN OR PIER SIDE [a]	TYPE	ELEVATION (ft) ABOVE FOOTER	ELEVATION (ft) Above High Tide	CRACK [b]	CRACK WIDTH (mm)	AGGREGATE TYPE	AGGREGATE MAX. SIZE (in)	STEEL EXPOSURE	CONCRETE COVER (cm)	CORE LENGTH (cm)	CORE MASS (gr) AS-RECEIVED	CONCRETE FACE [c]	CHLORIDE PROFILE	AS-RECEIVED RESISTIVITY (Kohm-cm)	WET RESISTIVITY (Kohm-cm)	MAGNETIC READING (mg-force)
581	32	06-09-98	HFB	150210	12		E	CIP	-1.1	1.4	N		Granite	5/8	N			13.7	526.9	Clean		109		90
582	33	06-09-98	HFB	150210	12		E	CIP	1.0	3.5	N		Granite	3/4	Y	7.6	0.0	297.5		x	117		270
583	34	06-09-98	HFB	150210	12		E	CIP	1.0	3.5	N		Granite	3/4	Y	8.3	0.0	312.8	Clean		131	27	137
584	35	06-09-98	HFB	150210	44		W	CIP	-1.2	0.8	Y		Granite	3/4	N			12.7	478.7	Moss		71		152
585	36	06-09-98	HFB	150210	44		W	CIP	-1.2	0.8	N		Granite	5/8	N		21.0	790.7	Moss		87		112
586	37	06-09-98	HFB	150210	44		W	CIP	1.0	2.2	N		Granite	5/8	N		16.2	601.8		x	104		140
587	38	06-09-98	HFB	150210	44		W	CIP	1.0	2.2	N		Granite	1	N		14.0	522.2	Clean		92	44	84
588	39	06-10-98	HFB	150210	12		E	CIP	-2.7	-0.2	Y	0.18	Granite	5/8	Y	12.1	12.1	432.5	Moss		51		77
589	40	06-10-98	HFB	150210	12		E	CIP	-2.7	-0.2	N		Granite	7/8	Y	13.3	13.3	510.6	Moss		125		88
590	41	06-10-98	HFB	150210	12		E	CIP	-2.5	-0.5	Y	0.13	Granite	3/4	N		15.2	577.8		x	61		173
591	42	06-10-98	HFB	150210	12		E	CIP	-2.5	-0.5	N		Granite	3/4	N		12.1	430.5		x	138		193
592	43	06-10-98	HFB	150210	12		E	CIP	-3.0	-1.0	Y	0.28	Granite	7/8	N		13.7	522.7	Moss		56		174
593	44	06-10-98	HFB	150210	12		E	CIP	-3.0	-1.0	N		Granite	3/4	N		14.3	577.3	Clean		89		194
594	45	06-10-98	HFB	150210	12		E	CIP	-2.0	0.0	Y	0.09	Granite	7/8	N		14.0	532.1	Clean		57		354
595	46	06-10-98	HFB	150210	49		N	CIP	0.5	3.0	Y	0.09	Granite	3/4	N		15.9	583.9	Clean		89		184
596	47	06-10-98	HFB	150210	49		N	CIP	0.5	3.0	N		Granite	3/4	N		14.0	507.9	Clean		126		168
597	48	06-10-98	HFB	150210	62		N	CIP	1.0	3.2	Y	0.23	Granite	1/2	N		9.8	339.7		x	92		134
598	49	06-10-98	HFB	150210	62		N	CIP	1.0	3.2	N		Granite	5/8	N		12.7	469.8		x	103		248
599	50	06-10-98	HFB	150210	65		S	CIP	1.0	3.2	Y	0.09	Granite	1/2	N		11.1	400.6			179		144
600	51	06-10-98	HFB	150210	65		S	CIP	1.0	3.2	N		Granite	3/4	N		15.6	564.1			182		202
568	19	04-17-98	BLP	150221	6	4	S	PC		1.0	N		Lime Stone	5/8	Y		10.5	10.5	379.7	Clean	x	83		40
569	20	04-17-98	BLP	150221	6	4	S	PC		1.0	N		Lime Stone	3/4	Y		9.6	9.6	347.8	Clean		89	48	41
570	21	04-17-98	BLP	150221	12	8	E	PC		1.0	N		Lime Stone	5/8	Y			15.2	557.4	Clean	x	65		23
571	22	04-17-98	BLP	150221	12	8	E	PC		1.0	N		Lime Stone	5/8	Y	8.9	8.9	323.9	Clean		82	42	20
572	23	06-08-98	BLP	150221	6	4	S	PC		-0.2	N		Lime Stone	5/8	Y	10.2	10.2	346.3		x	94		48

a) Direction (NSEW) faced by concrete surface.
b) Y: core on stress crack; SHR: shrinkage crack; N: no crack.
c) Appearance of external concrete surface at the core face.
d) Blank entries indicate not applicable or no available data.

Table 3. Cores Extracted (Continued)

GENERAL CORE NUMBER	LOCAL CORE No.	DATE EXTRACTED	BRIDGE	BRIDGE No.	PIER No.	COLUMN / PILE No.	COLUMN OR PIER SIDE a	TYPE	ELEVATION (ft) ABOVE FOOTER	ELEVATION (ft) Above High Tide	CRACK b	CRACK WIDTH (mm)	AGGREGATE TYPE	AGGREGATE MAX. SIZE (in)	STEEL EXPOSURE	CONCRETE COVER (cm)	CORE LENGTH (cm)	CORE MASS (gr) AS-RECEIVED	CONCRETE FACE c	CHLORIDE PROFILE	AS-RECEIVED RESISTIVITY (Kohm-cm)	WET RESISTIVITY (Kohm-cm)	MAGNETIC READING (mg-force)
573	24	06-08-98	BLP	150221	6	4	S	PC		-0.2	N		Lime Stone	3/4	Y	10.2	10.2	356.2	Clean		90		46
574	25	06-08-98	BLP	15221	12	8	E	PC		-0.5	N		Lime Stone	1/2	Y	9.5	9.5	317.8		x	104		21
575	26	06-08-98	BLP	15221	12	8	E	PC		-0.5	N		Lime Stone	5/8	Y	9.5	9.5	330.3	Barnacle		93		21
611	12	06-15-98	MAC	870772	8		E	CIP		6.0			Granite							x			
612	13	06-15-98	MAC	870772	8		E	CIP		6.0	Y*		Granite							x			
613	16	06-15-98	MAC	870772	8		E	CIP		3.0	N		Granite							x			
614	20	06-15-98	MAC	870772	8		E	CIP		2.5	Y		Granite							x			
615	21	06-15-98	MAC	870772	8		E	CIP		2.5	N		Granite							x			
616	31	06-15-98	MAC	870772	8		E	CIP		2.5	Y*		Granite							x			
650	0A	08-05-99	DPE	720518	North-Pier	North-Pier	N	CIP		0.0	N		Granite		N		16.7	627.6		x	42		46
651	0B	08-05-99	DPE	720518	North-Pier	North-Pier	N	CIP		0.0	N		Granite		N		15.9	569.6			29	20	50
652	0C	08-05-99	DPE	720518	North-Pier	North-Pier	N	CIP		0.0	Y	< 0.08	Granite		N		15.7	575.1		x	19		33
653	0D	08-10-99	DPE	720518	North-Pier	North-Pier	N	CIP		0.0	N		Granite		N		10.4	384.5		x	35		43
654	1A	08-05-99	DPE	720518	North-Pier	North-Pier	N	CIP		1.0	N		Granite		Y	10.3	10.3	386.4			31		47
655	1AA	08-05-99	DPE	720518	North-Pier	North-Pier	N	CIP		1.0	N		Granite		N		15.1	564.2		x	24		54
656	1B	08-10-99	DPE	720518	North-Pier	North-Pier	N	CIP		1.0	N		Granite		N		12.1	451.9			25		49
657	1BB	08-05-99	DPE	720518	North-Pier	North-Pier	N	CIP		1.0	N		Granite		N		17.2	603.3			13	13	44
658	1C	08-10-99	DPE	720518	North-Pier	North-Pier	N	CIP		1.0	Y	< 0.127	Granite		N		14.6	535.0		x	23		32
659	1D	08-10-99	DPE	720518	North-Pier	North-Pier	N	CIP		1.0	N		Granite		Y	8.1	8.1	312.4			24		52
660	1DD	08-10-99	DPE	720518	North-Pier	North-Pier	N	CIP		1.0	N		Granite		N		14.7	556.3		x	28		46
661	3A	08-05-99	DPE	720518	North-Pier	North-Pier	N	CIP		3.0	N		Granite		N		15.0	537.4		x	102		52
662	3B	08-05-99	DPE	720518	North-Pier	North-Pier	N	CIP		3.0	N		Granite		N		16.7	588.9			64	35	65
663	3C	08-10-99	DPE	720518	North-Pier	North-Pier	N	CIP		3.0	Y	0.25	Granite		N		8.0	296.4			105		97
664	3CC	08-10-99	DPE	720518	North-Pier	North-Pier	N	CIP		3.0	Y	0.25	Granite		N		5.7	226.4			112		49
665	3CCC	08-10-99	DPE	720518	North-Pier	North-Pier	N	CIP		3.0	Y	0.25	Granite		Y	8.4	8.4	320.8		x	53		72

a) Direction (NSEW) faced by concrete surface.
b) Y: core on stress crack; SHR: shrinkage crack; N: no crack.
c) Appearance of external concrete surface at the core face.
d) Blank entries indicate not applicable or no available data.

* Horizontal Lift Line

Table 3. Cores Extracted (Continued)

GENERAL CORE NUMBER	LOCAL CORE No.	DATE EXTRACTED	BRIDGE	BRIDGE No.	PIER No.	COLUMN / PILE No.	COLUMN OR PIER SIDE [a]	TYPE	ELEVATION (ft) ABOVE FOOTER	ELEVATION (ft) Above High Tide	CRACK [b]	CRACK WIDTH (mm)	AGGREGATE TYPE	AGGREGATE MAX. SIZE (in)	STEEL EXPOSURE	CONCRETE COVER (cm)	CORE LENGTH (cm)	CORE MASS (gr) AS-RECEIVED	CONCRETE FACE [c]	CHLORIDE PROFILE	AS-RECEIVED RESISTIVITY (Kohm-cm)	WET RESISTIVITY (Kohm-cm)	MAGNETIC READING (mg-force)
666	3D	08-10-99	DPE	720518	North-Pier	North-Pier	N	CIP		3.0	N		Granite		N		13.7	523.7		x	62		86
667	5A	08-05-99	DPE	720518	North-Pier	North-Pier	N	CIP		5.0	N		Granite		N		16.9	580.3		x	60		56
668	5B	08-05-99	DPE	720518	North-Pier	North-Pier	N	CIP		5.0	N		Granite		N		16.9	594.3			114	40	57
669	5C	08-10-99	DPE	720518	North-Pier	North-Pier	N	CIP		5.0	Y	0.33	Granite		Y	10.9	10.9	408.3		x	72		54
670	5D	08-10-99	DPE	720518	North-Pier	North-Pier	N	CIP		5.0	N		Granite		N		15.2	564.6		x	54		54
701	1	12-15-99	BSB	154259	196 - S.B.	4	S	PC		1.0	Y	0.10	Lime Stone	1/2	Y	5.6	5.6	152.2	Clean	x	134		-
702	2	12-15-99	BSB	154259	196 - S.B.	4	S	PC		-0.3	Y	0.15	Lime Stone	1/2	Y	8.5	8.5	263.3	Barnacle	x	114		19
703	3	12-15-99	BSB	154259	196 - S.B.	4	S	PC		-0.3	N		Lime Stone	1/2	Y	8.3	8.3	258.9	Barnacle	x	199		18
704	4	12-15-99	BSB	154259	196 - S.B.	4	S	PC		1.0	N		Lime Stone	1/2	Y	9.0	9.0	293.6	Clean	x	183		20
705	5	12-15-99	BSB	154259	196 - S.B.	4	S	PC		0.4	Y	0.15	Lime Stone	1/2	Y	8.6	8.6	273.4	Clean		114		17
706	6	12-15-99	BSB	154259	196 - S.B.	4	S	PC		0.4	N		Lime Stone	1/2	Y	8.7	8.7	287.1	Clean		168		19
707	7	12-15-99	BSB	154259	196 - S.B.	5	S	PC		1.0	Y	0.10	Lime Stone	3/8	Y	8.8	8.8	283.0	Clean		109		20
708	8	12-15-99	BSB	154259	196 - S.B.	5	S	PC		1.0	N		Lime Stone	5/8	Y	8.3	8.3	280.7	Clean	x	187		17
709	9	12-16-99	BSB	154259	29 - N.B.	5	S	PC		-0.5	N		Lime Stone	3/8	N		8.9	291.7	Barnacle	x	120		13
710	10	12-16-99	BSB	154259	29 - N.B.	5	S	PC		-0.5	N		Lime Stone	3/8	N		13.5	446.5	Barnacle	x	107		13
711	11	12-16-99	BSB	154259	29 - N.B.	5	S	PC		1.0	N		Lime Stone	3/8	Y	8.9	8.9	293.5	Clean		169		14
712	12	12-16-99	BSB	154259	29 - N.B.	5	S	PC		1.0	N		Lime Stone	3/8	N		9.5	313.1	Barnacle		144	56	14
713	13	12-16-99	BSB	154259	115 - N.B.	4	S	PC		-0.5	N		Lime Stone	3/8	N		7.3	255.2	Barnacle		133		12
714	14	12-16-99	BSB	154259	115 - N.B.	4	S	PC		-0.5	N		Lime Stone	5/8	N		11.9	410.6	Barnacle		111		11
715	15	12-16-99	BSB	154259	115 - N.B.	4	S	PC		0.8	N		Lime Stone	1/2	N		7.8	268.3	Clean		182		13
716	16	12-16-99	BSB	154259	115 - N.B.	4	S	PC		0.8	N		Lime Stone	5/8	N		8.6	294.2	Clean		176	78	12
717	17	12-16-99	BSB	154259	123 - N.B.	3 footer	E	CIP	-0.5	0.9	Y	0.15	Lime Stone	5/8	N		10.6	339.0	Barnacle		39		18
718	18	12-16-99	BSB	154259	123 - N.B.	3 footer	E	CIP	-1.0	0.4	Y	0.10	Lime Stone	3/4	N		14.1	460.3	Barnacle	x	42		17
719	19	12-16-99	BSB	154259	123 - N.B.	3 footer	E	CIP	-0.5	0.9	N		Lime Stone	5/8	N		11.6	381.3	Barnacle		95		19
720	20	12-16-99	BSB	154259	123 - N.B.	3 footer	E	CIP	-1.0	0.4	N		Lime Stone	5/8	N		9.4	327.3	Clean	x	92		18

a)   Direction (NSEW) faced by concrete surface.
b)   Y: core on stress crack; SHR: shrinkage crack; N: no crack.
c)   Appearance of external concrete surface at the core face.
d)   Blank entries indicate not applicable or no available data

Table 3. Cores Extracted (Continued)

GENERAL CORE NUMBER	LOCAL CORE No.	DATE EXTRACTED	BRIDGE	BRIDGE No.	PIER No.	COLUMN / PILE No.	COLUMN OR PIER SIDE [a]	TYPE	ELEVATION (ft) ABOVE FOOTER	ELEVATION (ft) Above High Tide	CRACK [b]	CRACK WIDTH (mm)	AGGREGATE TYPE	AGGREGATE MAX. SIZE (in)	STEEL EXPOSURE	CONCRETE COVER (cm)	CORE LENGTH (cm)	CORE MASS (gr) AS-RECEIVED	CONCRETE FACE [c]	CHLORIDE PROFILE	AS-RECEIVED RESISTIVITY (Kohm-cm)	WET RESISTIVITY (Kohm-cm)	MAGNETIC READING (mg-force)
721	21	12-16-99	BSB	154259	123 - N.B.	3 footer	E	CIP	0.0	-0.3	N		Lime Stone	3/4	N		10.5	362.9	Barnacle	x	57		16
722	22	12-16-99	BSB	154259	123 - N.B.	3 footer	E	CIP	0.0	-0.3	N		Lime Stone	5/8	N		10.5	362.2	Barnacle		79	52	17
723	23	12-16-99	BSB	154259	123 - N.B.	3 footer	E	CIP	1.0	2.4	N		Lime Stone	5/8	N		10.0	344.6	Barnacle	x	88		14
724	24	12-16-99	BSB	154259	123 - N.B.	3 footer	E	CIP	1.0	2.4	N		Lime Stone	3/4	N		9.6	340.7	Clean		91	23	15
725	25	12-16-99	BSB	154259	160 - N.B.	Strut	N	CIP	0.5	1.9	Y	0.08	Lime Stone	3/4	N		9.8	341.2	Clean		50		14
726	26	12-16-99	BSB	154259	160 - N.B.	Strut	N	CIP	1.0	2.4	Y	0.15	Lime Stone	5/8	N		10.5	368.8	Clean	x	34		12
727	27	12-16-99	BSB	154259	160 - N.B.	Strut	N	CIP	1.0	2.4	N		Lime Stone	5/8	N		10.7	248.4	Clean	x	75		13
728	28	12-16-99	BSB	154259	160 - N.B.	Strut	N	CIP	0.5	1.9	N		Lime Stone	1	N		10.4	315.6	Clean		51		14
741	1	02-24-00	SHB	150202	10	1	W	PC		1.0	N		Lime Stone	3/4	N		9.5	335.0	Clean		50		138
742	2	02-24-00	SHB	150202	10	1	W	PC		1.0	N		Lime Stone	5/8	N		10.5	381.3	Clean		55	22	124
743	3	02-24-00	SHB	150202	10	1	W	PC		-0.3	N		Lime Stone	3/4	N		9.9	363.6	Barnacle		45		140
744	4	02-24-00	SHB	150202	10	1	W	PC		-0.3	N		Lime Stone	1/2	N		9.8	358.3	Barnacle		45	32	142
745	5	02-24-00	SHB	150202	10	1	W	PC		2.3	Y	0.08	Lime Stone	5/8	N		10.2	377.4	Clean	x	42		150
746	6	02-24-00	SHB	150202	10	1	W	PC		2.3	N		Lime Stone	3/4	N		10.6	387.9	Clean	x	58		122
747	7	02-24-00	SHB	150202	11	6	E	PC		1.0	N		Lime Stone	1	N		9.6	346.1	Clean	x	99		98
748	8	02-24-00	SHB	150202	11	6	E	PC		1.0	N		Lime Stone	1	Y	8.7	8.7	309.4	Clean	x	99		110
749	9	02-24-00	SHB	150202	11	6	E	PC		-0.7	N		Lime Stone	1	N		8.8	320.1	Barnacle	x	70		110
750	10	02-24-00	SHB	150202	11	6	E	PC		-0.7	N		Lime Stone	5/8	N		8.9	326.2	Barnacle	x	61		111
751	11	02-24-00	SHB	150202	11	6	E	PC		2.5	Y	0.10	Lime Stone	3/4	N		8.5	310.9	Clean	x	68		114
752	12	02-24-00	SHB	150202	11	6	E	PC		2.5	N		Lime Stone	3/4	N		9.8	358.6	Clean	x	92		101
753	13	02-24-00	SHB	150202	16	1	E	PC		1.0	N		Lime Stone	3/4	N		10.0	366.3	Clean	x	67		122
754	14	02-24-00	SHB	150202	16	1	E	PC		1.0	N		Lime Stone	3/4	N		9.5	346.8	Clean	x	63		119
755	15	02-24-00	SHB	150202	16	1	E	PC		-0.3	N		Lime Stone	3/4	N		9.6	349.0	Barnacle	x	59		117
756	16	02-24-00	SHB	150202	16	1	E	PC		-0.3	N		Lime Stone	3/4	N		9.8	358.2	Barnacle	x	56		123
757	17	02-24-00	SHB	150202	16	1	E	PC		2.0	Y	< 0.08	Lime Stone	3/4	Y	8.4	8.4	308.9	Clean	x	61		115

a) Direction (NSEW) faced by concrete surface.
b) Y: core on stress crack; SHR: shrinkage crack; N: no crack.
c) Appearance of external concrete surface at the core face.
d) Blank entries indicate not applicable or no available data

Table 3. Cores Extracted (Continued)

GENERAL CORE NUMBER	LOCAL CORE No.	DATE EXTRACTED	BRIDGE	BRIDGE No.	PIER No.	COLUMN / PILE No.	COLUMN OR PIER SIDE [a]	TYPE	ELEVATION (ft) ABOVE FOOTER	ELEVATION (ft) Above High Tide	CRACK [b]	CRACK WIDTH (mm)	AGGREGATE TYPE	AGGREGATE MAX. SIZE (in)	STEEL EXPOSURE	CONCRETE COVER (cm)	CORE LENGTH (cm)	CORE MASS (gr) AS-RECEIVED	CONCRETE FACE [c]	CHLORIDE PROFILE	AS-RECEIVED RESISTIVITY (Kohm-cm)	WET RESISTIVITY (Kohm-cm)	MAGNETIC READING (mg-force)
758	18	02-24-00	SHB	150202	16	1	E	PC		2.0	N		Lime Stone	5/8	N		8.6	319.7	Clean	x	51		108
759	19	02-24-00	SHB	150202	19	6	W	PC		1.7	Y	< 0.08	Lime Stone	3/4	Y	8.4	8.4	307.6	Clean		73		102
760	20	02-24-00	SHB	150202	19	6	W	PC		1.7	N		Lime Stone	5/8	Y	8.9	8.9	322.4	Clean		72		107
761	21	02-24-00	SHB	150202	19	6	W	PC		-0.3	N		Lime Stone	3/4	Y	7.8	8.7	328.7	Barnacle		63		225
762	22	02-24-00	SHB	150202	19	6	W	PC		-0.3	N		Lime Stone	3/4	Y	7.6	7.6	280.4	Barnacle		75		116
763	23	02-24-00	SHB	150202	19	6	W	PC		2.2	Y	< 0.08	Lime Stone	5/8	Y	8.7	8.7	321.3	Clean		67		111
764	24	02-24-00	SHB	150202	19	6	W	PC		2.2	N		Lime Stone	5/8	N		7.9	295.2	Clean		53		116
781	1	06-07-00	NSB	790152	16		E	CIP	-2.0	-0.5	Y	4.0[e]	Lime Stone	3/4	N		10.2	349.3	Barnacle	x	6.4		0.0
782	2	06-07-00	NSB	790152	16		E	CIP	-1.1	0.4	Y	4.0[e]	Lime Stone	5/8	N		11.4	361.9	Moss	x	8.9		0.0
783	3	06-07-00	NSB	790152	16		E	CIP	-1.2	0.3	N		Lime Stone	5/8	N		11.3	406.7	Moss	x	5.6		0.0
784	4	06-07-00	NSB	790152	16		E	CIP	-1.9	-0.4	N		Lime Stone	3/4	N		10.0	356.7	Barnacle	x	6.6		0.0
785	5	06-07-00	NSB	790152	16		E	CIP	-1.2	0.3	Y	0.25	Lime Stone	3/4	N		11.0	396.2	Barnacle		6.1		0.0
786	6	06-07-00	NSB	790152	16		E	CIP	-1.2	0.3	N		Lime Stone	1	N		10.0	345.8	Moss		4.2		0.0
787	7	06-07-00	NSB	790152	15		W	CIP	-1.4	0.3	Y	0.5[e]	Lime Stone	3/4	N		9.4	333.8	Moss	x	9.4		0.0
788	8	06-07-00	NSB	790152	15		W	CIP	-1.3	0.3	N		Lime Stone	3/4	N		11.1	400.6	Clean	x	6.6		0.0
789	9 [f]	06-07-00	NSB	790152	15		W	CIP	-1.4	0.3	Y	0.10	Lime Stone		N		11.0	386.8	Moss		--		--
790	10	06-07-00	NSB	790152	15		W	CIP	-1.0	0.6	Y	0.10	Lime Stone	1	N		9.6	324.9	Moss		13		0.0
791	11	06-07-00	NSB	790152	15		W	CIP	-1.0	0.6	N		Lime Stone	3/4	N		10.5	371.1	Moss		10	6	0.0
792	12	06-07-00	NSB	790152	16		E	CIP	-1.2	0.3	Y	0.25[e]	Lime Stone	3/4	N		9.2	312.1	Moss	x	6.7		0.0
793	13	06-07-00	NSB	790152	16		E	CIP	-1.3	0.2	N		Lime Stone	3/4	N		10.4	360.5	Moss	x	3.9		0.0
794	14	06-07-00	NSB	790152	16		E	CIP	-0.4	1.1	Y	0.25[e]	Lime Stone	1	N		9.7	335.6	Clean	x	11		0.0
795	15	06-07-00	NSB	790152	16		E	CIP	-0.4	1.1	N		Lime Stone	3/4	N		10.5	370.2	Clean	x	6.4		0.0
796	16	06-07-00	NSB	790152	16		SE	CIP	-1.4	0.1	Y	0.25	Lime Stone	3/4	N		9.8	343.5	Moss	x	7.7		0.0
797	17	06-07-00	NSB	790152	16		SE	CIP	-1.4	0.1	N		Lime Stone	1	N		10.3	364.9	Moss	x	5.6		0.0
798	18	06-07-00	NSB	790152	16		SE	CIP	-0.5	1.0	Y	0.25	Lime Stone	1	N		10.7	368.9	Clean	x	19		0.0

a)   Direction (NSEW) faced by concrete surface.
b)   Y: core on stress crack; SHR: shrinkage crack; N: no crack.
c)   Appearance of external concrete surface at the core face.
d)   Blank entries indicate not applicable or no available data
e)   Epoxy-injected crack
f)   Core contaminated with seawater – not used.

Table 3. Cores Extracted (Continued)

GENERAL CORE NUMBER	LOCAL CORE No.	DATE EXTRACTED	BRIDGE	BRIDGE No.	PIER No.	COLUMN / PILE No.	COLUMN OR PIER SIDE [a]	TYPE	ELEVATION (ft) ABOVE FOOTER	ELEVATION (ft) Above High Tide	CRACK [b]	CRACK WIDTH (mm)	AGGREGATE TYPE	AGGREGATE MAX. SIZE (in)	STEEL EXPOSURE	CONCRETE COVER (cm)	CORE LENGTH (cm)	CORE MASS (gr) AS-RECEIVED	CONCRETE FACE [c]	CHLORIDE PROFILE	AS-RECEIVED RESISTIVITY (Kohm-cm)	WET RESISTIVITY (Kohm-cm)	MAGNETIC READING (mg-force)
799	19	06-07-00	NSB	790152	16		SE	CIP	-0.5	1.0	N		Lime Stone	3/4	N		10.0	341.8	Clean	x	10		0.0
800	20	06-07-00	NSB	790152	11		W	CIP	-1.4	-0.3	Y	0.30	Lime Stone	1	N		9.9	354.3	Barnacle		10		0.0
801	21	06-07-00	NSB	790152	11		W	CIP	-1.4	-0.3	N		Lime Stone	3/4	N		10.1	354.9	Barnacle		11	6	0.0
802	22	06-07-00	NSB	790152	11		W	CIP	-0.7	0.4	Y	0.30	Lime Stone	3/4	N		9.3	323.6	Clean		15		0.0
803	23	06-07-00	NSB	790152	11		W	CIP	-0.7	0.4	N		Lime Stone	1	N		10.2	348.4	Clean		17		0.0
804	24	06-07-00	NSB	790152	11		W	CIP	-1.4	-0.3	Y	0.15	Lime Stone	1	N		9.6	337.8	Moss	x	11		0.0
805	25	06-07-00	NSB	790152	11		W	CIP	-1.4	-0.3	N		Lime Stone	1	N		10.4	364.2	Clean	x	13		0.0
806	26	06-07-00	NSB	790152	11		W	CIP	-0.5	0.5	Y	0.15	Lime Stone	1	N		8.9	301.4	Clean	x	24		0.0
807	27	06-07-00	NSB	790152	11		W	CIP	-0.5	0.5	N		Lime Stone	3/4	N		8.7	298.4	Clean	x	19		0.0
821	1	06-08-00	MIB	780097	9	6	W	PC		-0.5	N		Lime Stone	3/4	N		4.8	173.4	Moss	x	79		29
822	2	06-08-00	MIB	780097	9	6	W	PC		-0.5	N		Lime Stone	5/8	N		5.7	205.7	Barnacle	x	12		35
823	3	06-08-00	MIB	780097	9	5	E	PC		-0.5	N		Lime Stone	3/4	N		4.7	170.1	Barnacle	x	6.2		28
824	4	06-08-00	MIB	780097	9	5	E	PC		-0.5	N		Lime Stone	3/4	N		3.7	131.0	Barnacle	x	4.9		30
825	5	06-08-00	MIB	780097	9	5	E	PC		0.5	N		Lime Stone	5/8	N		2.6	90.1	Moss	x	0.8		24
826	6	06-08-00	MIB	780097	9	5	E	PC		0.5	N		Lime Stone	3/4	N		5.3	188.2	Moss	x	13		32
827	7	06-08-00	MIB	780097	9	6	W	PC		0.5	N		Lime Stone	3/4	N		5.5	194.1	Moss	x	10		31
828	8	06-08-00	MIB	780097	9	6	W	PC		0.5	N		Lime Stone	3/4	N		4.7	163.3	Moss	x	10		32
829	9 [f]	06-08-00	MIB	780097	5	6	W	PC		0.5	N		Lime Stone	5/8	N		3.8	144.6	Moss		4.5		50
841	1	07-26-00	BCB	150200	9	1	N	PC		-0.3	N		Lime Stone	3/4	Y	9.5	15.8	562.7	Barnacle	x	9.1		5.0
842	2	07-26-00	BCB	150200	9	1	N	PC		-0.3	N		Lime Stone	3/4	N		14.7	525.7	Barnacle		14	8	0.0
843	3	07-26-00	BCB	150200	9	1	N	PC		1.0	N		Lime Stone	3/4	Y	9.5	15.0	531.7	Clean		15		16
844	4	07-26-00	BCB	150200	9	1	N	PC		1.0	N		Lime Stone	3/4	Y	9.5	15.3	546.3	Clean	x	22		11
845	5	07-26-00	BCB	150200	6	5	S	PC		-0.3	N		Lime Stone	3/4	Y	7.0	13.6	500.4	Barnacle		31		11
846	6	07-26-00	BCB	150200	6	5	S	PC		-0.3	N		Lime Stone	3/4	Y	7.2	7.2	261.6	Barnacle	x	43		0.0
847	7	07-26-00	BCB	150200	6	5	S	PC		1.0	N		Lime Stone	1	N		13.5	493.2	Clean		80	10	0.0

a) Direction (NSEW) faced by concrete surface.
b) Y: core on stress crack; SHR: shrinkage crack; N: no crack.
c) Appearance of external concrete surface at the core face.
d) Blank entries indicate not applicable or no available data.
e) Epoxy-injected crack
f) Core contaminated with seawater – not used.

Table 3. Cores Extracted (Continued)

GENERAL CORE NUMBER	LOCAL CORE No.	DATE EXTRACTED	BRIDGE	BRIDGE No.	PIER No.	COLUMN / PILE No.	COLUMN OR PIER SIDE [a]	TYPE	ELEVATION (ft) ABOVE FOOTER	ELEVATION (ft) Above High Tide	CRACK [b]	CRACK WIDTH (mm)	AGGREGATE TYPE	AGGREGATE MAX. SIZE (in)	STEEL EXPOSURE	CONCRETE COVER (cm)	CORE LENGTH (cm)	CORE MASS (gr) AS-RECEIVED	CONCRETE FACE [c]	CHLORIDE PROFILE	AS-RECEIVED RESISTIVITY (Kohm-cm)	WET RESISTIVITY (Kohm-cm)	MAGNETIC READING (mg-force)
848	8	07-26-00	BCB	150200	6	5	S	PC		1.0	N		Lime Stone	3/4	Y	6.5	6.5	235.5	Clean	x	70		0.0
849	9	07-26-00	BCB	150200	7	1	W	CIP		1.0	Y	0.40	Lime Stone	5/8	N		15.0	545.1	Clean	x	35		103
850	10	07-26-00	BCB	150200	7	1	W	CIP		1.0	N		Lime Stone	3/4	N		14.4	513.6	Clean	x	43		95
851	11	07-26-00	BCB	150200	7	1	W	CIP		2.0	N		Lime Stone	3/4	N		15.1	524.1	Clean	x	39		102
852	12	07-26-00	BCB	150200	7	1	W	CIP		2.0	Y	0.30	Lime Stone	3/4	N		9.8	340.9	Clean	x	23		104
853	13	07-26-00	BCB	150200	7	2	W	CIP		1.0	N		Lime Stone	3/4	N		14.9	542.1	Clean		36		0.0
854	14	07-26-00	BCB	150200	7	2	W	CIP		1.0	N		Lime Stone	3/4	N		14.9	520.2	Clean	x	56		0.0
855	15	07-26-00	BCB	150200	7	2	W	CIP		1.0	N		Lime Stone	1	N		9.0	328.9	Clean		43	5	0.0
856	16	07-26-00	BCB	150200	7	2	W	CIP		2.0	N		Lime Stone	1	N		13.5	483.0	Clean		26		3.0
857	17	07-26-00	BCB	150200	7	2	W	CIP		2.0	N		Lime Stone	3/4	N		12.6	444.5	Clean	x	22		0.0
871	1	07-26-00	BPB	150211	10	6	W	PC		-0.4	N		Lime Stone	3/4	Y	8.8	8.8	313.5	Barnacle	x	91		24
872	2	07-26-00	BPB	150211	10	6	W	PC		-0.4	N		Lime Stone	3/4	Y	9.4	9.4	332.4	Barnacle		88	35	19
873	3	07-26-00	BPB	150211	10	6	W	PC		0.8	N		Lime Stone	3/4	Y	7.4	7.4	266.3	Clean	x	159		19
874	4	07-26-00	BPB	150211	10	6	W	PC		0.8	N		Lime Stone	3/4	Y	9.4	9.4	338.7	Clean		164		21
875	5	07-26-00	BPB	150211	10	5	E	PC		-0.4	N		Lime Stone	5/8	N		5.4	194.0	Barnacle		142		20
876	6	07-26-00	BPB	150211	10	5	E	PC		-0.4	N		Lime Stone	3/4	N		7.8	281.7	Barnacle	x	87		30
877	7	07-26-00	BPB	150211	10	5	E	PC		0.7	N		Lime Stone	3/4	Y	9.6	9.6	345.1	Clean		134	40	26
878	8	07-26-00	BPB	150211	10	5	E	PC		0.8	N		Lime Stone	5/8	N		4.9	165.9	Clean	x	120		19
879	9	07-26-00	BPB	150211	6	3	N	PC		-0.4	N		Lime Stone	5/8	Y	7.9	7.9	284.9	Barnacle		113		19
880	10	07-26-00	BPB	150211	6	3	N	PC		-0.4	N		Lime Stone	1	N		11.3	406.4	Barnacle	x	107		23
881	11	07-26-00	BPB	150211	6	3	N	PC		0.8	N		Lime Stone	3/4	Y	6.3	6.3	227.8	Clean	x	167		18
882	12	07-26-00	BPB	150211	6	3	N	PC		0.8	N		Lime Stone	3/4	Y	8.6	8.6	307.3	Clean		124		23
891	1	07-27-00	NPB	170158	10	1	S	CIP	-1.3	0.1	Y	0.10	Lime Stone	3/4	Y	8.2	8.2	278.5	Clean	x	49		30
892	2	07-27-00	NPB	170158	10	1	S	CIP	-1.3	0.1	N		Lime Stone	5/8	Y		9.1	320.7	Clean	x	171		32
893	3	07-27-00	NPB	170158	10	1	S	CIP	-1.3	0.1	N		Lime Stone	5/8	Y	9.2	10.0	337.8	Clean		157	48	33

a) Direction (NSEW) faced by concrete surface.
b) Y: core on stress crack; SHR: shrinkage crack; N: no crack.
c) Appearance of external concrete surface at the core face.
d) Blank entries indicate not applicable or no available data.

Table 3. Cores Extracted (Continued)

GENERAL CORE NUMBER	LOCAL CORE No.	DATE EXTRACTED	BRIDGE	BRIDGE No.	PIER No.	COLUMN / PILE No.	COLUMN OR PIER SIDE [a]	TYPE	ELEVATION (ft) ABOVE FOOTER	ELEVATION (ft) Above High Tide	CRACK [b]	CRACK WIDTH (mm)	AGGREGATE TYPE	AGGREGATE MAX. SIZE (in)	STEEL EXPOSURE	CONCRETE COVER (cm)	CORE LENGTH (cm)	CORE MASS (gr) AS-RECEIVED	CONCRETE FACE [c]	CHLORIDE PROFILE	AS-RECEIVED RESISTIVITY (Kohm-cm)	WET RESISTIVITY (Kohm-cm)	MAGNETIC READING (mg-force)
894	4	07-27-00	NPB	170158	10	1	S	CIP	1.0	2.3	N		Lime Stone	3/4	Y	11.5	11.5	401.8	Clean		154		14
895	5	07-27-00	NPB	170158	10	1	S	CIP	1.0	2.3	N		Lime Stone	3/4	N		19.8	679.0	Clean	x	92		14
896	6	07-27-00	NPB	170158	8	2	S	CIP	-1.0	0.3	Y	0.08	Lime Stone	5/8	N		15.1	517.5	Clean	x	155		28
897	7	07-27-00	NPB	170158	8	2	S	CIP	-1.0	0.3	N		Lime Stone	3/4	N		14.2	481.3	Clean	x	116		25
898	8	07-27-00	NPB	170158	8	2	S	CIP	1.0	2.3	N		Lime Stone	3/4	N		5.8	215.0	Clean		162		18
899	9	07-27-00	NPB	170158	8	2	S	CIP	1.0	2.3	N		Lime Stone	3/4	N		14.3	504.4	Clean	x	157		14
900	10	07-27-00	NPB	170158	8	2	S	CIP	1.0	2.3	N		Lime Stone	3/4	N		10.5	367.3	Clean		189	40	14
901	11	07-27-00	NPB	170158	8	1	W	CIP	3.2	4.5	Y	0.15	Lime Stone	3/4	Y	11.9	11.9	431.0	Clean	x	76		16
902	12	07-27-00	NPB	170158	8	1	W	CIP	3.2	4.5	N		Lime Stone	3/4	Y	11.9	11.9	427.0	Clean	x	117		18
903	13	07-27-00	NPB	170158	8	1	W	CIP	3.2	4.5	N		Lime Stone	3/4	Y	12.0	12.0	441.5	Clean		110	40	15
904	14	07-27-00	NPB	170158	5	wall	S	CIP		0.5	N		Lime Stone	5/8	N		11.9	419.8	Clean	x	76		17
905	15	07-27-00	NPB	170158	5	wall	S	CIP		0.5	Y	0.08	Lime Stone	3/4	Y	12.5	12.6	449.9	Clean	x	63		14
906	16	07-27-00	NPB	170158	5	wall	S	CIP		-0.7	N		Lime Stone	3/4	N		11.9	429.1	Barnacle	x	59		15
907	17	07-27-00	NPB	170158	5	wall	S	CIP		-0.7	N		Lime Stone	3/4	N		12.3	437.2	Barnacle		54		17

a) Direction (NSEW) faced by concrete surface.
b) Y: core on stress crack; SHR: shrinkage crack; N: no crack.
c) Appearance of external concrete surface at the core face.
d) Blank entries indicate not applicable or no available data.

Table 4. Core Slicing Schemes

Key	Depth Key (in)					
	A	B	C	D	E	F
1		0.11	0.38	0.75	1.50	
2		0.11	0.38	0.75	1.25	2.00
3	0.04	0.19	0.45	0.70	0.95	1.33
4	0.04	0.19	0.45	0.83	1.33	2.08
5	0.06	0.22	0.49	0.74	0.99	1.37
6	0.08	0.26	0.53	0.78	1.03	1.41

Each core sliced for chloride analysis was cut according to either one of 6 schemes, labeled 1 to 6 per the indicated key number. The entries A to F indicate the depth of the center of each slice from the external concrete surface. An additional sample (G) was obtained by cutting an ~1" thick slice near the end of the core opposite to the external concrete surface. The center depth for sample G is indicated for each core in Table 5. Sample A (acquired only for schemes 3-6) was obtained by directly machining powder from the core face to twice the indicated center depth. All the other samples were prepared by grinding the cut slice into powder.

Table 5   Chloride Concentration Data and Calculated Diffusion Parameters

General Core Number	Local Core No.	Bridge	Bridge No.	Age (years)	Water Chloride Content (ppm)	Cracked (C)/Sound (S) Concrete	Elevation above High Tide (ft)	A	B	C	D	E	F	Depth Key (Table 4)	Center Depth Sample G (in)	G	D (in^2/y)	Cs (pcy)	Co (pcy)
524	03 at 6'	SSK	150189	11	18504	c	6.00		37.24	23.97	12.42	6.47		1	2.52	2.22			
526	04 at 6'	SSK	150189	11	18504	s	6.00		27.43	8.23	0.55	0.08		1	2.52	0.11	0.0038	39.6	0.01
543	5 at 3	SSK	150189	11	18504	c	3.00				Special			a					
531	09 at 3'	SSK	150189	11	18504	c	3.00		38.00	25.98	18.16	13.13		1	2.52	6.23			
534	10 at 3'	SSK	150189	11	18504	s	3.00		32.41	13.61	3.88	0.14		1	2.52	0.10	0.0064	42.5	0.37
535	11 at 3'	SSK	150189	11	18504	s	3.00		32.14	15.16	4.55	0.14		1	2.52	0.15	0.0080	40.9	0.26
536	14 at 3'	SSK	150189	11	18504	c	3.00		27.27	23.34	15.45	6.36		1	2.52	5.98			
537	15 at 3'	SSK	150189	11	18504	s	3.00		31.14	14.66	7.65	0.29		1	2.52	0.12	0.010	37.6	0.58
538	16 at 3'	SSK	150189	11	18504	s	3.00		20.98	10.54	5.17	0.57		1	2.52	0.13	0.011	25.2	0.48
539	17 at 3'	SSK	150189	11	18504	s	3.00		31.85	18.46	11.22	1.24		1	2.52	0.36	0.019	36.1	0.43
521	01 at 18'	SSK	150189	11	18504	c	18.0		4.82	1.5	0.44	0.15		1	2.52	0.12			
522	02 at 18'	SSK	150189	11	18504	s	18.0		5.37	1.22	0.24	0.06		1	2.52	0.05	0.0027	8.3	0.09
523	03 at 18'	SSK	150189	11	18504	c	18.0		6.74	2.16	0.33	0.21		1	2.52	0.23			
525	04 at 19'	SSK	150189	11	18504	c	19.0		4.99	3.09	0.32	0.13		1	2.52	0.16			
527	05 at 19'	SSK	150189	11	18504	s	19.0		5.46	1.71	0.36	0.06		1	2.52	0.07	0.0039	7.8	0.10
528	06 at 19'	SSK	150189	11	18504	c	19.0		6.52	2.41	0.26	0.14		1	2.52	0.13			
529	07 at 60'	SSK	150189	11	18504	c	60.0		5.14	3.30	0.51	0.19		1	2.52	0.14			
530	08 at 60'	SSK	150189	11	18504	s	60.0		3.30	0.72	0.26	0.11		1	2.52	0.10	0.0024	5.2	0.15
532	09 at 60'	SSK	150189	11	18504	c	60.0		3.60	0.84	0.48	0.28		1	2.52	0.26			
533	10 at 120'	SSK	150189	11	18504	c	120.0		1.54	0.61	0.43	0.21		1	2.52	0.18			
562	13	HFB	150210	8	17143	c	1.67		38.07	13.56	18.61	7.89		1	2.52	1.82			
563	14	HFB	150210	8	17143	c	1.67		33.35	20.25	9.10	1.10		1	2.52	0.24			
564	15	HFB	150210	8	17143	c	1.33		27.75	20.81	9.85	4.16		1	2.52	2.849			
565	16	HFB	150210	8	17143	s	1.33		33.78	10.57	1.55	0.83		1	2.52	0.56	0.0053	48.5	0.67

Table 5   Chloride Concentration Data and Calculated Diffusion Parameters (Continued)

General Core Number	Local Core No.	Bridge	Bridge No.	Age (years)	Water Chloride Content (ppm)	Cracked (C)/ Sound (S) Concrete	Elevation above High Tide (ft)	A	B	C	D	E	F	Depth Key (Table 4)	Center Depth Sample G (in)	G	D (in^2/y)	Cs (pcy)	Co (pcy)
566	17	HFB	150210	8	17143	c	3.50		7.32	6.64	2.50	1.05		1	2.52	0.93			
567	18	HFB	150210	8	17143	s	3.50		9.35	7.02	3.42	0.78		1	2.52	0.14	0.035	10.8	0.11
578	29	HFB	150210	8	17143	c	0.01		24.72	17.31	10.77	5.61		1	2.52	3.64			
579	30	HFB	150210	8	17143	s	0.01		41.19	33.57	19.52	3.09		1	2.52	0.40	0.045	48.2	0.00
582	33	HFB	150210	8	17143	s	3.50		11.26	8.17	5.94	0.66		1	2.52	0.24	0.048	12.7	0.00
586	37	HFB	150210	8	17143	s	2.17		12.72	12.36	6.61	1.98		1	2.52	0.59	0.065	15.0	0.08
590	41	HFB	150210	8	17143	c	0.01		41.07	25.48	16.97	11.29		1	2.52	5.92			
591	42	HFB	150210	8	17143	s	0.01		45.32	33.17	9.93	0.67		1	2.52	0.28	0.021	56.3	0.00
597	48	HFB	150210	8	17143	c	3.17		9.78	8.14	3.58	1.36		1	2.52	0.83	0.033	11.5	0.74
598	49	HFB	150210	8	17143	s	3.17		8.84	5.72	1.80	0.24		1	2.52	0.14	0.019	10.8	0.07
550	1	CCC	150138	6	14181	s	3.25		8.41	12.98	2.07	0.15		1	2.52	0.07	0.042	13.0	0.00
551	2	CCC	150138	6	14181	c	3.25		18.68	9.90	2.53	0.44		1	2.52	0.22			
552	3	CCC	150138	6	14181	s	2.17		16.74	19.60	0.42	0.21		1	2.52	0.18	0.024	24.5	0.00
553	4	CCC	150138	6	14181	c	2.17		26.66	18.80	5.16	0.59		1	2.52	0.32			
555	6	CCC	150138	6	14181	s	0.01		20.57	9.76	1.66	0.29		1	2.52	0.22	0.013	26.8	0.11
556	7	CCC	150138	6	14181	s	1.00		28.39	14.94	2.34	0.83		1	2.52	0.29	0.015	36.6	0.20
559	10	CCC	150138	6	14181	s	0.01		30.68	12.02	2.06	0.28		1	2.52	0.17	0.010	41.5	0.22
560	11	CCC	150138	6	14181	s	1.00		32.29	9.18	1.91	0.27		1	2.52	0.16	0.006	47.1	0.49
576	27	CCC	150138	6	14181	s	0.01		18.82	11.10	3.15	0.49		1	2.52	0.43	0.020	23.3	0.29
577	28	CCC	150138	6	14181	s	0.01		36.42	16.41	6.80	0.43		1	2.52	0.35	0.028	31.4	0.12
568	19	BLP	150221	2	19356	s	1.00		53.22	32.65	4.96	0.37		1	2.52	0.29	0.051	69.1	0.00
570	21	BLP	150221	2	19356	s	1.00		34.30	6.37	0.43	0.29		1	2.52	0.46	0.013	55.3	0.32
572	23	BLP	150221	2	19356	s	0.01		29.80	33.78	4.68	0.61		1	2.52	0.30	0.095	41.7	0.00
574	25	BLP	150221	2	19356	s	0.01		19.65	7.31	0.91	0.90		1	2.52	0.36	0.026	27.2	0.48

62

Table 5 Chloride Concentration Data and Calculated Diffusion Parameters (Continued)

General Core Number	Local Core No.	Bridge	Bridge No.	Age (years)	Water Chloride Content (ppm)	Cracked (C)/Sound (S) Concrete	Elevation above High Tide (ft)	A	B	C	D	E	F	Depth Key (Table 4)	Center Depth Sample G (in)	G	D (in^2/y)	Cs (pcy)	Co (pcy)
611	12	MAC	870772	2.5	20306	c	5.73		3.70	0.67	0.24	0.20		1	2.52	0.17			
612	13	MAC	870772	2.5	20306	c	5.75		1.37	0.14	0.21	0.19		1	2.52	0.13			
613	16	MAC	870772	2.5	20306	s	2.71		10.57	5.96	1.37	0.15		1	2.52	0.11	0.044	13.3	0.03
614	20	MAC	870772	2.5	20306	c	2.63		11.57	5.56	1.65	0.81		1	2.52	0.32			
615	21	MAC	870772	2.5	20306	s	2.65		8.56	3.04	0.26	0.10		1	2.52	0.10	0.020	11.9	0.05
616	31	MAC	870772	2.5	20306	c	2.50		12.05	7.32	1.14	0.18		1	2.52	0.14			
650	0A	DPE	720518	11	16540	s	0.01	16.18	22.80	18.69	7.12	1.94	0.72	3	6.09	0.16	0.017	33.3	0.00
652	0C	DPE	720518	11	16540	c	0.01	6.385	14.35	10.68	8.17	8.23	4.68	4	5.70	0.49			
653	0D	DPE	720518	11	16540	s	0.01	21.07	15.46	16.75	12.58	7.72	2.44	3	3.61	0.29	0.052	20.8	0.00
655	1AA	DPE	720518	11	16540	s	1.00	5.061	2.38	3.52	2.18	1.33	1.08	3	5.46	0.19	0.082	3.4	0.15
658	1C	DPE	720518	11	16540	c	1.00	5.622	7.72	4.17	3.87	3.58	2.95	4	5.27	1.35			
660	1DD	DPE	720518	11	16540	s	1.00	2.391	3.75	4.07	3.38	2.42	1.91	3	5.31	0.20	0.126	4.5	0.18
661	3A	DPE	720518	11	16540	s	3.00	8.861	2.35	0.69	0.29	0.17	0.06	3	5.43	0.02	0.0048	3.9	0.09
665	3CCC	DPE	720518	11	16540	c	3.00	3.871	5.89	1.99	0.68	0.25	0.19	4	2.96	0.15			
666	3D	DPE	720518	11	16540	s	3.00	3.045	2.04	0.67	0.26	0.22	0.18	3	4.91	0.12	0.0045	3.4	0.17
667	5A	DPE	720518	11	16540	s	5.00	4.354	1.33	0.36	0.26	0.31	0.15	6	6.17	0.16	0.0031	3.5	0.22
669	5C	DPE	720518	11	16540	c	5.00	2.239	1.98	0.67	0.29	0.10	0.08	4	3.81	0.25			
670	5D	DPE	720518	11	16540	s	5.00	4.222	1.66	0.60	0.23	0.19	0.11	3	5.50	0.13	0.0052	2.6	0.14
701	1	BSB	154259	7	19850	c	1.00	0.223	16.06	7.42	5.07	4.16	4.08	4	2.71	2.96			
702	2	BSB	154259	7	19850	c	0.01	45.17	31.88	18.97	6.42	2.19	1.83	4	2.98	2.17			
703	3	BSB	154259	7	19850	s	0.01	51.16	29.78	11.41	1.55	0.81	0.49	3	2.79	0.52	0.010	47.2	0.21
704	4	BSB	154259	7	19850	s	1.00	18.86	8.47	0.92	0.66	0.41	0.38	3	3.06	0.32	0.0026	22.0	0.44
707	7	BSB	154259	7	19850	c	1.00		5.41	3.63	3.57	4.18	2.15	4	3.04	2.84			
708	8	BSB	154259	7	19850	s	1.00		6.14	3.62	0.40	0.50	0.47	3	2.79	0.29	0.013	9.0	0.22

Table 5   Chloride Concentration Data and Calculated Diffusion Parameters (Continued)

General Core Number	Local Core No.	Bridge	Bridge No.	Age (years)	Water Chloride Content (ppm)	Cracked (C)/ Sound (S) Concrete	Elevation above High Tide (ft)	A	B	C	D	E	F	Depth Key (Table 4)	Center Depth Sample G (in)	G	D (in²/y)	Cs (pcy)	Co (pcy)
709	9	BSB	154259	7	19850	S	0.01		13.36	7.67	2.27	0.57	0.33	3	3.02	0.33	0.017	18.9	0.03
710	10	BSB	154259	7	19850	S	0.01		13.11	7.65	3.00	0.85	0.45	3	4.83	0.37	0.019	18.2	0.11
718	18	BSB	154259	7	19850	C	0.38		47.95	40.18	21.18	11.05	2.03	4	5.07	0.29			
720	20	BSB	154259	7	19850	S	0.38		42.92	28.10	31.53	17.14	3.74	3	3.22	0.29	0.063	51.7	0.00
721	21	BSB	154259	7	19850	S	0.01		29.93	29.14	25.88	14.62	9.32	3	3.65	0.45	0.112	37.3	0.00
723	23	BSB	154259	7	19850	S	2.38	22.4	30.40	15.98	11.35	4.44	0.67	6	3.46	0.14	0.026	38.8	0.00
726	26	BSB	154259	7	19850	C	1.88	6.386	11.45	21.37	9.65	6.18	2.42	4	3.65	0.47			
727	27	BSB	154259	7	19850	S	2.38		10.45	16.44	12.53	6.48	2.53	3	3.73	0.19	0.113	16.8	0.00
745	5	SHB	150202	10	10990	C	2.33	4.15	17.22	7.22	3.69	0.92	0.21	4	3.53	0.06			
746	6	SHB	150202	10	10990	S	2.33	3.39	9.55	7.14	4.48	3.14	0.34	3	3.69	0.00	0.029	12.2	0.00
747	7	SHB	150202	10	10990	S	1.00	6.28	12.94	20.69	14.02	8.39	1.01	3	3.30	0.04	0.057	21.5	0.00
748	8	SHB	150202	10	10990	S	1.00	6.25	16.67	19.83	13.16	7.57	1.47	3	2.94	0.04	0.045	24.2	0.00
749	9	SHB	150202	10	10990	S	0.01	2.94	21.76	11.84	9.42	6.36	1.27	3	2.98	0.04	0.027	25.8	0.01
750	10	SHB	150202	10	10990	S	0.01	4.66	17.70	11.45	8.46	6.74	1.55	3	3.02	0.03	0.035	21.0	0.00
751	11	SHB	150202	10	10990	C	2.50	2.25	13.31	5.07	1.38	0.43	0.20	4	2.98	0.04			
752	12	SHB	150202	10	10990	S	2.50	2.36	7.44	3.05	0.66	0.27	0.04	3	3.38	0.01	0.0078	11.4	0.00
753	13	SHB	150202	10	10990	S	1.00	4.93	15.27	15.14	11.35	7.87	1.86	3	3.46	0.05	0.051	20.2	0.00
754	14	SHB	150202	10	10990	S	1.00	4.46	14.13	12.88	10.08	7.71	1.02	3	3.26	0.00	0.048	18.4	0.00
755	15	SHB	150202	10	10990	S	0.01	7.28	15.90	12.22	8.15	5.70	1.06	3	3.30	0.05	0.033	20.0	0.00
756	16	SHB	150202	10	10990	S	0.01	10.05	16.72	7.65	8.96	5.54	1.60	3	3.38	0.05	0.034	18.6	0.08
757	17	SHB	150202	10	10990	C	2.00	2.48	9.18	7.70	3.69	1.20	0.30	4	2.96	0.03			
758	18	SHB	150202	10	10990	S	2.00	3.34	7.15	3.95	1.72	0.50	0.05	3	2.90	0.00	0.013	10.0	0.00
781	1	NSB	790152	10	17700	C	0.01		41.09	32.39	27.35	20.05	23.38	2	3.53	19.76			
782	2	NSB	790152	10	17700	C	0.42		27.09	27.94	23.48	23.95	20.30	2	4.01	14.51			
783	3	NSB	790152	10	17700	S	0.33	7.53	11.15	11.52	7.90	6.35	7.18	5	3.97	1.75	0.132	12.7	1.64

Table 5   Chloride Concentration Data and Calculated Diffusion Parameters (Continued)

General Core Number	Local Core No.	Bridge	Bridge No.	Age (years)	Water Chloride Content (ppm)	Cracked (C)/Sound (S) Concrete	Elevation above High Tide (ft)	A	B	C	D	E	F	Depth Key (Table 4)	Center Depth Sample G (in)	G	D (in^2/y)	Cs (pcy)	Co (pcy)
784	4	NSB	790152	10	17700	S	0.01	19.88	17.22	14.96	13.41	12.72	8.89	3	3.46	2.61	0.164	18.6	1.57
787	7	NSB	790152	10	17700	C	0.25		23.46	22.76	23.25	19.32	14.28	2	3.22	12.57			
788	8	NSB	790152	10	17700	S	0.29	13.79	11.49	11.30	10.95	10.06	8.84	3	3.89	1.92	0.405	13.1	0.00
792	12	NSB	790152	10	17700	C	0.29		25.35	9.81	11.19	9.19	9.46	2	3.14	10.98			
793	13	NSB	790152	10	17700	S	0.21	10.94	11.06	9.89	8.74	6.17	6.75	3	3.61	2.55	0.111	11.9	2.43
794	14	NSB	790152	10	17700	C	1.13		14.01	14.50	9.46	10.43	9.64	2	3.34	8.10			
795	15	NSB	790152	10	17700	S	1.13	9.23	9.68	4.73	5.57	5.70	2.90	3	3.65	1.00	0.064	9.5	1.11
796	16	NSB	790152	10	17700	C	0.08		26.86	23.23	18.56	13.52	9.58	2	3.38	8.15			
797	17	NSB	790152	10	17700	S	0.08	1.53	24.30	22.09	15.85	17.15	10.41	3	3.57	4.50	0.085	27.2	4.24
798	18	NSB	790152	10	17700	C	1.04		22.25	19.33	13.07	9.70	8.88	2	3.73	6.95			
799	19	NSB	790152	10	17700	S	1.04	3.28	6.40	6.50	6.03	4.88	2.23	3	3.46	0.15	0.115	8.0	0.00
804	24	NSB	790152	10	17700	C	0.01		20.70	14.22	12.15	10.45	8.88	2	3.30	6.15			
805	25	NSB	790152	10	17700	S	0.01	12.99	12.66	7.72	6.50	4.99	5.27	3	3.61	0.82	0.051	13.1	1.28
806	26	NSB	790152	10	17700	C	0.54		13.34	11.90	8.65	8.42	6.89	2	3.02	6.52			
807	27	NSB	790152	10	17700	S	0.54	7.00	5.10	3.59	3.57	2.31	1.60	3	2.94	0.26	0.063	5.7	0.21
821	1	MIB	780097	7	18855	S	0.01	25.53	25.35	12.99	5.29	1.39	0.57	3	1.75	0.58	0.016	35.8	0.22
822	2	MIB	780097	7	18855	S	0.01	25.48	24.61	15.10	6.33	1.61	1.06	3	1.93	1.02	0.020	33.9	0.37
823	3	MIB	780097	7	18855	S	0.01	32.94	24.76	14.38	8.78	2.10	0.68	5	1.75	1.20	0.025	34.7	0.25
824	4	MIB	780097	7	18855	S	0.01	31.94	30.80	18.08	7.52	2.56		5	1.31	0.15	0.020	46.2	0.00
825	5	MIB	780097	7	18855	S	0.50	17.09	16.72	10.97	6.97			3	0.95	3.80	0.037	20.8	0.00
826	6	MIB	780097	7	18855	S	0.50	42.08	17.32	11.98	5.92	1.96	0.44	3	1.85	0.43	0.026	23.3	0.00
827	7	MIB	780097	7	18855	S	0.50	22.62	16.37	14.07	7.20	2.58	0.69	5	1.91	0.84	0.036	23.3	0.00
828	8	MIB	780097	7	18855	S	0.50	30.64	16.86	13.00	6.17	1.57	0.57	3	1.73	0.50	0.028	24.7	0.00

Table 5   Chloride Concentration Data and Calculated Diffusion Parameters (Continued)

General Core Number	Local Core No.	Bridge	Bridge No.	Age (years)	Water Chloride Content (ppm)	Cracked (C)/ Sound (S) Concrete	Elevation above High Tide (ft)	A	B	C	D	E	F	Depth Key (Table 4)	Center Depth Sample G (in)	G	D (in²/y)	Cs (pcy)	Co (pcy)
841	1	BCB	150200	14	19356	S	0.01	4.432	7.44	7.89	6.21	7.79	5.16	3	5.74	0.52	0.357	8.4	0.00
844	4	BCB	150200	14	19356	S	1.00	11.73	15.10	11.00	11.23	11.26	9.70	5	5.54	0.32	0.238	15.1	0.00
846	6	BCB	150200	38	19356	S	0.01	12.23	17.10	29.08	19.96	14.86	12.53	3	2.35	8.94	0.077	24.3	0.66
848	8	BCB	150200	38	19356	S	1.00	13.57	16.39	16.44	18.20	14.50	11.91	3	2.09	6.13	0.074	19.9	0.00
849	9	BCB	150200	14	19356	C	1.00		21.32	15.24	13.88	10.71	8.17	2	5.43	3.12			
850	10	BCB	150200	14	19356	S	1.00	21.79	15.93	11.92	11.07	7.54	3.30	3	5.19	0.29	0.043	18.4	0.08
851	11	BCB	150200	14	19356	S	2.00	7.093	10.25	11.92	9.60	7.16	4.76	3	5.46	0.38	0.097	12.9	0.28
852	12	BCB	150200	14	19356	C	2.00		8.95	12.64	9.29	6.96	4.38	2	3.38	1.46			
854	14	BCB	150200	38	19356	S	1.00	9.991	14.92	15.25	15.28	13.97	13.23	3	5.39	2.20	0.187	17.0	0.00
857	17	BCB	150201	38	19356	S	2.00	16.26	3.97	7.35	9.59	12.60	11.55	3	4.48	2.744	b	b	b
871	1	BPB	150211	9	25902	S	0.01	9.15	14.97	8.93	2.64	0.96	0.22	3	2.98	0.12	0.014	21.4	0.00
873	3	BPB	150211	9	25902	S	0.83	12.38	22.74	19.48	8.28	3.02	1.03	3	2.43	0.13	0.023	31.8	0.00
876	6	BPB	150211	9	25902	S	0.01	13.76	21.93	10.90	1.37	5.06	0.21	3	2.59	0.14	0.010	31.9	0.86
878	8	BPB	150211	9	25902	S	0.83	24.08	20.91	13.97	5.42	0.40	0.11	3	1.77	0.19	0.014	30.4	0.00
880	10	BPB	150211	9	25902	S	0.01	17.64	16.79	12.07	4.77	1.55	0.42	3	3.97	0.44	0.019	23.2	0.00
881	11	BPB	150211	9	25902	S	0.75	13.26	24.39	20.83	12.82	4.41	0.40	3	2.05	0.22	0.027	33.9	0.00
891	1	NPB	170158	14	20915	C	0.08		30.63	32.76	44.08	26.10	12.61	2	2.88	1.90			
892	2	NPB	170158	14	20915	S	0.08	43.42	53.89	32.22	27.77	22.95	9.35	3	3.10	1.28	0.030	60.0	1.38
895	5	NPB	170158	14	20915	S	2.33	23.16	20.10	23.85	21.11	16.57	7.97	3	7.31	0.14	0.103	26.4	0.00
896	6	NPB	170158	14	20915	C	0.33		42.58	35.44	28.61	17.50	2.47	2	5.46	0.31			
897	7	NPB	170158	14	20915	S	0.33	23.51	27.42	22.89	14.95	10.10	3.81	3	5.11	0.31	0.029	34.1	0.00
899	9	NPB	170158	14	20915	S	2.33	16.7	17.18	24.19	20.04	10.31	3.19	3	5.15	0.20	0.051	26.4	0.00
901	11	NPB	170158	14	20915	C	4.50		8.73	12.89	3.13	0.85	0.54	2	4.20	0.22			
902	12	NPB	170158	14	20915	S	4.50	2.84	6.75	10.55	6.81	2.12	0.35	6	4.20	0.24	0.031	11.2	0.00

Table 5   Chloride Concentration Data and Calculated Diffusion Parameters (Continued)

General Core Number	Local Core No.	Bridge	Bridge No.	Age (years)	Water Chloride Content (ppm)	Cracked (C)/ Sound (S) Concrete	Elevation above High Tide (ft)	Chloride Concentration (pcy) at the Depth from the Surface Indicated by the Slicing Scheme in Table 4.									Calculated		
								A	B	C	D	E	F	Depth Key (Table 4)	Center Depth Sample G (in)	G	D (in^2/y)	Cs (pcy)	Co (pcy)
904	14	NPB	170158	14	20915	S	0.50	32.95	35.74	32.85	29.64	25.29	17.18	3	4.20	0.34	0.108	40.9	0.00
905	15	NPB	170158	14	20915	C	0.50		32.53	31.90	21.25	10.96	3.20	2	4.48	0.15			
906	16	NPB	170158	14	20915	S	0.01	28.36	24.41	15.17	10.38	5.90	1.62	3	4.20	0.15	0.018	30.0	0.00
907	17	NPB	170158	14	20915	S	0.01	32.39	31.01	21.99	13.64	9.99	2.83	3	4.36	0.15	0.022	38.0	0.00

Note:

a)   Core No. 543 (local No. 5 at 3'), SSK: Special analysis per figure 13.

(pcy)		Y (in)		
		0.3125	1.011	1.625
X (in)	0.125	42.8	18.67	7.94
	0.375	35.2	15.81	8.26
	0.625	32.76	9.39	7.46
	0.875	28.22	11.79	7.36

b)   Core No.857 (local No.17), BCB: profile inadequate for analysis.

Table 6. Apparent Chloride Diffusion Coefficient (in^2/y) - Tidal to 6 ft (1.8 m) AHT

Bridge	CIP			PC		
	Aver	Max	Min	Aver	Max	Min
SSK	-	-	-	0.010	0.019	0.004
HFB	0.034	0.065	0.005	-	-	-
BLP	-	-	-	0.046	0.095	0.013
CCC	-	-	-	0.020	0.042	0.006
MAC	0.032	0.044	0.020	-	-	-
DPE	0.037	0.126	0.003	-	-	-
BSB	0.078	0.113	0.026	0.012	0.019	0.003
SHB	-	-	-	0.034	0.057	0.008
NSB	0.132	0.405	0.051	-	-	-
MIB	-	-	-	0.026	0.037	0.016
BCB62	0.187	0.187	0.187	0.076	0.077	0.074
BCB86	0.070	0.097	0.043	0.298	0.357	0.238
BPB	-	-	-	0.018	0.027	0.010
NPB	0.049	0.108	0.018	-	-	-

Table 7. Crack Survey[a,b]

Bridge	Bridge Number	Crack Types and Other Features Observed	Bridge Piers-Bents Surveyed	# Stress Cracks Counted		Approximate Perimeter Surveyed (m)		Stress Crack Index (cracks / m)	
				CIP	PC	CIP	PC	CIP	PC
SSK[c]	150189	stress	88 - 135	--	23	--	950	--	0.024
HFB	150210	shrink/stress	9 – 21, 52	25	--	200	--	0.12	--
CCC	150138	shrink	4 - 7	--	0	--	55	--	0
BLP	150221	shrink	2 - 15	--	0	--	260	--	0
MAC	870772	cold joint/ stress	Pier 8 (E face)	2	--	30	--	*0.068*[e]	--
DPE	720518	stress	North Pier	1	--	43	--	0.023	--
BSB	154259	shrink/stress	*90-196 (53/107 NB)*[e] *97-191 (54/95 SB)*[e]	36	9	2700	*420*[e]	0.013	*0.021*[e]
SHB	150202	shrink/stress	6 - 27	--	4[d]	--	280	--	0.014
NSB	790152	stress	10 - 17	69	--	500	--	0.14	--
MIB	780097	shrink	5 - 10	--	0	--	*127*[e]	--	0
BPB	150211	shrink	2 - 10	--	0	--	160	--	0
NPB	170158	shrink/stress	2 - 10	23	--	120	--	0.19	--

Notes: a) Listings are semi-quantitative due to uncertainty in crack identification and detection. Estimate of perimeter surveyed is only approximate. All entries subject to revision.
b) BCB not listed as it contained mixed components of unknown history.
c) Based on 2/97 preliminary survey. Only larger visible cracks documented. Includes cracks at higher elevations on columns.
d) Stress/shrink crack distinction unclear.
e) *Modified to correct erratum in original printed version*

Table 8. Examples of projections of time to corrosion initiation using the integrated time to initiation model (Section 2.3.1).

		Conservative		Less Conservative	
		Extreme	Typical	Extreme	Typical
Surface and Threshold Regimes	C_S (pcy)	40	30	40	30
	C_T (pcy)	1.2	1.2	0.5% of CF	0.5% of CF
Class V[a], FA, 0.32 w/c, 3 in cover	D (in²/y)	0.02	0.01	<0.01	<0.005
	t_i (y) Flat Wall	**42**	**92**	**>136**	**>320**
	t_i (y) Corner	**39**	**85**	**>115**	**>264**
Just Meeting Class IV, FA, 4 in cover	D (in²/y)	0.08	0.04	<0.04	<0.02
	t_i (y) Flat Wall	**19**	**41**	**>56**	**>133**
	t_i (y) Corner	**17**	**38**	**>48**	**>110**

Table notes:

<u>Conservative-Typical</u> projections assume C_T=1.2 pcy, C_S=30 pcy (typical of observed surface concentrations), and diffusion coefficient as given by Eq.(2) derived from average values in decade-old bridges.

<u>Less Conservative-Typical</u> projections assume C_S=30 pcy as above but C_T = 0.5% of cement factor. Also, to represent the beneficial effect of aging, the diffusion coefficient is <1/2 the value estimated by Eq.(2) for young bridges.

<u>Extreme</u> projections assume high end (typically upper 10th percentile) surface chloride concentrations, and diffusion coefficient twice as high as the value used in the corresponding Typical projections. These projections reflect possible more severe conditions in a small fraction of the substructure.

The Class V projections assumed CF = 752 pcy, pozzolanic admixture, 3 in cover, and w/c = 0.32 as in the best performing structures examined.

The Class IV projections assumed CF = 658 pcy and 4 in cover, as in a typical CIP substructure, and w/c = 0.41 as in concrete just meeting specification. Pozzolanic admixture also assumed.

The flat wall projections assume a fixed rebar effect derating factor T_f = 0.85 (reflecting typical substructure conditions with Φ/x_C ~ 0.2; see Figure 14, and C_T/C_S ~ 0.1 comparable to the cases considered here). The corner projections are for a 2-way corner and include no rebar effect derating as it appears to be less relevant for corner cases.

a) Modified to correct erratum in original printed version

Table 9. Average polarization (mV) of each rebar segment for each of the 4 columns and grouped by column set.

Segment	W1	W2	Average Set W	D1	D2	Average Set D
1	125	116	121	25	27	26
2	130	130	130	26	29	28
3	142	140	141	35	36	36
4	163	160	161	47	47	47
5	199	195	197	73	70	72
6	265	252	259	137	129	133
7	382	366	374	259	280	270
8	525	513	519	363	383	373
9				717	716	716

9. FIGURES
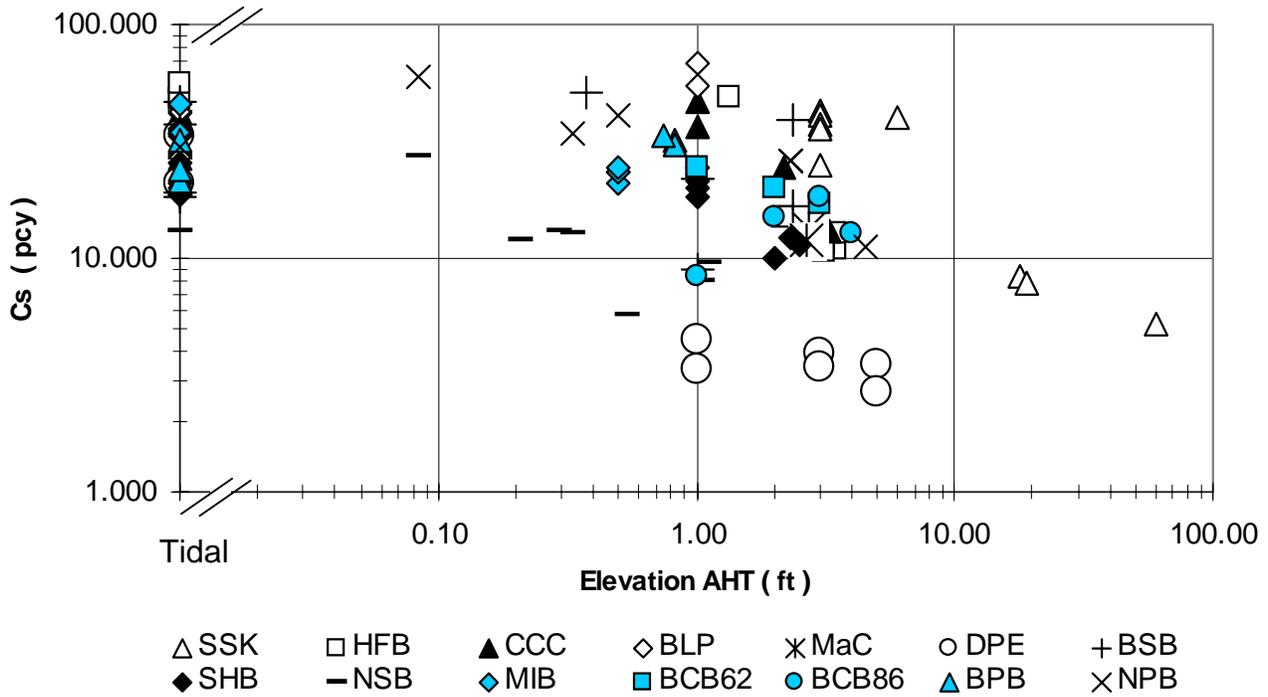
Figure 1. Calculated chloride surface concentration (Cs) as function of elevation above high tide (AHT) of the cores extracted from each bridge. Results for cores at or below the high tide line are plotted with elevation indicated as "Tidal".

BCB62 – BCB86: indicate dates of construction / modification (table 1).
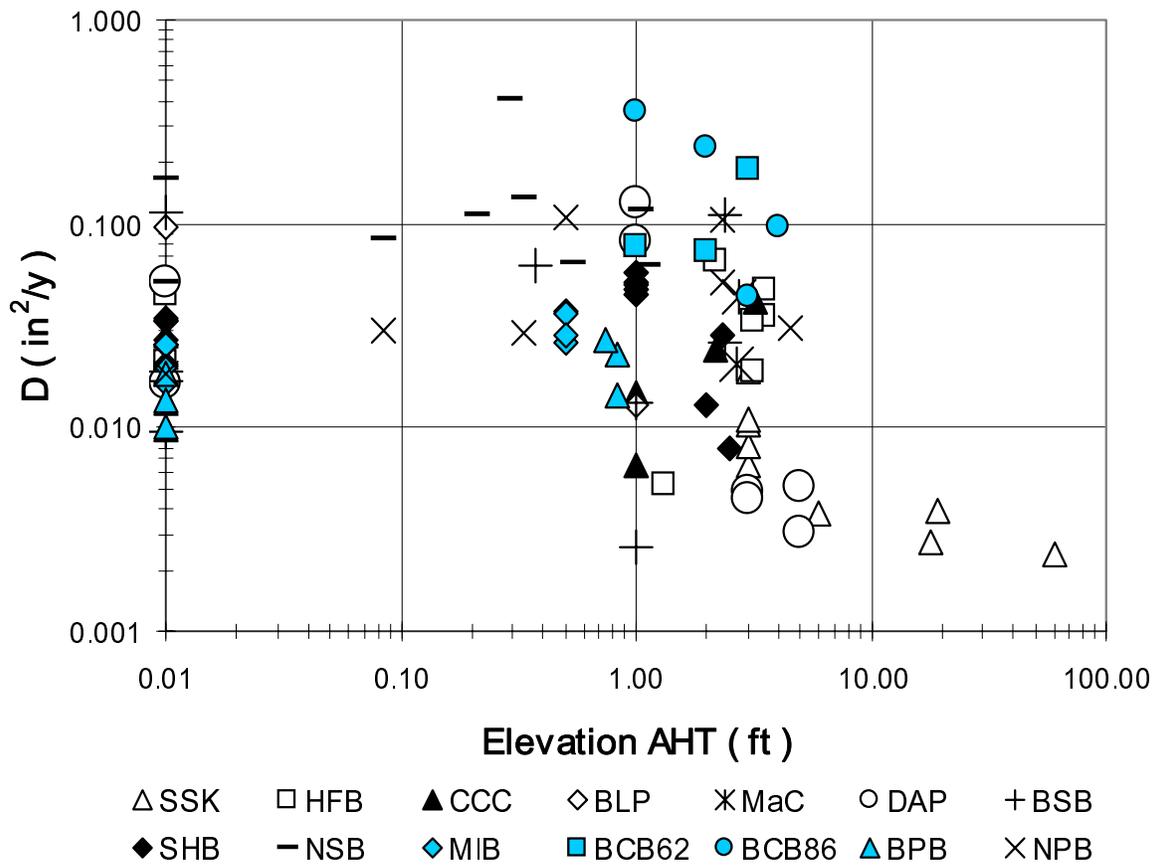
Figure 2. Apparent chloride diffusion coefficient (D) as function of elevation above high tide (AHT) of the cores extracted from each bridge. Results for cores at or below the high tide line are plotted with elevation indicated as "Tidal".

BCB62 – BCB86: indicate dates of construction / modification (table 1).
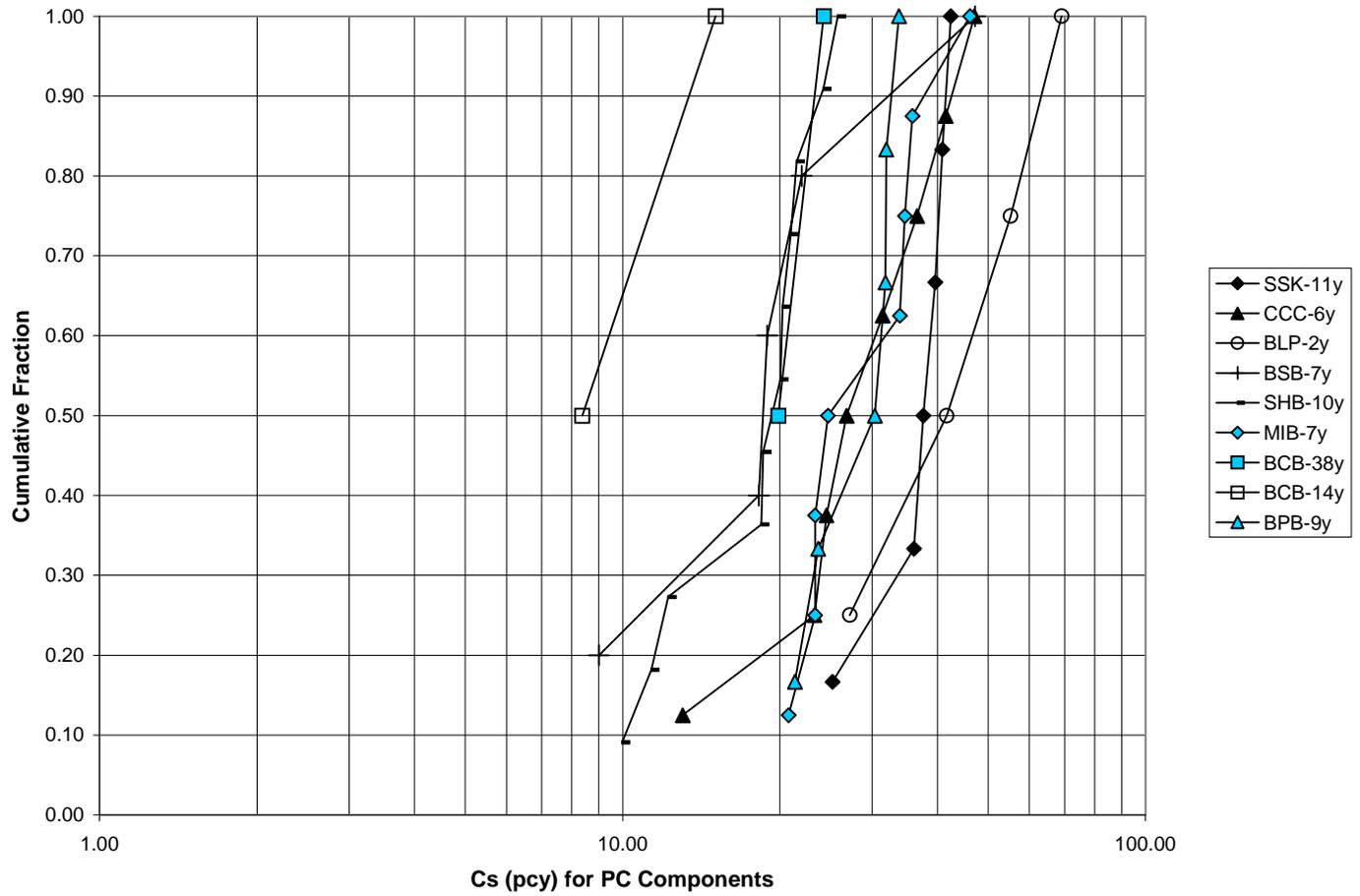
Figure 3. Cumulative distributions of Cs for Pre-Cast components (Tidal – 6 ft AHT).
The age of the components at the time of inspection is indicated.
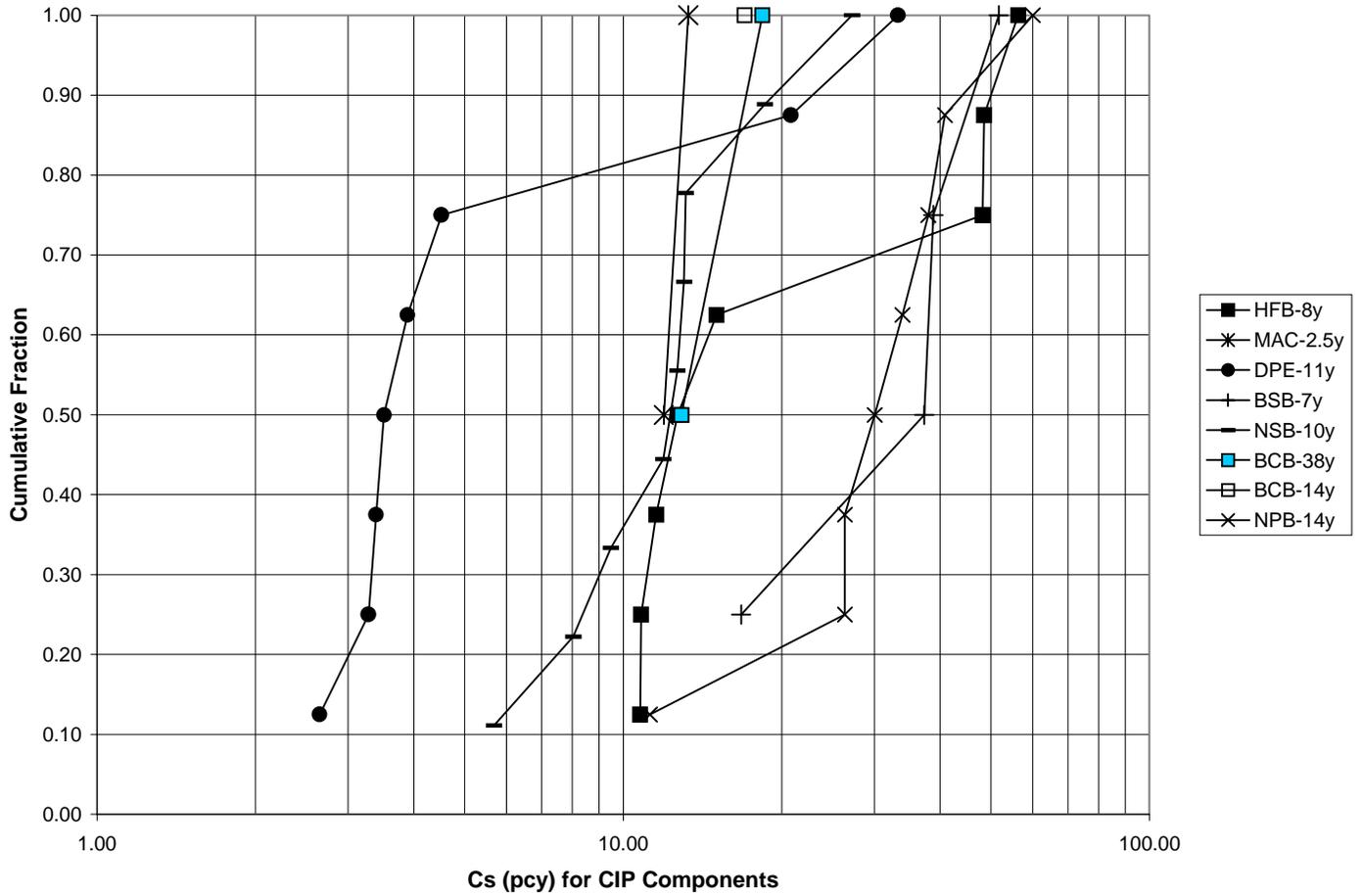
Figure 4. Cumulative distributions of Cs for Cast in Place components (Tidal – 6 ft AHT).
The age of the components at the time of inspection is indicated.
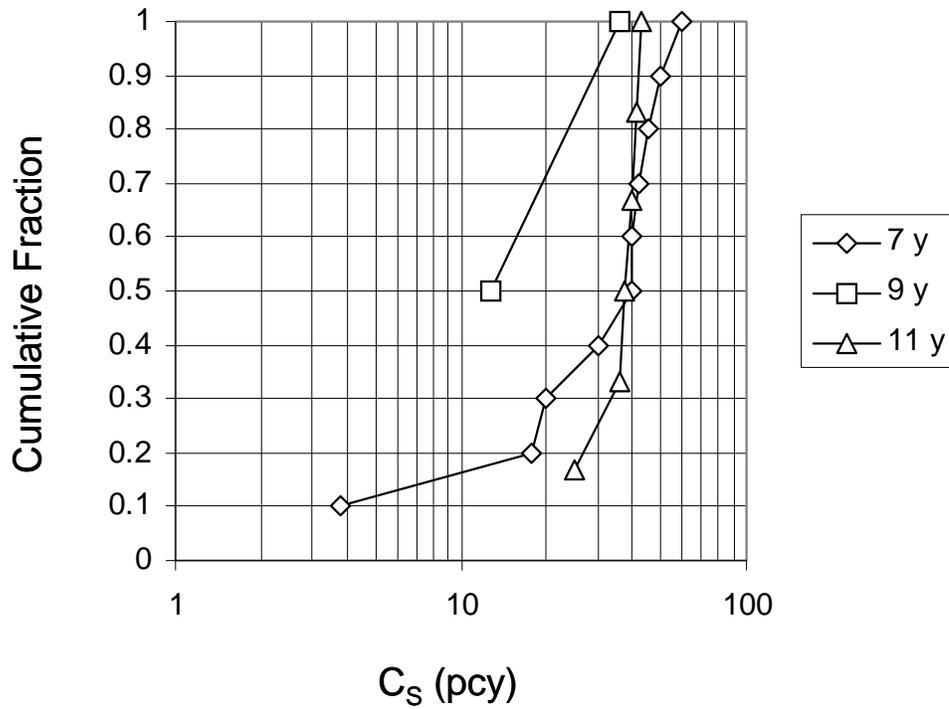
Figure 5. Cumulative fraction of C_S values for SSK PC columns at elevations from Tidal to ~12 ft (~4m), obtained at ages 7, 9 and 11 years. Average C_S values are 35 pcy, 24 pcy, and 37 pcy respectively.
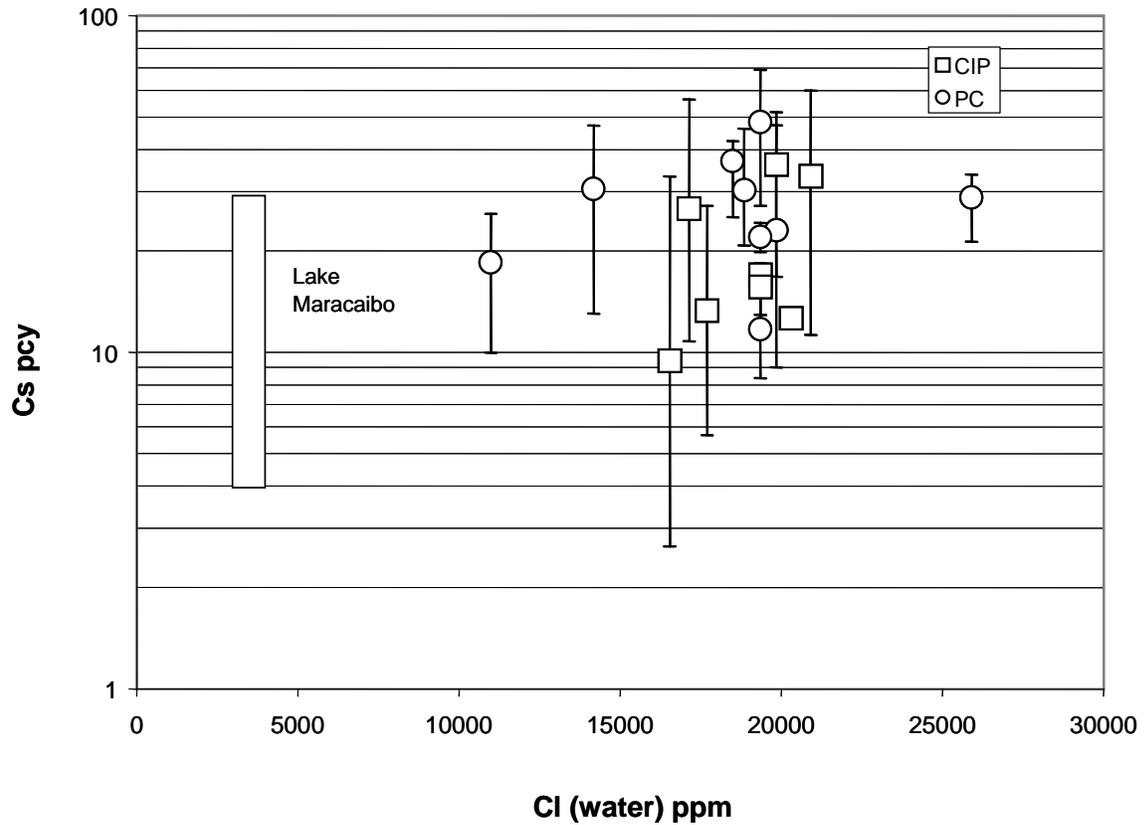
Figure 6. Average and range of Cs values (Tidal – 6 ft AHT) obtained as function of chloride concentration in the water. Results for a bridge in Lake Maracaibo [12] are shown for comparison.
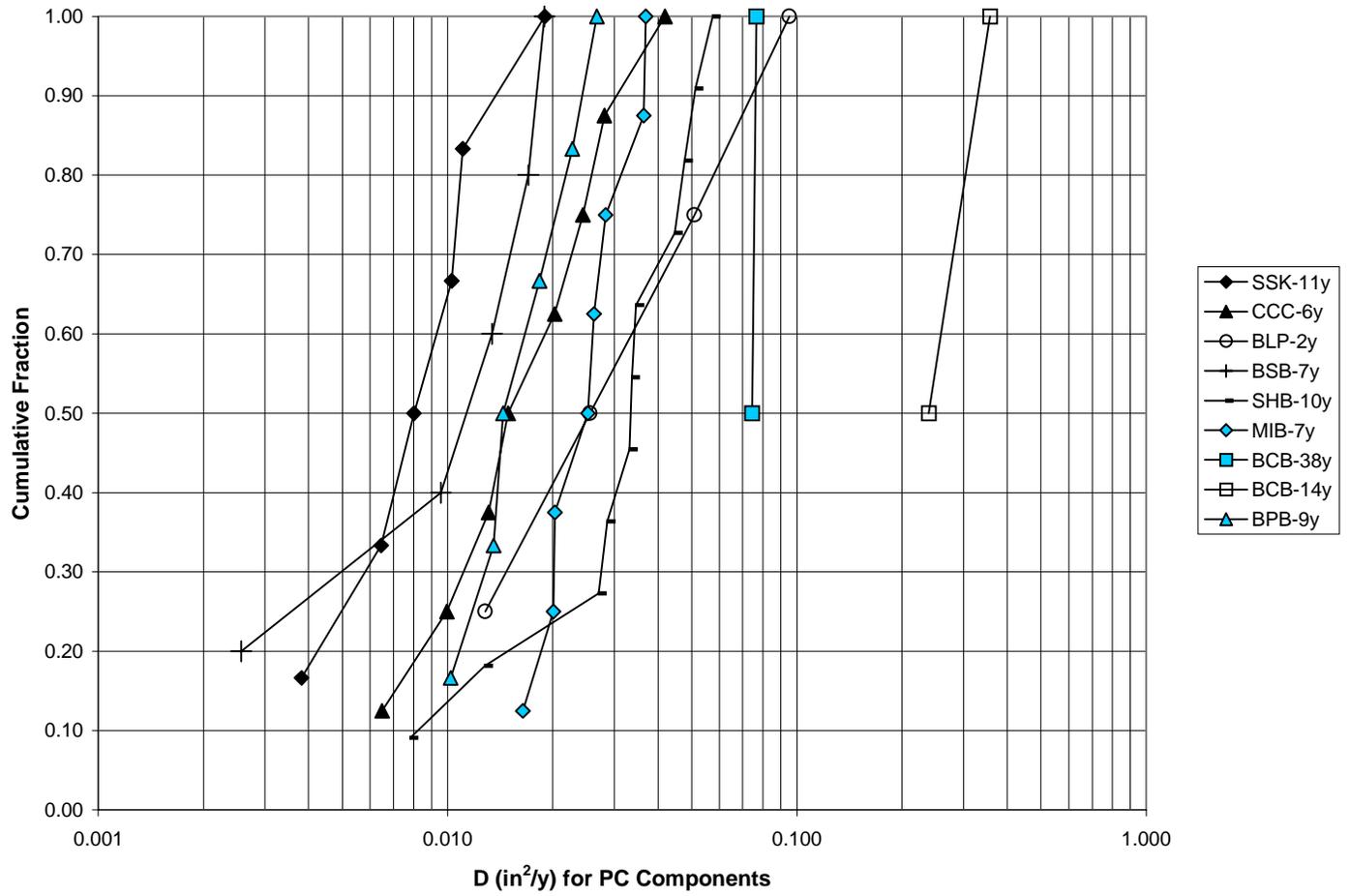
Figure 7. Cumulative distribution of D for Pre-Cast components (Tidal – 6 ft AHT). The age of the components at the time of inspection is indicated.
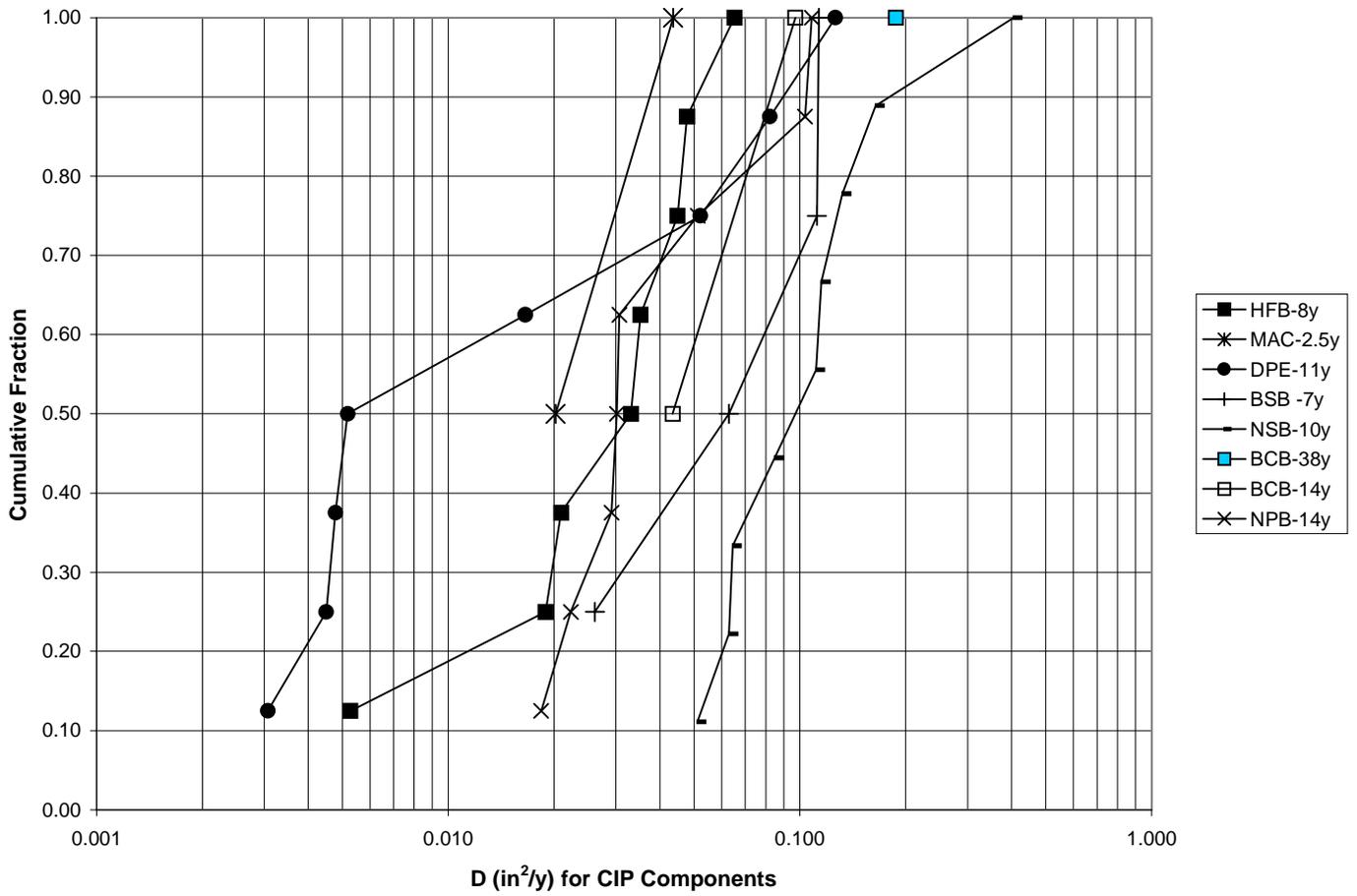
Figure 8. Cumulative distributions of D for Cast in Place components (Tidal – 6 ft AHT). The age of the components at the time of inspection is indicated.
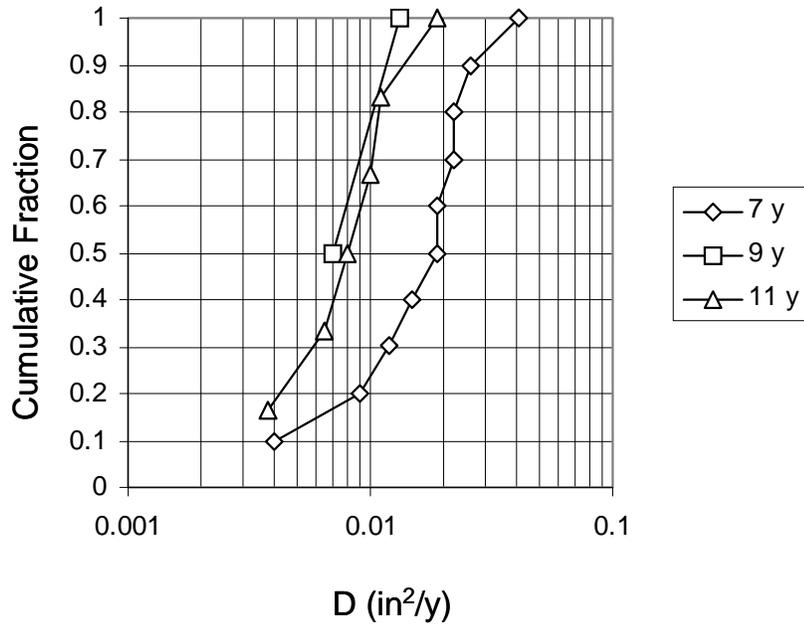
Figure 9. Cumulative fraction of D values for SSK PC columns at elevations from Tidal to ~12 ft (~4m), obtained at ages 7, 9 and 11 years. Average D values are 0.019 in^2/y, 0.010 in^2/y, and 0.010 in^2/y respectively.
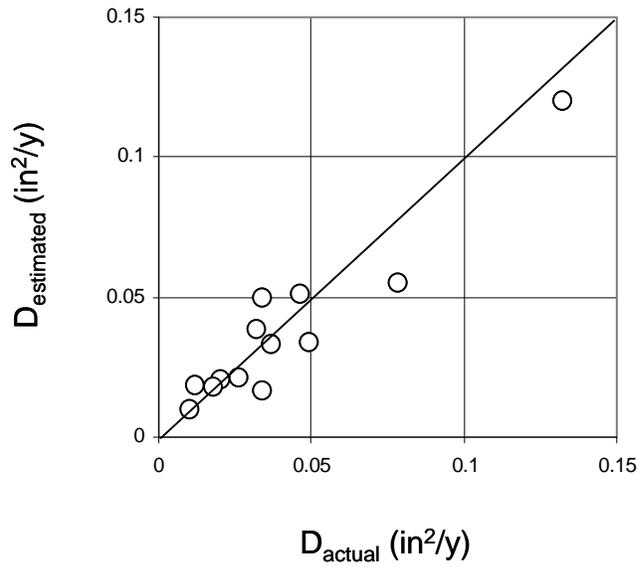
Figure 10. Comparison of actual (average for each bridge, Table 6) with estimated (using Eq.(2) further corrected for bridge age) D values of each bridge except BCB. The diagonal line represents ideal agreement.
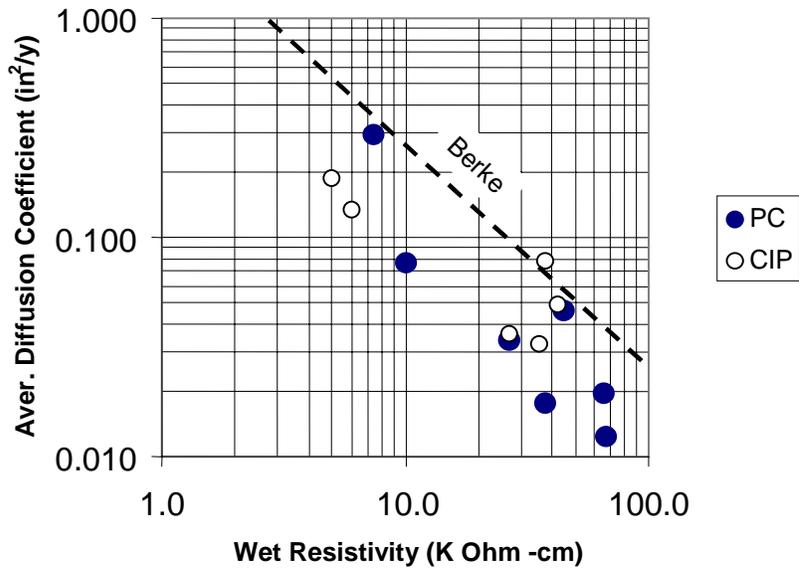
Figure 11. Average (see Section 1.3.3) value of D for PC or CIP components of each bridge as function of resistivity (averaged as indicated in text) of available cores for the same type of components in the same bridge. The correlation observed by Berke [15] between chloride diffusivity and wet resistivity of laboratory concrete specimens is shown by comparison.
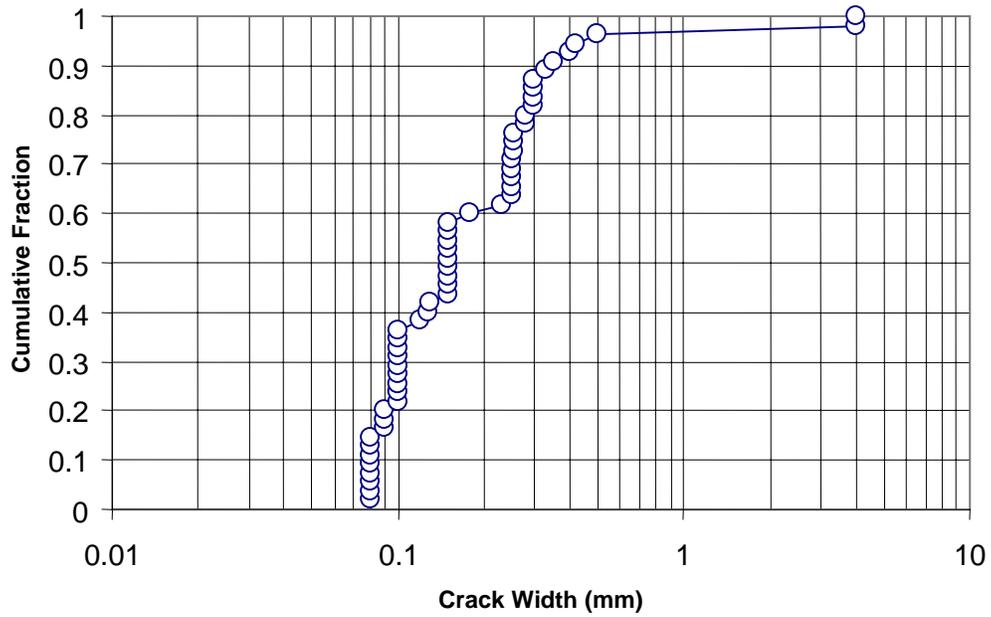
Figure 12.   Cumulative distribution of stress crack widths listed in Table 3. The widest cracks were in the CIP substructure of NSB and had been previously epoxy-injected.
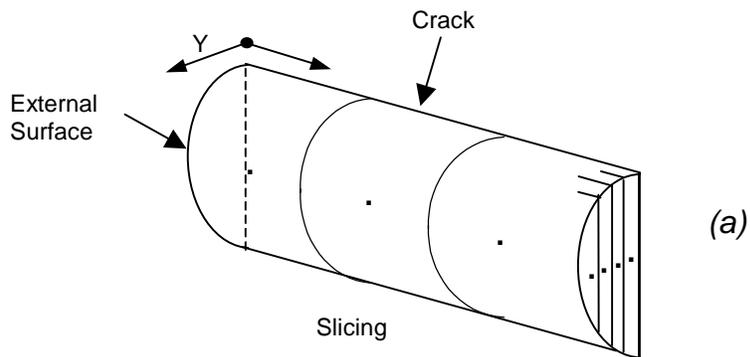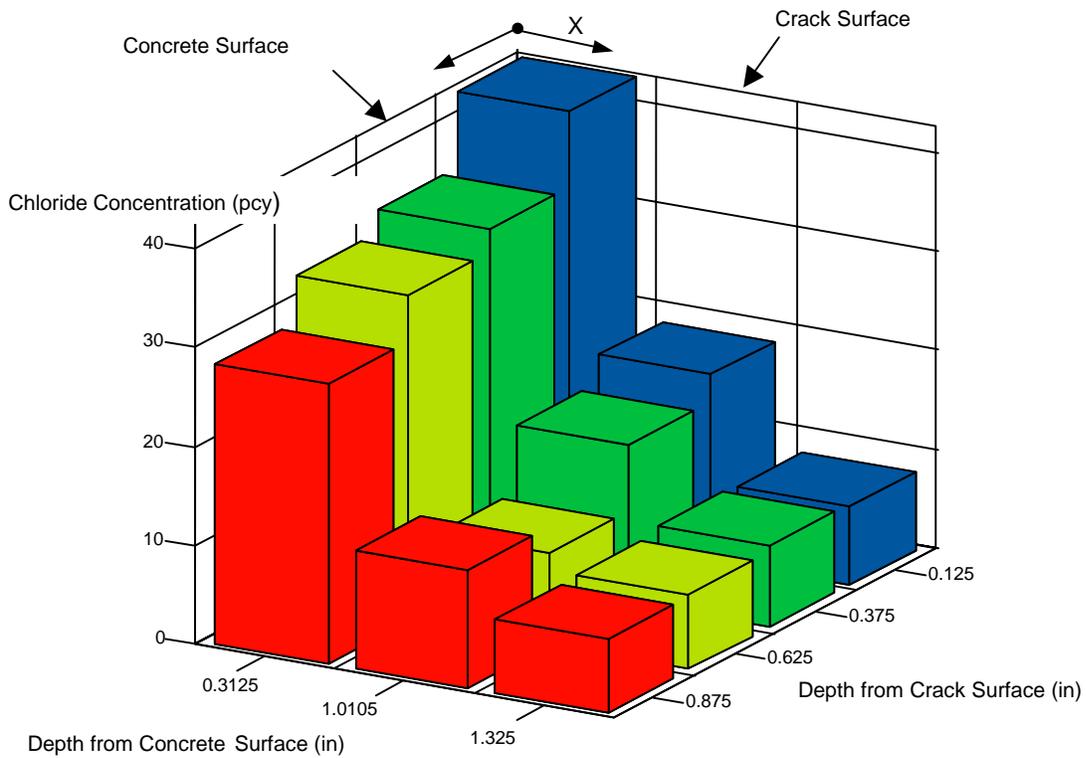
Figure 13. Two-dimensional chloride analysis of core No.543 (3 ft (0.9 m)) elevation above high tide) showing preferential transport along the crack and lateral diffusion into the concrete on the side of the crack.

(a) Drawing modified to correct error in original printed version
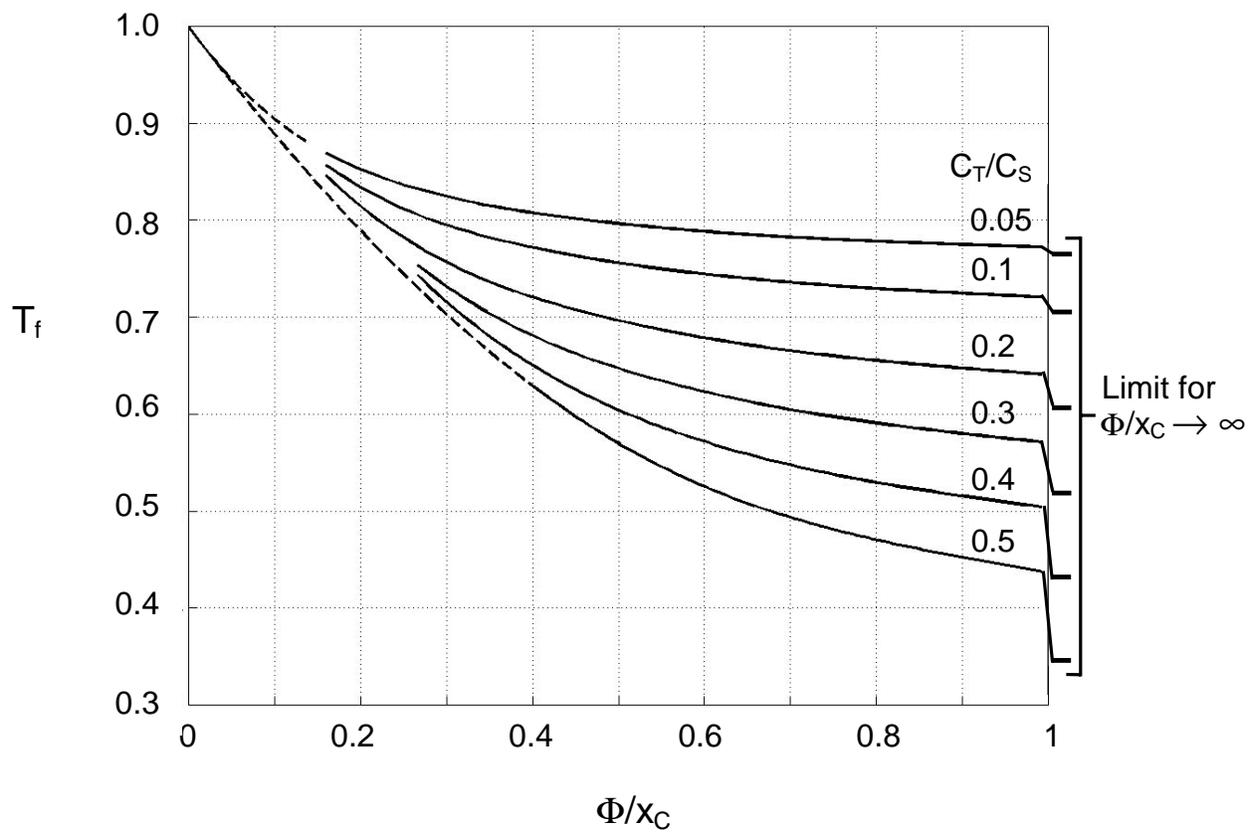
Figure 14. Nondimensional time derating factor T_f as function of Φ/x_C and with C_T/C_S as parameter. Limit values for T_f as $\Phi/x_C \rightarrow \infty$ are shown on the right.
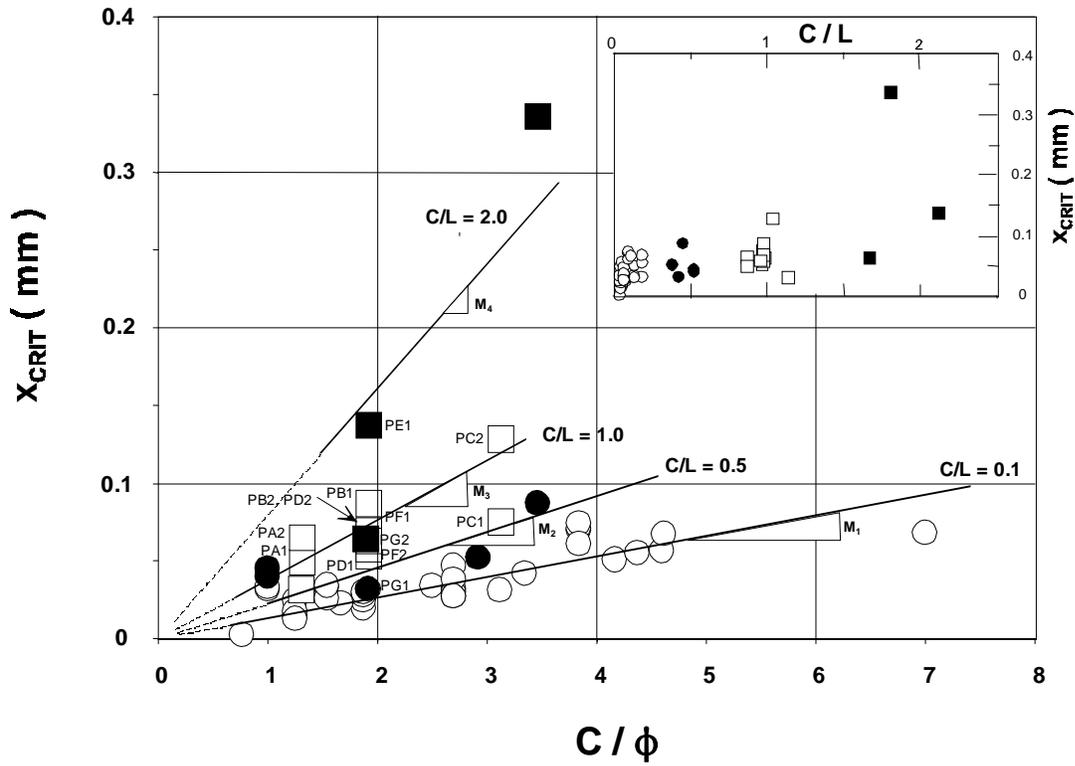
Figure 15. Critical Corrosion Penetration (x_{CRIT}) vs. C/φ Ratio. The Lines Represent Equation (3) Predictions. The Insert Corresponds to x_{CRIT} vs. C/L Ratio. From Ref. [25]. Note: in this figure C represents the rebar cover, x_C.
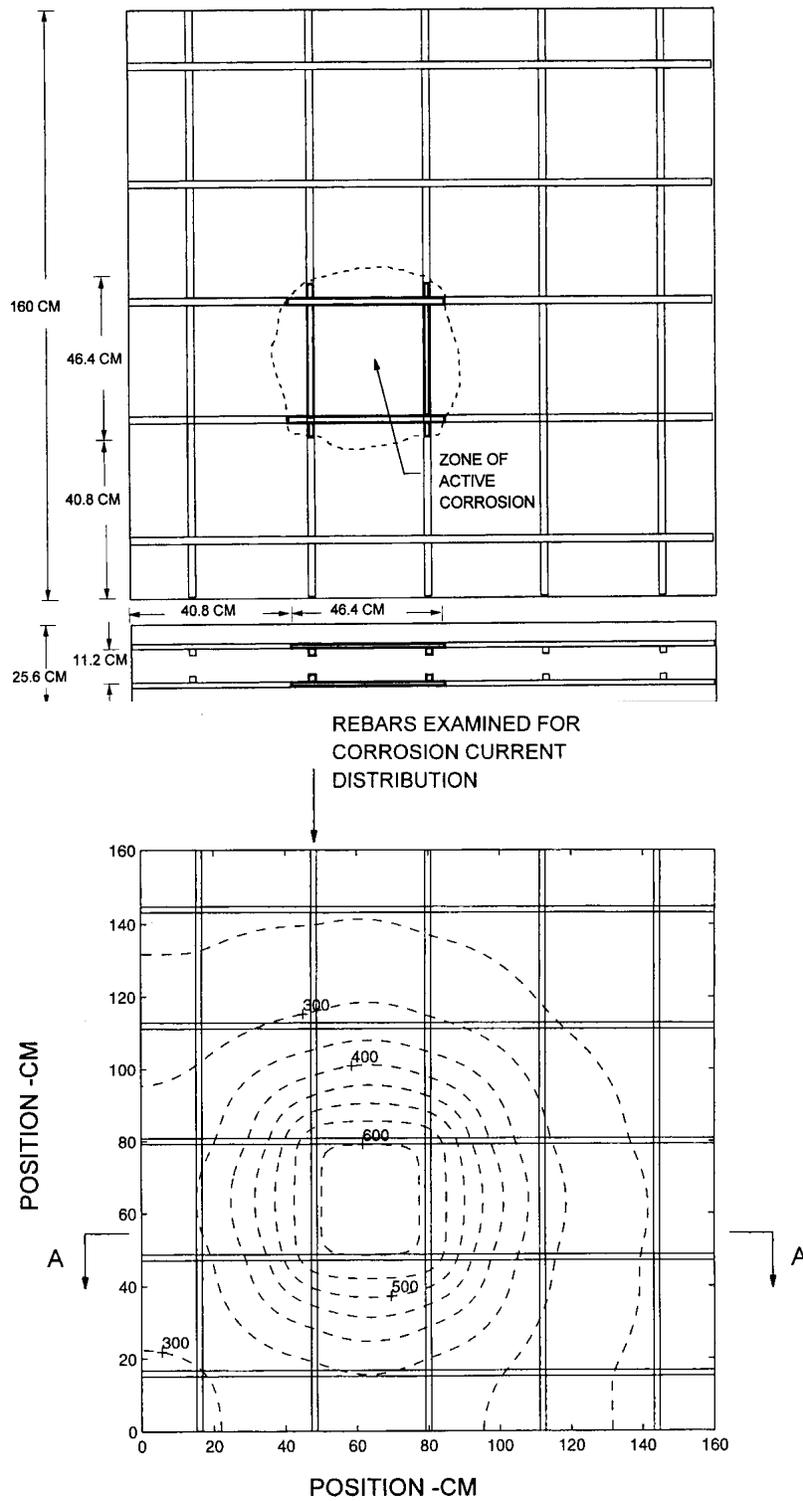
Figure 16. Example of implementation of the computational solution scheme for a double-mat reinforced concrete system (top) with solution showing predicted equipotential contour on upper slab surface as it would appear on a half-cell survey [27].
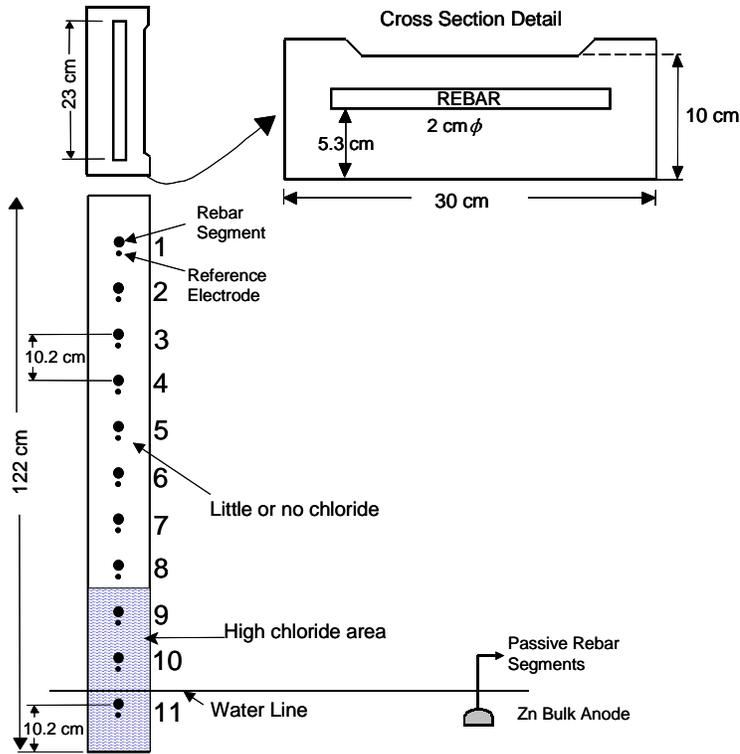
Figure 17. Column configuration.
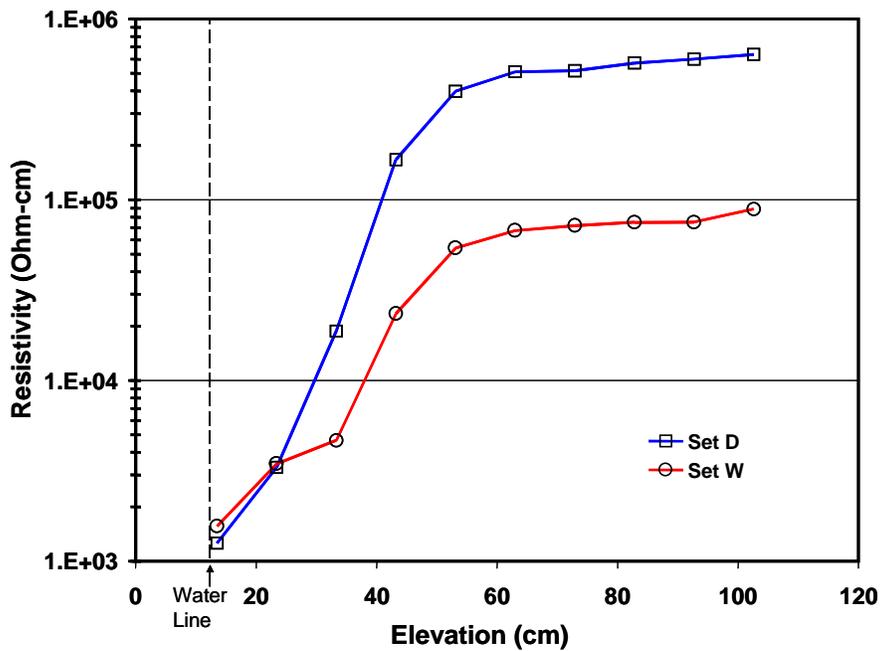
Figure 18. Resistivities measured 7 days before connecting the anodes. Average of each set.
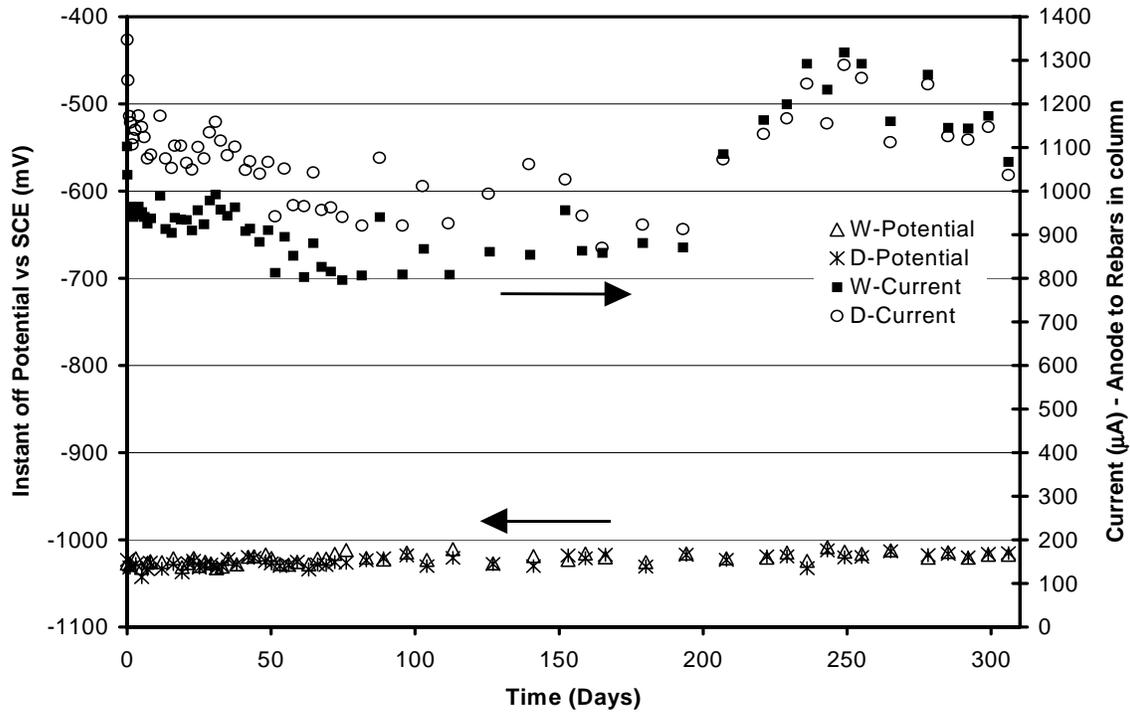
Figure 19. Zn anode instant off potential and current delivered to the rebar group, averaged by column set during CPrev application.
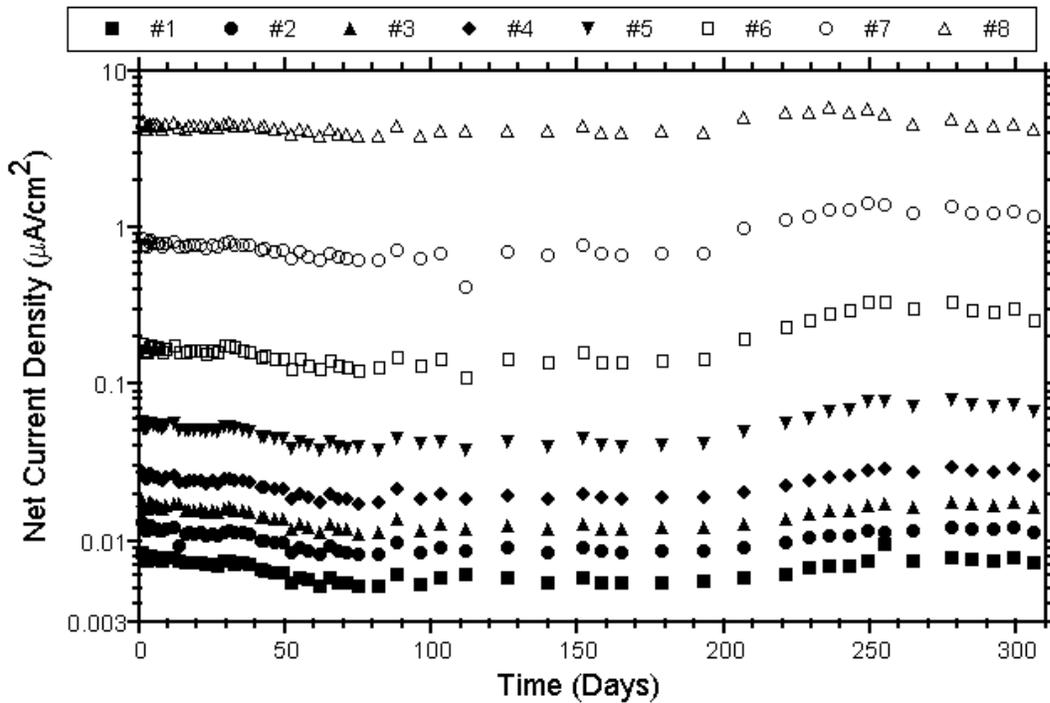
Figure 20. Applied cathodic current densities measured for each rebar segment in column W1 during CPrev application (after the first day).
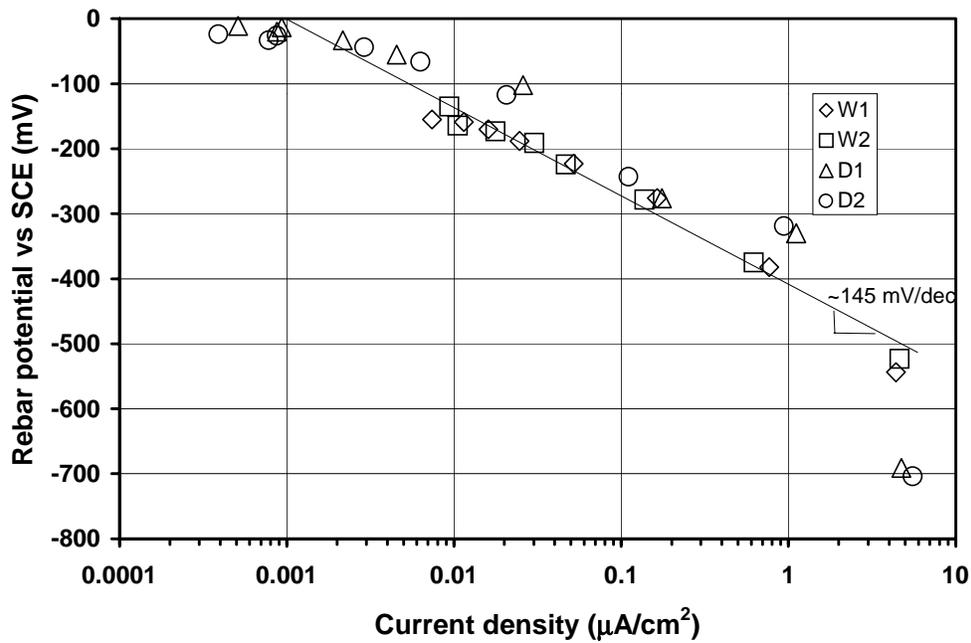
Figure 21. Potential vs current density associated with each rebar segment after applying cathodic prevention for 80 days.
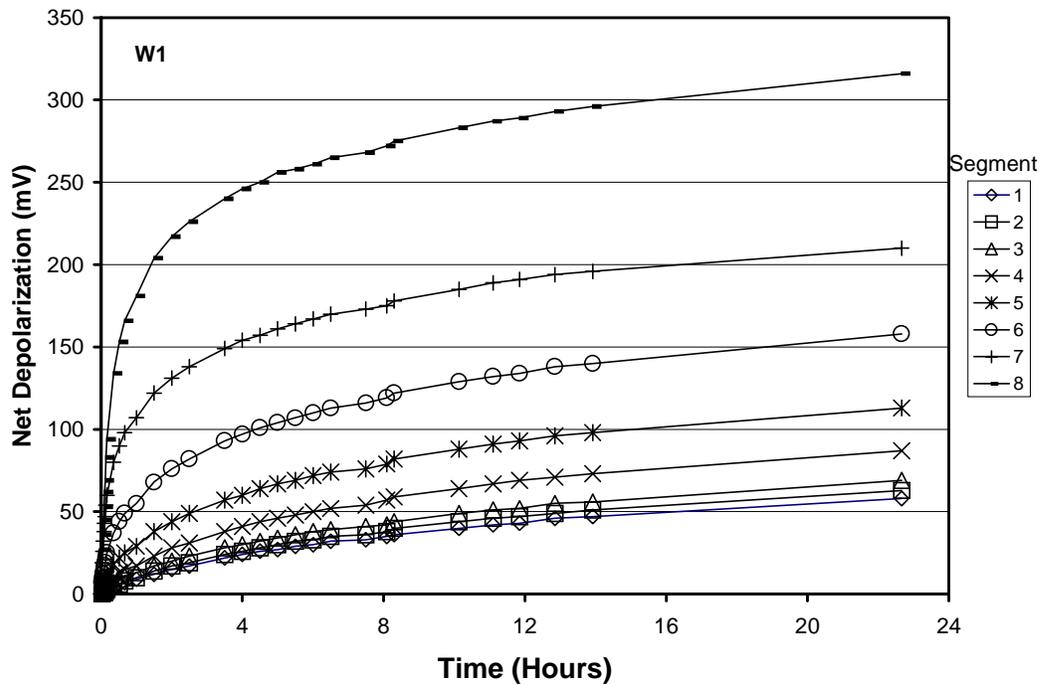
Figure 22. Net depolarization measured for rebar segments of column W1.
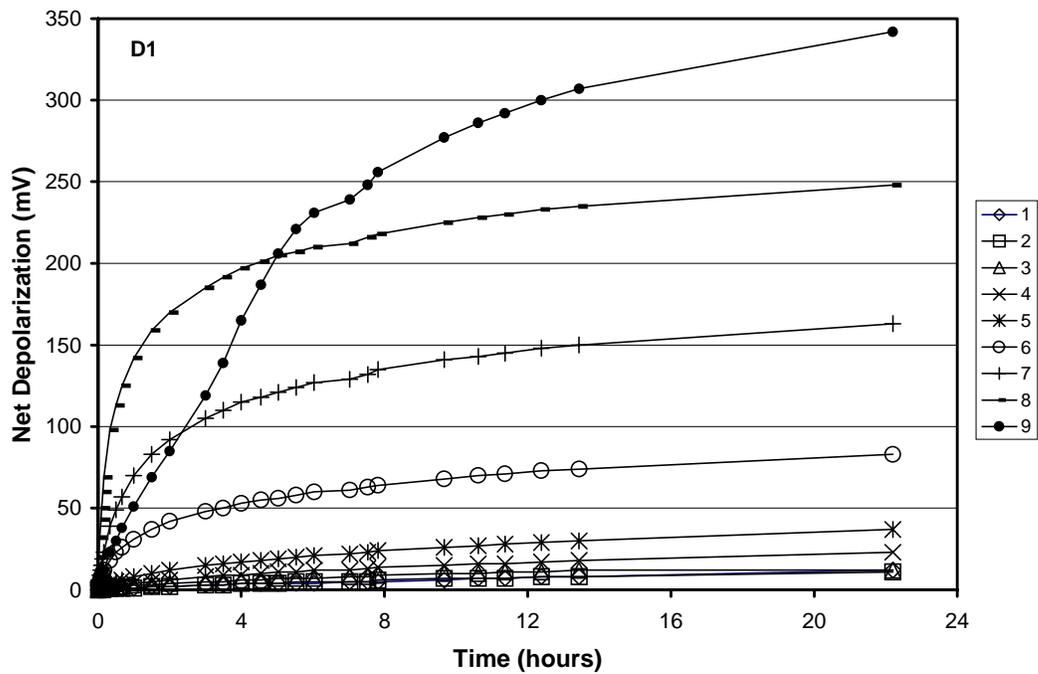
Figure 23. Net depolarization measured for rebar segments of column D1
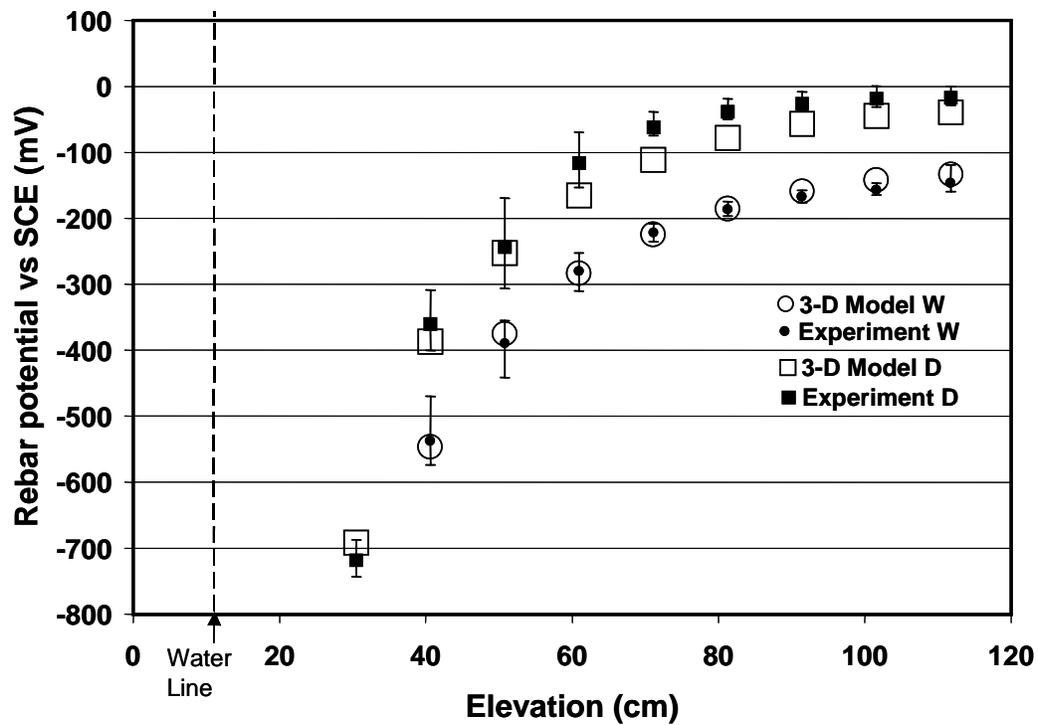
Figure 24. Rebar segment potentials after the Zn anode was connected, comparison of 3-D model and experimental results.
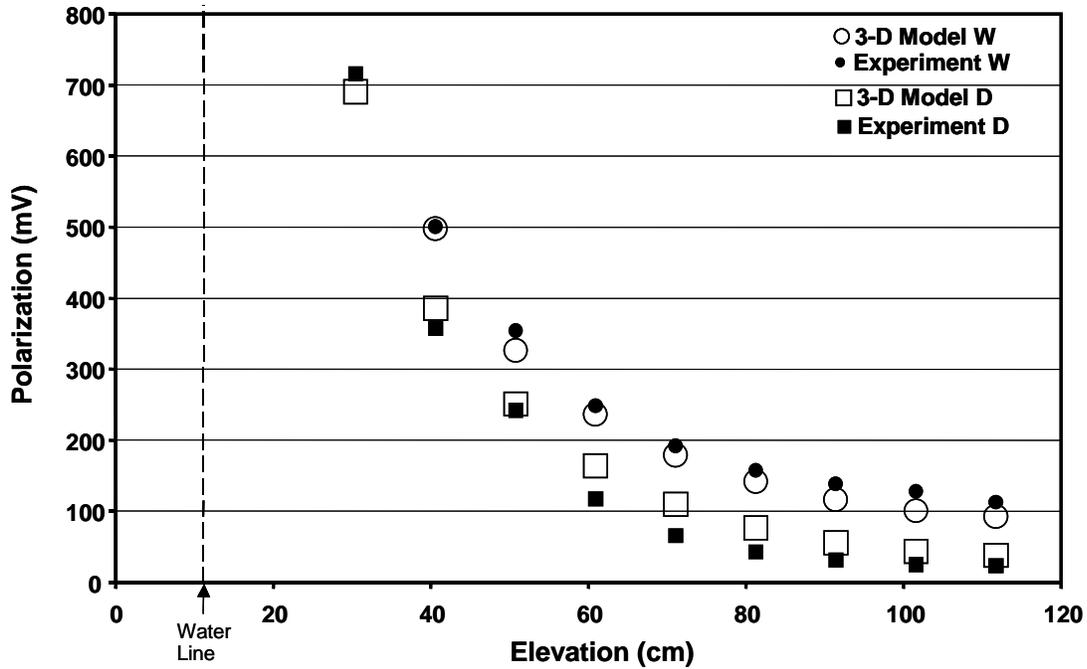
Figure 25. Polarization observed at each rebar segment for both column types, comparison of 3-D model and experimental results.
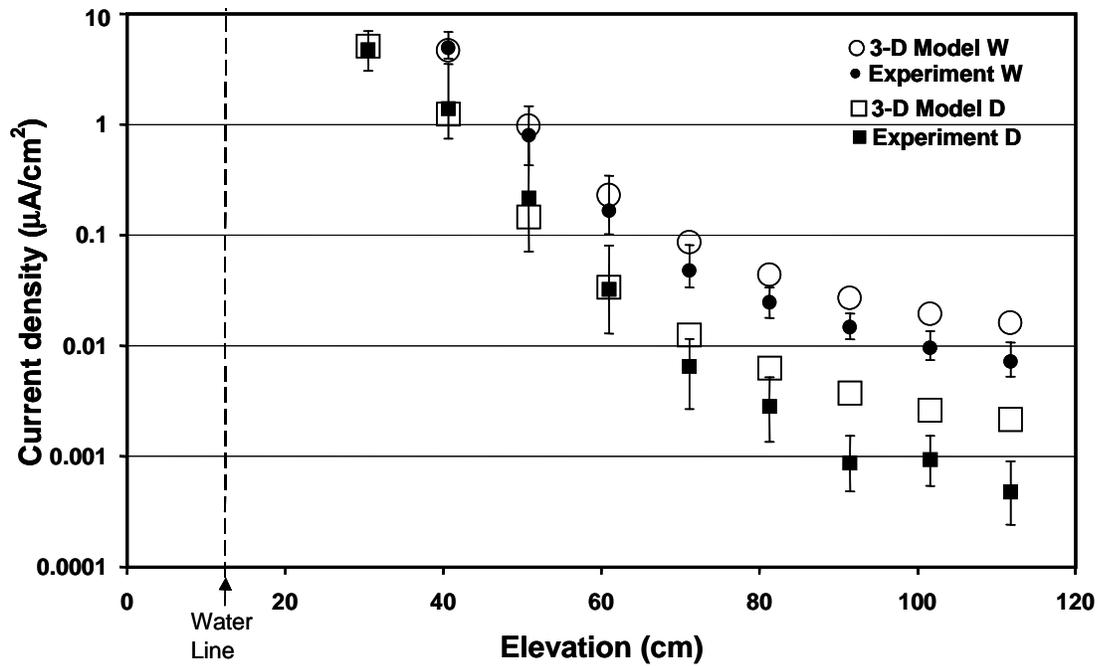
Figure 26. Current density delivered by the anode to each rebar segment, comparison of 3-D model and experimental results. Experimental results show the range and average current density values measured for each rebar segment (grouped per column set).
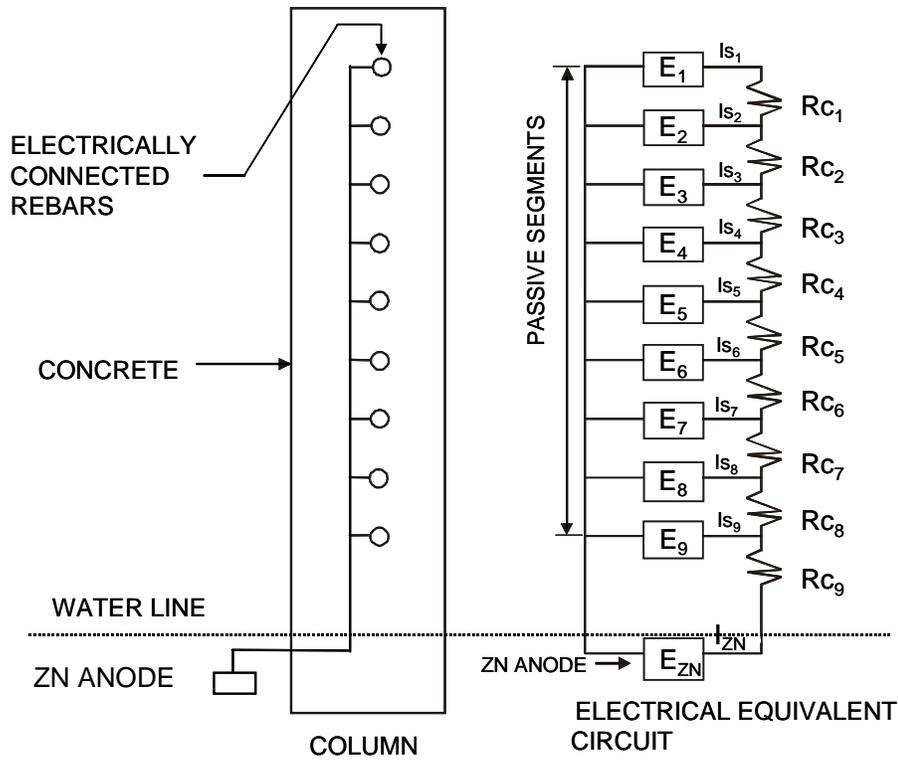
Figure 27. Schematic of electrical equivalent for 1-D model.
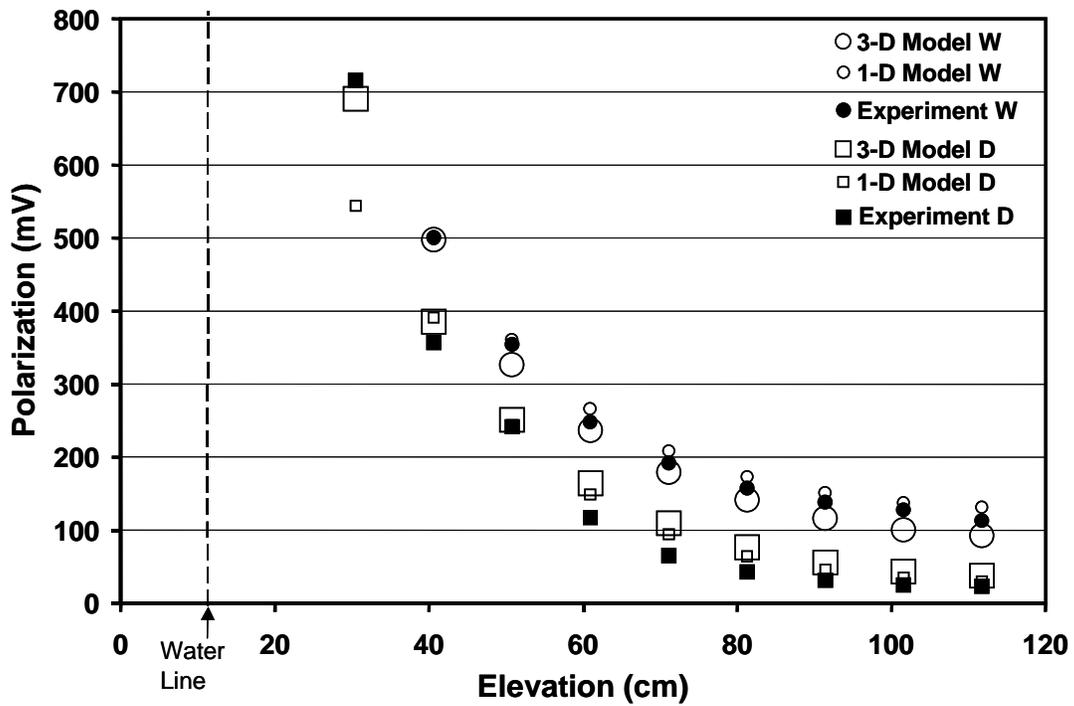
Figure 28. Comparison of the polarization obtained with 1-D model, 3-D model and the experimental results, for both column sets.
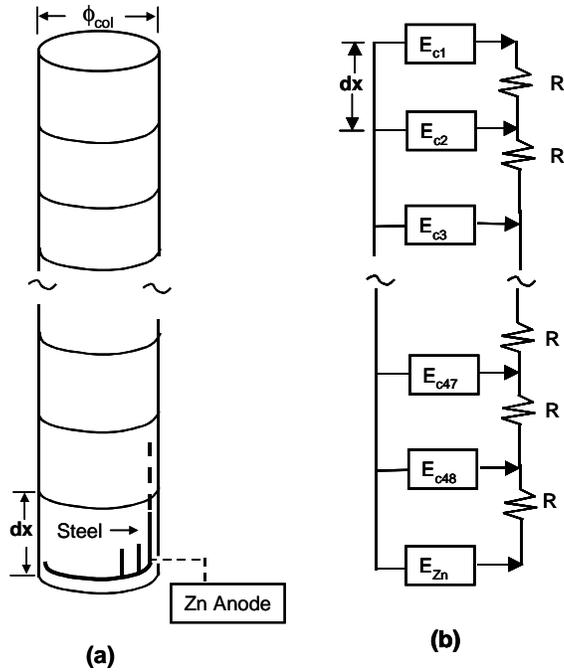
Figure 29. a) Column discretization, b) Equivalent Circuit
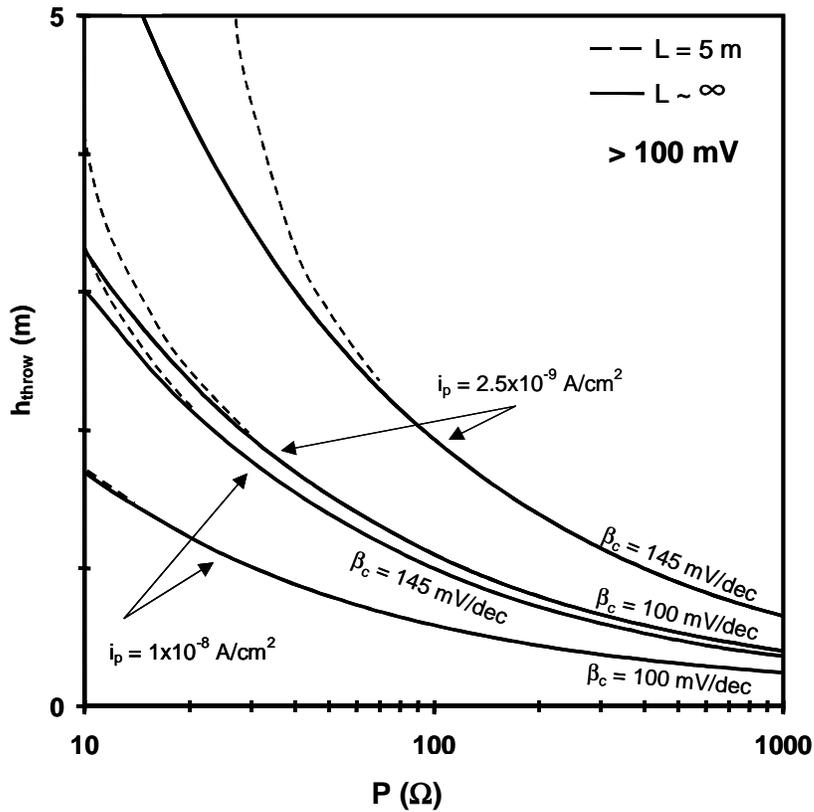
Figure 30. Performance curves derived from the 1-D model for 5 m and ~∞ long columns, for polarizations > 100 mV.
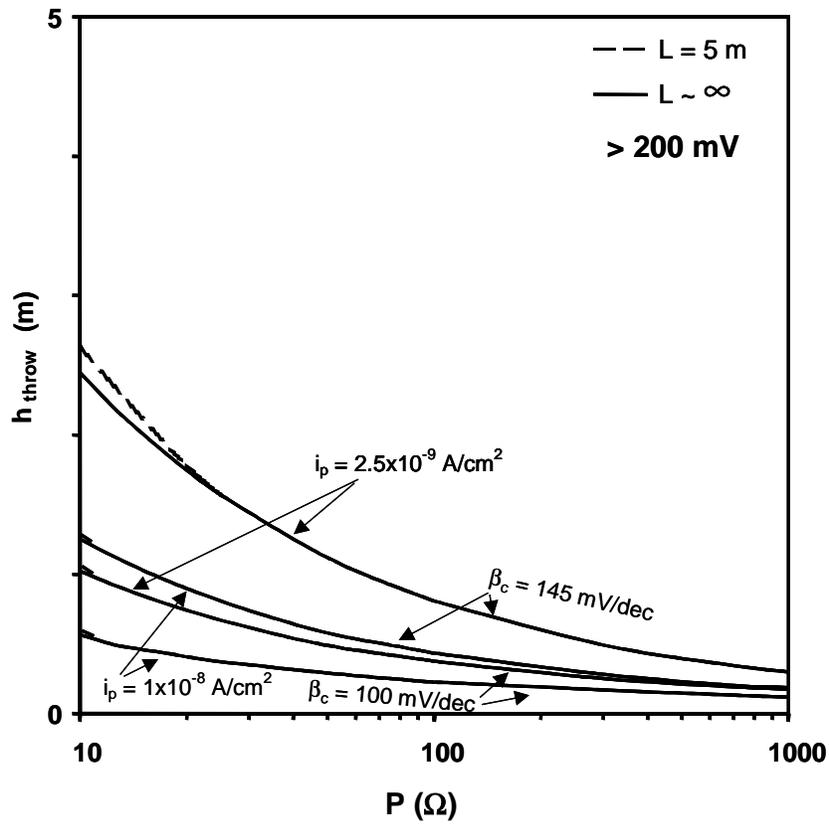
Figure 31. Performance curves derived from the 1-D model for 5 m and ~∞ long columns, for polarizations > 200 mV.

APPENDIX 1 - Information and assumptions on bridge and concrete properties.

General note: Substructures in service conditions with environmental chloride greater than 2,000 ppm are considered to fall within the "extremely corrosive" FDOT classification [4]. All bridges in this survey fall under that classification. For those conditions Section 346 of current FDOT Standard Specifications for Road and Bridge Construction (SSRBC) [4] specifies, for CIP concrete, the use of Class IV concrete with Type II cement, 18-22% FA as cement replacement, a minimum cementitious content of 7 bags (658 pcy (390 kg/m^3)), and a maximum w/c=0.41 (throughout this report w/c refers to the water-to-cementitious ratio). For PC concrete partially submerged piling (the type examined in all structures except for SSK where PC elliptical segments were used) in the same service conditions, it is specified that Class V concrete with minimum cementitious content 752 pcy (446 kg/m^3), maximum w/c=0.35, 18-22% FA replacement, and microsilica (8% cement replacement), be used. The above specifications were followed in several of the structures examined, but departures existed for some of the older structures or due to special circumstances. As detailed below, the bridge information listed in Table 2 represents precise information in some instances but also includes assumptions based on expected practice when other records were not available. Unless otherwise indicated, it was assumed that the FA was Class F. The listings in Table 2 are therefore subject to update should additional information become available in the future.

SSK

Concrete properties are for precast elliptical segments, based on specifications on Sunshine Skyway Bridge Contract 2, Revised 6/30/82, Job No. 15170-3415. The specifications (p.29 in that contract) indicated 611 pcy (362 kg/m^3) cement and 150 pcy (90 kg/m^3)FA, w/c<0.41. Cement was specified as either Type II or Type V and FA ASTM C-618 Type F (p.7). No MS was specified. Additional communication (3/24/99 letter by L.M. Sessions, FDOT and subsequent phone conversation) reports that Pam Chakktak was QA Engineer at Palmco prestress yard where the elliptical pier segments were cast and that he indicated that for these components the typical w/c was 0.32 and always <0.35, the in-place concrete temperature was ≤90 $^\circ$ F, and C$_3$A was ≤ 7%.

HFB

Bridge construction drawings indicate CIP Class IV (non-mass) concrete.   No MS was specified. Per conversations with FDOT personnel a maximum 35% Type C FA replacement was used. It was assumed the concrete followed otherwise the current SSRBC Section 346 specifications. The aggregate was identified as granite from observation of the extracted cores.

CCC

The concrete in the piles examined is assumed to conform the "Field Mixture – Jobsite" listing for the Courtney Campbell Bridge widening in the paper "High Performance Concrete in Florida Bridges" by J. Armaghani, D. Romano, M. Bergin and J. Moxley, in "High Performance Concrete in Severe Environments", ACI SP 140-1, American Concrete Institute, 1993. That formulation followed SSRBC Section 346 Class V as indicated above (listing CF = 752 pcy (446 kg/m^3), 20% FA Type F, 8% MS, w/c 0.35), but included also 4.5 gal/c.y (20 liter/m^3) calcium nitrite inhibitor (DCI product by W.R. Grace). Analysis confirming nitrite presence was performed under a separate FWHA investigation on performance of corrosion inhibitors, to be published as "Corrosion Inhibitors in Concrete – Interim Report", by R.G. Powers and A.A. Sagüés, W.D. Cerlanek, C.A. Kasper, L. Li, H. Liang, N. Poor and R. Baskaran, 2002.

BLP

The information on admixed calcium nitrite inhibitor in PC piles used for this bridge is per listing in 12/18/96 letter by L.M. Sessions, FDOT. Based on date of construction it was assumed that the concrete was per Class V of Section 346 of the current SSRBC. Analysis confirming nitrite presence was performed using similar techniques to those used in the FHWA investigation mentioned under CCC.

MAC

Information for this bridge was obtained from actual construction records on file with FDOT, per information provided by R. Powers.

DPE

Per 3/30/99 conversation with L.M. Sessions, FDOT (who received verbal information from T. DeMaggio, Tarmac) the CIP footing portion in this bridge was constructed with Class IV concrete with 658 pcy (390 kg/m^3) cementitious material, w/c = 0.38, the footing and below water portions having 70% Blast Furnace Slag (BFS) and 30% cement, and the above-water portions having 50% BFS and 50% cement.

BSB

Per 1999 conversation with Peter Rogas the PC piles in this bridges were designed to approach SSRBC Section 346 Type V proportions, but with 10% instead of 8% MS replacement. However, at the S end of the bridge the 150 pcy (90 kg/m^3) FA (average of 18-22% of 752 pcy (446 kg/m^3)) were used in addition to instead of as replacement for cement, so that the cementitious content at the S end piles was ~ 900 pcy (~534 kg/m^3). Per the same source, CIP substructure was per SSRBC Section 346 Class IV concrete.

SHB

This bridge was part of a group of 18 structures selected in 1986 for implementation of the specifications that became established as part of Section 346 of the current SSRBC. Because of date of placement in service, the PC piling of this bridge was assumed to comply with current SSRBC Section 346 Class V specifications but not to contain MS. Consequently, it was assumed that the w/c would be 0.37 maximum, in keeping with the present SSRBC specifications for Class V without MS.

NSB

The CIP substructure was assumed to comply with SSRBC Section 346 Class IV specifications, but without FA replacement as the magnetic indication from the extracted cores was negative.

MIB

Based on date of construction the PC piles in this bridge were assumed to comply with SSRBC Section 346 Class V specifications except for absence of MS.

BCB

Based on estimated date of construction the earlier PC piles in this bridge are likely to adhere to the SSRBC in place to 1966, which per information from R.G. Powers indicated Class P concrete with 611 pcy (362 kg/m^3) cement and w/c<0.42, and had no requirements for use of early strength cement but it is likely to have been used by the manufacturer. The 1966 SSRBC did not call for use of FA, and the negligible magnetic attraction reading for cores from PC piles in this bridge suggest that no FA was used. MS was not in regular use at the estimated time of construction. Information for the other components is unknown.

BPB

Based on date of construction the PC piles in this bridge were assumed to comply with SSRBC Section 346 Class V specifications except for absence of M.S. Same assumptions as for SHB.

NPB

The CIP substructure was assumed to comply with SSRBC Section 346 Class IV specifications.

Appendix 2. CORE EXTRACTION LOCATIONS.

Each figure shows schematic representations of substructure elements of each bridge investigated, positions of extracted cores, and their relationship to existing cracks if any. Bridge abbreviations, pier designations and core numbers are keyed to the information presented in table 1-3. "Sound" indicates core extracted from sound concrete. "Crack" indicates core centered on a crack that intersected the surface. "Wet resistivity" indicates a core (always from sound concrete) used for wet resistivity measurements.

Pier #117-2

Pier 117-1

Pier #106-1
SW Face

Pier #106-1
NW Face

Pier #116
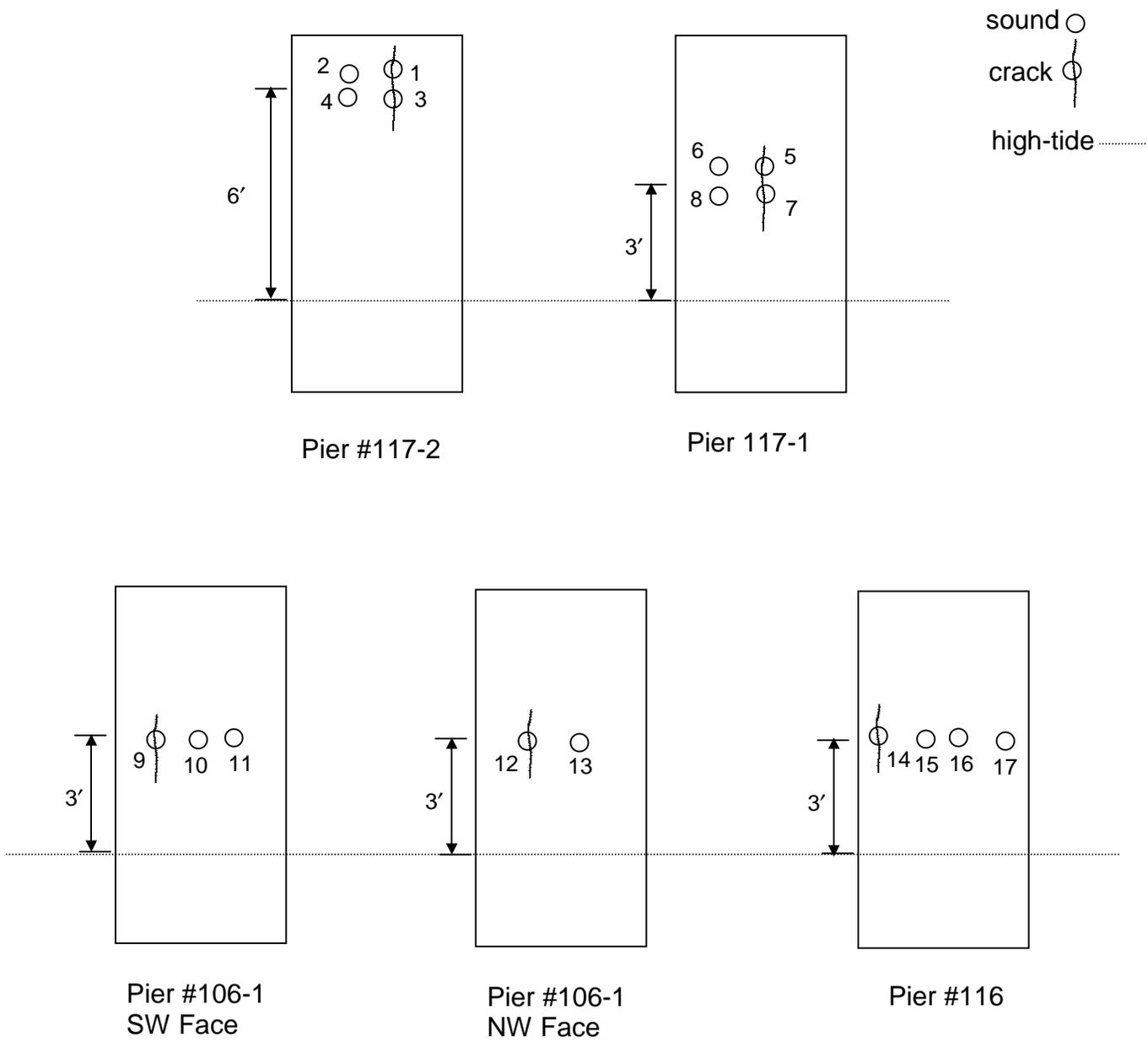
High elevation cores extracted at Piers 155, 151, 126-1, 117-1

Figure A2-1   Core Extraction Locations at the SSK Bridge
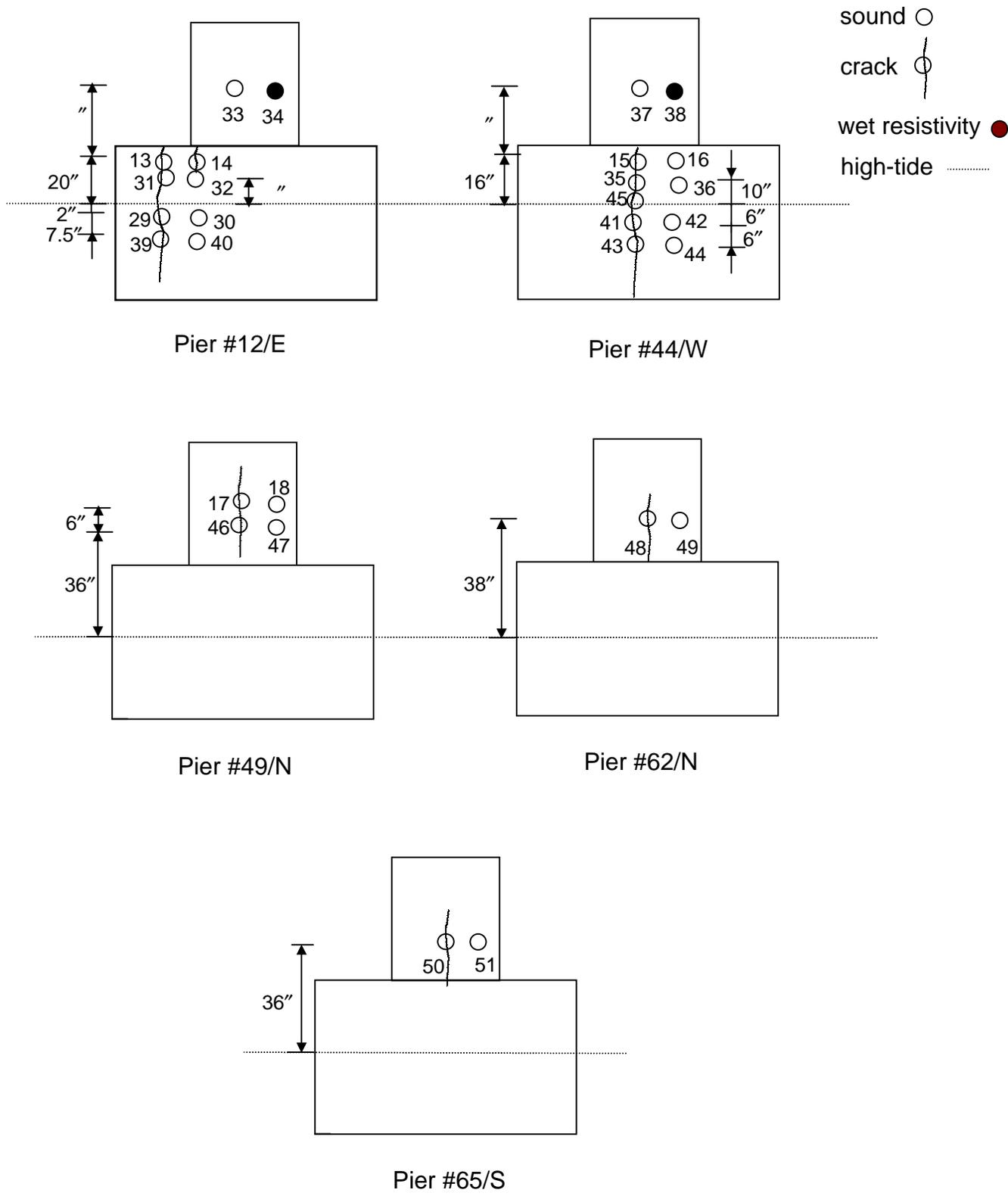
Figure A2-2   Core Extraction Locations at the HFB Bridge
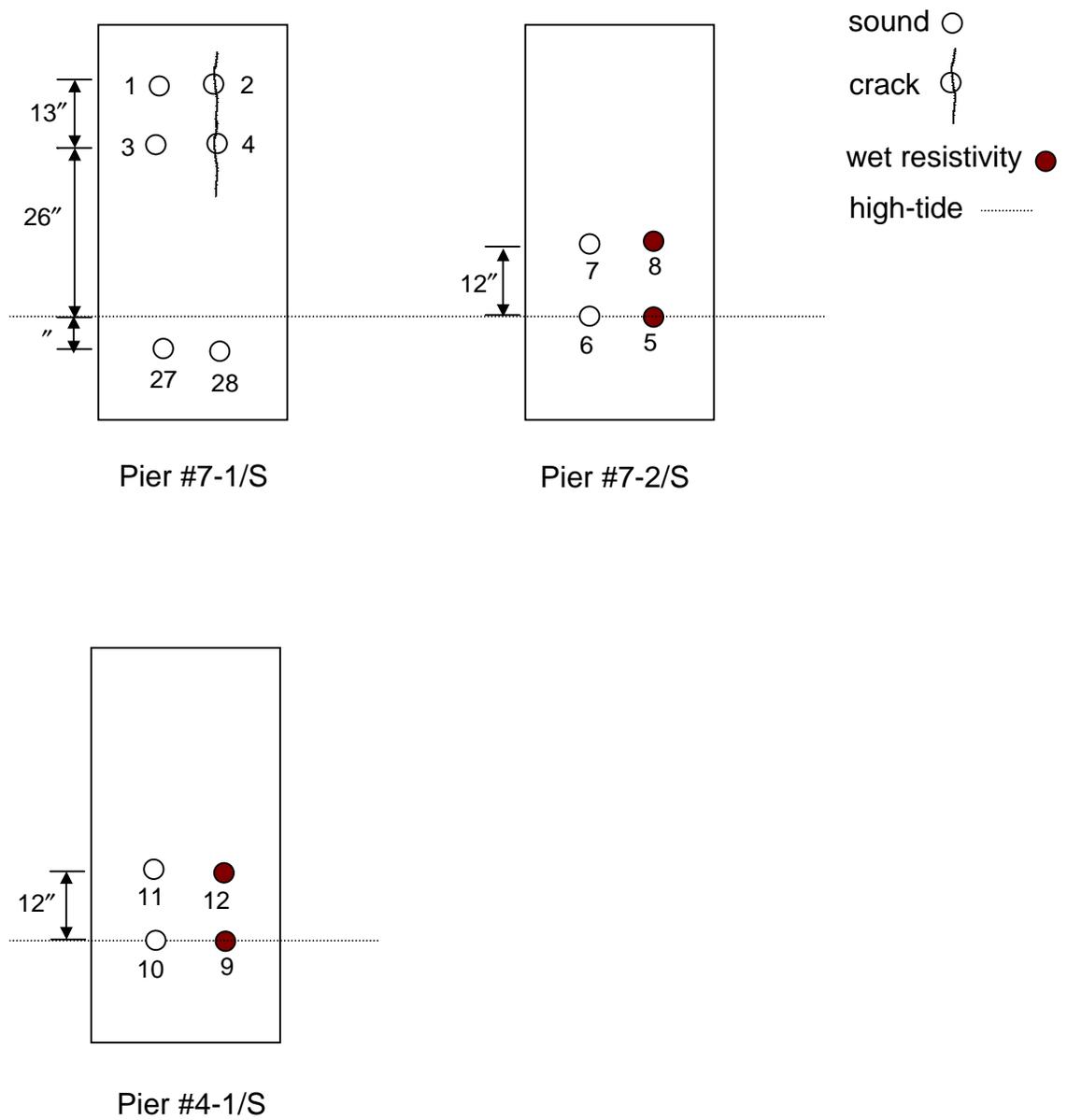
Figure A2-3   Core Extraction Locations at the CCC Bridge
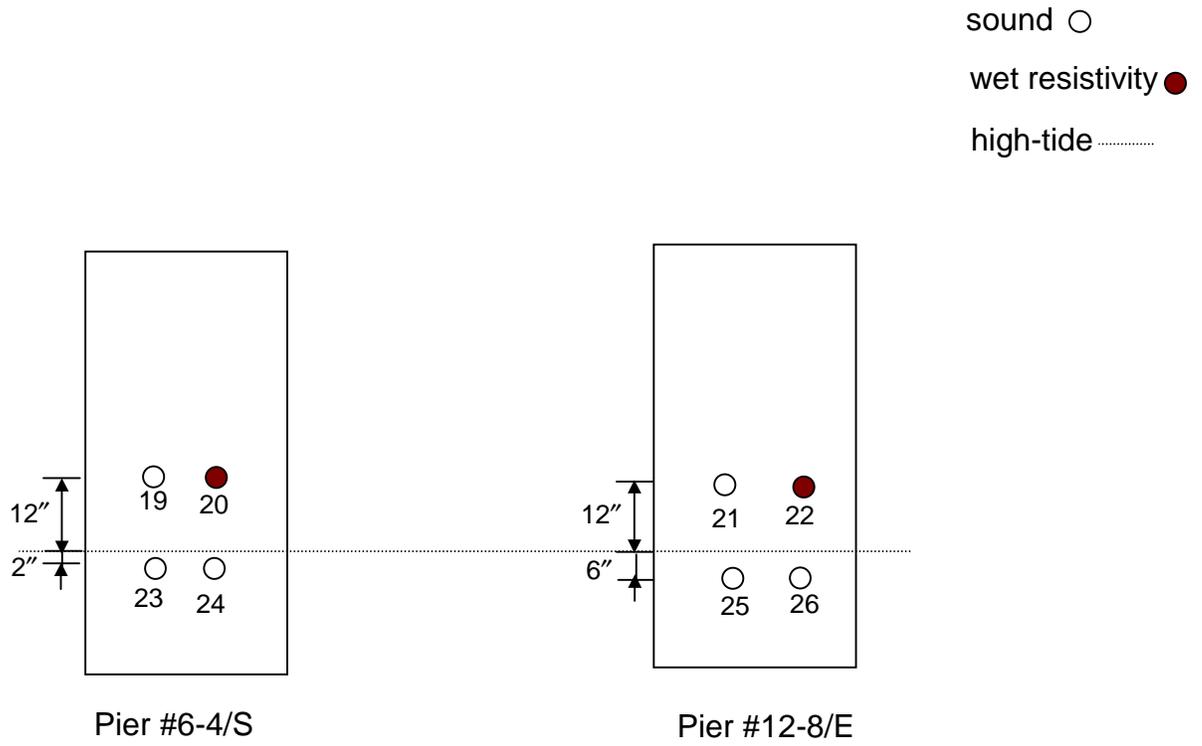
Figure A2-4   Core Extraction Locations at the BLP Bridge

sound ○

crack ○

high-tide ⋯⋯⋯

Lift Line

16 ○ ↕ 6″

31

20 ○ ○ 21

2.5′
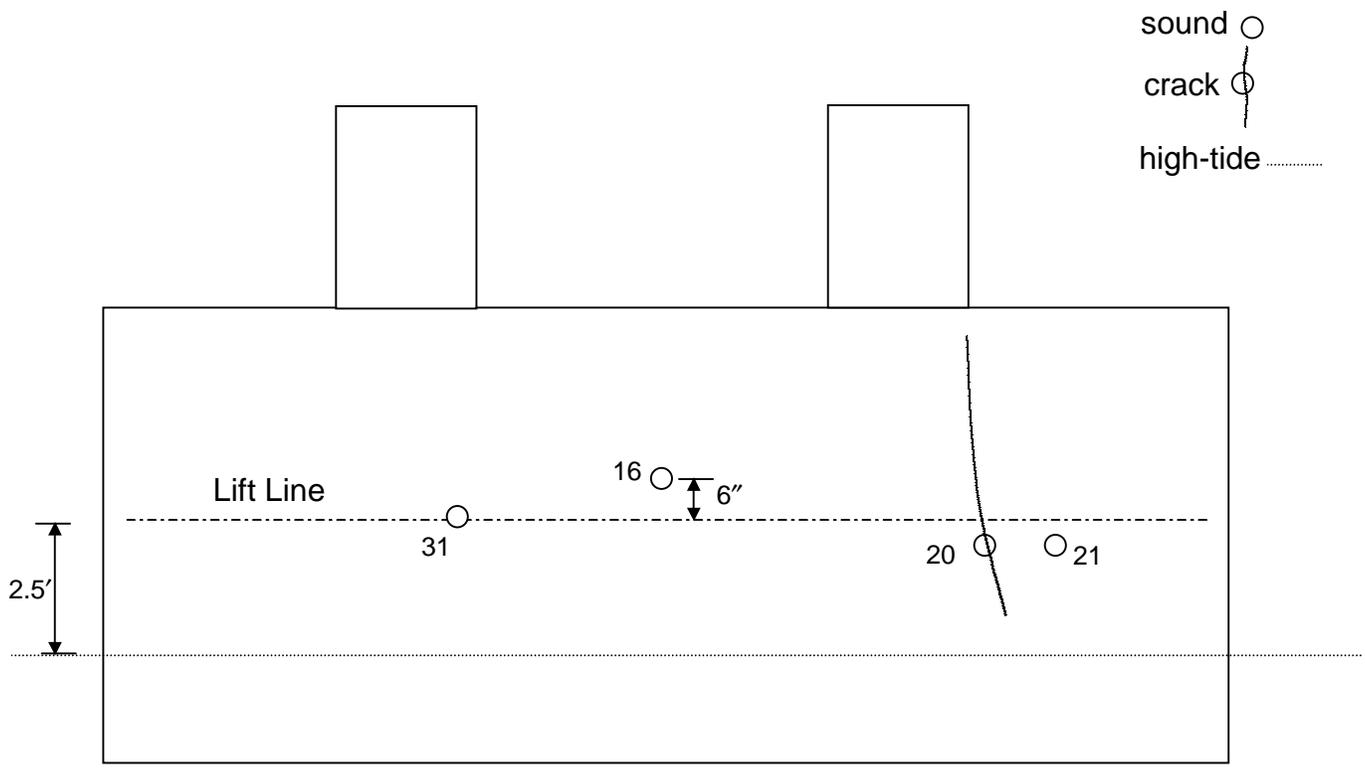
Pier 8

Core 12 and 13 on lift line 6 ft AHT

Figure A2-5   Core Extraction Locations at the MAC Bridge

5C ○   5D ○   5A ○ ● 5B

2′

3C ○
3CC ○   3D ○   3A ○ ● 3B
3CCC ○

2′

1C ○   1D ○   1AA ○ 1BB ●   ○ 1B
        1D ○   1A ○

1′

0C ○   0D ○   0A ○ ● 0B

North-Pier/N
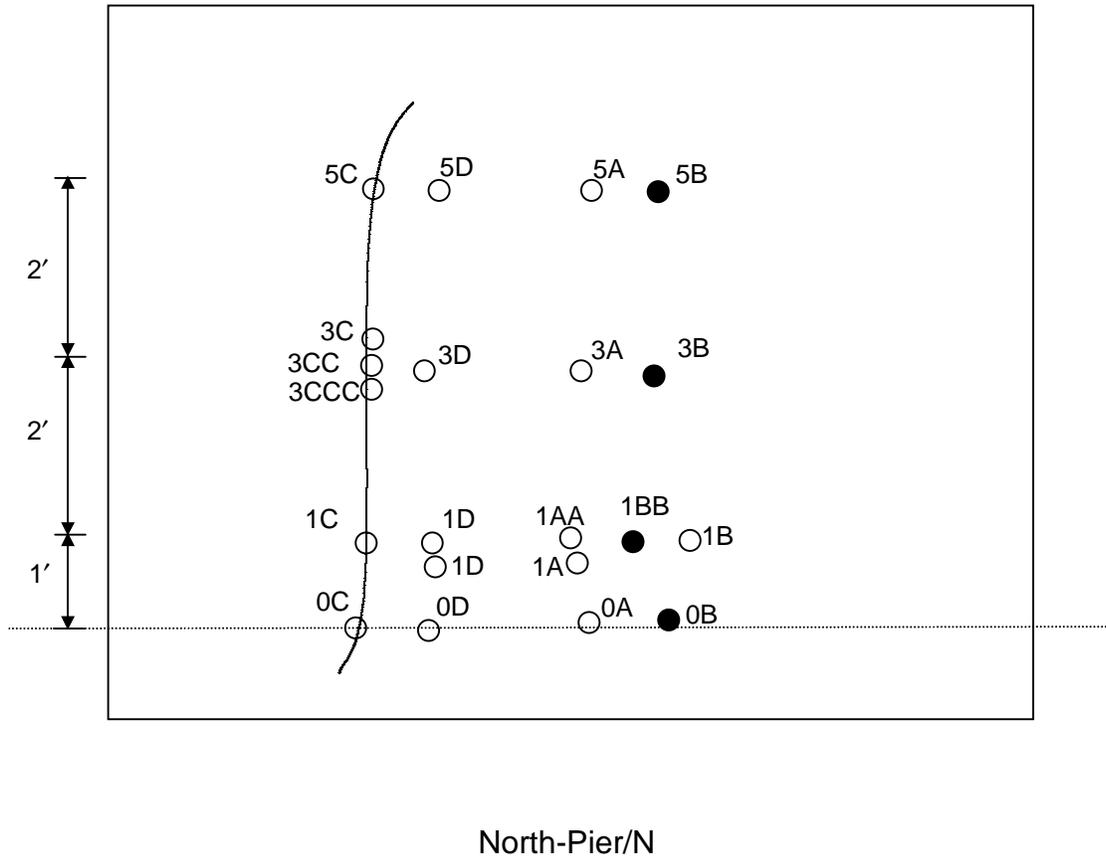
Figure A2-6   Core Extraction Locations at the DPE Bridge

sound ○
crack ◐
wet resistivity ●
high-tide ·········

Pier #196-4/S

Pier #196-5/S

Pier #29-5/N

Pier #115-4/N

Pier #123-3/N

Pier #160-Strut /N
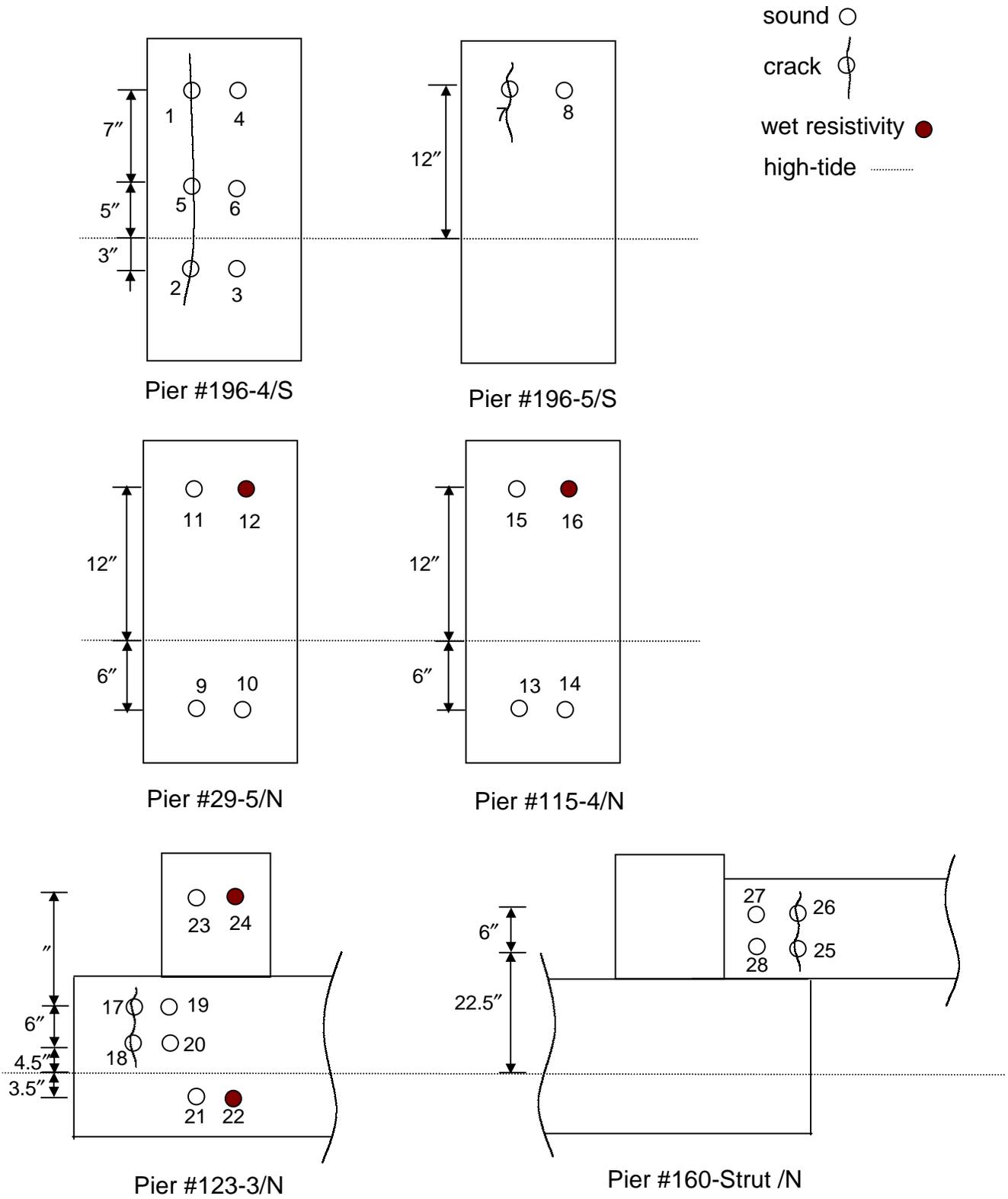
Figure A2-7   Core Extraction Locations at the BSB Bridge

sound ○
crack ○
wet resistivity ●
high-tide ·······

Pier #10-1/W

16″
12″
4″

5   6
1   2
3   4

Pier #11-6/E

18″
12″
8″

11   12
7   8
9   10

Pier #16-1/E

12″
12″
4″

17   18
13   14
15   16

Pier #19-6/W

6″
20″
3″

23   24
19   20
21   22
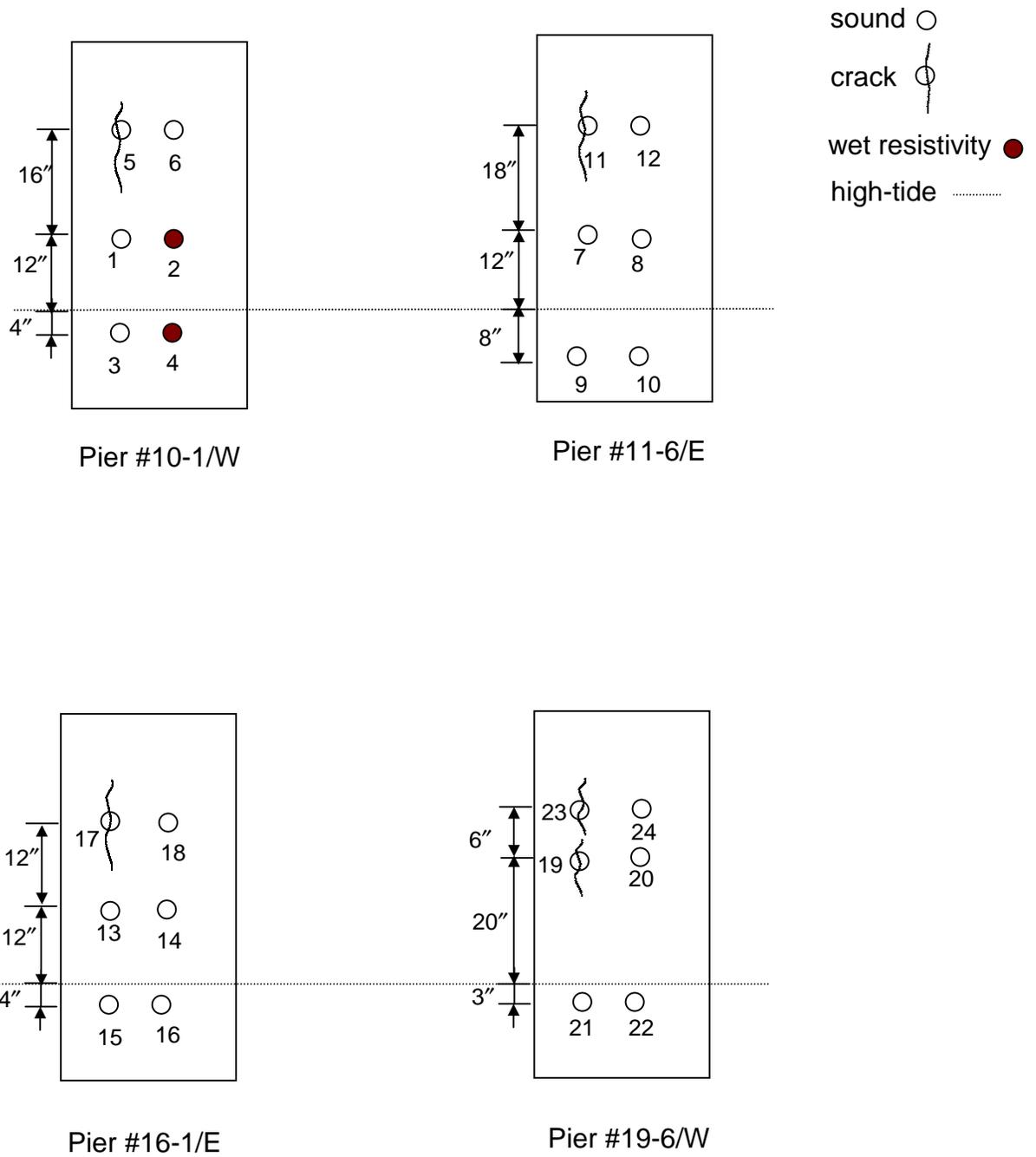
Figure A2-8   Core Extraction Locations at the SHB Bridge

106
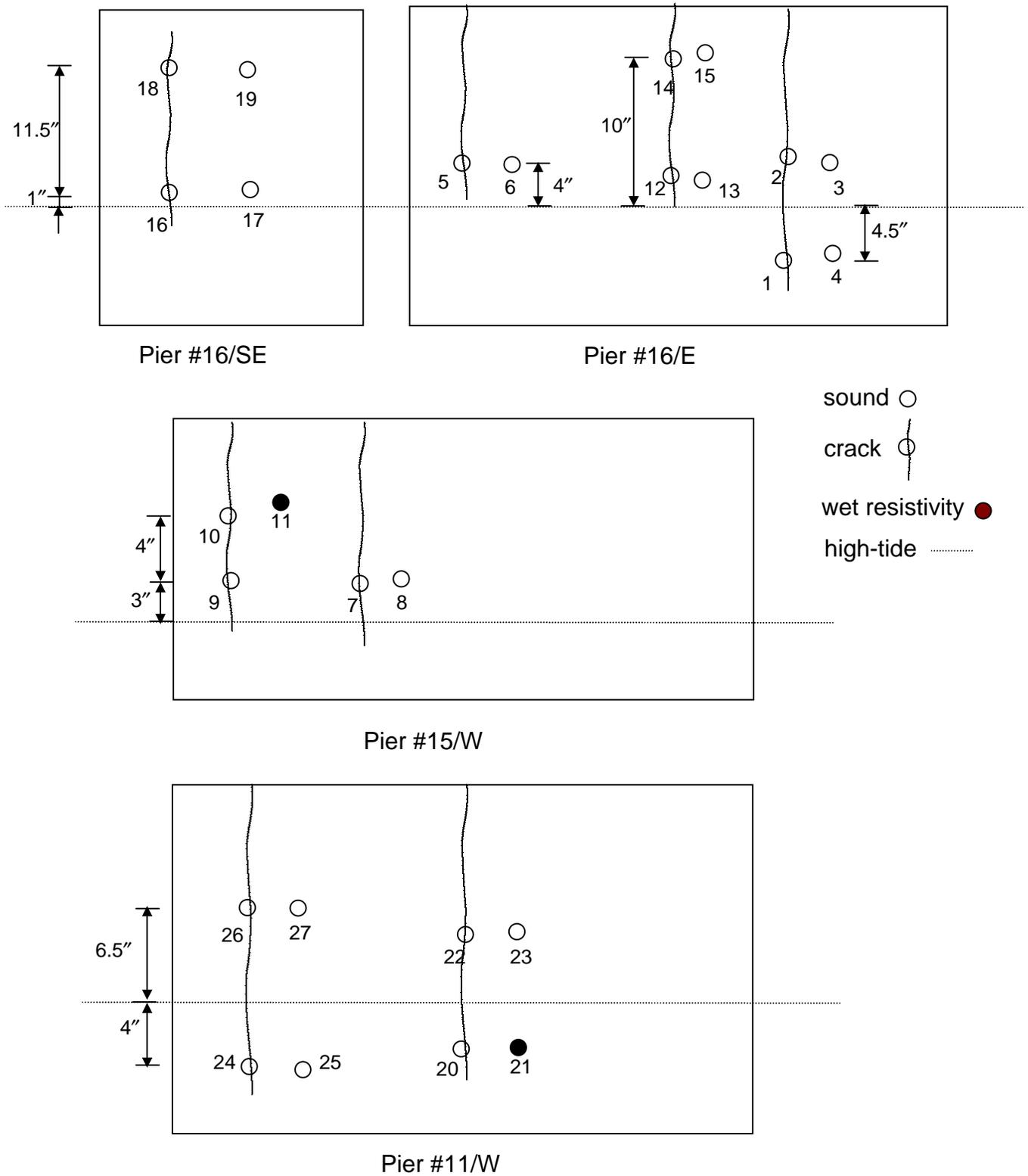
Figure A2-9   Core Extraction Locations at the NSB Bridge
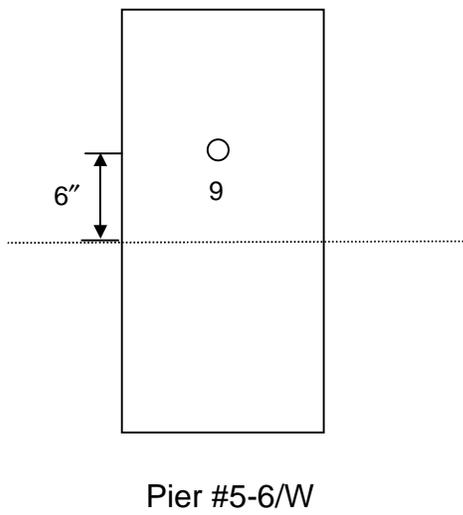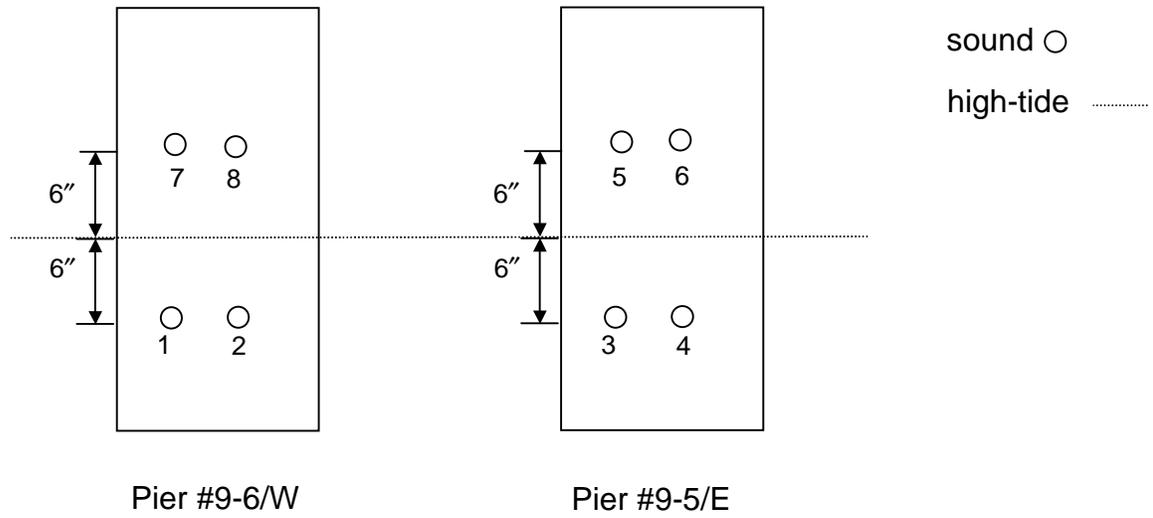
Figure A2-10   Core Extraction Locations at the MIB Bridge

sound ○
crack ⦶
wet resistivity ●
high-tide ┄┄

3
4
12″
3″
2
1

Pier #9-1/N

8
7
12″
3″
6
5

Pier #6-5/S

11
12
12″
10
9
12″

Pier #7-1/W

17
16
12″
14 15 13
12″
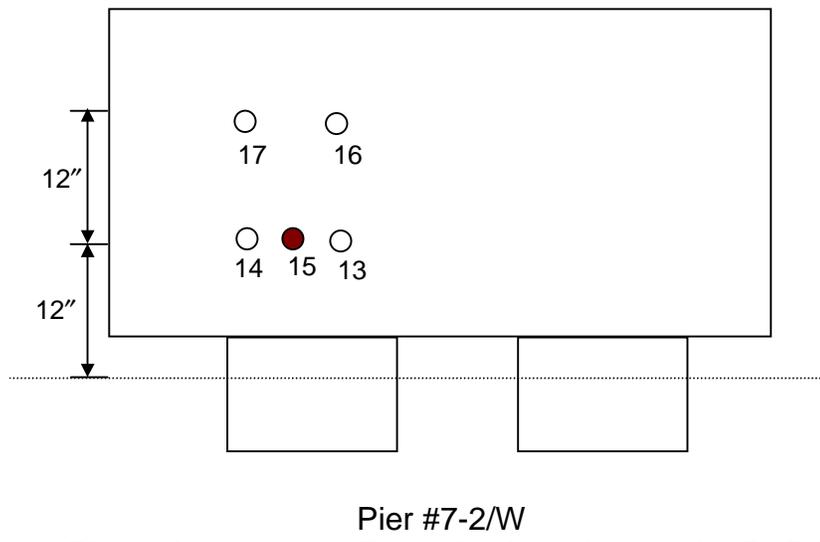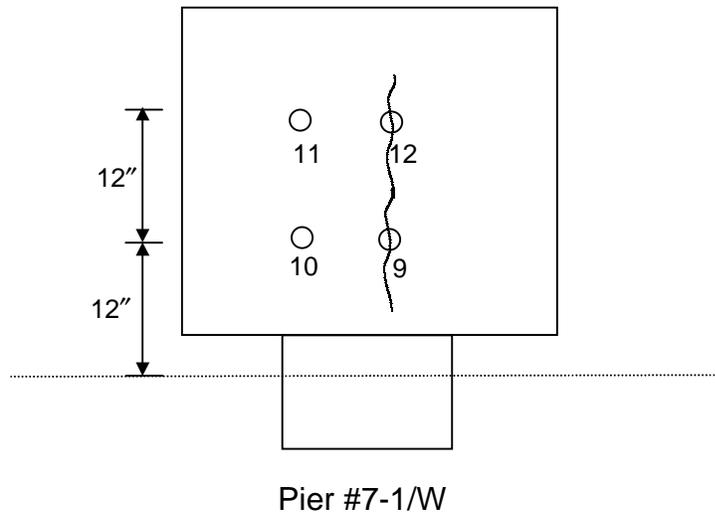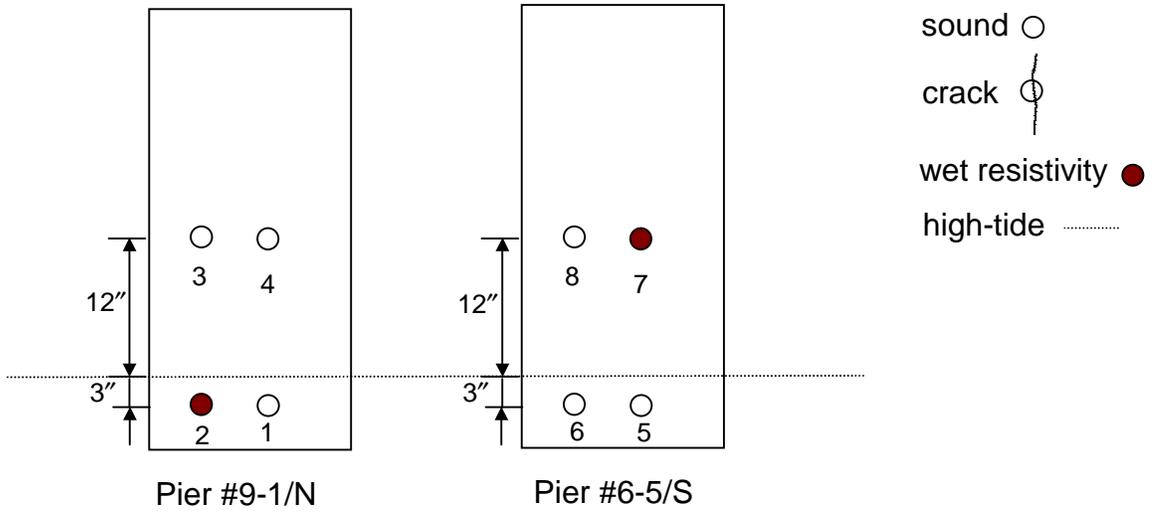
Pier #7-2/W
Figure A2-11   Core Extraction Locations at the BCB Bridge

109
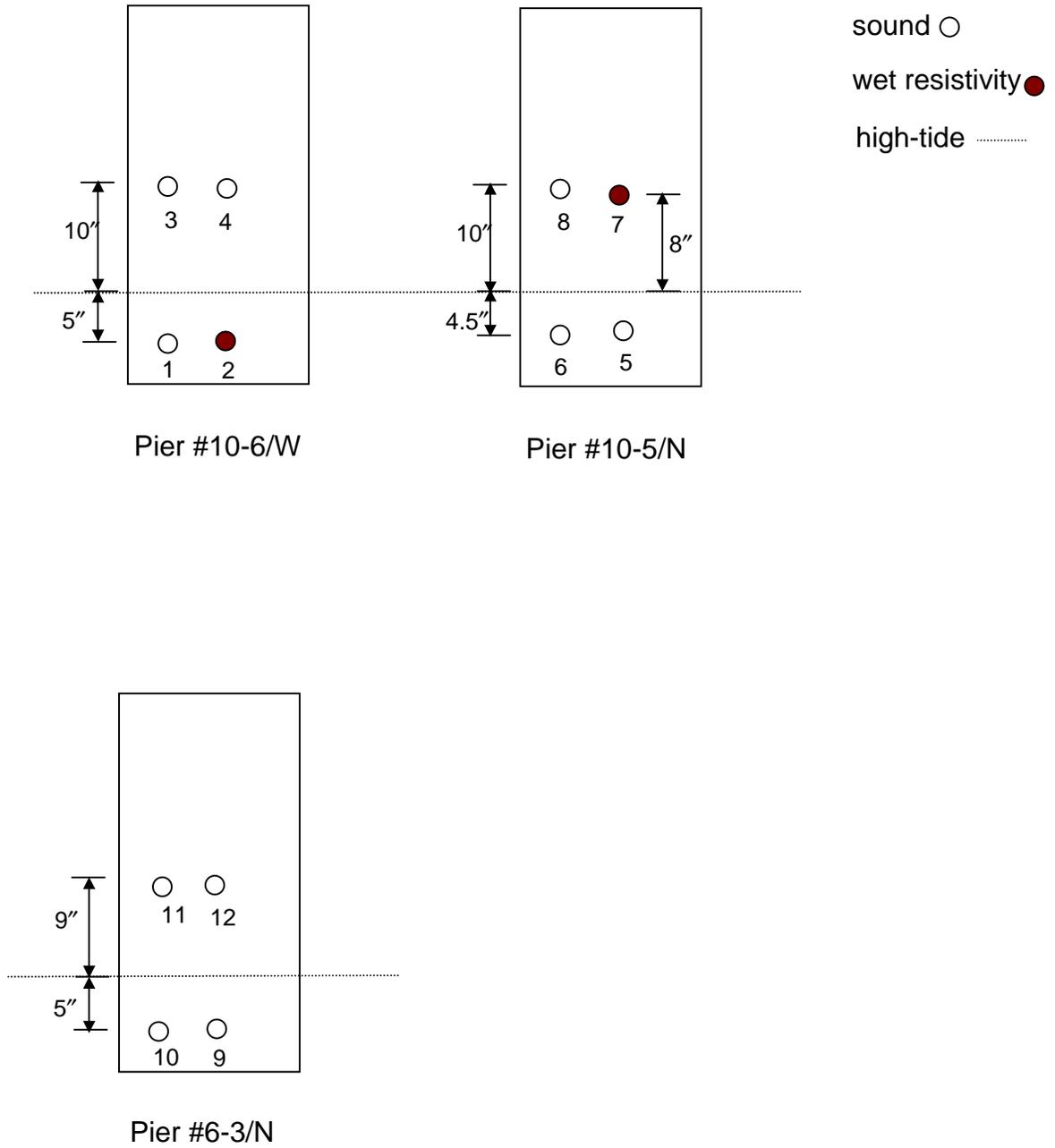
Figure A2-12   Core Extraction Locations at the BPB Bridge
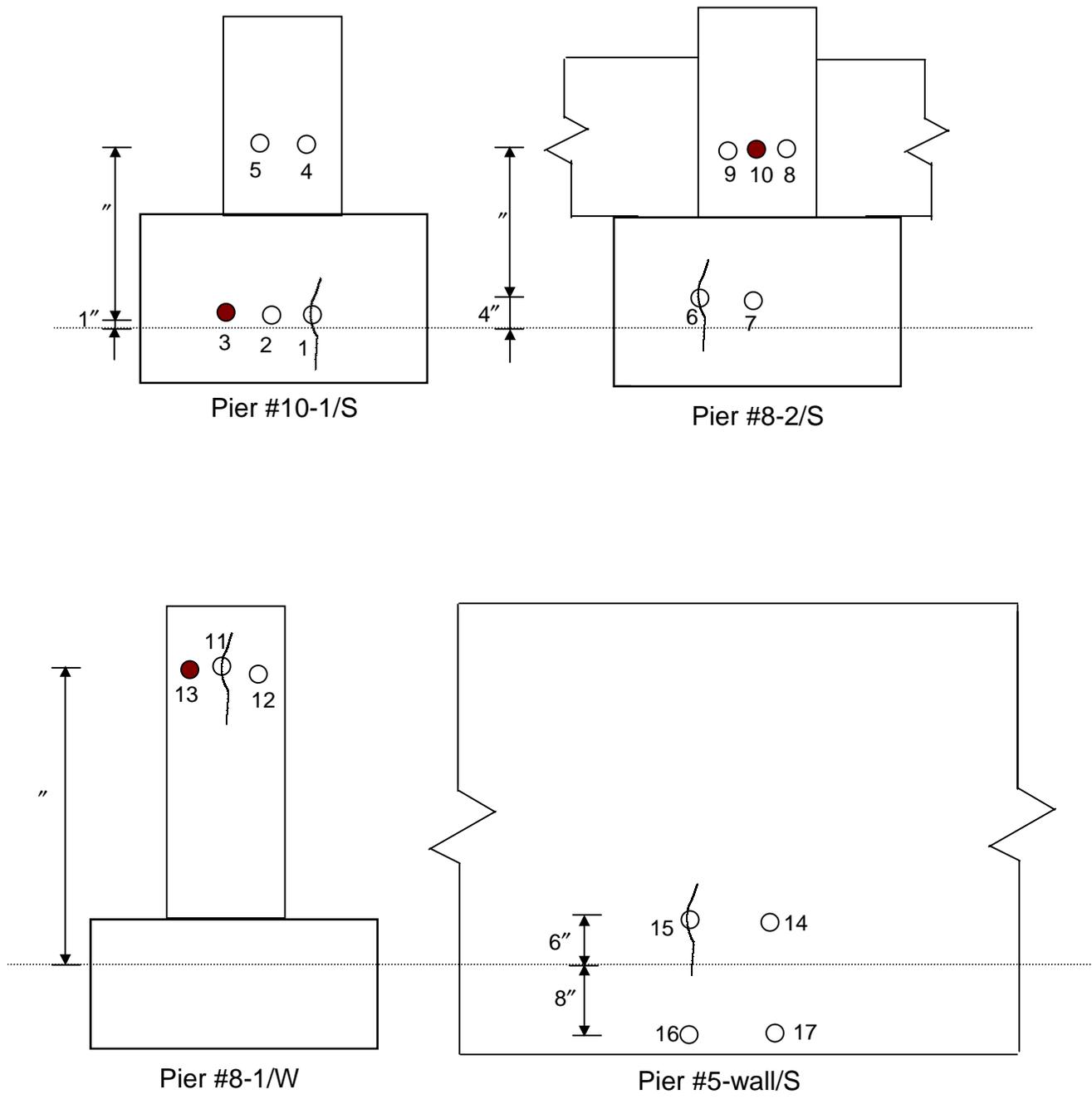
Figure A2-13   Core Extraction Locations at the NPB Bridge

Appendix 3 — Chloride profiles for sound and cracked concrete
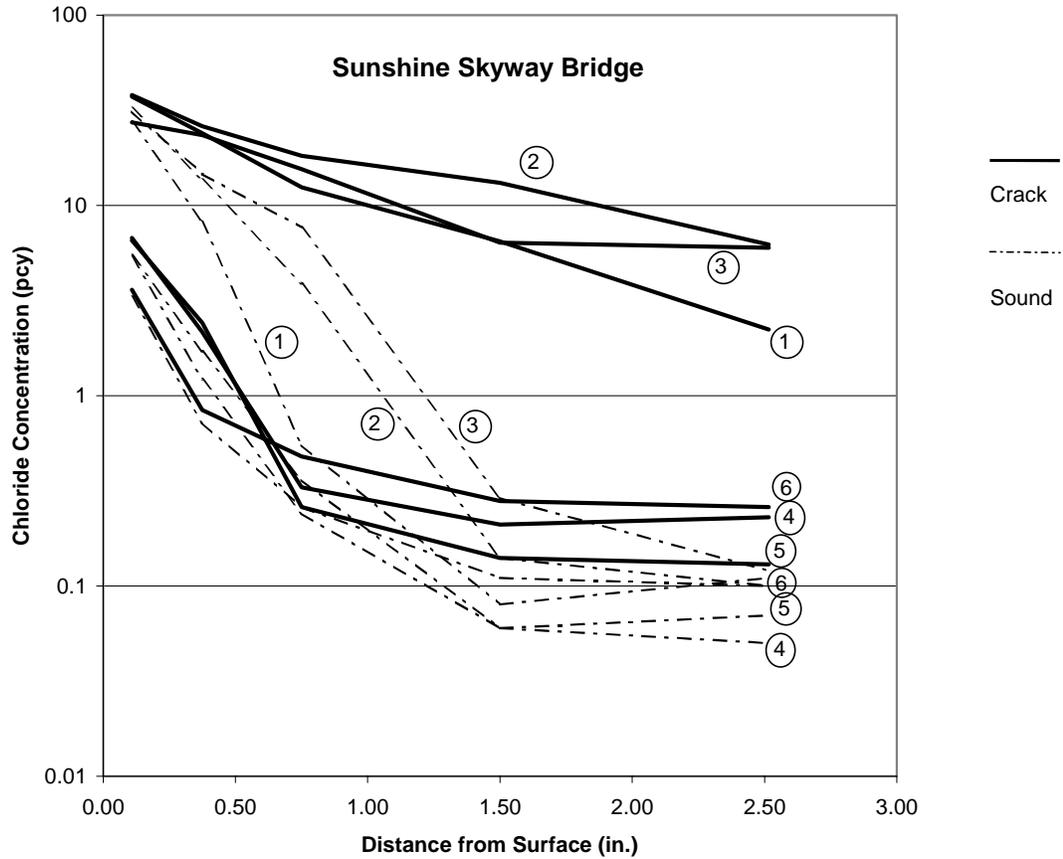
Figure A3-1 Comparison of chloride penetration in core pairs on a crack and on sound concrete, extracted from SSK at various positions and elevations. Each pair is represented by a circled number. The following core identification is keyed to the general core number in tables 3 and 5 as [pair, crack core, sound core]: [1,524,526]; [2,531,534]; [3,536,537]; [4,523,522]; [5, 528, 527]; [6,532,530].
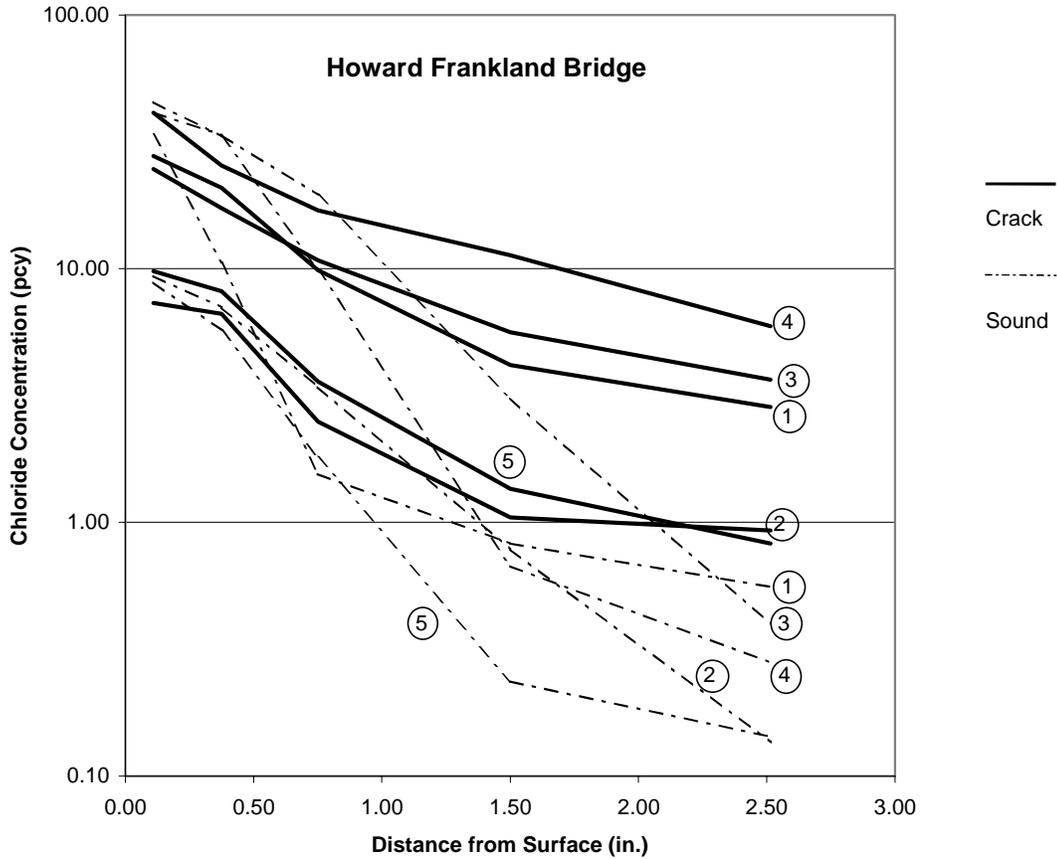
Figure A3-2 Comparison of chloride penetration in core pairs on a crack and on sound concrete, extracted from HFB at various positions and elevations. Each pair is represented by a circled number. The following general core identification is keyed to the core number in tables 3 and 5 as [pair, crack core, sound core]: [1,564,565]; [2,566,567]; [3,578,579]; [4,590,591]; [5,597,598].
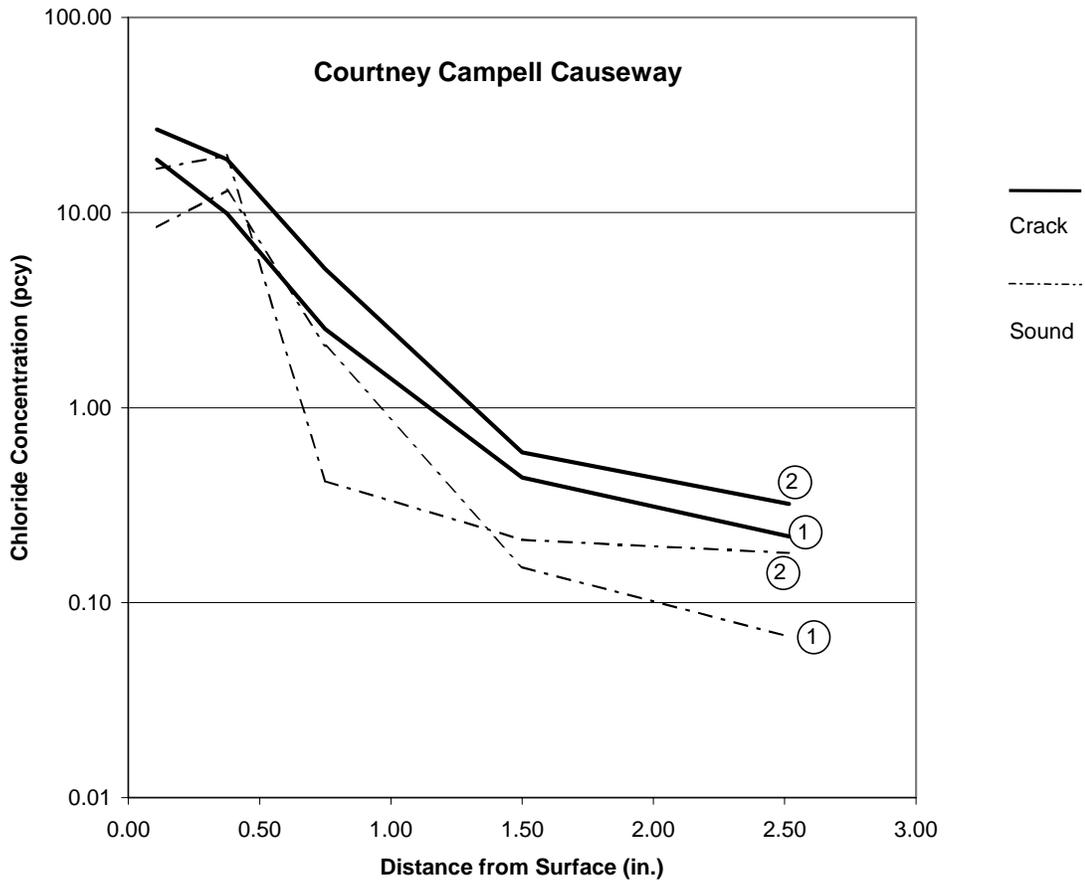
Figure A3-3 Comparison of chloride penetration in core pairs on a crack and on sound concrete, extracted from CCC at various positions and elevations. Each pair is represented by a circled number. The following general core identification is keyed to the core number in tables 3 and 5 as [pair, crack core, sound core]: [1,551,550]; [2,553,552].
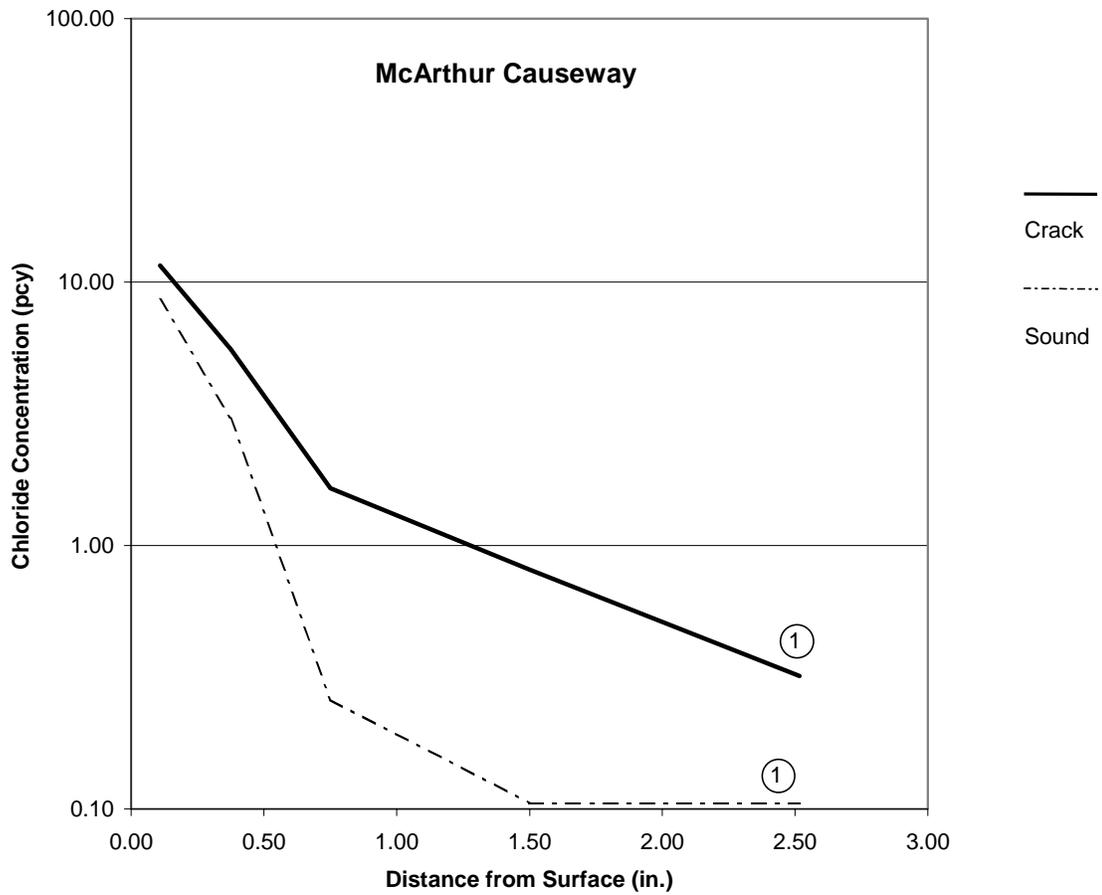
Figure A3-4 Comparison of chloride penetration in core pairs on a crack and on sound concrete, extracted from MAC at various positions and elevations. Each pair is represented by a circled number. The following general core identification is keyed to the core number in tables 3 and 5 as [pair, crack core, sound core]: [1,614,615].
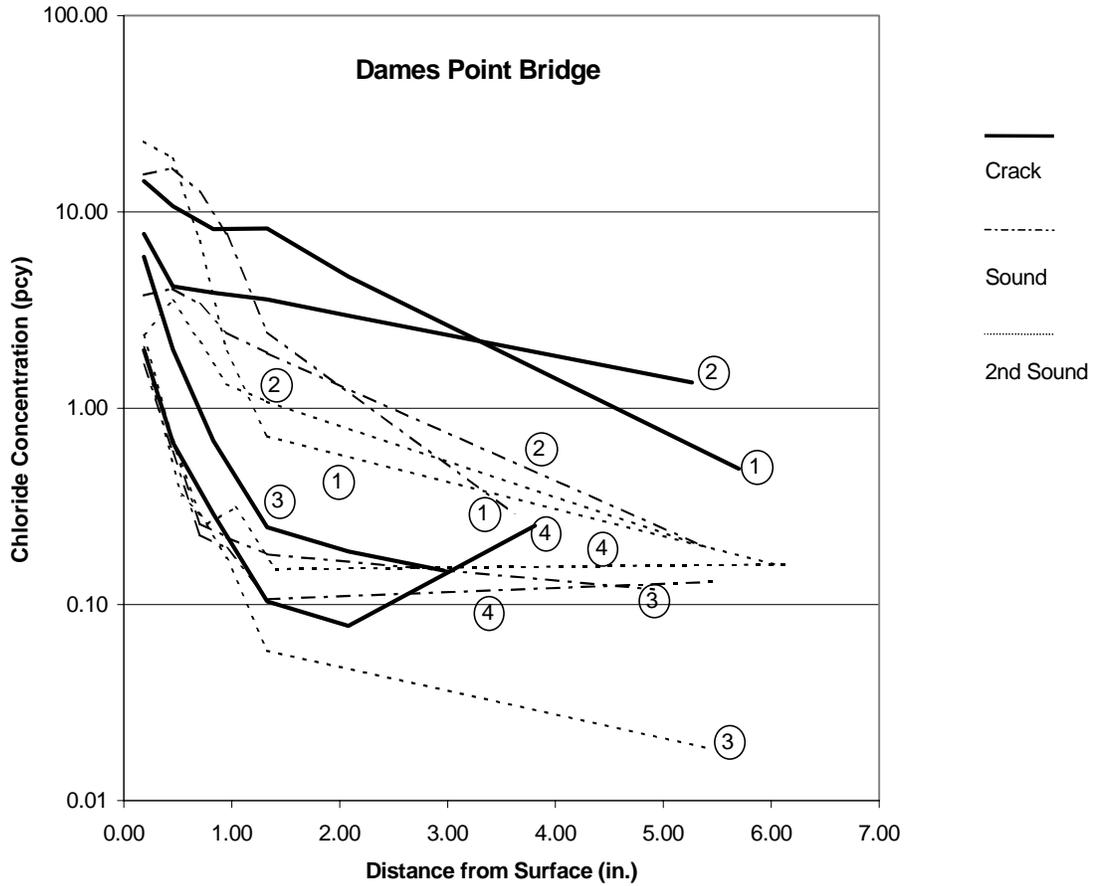
Figure A3-5 Comparison of chloride penetration in core pairs on a crack and on sound concrete, extracted from DPE at various positions and elevations. Each pair is represented by a circled number. The following core identification is keyed to the general core number in tables 3 and 5 as [pair, crack core, sound core, second sound core]: [1,652,653,650]; [2,658,660,655]; [3,665,666,661]; [4,669,670,667].
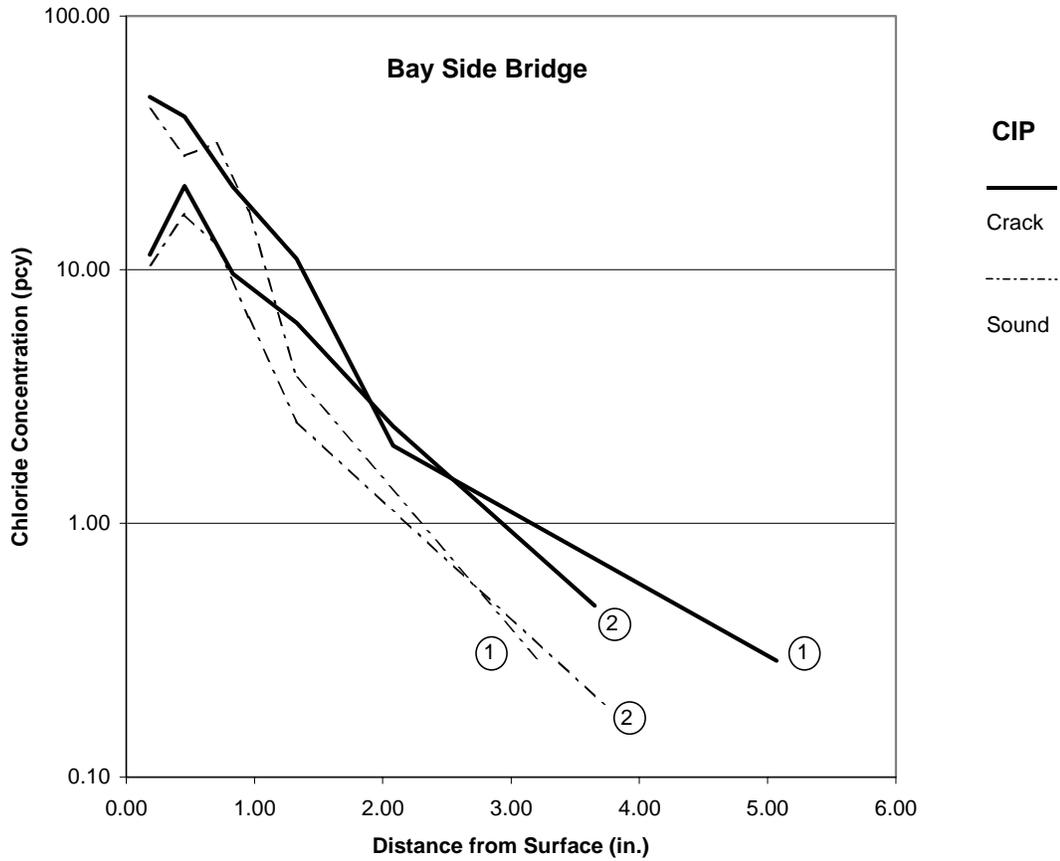
Figure A3-6 Comparison of chloride penetration in core pairs on a crack and on sound concrete, extracted from BSB (CIP) at various positions and elevations. Each pair is represented by a circled number. The following core identification is keyed to the general core number in tables 3 and 5 as [pair, crack core, sound core]: [1,718,720]; [2,726,727].
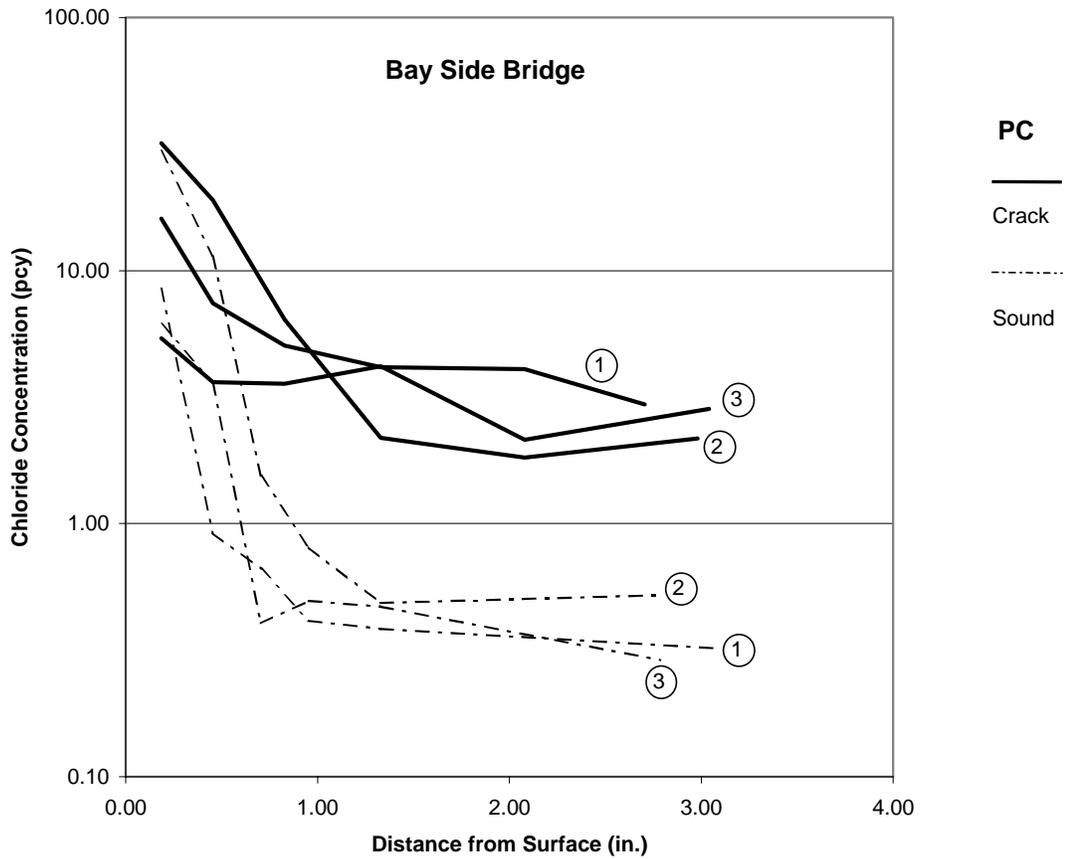
Figure A3-7 Comparison of chloride penetration in core pairs on a crack and on sound concrete, extracted from BSB (PC) at various positions and elevations. Each pair is represented by a circled number. The following core identification is keyed to the general core number in tables 3 and 5 as [pair, crack core, sound core]: [1,701,704]; [2,702,703]; [3,707,708].
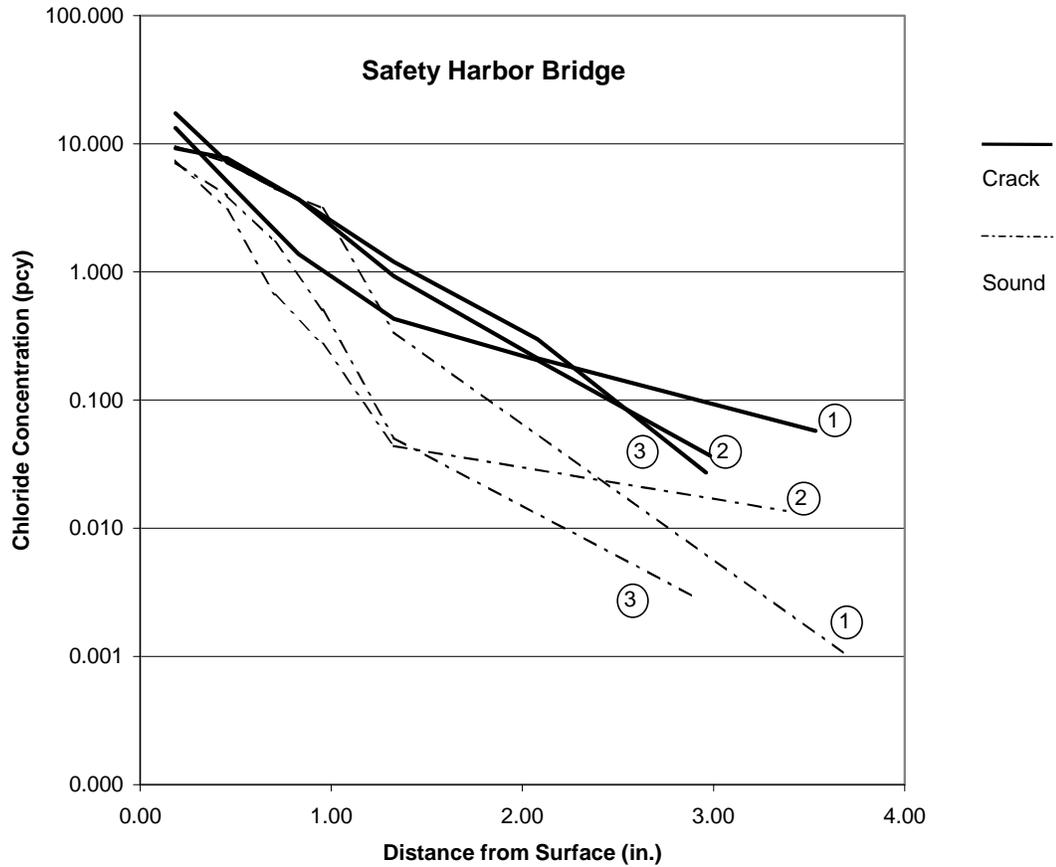
Figure A3-8 Comparison of chloride penetration in core pairs on a crack and on sound concrete, extracted from SHB at various positions and elevations. Each pair is represented by a circled number. The following core identification is keyed to the general core number in tables 3 and 5 as [pair, crack core, sound core]: [1,745,746]; [2,751,752]; [3,757,758].
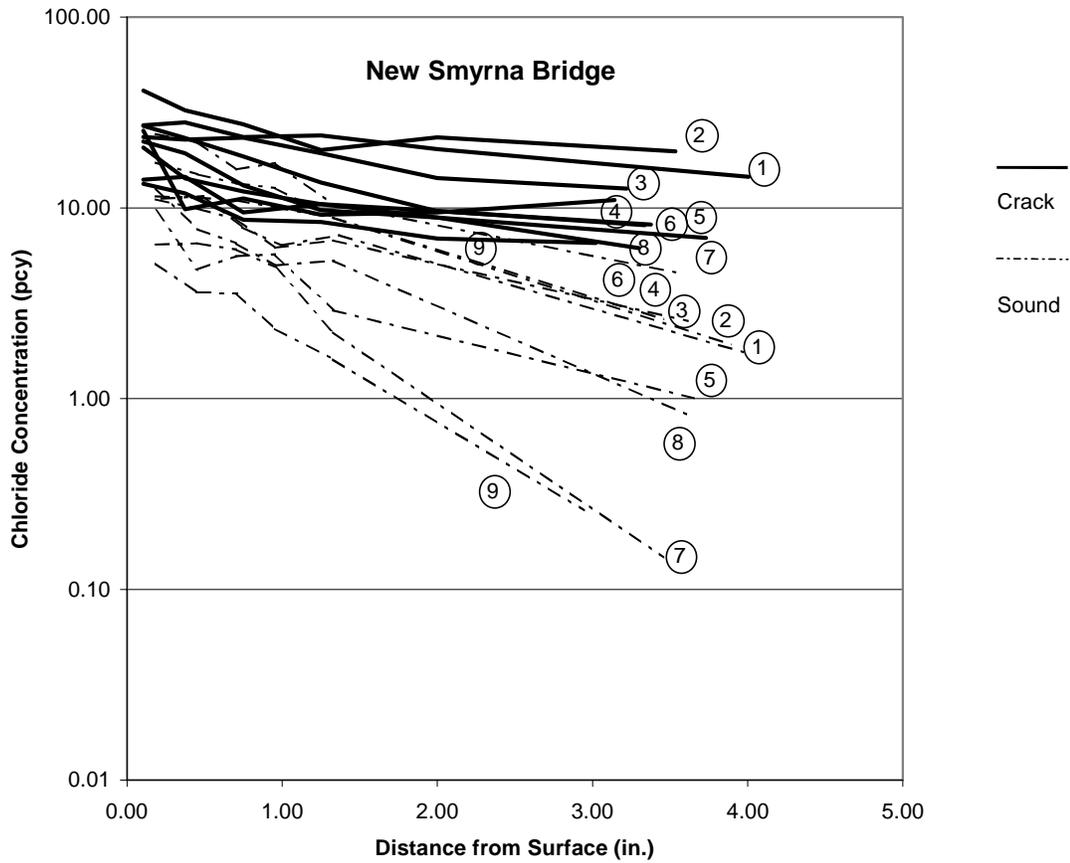
Figure A3-9 Comparison of chloride penetration in core pairs on a crack and on sound concrete, extracted from NSB at various positions and elevations. Each pair is represented by a circled number. The following core identification is keyed to the general core number in tables 3 and 5 as [pair, crack core, sound core]: [1,782,783]; [2,781,784]; [3,787,788]; [4,792,793]; [5,794,795]; [6,796,797]; [7,798,799]; [8,804,805]; [9,806,807].
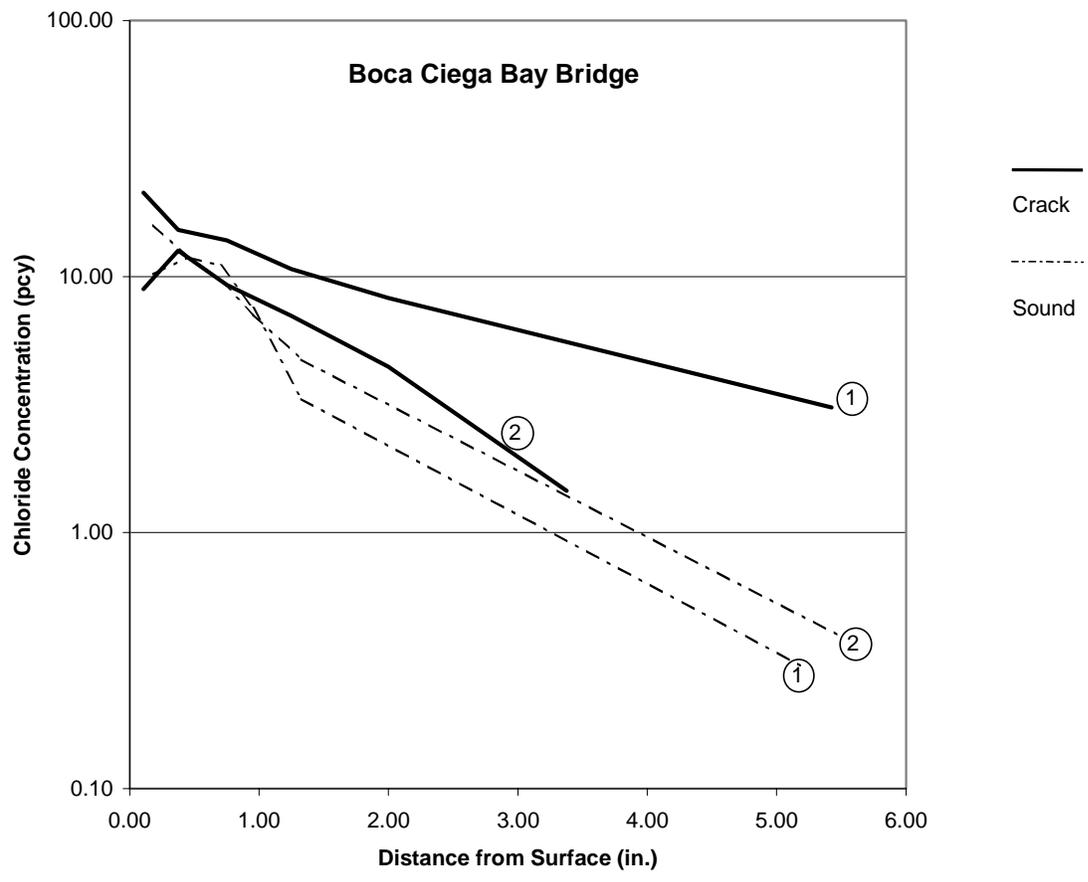
Figure A3-10 Comparison of chloride penetration in core pairs on a crack and on sound concrete, extracted from BCB at various positions and elevations. Each pair is represented by a circled number. The following core identification is keyed to the general core number in tables 3 and 5 as [pair, crack core, sound core]: [1,849,850]; [2,852,851].
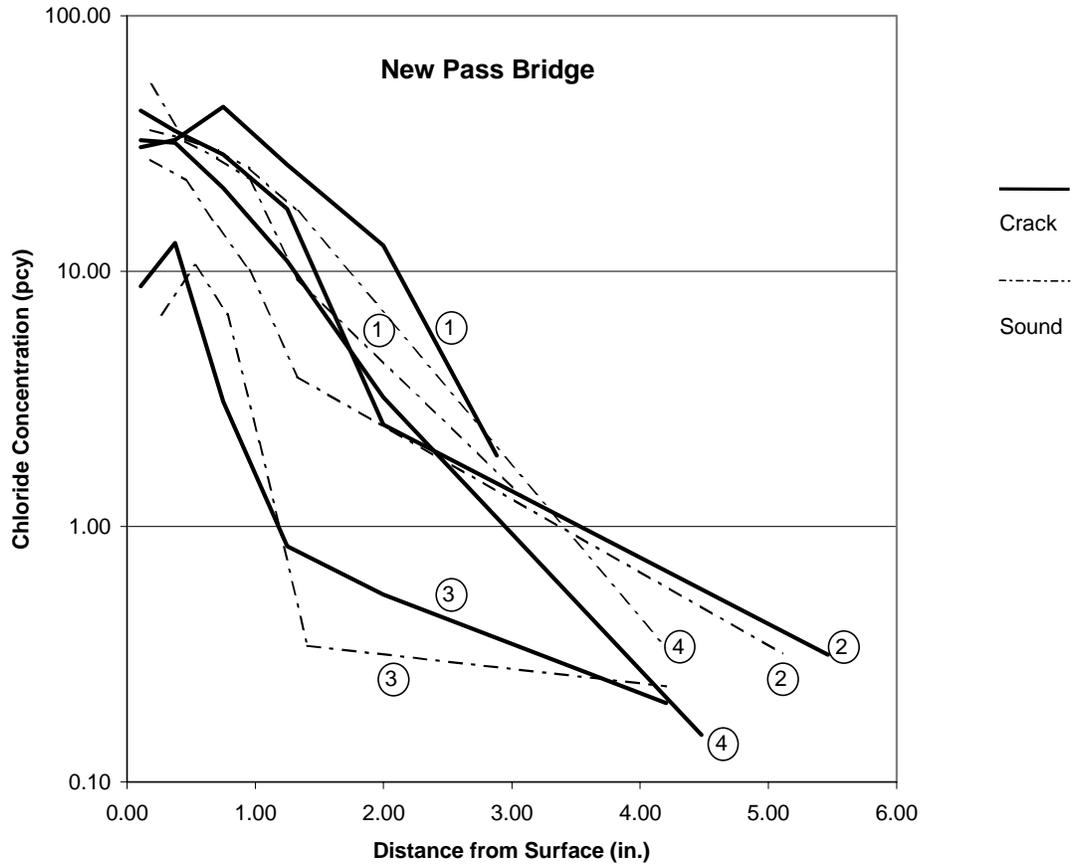
Figure A3-11 Comparison of chloride penetration in core pairs on a crack and on sound concrete, extracted from NPB at various positions and elevations. Each pair is represented by a circled number. The following core identification is keyed to the general core number in tables 3 and 5 as [pair, crack core, sound core]: [1,891,892]; [2,896,897]; [3,901,902]; [4,905,904].

APPENDIX 4. Decreased corrosion initiation time of steel in concrete due to rebar obstruction of diffusional flow.

This Appendix is in the form of a self-standing paper, which forms the basis of an independent submission to the technical literature.

Title: Decreased corrosion initiation time of steel in concrete due to rebar obstruction of diffusional flow.

Authors: Stanley C. Kranc, Alberto A. Sagüés and Francisco J. Presuel-Moreno

ABSTRACT

When chlorides migrate into concrete by diffusion, rebars act as a barrier to transport, causing a more rapid increase in concentration at the leading face of the rebar than would be expected from simple one dimensional predictions. The time interval to reach the critical concentration to initiate corrosion can be significantly shortened, reducing the effectiveness of the concrete cover in protecting the steel reinforcing. Estimates of the magnitude of this effect are presented.

INTRODUCTION

It is generally understood that reinforcing steel in concrete remains passive due to contact with high pH pore water, however this circumstance can change if aggressive agents such as chloride ions are present.   Depassivation can occur if the concentration ratio of chloride ions to hydroxide ions reaches a critical value at the steel surface. The actual value of this critical ratio depends on several factors including the presence of inhibiting agents, and the local electrical potential [1-4]. In addition to background levels, chlorides may be transported (mainly by diffusion and moisture penetration) into the concrete from the surrounding environment as a result of deicing operations by salt addition on pavement surfaces or from marine exposure of bridge substructural elements. The purpose of the present discussion is to assess the importance of the rebar, acting as a local barrier to diffusive transport, on the development of critical concentration ratios.

ANALYSIS

Tuuti [5] has characterized the deterioration of reinforced concrete as a two stage process (or damage function), where the initiation phase is the period from construction until depassivation occurs, followed by a corrosion propagation phase where metal dissolution proceeds until the structural element eventually becomes unserviceable due to a combination of loss of metal cross section and cracking of the concrete. The length t_i of the initiation phase is determined in large part by the rate at which the chloride concentration builds adjacent to the rebar. The transport of chlorides through concrete is complex, and likely involves diffusion coupled with water movement as well as possible reactions such as binding by various chemical and physical mechanisms. Many investigators have attempted to analyze the transport of chlorides, using simple Fickian diffusional models [6,7], as well as models taking into account binding, concrete surface conditions, and transport processes on a microscopic scale [8-12]. Evidence

123

indicates that both aging of the concrete and structural geometry affect the transport processes involved [6,13,14]. For simplicity, the present discussion is limited to diffusional transport. Fick's second law may be written for diffusion coefficient D, constant in space and time, as

$$\frac{\partial C}{\partial t} = D\nabla^2 C \tag{1}$$

where C is the chloride concentration in mass per unit volume of concrete. Here the influence of non-linear binding has been ignored, although the effect of linear binding could be included by using a reduced diffusion coefficient [8,14]. To estimate t_i, it is common practice to evaluate C as function of time using a solution for Equation 1 that takes into account the overall system shape and dimensions as well as the chloride concentration at the surface, but disregards the presence of embedded rebar. It will be shown below that neglecting the presence of the rebar can lead to significant overestimation of t_i.

The effect of the rebar presence will be illustrated for the case of a one-dimensional semi-infinite slab with constant surface concentration C_S and initial background concentration C_0 (a similar analysis can be applied to more complex cases). For the example chosen the solution for the total chloride concentration at any depth can be expressed in terms of the error function (erf)

When an effective value for D is known beforehand (e.g. from experimental data), a conventional approach is to use Equation 2 to calculate the value of time t_i, to

$$\frac{C - C_0}{C_s - C_0} = 1 - \text{erf}(x/\sqrt{4Dt}) \tag{2}$$

develop a critical threshold chloride concentration C_T at cover depth $x = x_C$. This approach ignores the presence of rebar embedded in the concrete at cover depth, which changes the geometry of the problem somewhat, since the pathway for transport is interrupted by the rebar itself. The rebar is impervious to the passage of chlorides, which in turn causes the chloride concentration to build up faster in the region adjacent to the side of the rebar closest to the exposed surface. This effect has been noted previously in comparable systems for both rebar and for large aggregates [10,11]. Figure 1 shows a two dimensional solution to Equation 1 including the rebar (obtained numerically using a conventional Forward Time - Central Space algorithm [12]). In this analysis the rebar cross section was modeled as an octagon. Several numerical consistency checks were conducted to help ensure accuracy of these calculations.

The isocontour map of chloride distribution clearly shows the faster buildup at the leading edge of the rebar compared to that at the bulk of the concrete at the same distance from the external surface, but away from the rebar. Equation 2 estimates the

latter. Thus, the conventional forecast of corrosion initiation in structural elements, based on a solution to Equation 1 that ignores the rebar, is inherently generous as it will predict a value of t_i that is too long. A nondimensional time derating factor T_f that is independent of D can be defined as the ratio of t_i calculated based on the concentration at the leading edge of the rebar (point P in Figure 1), to the value of t_i obtained using Equation 2. Computations of chloride distribution with time to evaluate T_f were made for various cases with the same model used to generate Figure 1, adopting the distances indicated there for x_C and Φ (the nominal rebar diameter). Results of these computations are shown in Figure 2, expressed as a function of the ratio of Φ to x_C, using as a parameter the ratio of C_T to concentration at the concrete surface C_S (or (C_T - C_0) / (C_S - C_0) if C_0 is not negligible). As might be expected, when the ratio Φ/x_C is very small the reduction in t_i is of little importance (derating factor $T_f \rightarrow 1$). The effect becomes more noticeable and then substantial as Φ/x_C and C_T/C_S increase. For very large values of Φ/x_C the behavior approaches the limit of a slab of finite thickness x_C. The corresponding terminal values of T_f were calculated using published solutions for that case [18] and are displayed in Figure 2 as well.

During the course of this investigation a study was made to determine the importance of rebar shape on the derating factor as presented here. To maintain consistency, the total cross sectional area was held constant as was the location of the leading edge of the rebar. It was found that as the shape was varied from round to square, the derating factor became smaller (e.g. by about 10% when both Φ/x_C and C_T/C_S were 0.5). This result was expected since the flat face of a square face shape offers a more serious obstruction to diffusive transport. Obviously the true cross sectional shape of rebar is complex due to ribbing on the surface of the rebar and cannot be represented by a simple geometry. The octagon was chosen here as a compromise both to recognize this fact and for simplicity of computation.

As an illustration of the magnitude of the rebar presence effect, consider the use of plain steel in an application with x_C=100 mm, Φ=25 mm, C_S = 20 kg/m^3 and C_T = 2 kg/m^3 (C_0~0). The results in Figure 2 indicate that there is an approximate 17% reduction in t_i from that calculated by Equation 2. Now consider an alternative scenario where the concrete mix, Φ, C_S and C_0 all remain the same but construction constraints impose a need for lowering x_C to 50 mm. As compensation, a corrosion inhibitor or corrosion resistant rebar alloy is chosen that increases C_T to 8 kg/m^3. In this case the reduction in estimated t_i increases to about 40% of the value that would have been obtained using Equation 2. It should be noted also that the parameters for both scenarios were chosen to yield comparable values of t_i when Equation 2 is used, however, correction for the rebar presence indicates that the second case would yield a distinctly shorter initiation period.

The examples presented above indicate that the reduction in t_I can be significant, especially when corrosion control relies on increasing C_T. It is proposed that this effect should be incorporated in durability estimates as is normally done for other geometric factors, such as the presence of corners, finite slab dimensions, or circular geometries [3,14]. Calculations are in progress to evaluate the combined effect of those other geometric factors with the presence of rebar (and rebar arrays), as well as to further explore the importance of the shape of the rebar cross section.

Several issues concerning the nature of this effect merit discussion. The calculations presented above treat the bulk of the concrete as a homogeneous medium, while in actuality heterogeneities such as coarse aggregates create disturbances of the diffusional flow that can be locally as important as those created by the presence of the rebar. However, the effect of those other heterogeneities is already incorporated as a statistical influence in the effective value of D (and to some extent in C_T as well) while the rebar presence acts as an added systematic disturbance.

It might be argued that chloride diffusivity could be higher in the interfacial region surrounding the rebar than in the bulk of the concrete, because of microstructural differences between the transition zones around aggregates and rebar [12], and of macroscopic effects from consolidation and settling. In such cases the resulting improved transport around the rebar might reduce or eliminate the concentration increase that would have occurred otherwise. However, there is no assurance that those favorable conditions will be met, and a conservative assumption for the full accumulation effect is in order.

Another mitigating circumstance may occur if the value of D used for durability prediction were to be estimated from chloride concentration profiles that consistently included concrete sampling in the region immediately next to the rebar, but using an analysis that assumed unrestricted diffusion. In such case an apparent value of D higher than that for the bulk of the concrete would be obtained, which could at least partly compensate for not considering the geometric rebar effect in the t_i calculations. However, any credit for this benefit would require special proof for each case and cannot be taken in a general, conservative design approach.

CONCLUSIONS

The importance of including rebar restriction geometry in altering the diffusion pattern of chlorides in concrete has been demonstrated. An estimate of the reduction in time to corrosion initiation from that predicted by simple planar diffusion ignoring the rebar has been made. The effect can be substantial, especially with increasing ratio of rebar diameter to concrete cover, and increasing ratio of threshold to surface chloride concentration.

ACKNOWLEDGMENTS

REFERENCES

1.   Li, L. and Sagüés, A.A. "Chloride Corrosion Threshold of Reinforcing Steel in Alkaline Solutions - Open-circuit Immersion Tests", Corrosion, Vol. 57, p.19-28, 2001.

2.   Glass, G.K. and Buenfeld, N.R., "The Presentation Of The Chloride Threshold Level For Corrosion Of Steel In Concrete", Corrosion Sci. Vol. 39, p. 1001-1013, 1997.

3.   Berke, N.S. and Hicks, M.C., "Estimating the Life Cycle of Reinforced Concrete Decks and Marine Piles Using Laboratory Diffusion and Corrosion Data", p.207-231 in "Corrosion Forms and Control for Infrastructure", ASTM STP 1137, Victor Chacker, Ed., American Society for Testing and Materials, Philadelphia, 1992.

4.   Pedeferri, P., "Cathodic Protection and Cathodic Prevention", Construction and Building Materials, Vol. 10, p.391-402, 1996

5.   Tuutti, K., "Corrosion of Steel in Concrete" (ISSN 0346-6906), Swedish Cement and Concrete Research Institute, Stockholm, 1982.

6.   Bamforth, P. B., "The Derivation Of Input Data For Modelling Chloride Ingress From Eight-Year UK Coastal Exposure Trials", Magazine of Concrete Research, Vol. 51, p.87-96, 1999

7.   Cady, P.D. and Weyers, R.E., "Deterioration Rates of Concrete Bridge Decks", J. Transportation Engineering, Vol. 110 No.1, p. 34-44, 1984.

8.   Tang, L. and Nilsson, L.O., "Chloride Binding Capacity And Binding Isotherms Of OPC Pastes And Mortars", Cement and Concrete Research, Vol. 23, p. 247-253, 1993.

9.   Boddy, A., Bentz, E., Thomas, M.D.A., and Hooton, R.D., "An Overview And Sensitivity Study Of A Mutimechanistic Chloride Transport Model" Cement and Concrete Research, Vol. 29, p. 827-837, 1999

10.   Andrade, C., Diez, J.M., and Cruz Alonso, M., "Mathematical Modeling Of A Concrete Surface "Skin Effect" On Diffusion In Chloride Contaminated Media", Advn. Cem. Bas. Mat., Vol.6, p.39-44, 1997.

11.   Xi, Y., and Bazant, Z., "Modeling Chloride Penetration In Saturated Concrete", J. Materials in Civil Engineering, Vol. 11, p. 58-65, 1999.

12.   Bentz, D.P., Garboczi, E.J., and Lagergreen, E.S., "Multi-Scale Microstructural Modeling Of Concrete Diffusivity: Identification Of Significant Variables" Cement, Concrete and Aggregates, Vol. 20, p. 129-139, 1998.

13.   Saetta, A., Scotta, R. and Vitaliani, R., "Analysis of Chloride Diffusion into Partially Saturated Concrete", ACI Materials Journal, Vol 47, pp.441-451, 1993

14.   Sagüés, A.A. and Kranc, S.C. "Effect of Structural Shape and Chloride Binding on Time to Corrosion of Steel in Concrete in Marine Service", , p. 105-114 in Corrosion of Reinforcement in Concrete Construction, C.L. Page, P.B. Bamforth and J.W. Figg, Eds, The Royal Society of Chemistry, Cambridge, 1996.

15.   Hansen, E. J. and Saouma, V.E., "Numerical Simulation of Reinforced Concrete Deterioration - Part 1: Chloride Diffusion", ACI Materials Journal, Vol 96, pp.173-180, 1999

16.   Gospodinov, P.N., Kazandjiev, R.F, Partalin, T.A. and Mironova, M.K., "Diffusion Of Sulfate Ions Into Cement Stone Regarding Simultaneous Chemical Reactions And Resulting Effects", Cement and Concrete Research, Vol. 29, pp. 1591-1596, 1999.

17.   Burden, R. and Faires, J., Numerical Analysis, 4th Ed, PWS-Kent Pub., Boston, 1985

18.   Shewmon, P. G., "Diffusion in Solids", McGraw-Hill, New York, 1963.

NOMENCLATURE

C   Chloride concentration in concrete

C_S Chloride concentration at the concrete surface

C_T Critical chloride concentration threshold

C_0 Background concrete chloride concentration

D   Effective chloride diffusivity

T_f Derating factor

ti   Time to corrosion initiation

x_C Concrete cover thickness

Φ   Nominal rebar diameter
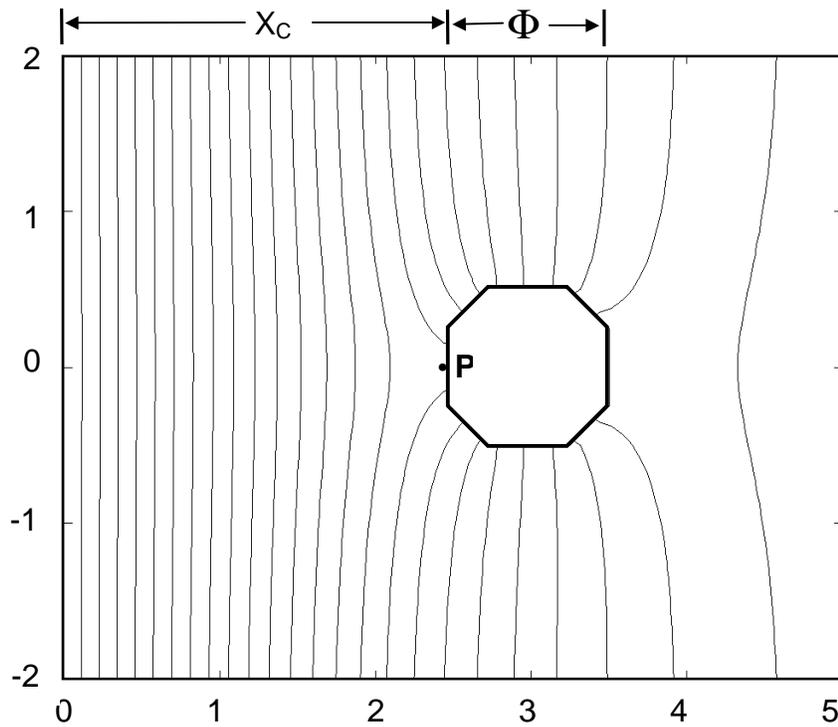
Figure 1. Solution of Equation 1 for a two-dimensional problem where chloride concentration is constant and equal to C_S at the left edge of the frame C_0=0, and a rebar is placed with nominal diameter to concrete cover ratio Φ / X_C = 0.4. The horizontal and vertical segments of the rebar cross section perimeter have length $\Phi/2$. The isocontour lines are spaced at 0.04 C_S, and correspond to the moment t = 1.58 Φ^2 / D for which C ~ 0.36 C_S at the leading edge of the rebar (point P). The coordinates are expressed in rebar diameter units. The numerical solution space extends far beyond the top, bottom and right edges of the frame, which delimit the graphic representation but are not boundary lines.
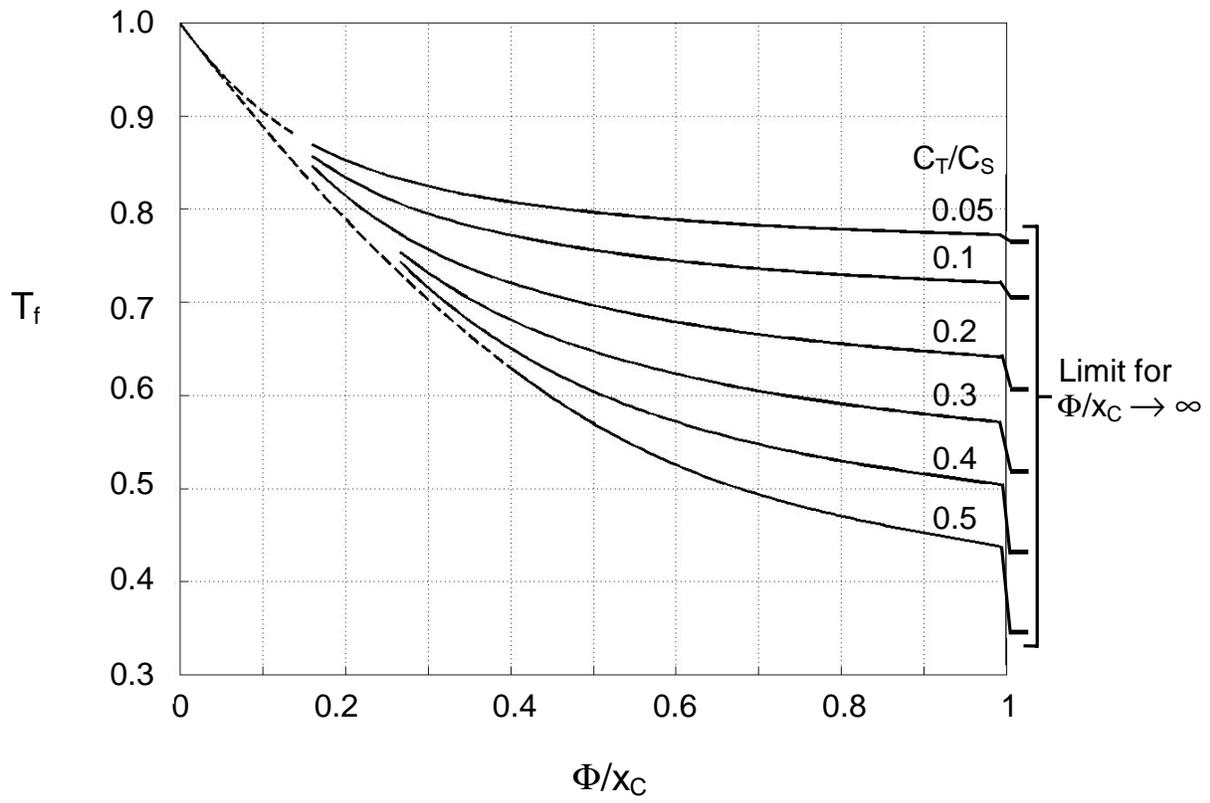
Figure 2. Nondimensional time derating factor T_f as function of Φ/x_C and with C_T/C_S as parameter. Limit values for T_f as $\Phi/x_C \to \infty$ are shown on the right.

APPENDIX 5 - Analysis of preferential chloride penetration along preexisting cracks.

This Appendix is in the form of a self-standing paper, which will form the basis of an independent submission to the technical literature.

Title: The influence of cover cracks on the initiation of corrosion of reinforcing steel in concrete

Authors: S.C. Kranc[+] and Alberto A. Sagüés[+]

ABSTRACT

The time interval between the construction of a reinforced concrete structural element and the first development of steel corrosion is usually quite long because the aggressive agents such as chloride ions that initiate corrosion must travel through the concrete cover to the depth of the rebar by slow transport mechanisms. Circumstances may be radically different however, if early cracks develop in the concrete covering the reinforcing steel, since more direct channels to the steel are opened. Such cracks occur as the result of mechanical stresses during the curing process, or structural loads.

The purpose of this paper is to examine the consequences of crack development on the transport of chloride ions to the reinforcing steel. Cracks in the concrete have been treated in an idealized fashion, in order to construct a simple model amenable to numerical solution. Questions concerning rapid initiation of corrosion due to the cracks, the consequences of repair, and the physical manifestations of cracks in field extracted core samples have been addressed. Computational results indicate that corrosion may begin very quickly on steel in the vicinity of the crack, due to the accelerated transport of chloride ions.

INTRODUCTION

In sound concrete, uncontaminated by chloride ions (above acceptable background levels), rebar is normally protected from corrosion by the high pH environment of the pore water. Structural elements in marine service experience chloride ion penetration through the porous concrete via relatively slow transport mechanisms such as diffusion in the pore water. Usually, the external surface of concrete in such service is highly saturated, at least near the water level. Wetting of the concrete surface need not be the result of total immersion but may also occur as a result of the humid environment or incidental wetting in the splash/tidal region. After a period of time, breakdown of the passive layer at the steel surface takes place when the concentration of chloride ions in the pore water adjacent to the steel exceeds a critical ratio with the concentration of the hydroxide ion. This event marks the end of the initiation phase of the total service life of the structure and begins the propagation

phase, characterized by active corrosion at some location. It is generally accepted that corrosion begins when the concentration of chloride ions in the concrete adjacent to the rebar reaches a critical ratio with respect to the concentration of OH^- [1]. The value of this ratio has been variously reported to be about 0.7 in concrete (depending on porosity), but may depend on several other factors, including the composition of the concrete and local electrical potential. The issue of critical concentration of chloride ions is further complicated by chloride binding of chloride ions in the concrete, in that the critical concentration is determined by the presence of free chloride ions in the pore water only, and not the total concentration.

The slow transport of chlorides in sound concrete during the initiation phase has been the subject of extensive investigation[2-5]. Relatively little attention has been given to the role of cracks in the concrete as a contributing factor for chloride penetration into the concrete, however. Here, early cracks that appear as the result of curing, loading or other factors are of principal interest. Later in the life of the structure, the corrosion process may itself cause cracking as the products of the reaction swell at the concrete-steel interface. This type of cracking is not of interest in the present discussion, but has been discussed elsewhere [6].

The purpose of this paper is to examine the importance of enhanced transport of chloride ions through early cracks in structural elements fabricated with steel reinforced concrete. If a crack occurs in new concrete, water (necessary for diffusive transport) can penetrate deep into the cover by partially bridging or completely filling the crack opening. Chloride ions can travel from the surface of the concrete (presumably a point of high chloride concentration) to the rebar via this pathway. Simultaneously, however, some ions present in the crack water move laterally through the sides of the crack into the adjacent concrete pore water, slowing the rate of chloride ion concentration increase at the depth of the rebar into the concrete. Here the possibility of convective transport via water flow into the crack is ignored and it is (conservatively) assumed that initially fresh water fills the crack.

Questions arising from this set of circumstances are concerned with the influence of crack size and concrete parameters on the rate of transport of chloride ions into the concrete. If a sufficiently high concentration of chloride ions develops locally around a crack , premature depassivation of any rebar in the vicinity of the crack may occur, resulting in corrosion that ultimately reduces the service life of the structural element. In this paper, a simple model for chloride transport in the region of an early crack is introduced. Ultimately, insights and information gathered from application of this model can be used to estimate the reduction in length of the initiation phase of the service life of steel reinforced concrete structures brought about by early cracks. Furthermore this type of modeling can help interpret field sampling of existing structures for prediction of remaining lifetime.

It should be noted that the simple picture of chloride ion transport in the crack presented here ignores several complex collateral issues. Among these are enhanced

transport promoting carbonation of the concrete around the crack and once depassivation has occurred, for oxygen and ferric/ferrous ions. At this point, the actual corrosion state must be computed with a different model [7] (and may be further influenced by rebar coatings, if applied).

DIFFUSIVE TRANSPORT IN SOUND CONCRETE

A simple diffusional model to describe the transport of chloride through uncracked regions of concrete, as described by others will be adopted here. Transport is described in terms of an "effective" Fickian diffusion coefficient. While it is recognized that a number of more advanced models have been suggested for chloride transport in sound concrete [2], in the present discussion, only a relatively simple model is necessary to address the questions posed in the introduction to this paper.   Restricting transport of chloride ions through saturated concrete, for a liquid in the pores a one dimensional flux analogous to that in free water can be defined

$$j_x = -D\frac{\partial C_f}{\partial x} \tag{1}$$

The diffusion coefficient D is understood to be similar to that of free water but modified by tortuosity and constriction [8]. Here the lower case subscript f designates concentration in the volume of pore water rather than a material volume of porous concrete.   To convert the concentration of free chlorides to a material basis (upper case subscript) requires division by the porosity since this ratio is equivalent to the open area/material area.   Assuming porosity constant in space and time,

$$C_f = \frac{C_F}{\varepsilon} \tag{2}$$

The rate of change of total chlorides in a unit material volume per time is given by the flux of free chlorides, but transport is permitted only through the open pores. Then, based on the surface area of the material,

$$\frac{\partial C_T}{\partial t} = \nabla \bullet (\varepsilon \, j_x) \tag{3}$$

Thus the porosity factor is removed by cancellation and

133

$$\frac{\partial C_T}{\partial t} = \nabla \bullet (D \nabla C_F) \tag{4}$$

Many types of concrete show some evidence of chloride binding capacity and this mechanism is included here for generality. The total concentration of chlorides can be expressed in terms of the bound and free concentrations (material volume basis) as

$$C_T = C_B + C_F \tag{5}$$

or, taking differentials

$$dC_T = dC_F \; (1 + \frac{\partial C_B}{\partial C_F}) \tag{6}$$

Substituting for the free chloride concentration, Equation 1 becomes (for the x direction)

$$j_x = \frac{-D}{1 + \frac{\partial C_B}{\partial C_F}} \frac{\partial C_T}{\partial x} \tag{7}$$

The time rate of change of total chloride concentration in a material volume is then equated to the flux of free chlorides into the volume, expressed in terms of the total concentration:

$$\frac{\partial C_T}{\partial t} = \nabla \bullet (\frac{D}{1 + \frac{\partial C_B}{\partial C_F}} \nabla C_T) \tag{8}$$

Boundary conditions are imposed at the concrete surface exposed to a saline solution. The pore water is assumed to be in equilibrium with the water at the surface in accord with Equation 2. At the other extreme, a semi-infinite condition can be imposed, or more conveniently for numerical work, an insulated condition deep in the concrete

can be used to represent a plane of symmetry for a slab of finite thickness.   At the sides of the computational region an insulated boundary condition is also imposed.

A simple model for binding [3] as a very rapid reaction has been adopted here, so that the bound and free chlorides are presumed to be in an equilibrium relationship which can be described by an idealized Langmuir isotherm (other relationships including simple linear binding have been proposed [2-5]).

$$\frac{1}{C_B} = \frac{1}{C_F kC} + \frac{1}{C}$$

(9)

At small values of the free chloride concentration C_F, $C_B \approx k\, C\, C_F$, and the behavior approaches linear binding with a coefficient $k_o = k\, C$. At large values of C_B, $C_B \approx C$ and the behavior resembles unbound chloride diffusion since the binding effect has reached saturation. The diffusive transport in situations with no binding mechanism can be handled as a limiting case ($C_F = C_T$) and the result is the familiar Fick's law

$$\frac{\partial C_F}{\partial t} = \nabla \bullet (D \nabla C_F)$$

(10)

If the binding can be described by a linear mechanism, the same equation is obtained but with a reduced diffusion coefficient.

MODELING OF CHLORIDE DIFFUSION IN A CRACK

A simplified crack geometry is envisioned as shown in Figure 1. The crack opens with constant width w, along a straight, normal line from the surface to a depth d. The width w of the crack is assumed to be very small in comparison to the depth. Furthermore, it is assumed that the crack extends vertically for a substantial distance along the concrete surface so that a two dimensional geometry in the horizontal plane can be assumed to describe the transport process and elevation is not a factor. This geometry could easily be extended to include cracks in more complex geometries, as near corners on structural elements. It is assumed that the crack is filled with water initially containing no chloride ions.   Chlorides flow from the surface by diffusion into the concrete and also into the crack, but at different rates. Convection of water into the crack is ignored. In the direction along the crack the time rate of change of chloride concentration is given by Fick's Second Law, with constant diffusivity in the crack water (variation in concentration across the crack is ignored). To this flux must be added the flux into the side walls, since at the interior walls of the crack, lateral transport into the concrete will also occur. The concentration of chlorides in the pore water immediately

adjacent to the crack is taken to be in equilibrium with the concentration in the crack water locally.

At the side wall of the crack the flux of free chloride ions can be expressed in the same manner as that through any other plane, evaluating flux at the boundary between the concrete and the crack. A mass balance for an elemental volume inside the crack then yields

$$\frac{\partial C_C}{\partial t} = D_0 \frac{\partial^2 C_C}{\partial y^2} + \frac{D}{1 + \dfrac{\partial C_B}{\partial C_F}} \frac{\partial C_T}{w \, \partial x}\bigg|_+ + \frac{D}{1 + \dfrac{\partial C_B}{\partial C_F}} \frac{\partial C_T}{w \, \partial x}\bigg|_- \tag{11}$$

where the symbols $\pm$ indicates evaluation of the flux from both sides of the crack (x coordinate). Here D_0 represents the diffusion of chloride in free water and w represents the crack width which appears as a result of the difference in area between the side wall and the width of the crack.

Equations 8 and 11 must be solved simultaneously. To solve the diffusion equation in the bulk of the concrete, a conventional forward time, central space difference scheme was utilized.   A two dimensional half slab with no flux along the sides as discussed above was assumed.   The problem was further divided by the line of symmetry along the crack. The equation governing the diffusion process in the crack (Equation 11) was first satisfied along the node points corresponding to the crack. This solution was then used as a boundary condition to replace the values for the equivalent node points during the numerical solution for the bulk of the concrete (Equation 8). In the case of chloride binding, the equilibrium value of the total chloride was substituted at these points, using an appropriate binding relationships.

Boundary conditions for Equation 11 on the concrete side of the interface (denoted by subscript 0) require that the concentration in the pore water equal that in the free water in the crack.

$$C_{f0} = C_C \tag{12}$$

along with

$$C_{f0} = \frac{C_{F0}}{\varepsilon} \tag{13}$$

and the binding relationships yield

$$\frac{1}{C_{B0}} = \frac{1}{\varepsilon C_C kC} + \frac{1}{C} \tag{14}$$

$$C_{T0} = C_{B0} + \varepsilon C_C \tag{15}$$

Initially, the concentration of chlorides in both the bulk of the concrete and water contained in the crack were taken as zero (in many problems of interest there may be some chloride background concentration). The boundary conditions at the surface of the concrete were taken as constant concentration, including possibly the effect of binding (this boundary condition could be modified to accommodate time dependent concentration or flux limited conditions). At the end of the crack, it was assumed that no transport takes place along the direction of the crack into the bulk, simulating a crack which tapers to zero width just at the end.

MODELING EXAMPLES

Five test cases (Table 1) were analyzed by means of the computational model developed above, on a solution domain consisting of a half slab of 20 cm width. Case A ("base case") is considered to be typical of cracks seen in the field, not due to underlying corrosion. A typical diffusion coefficient for a medium quality concrete was chosen for the concrete (a porosity of 0.1 was assumed), and the surface concentration typical of a splash evaporation zone was chosen. The remainder of the cases represent realistic variation of the parameters to provide comparative results.

137

Table 1: Crack parameters selected for cases analyzed. In all cases the slab had a half thickness of 20 cm, and the concentration in crack was initially 0. The concrete is assumed to be saturated.

Parameter	Case A	Case B	Case C	Case D	Case E
crack width (cm)	0.01	0.001	0.01	0.01	0.01
crack depth (cm)	15	15	5	15	15
D_{Cl} (cm^2/s)	4×10^{-9}	4×10^{-9}	4×10^{-9}	4×10^{-8}	4×10^{-9}
D_W(cm^2/s)	2×10^{-5}	2×10^{-5}	2×10^{-5}	2×10^{-5}	2×10^{-5}
C_S(kg/m^3)	200	200	200	200	200
C_C(kg/m^3)	0	0	0	0	5
kC_C	0	0	0	0	30
ρ	0.1	0.1	0.1	0.1	0.1

A contour map of the concentration of chloride ions for Case B is presented in Figure 2. The computational results illustrate the buildup of chloride ion concentration in the concrete adjacent to the crack at time t=4e7seconds. Concentration quickly builds up in the crack water, then diffuses into the concrete at the sides of the crack. This increase occurs rapidly in comparison to diffusion into sound concrete from the surface. The rate at which the chloride concentration builds in the crack gap is still slower than diffusion into unconfined media because of the competing effect of lateral transport into the concrete, as would be expected. It can also be seen that not much chloride penetrates beyond the end of the concrete until very late since the concentration builds up primarily by lateral transport.

The development of the profile of chloride concentration in the concrete adjacent to the crack for various crack depths at time t=4e7 sec is shown in Figure 3 (all conditions except depth are the same as Case A). Deeper cracks result in lower concentration of chlorides in the concrete. In Figure 4, the computational results for Case A may be compared to Case B (reduced width) and Case D (reduced diffusion coefficient in concrete). Case E involves binding assuming a Langmuir isotherms assuming a maximum concentration of bound chlorides C_C=5 kg/m^3, k C_C = 3 ('soft' binding case, representative of values often reported in the literature). Computational results for Case E are compared to those for Case A in Figure 5.

As would be expected, chloride concentration builds up less rapidly around narrow cracks than for large cracks. For the same quality concrete and the same width, deep cracks have lower rates of buildup, since there is more area for transverse transport. Lower rates of build up may also result when poor quality concrete is employed, since the lateral transport is more rapid. On the other hand, binding may delay the ingress of chloride so that the local concentration is higher near the crack, but the importance of this effect depends on choice of parameters.

In all cases examined, the crack served as a conduit for rapid transport of chloride ions into the concrete. If the crack extended to rebar depths then critical ratios for depassivation were observed to occur very rapidly on the time scale of the expected service life of the reinforced concrete. Furthermore, the crack itself may expose the rebar directly to aggressive chloride attack. While it might be argued that the simplified model presented here results in a pessimistically fast transport down the crack, further computations made by reducing the diffusion coefficient for the water in the crack by an order of magnitude to simulate partial bridging or the effects of tortuosity in the passage still resulted in concentrations of chloride ions substantially elevated over those found in sound concrete.

APPLICATION TO FIELD STUDIES

In field investigations of existing structures, cylindrical cores may be cut from the concrete at various locations. These samples are sliced normal to the coring direction, then the individual slices are crushed and analyzed for total chloride content, yielding a profile of the total chloride penetration into the concrete at the time of sampling. Because the analysis each slice actually represents an average over the volume, the resulting data cannot be directly fitted to physical models (such as Fickian diffusion, for example), but such fits can be accomplished by locally averaging the proposed model in the same manner as the specimen, then using a regression technique. When a core sample includes a crack, the situation is more complicated because the chloride contamination is not uniform across the sliced segments in the radial direction. As discussed previously, the concentration near the crack may be very high in comparison to values only a slight distance away from the crack, so that the severity of contamination may be underestimated if the slice averaged value is used uncritically. If averaged slices indicate chloride contamination exceeds the critical level for depassivation at the rebar depth, then levels may much exceed critical levels close to the crack. On the other hand, because it is not usually known whether or not binding mechanisms are important in the sample, relying on the total chloride content may overestimate the seriousness of chloride contamination, since depassivation really depends on the concentration of free chlorides in the pore water.

As part of an experimental investigation, a set of cores were obtained from the Sunshine Skyway Bridge in Tampa, Florida at eleven years after construction [9]. From this set, a group of four core pairs were selected, one cracked and one uncracked, both from the same elevation on the same pier. Cracked cores with obvious efflorescence were rejected. Crack widths in samples selected were estimated to be less than .03 cm. The uncracked core pair specimens were analyzed and fit by a least square error criterion to a simple Fickian model as described above to obtain an estimate of surface and background concentrations, as well as an apparent diffusion coefficient.

139

Table 2. Core pair samples at 11 years from the Sunshine Skyway Bridge (S indicates sound concrete, C indicates cracked) add analysis results

CORE	PIER	Elevation above high tide (m)
2 (S)	155	5.5
3 (C)	155	5.5
8 (S)	126-1	18.3
9 (C)	126-1	18.3
9A(C)	106-1	0.9
10(S)	106-1	0.9
14(C)	116-1	0.9
15(S)	116-1	0.9

Chloride concentration data obtained from these core pairs by dry slicing is presented in Figures 6a-d. For the core pairs taken from lower elevations, the chloride concentration with depth for cracked specimens is noticeably higher than that for the uncracked specimens.   However, the core pair profiles obtained from higher elevations were not much different. At higher elevations, it seems probable that the crack is incompletely filled with water so that transport in the crack does not substantially contribute chloride penetration. At lower elevations the penetration of the chloride deep into the concrete near the crack is evident, and it is likely that a critical concentration has already been developed at rebar depth.

Although nothing specific is known regarding the depth of the crack in any of the specimens and the width (<.03 cm) is only an estimate, it is still possible to attempt a comparison with the crack model under development. The model developed above can be utilized to interpret core samples taken from cracked areas. For comparative purposes, the results of model computations for the chloride concentration in the vicinity of a crack can be utilized in the following manner. As a result of the two dimensional analysis, at each depth a single profile, F(x), is available across the crack. The total chloride content of a disk can be computed by numerically integrating this profile over the circular area. Thus

$$C_{core}(depth) \bullet AREA = \int_{0}^{R} \int_{0}^{\sqrt{R^2-y^2}} F(x)\,dx\,dy \qquad (16)$$

This integral may be evaluated by using a cubic spline for interpolation of F(x). The results are the concentration as a function of depth. Since actual experiments usually involve core averages, this data must be averaged over equivalent slices for comparison to actual specimens. Computational modeling was attempted for Cores 10 and 15 taken from the splash zone. These specimens were assumed to be cracked to

a depth of 10 cm, have no binding, a porosity of 0.1, and have the same age (11 years=3.5x10^{8}sec) and underlying properties as the uncracked specimens taken from the same region, as follows.

Core10 (43.55, .391,.0062)
Cs=25.86 kg/m^3)
C0=0.232 kg/m^3
D=1.2684e-9 cm^2/s

Core 15 (39.94, .706,.0092)
Cs=23.72 kg/m^3
C0=0.41924 kg/m^3
D=1.8821e-9 cm^2/s

These two sets of parameters were averaged to provide an estimate of parameters appropriate to the region from which Core #9 was extracted. As in the previous discussion, the model geometry was assumed to be a slab with a half thickness of 20 cm. Two crack widths were assumed, 0.01 cm and 0.001 cm and a crack depth of 10 cm. The concentration of chloride in the crack water was initially zero. Analysis of chloride concentration was accomplished by the integration of very thin slice data over the core area, using a diameter of 5.08 cm.   This data was reintegrated in the coring direction to yield slice data comparable with that taken for the cracked samples.

The results of the modeling computations are shown in Figure 7 superposed on the slice analyzed data from a field specimen. For comparison, the profile of chloride concentration in the concrete directly adjacent to the crack has been added.   Due to uncertainties in the parameters (particularly the crack dimensions) only qualitative observations can be made. It is apparent that the measured profile falls between the two computed results for much of the distance into the concrete and that the general features of integrated profiles resemble the results for the extracted core. Regarding the apparent background concentration of chlorides in cracked specimens, it is apparent that if the slice averaged data is at or near critical concentration, then the local value in the vicinity of the crack would be expected to be much larger, so that corrosion may already be ongoing.

These observations have been further substantiated by a qualitative comparison of chloride concentration in the vicinity of a crack from an extracted core as shown in Figure 8. Here the core was dissected not only by slicing with depth but these slices were also cut to resolve a lateral profile (Core extracted from Sunshine Skyway bridge). A similar representation can be obtained by plotting the results of modeling computations (Figure 7, width 0.01 cm).

CONCLUSIONS

Early cracks in steel reinforced concrete structural elements can lead to rapid development of chloride ion concentration in the concrete surrounding the crack. If the crack extends to the depth of rebar or beyond, a critical concentration of chloride for depassivation of the steel may occur much earlier than for sound concrete. The rate of chloride increase along the crack wall is governed in part by the geometry of the crack and also by the characteristics of the concrete. Narrow cracks provide less of a pathway for chlorides while deep cracks provide increased wall area for lateral transport into the adjacent concrete.   Low quality, porous concrete permits rapid lateral transport, but concrete that develops substantial binding slows the lateral transport. There is little advance beyond the end of the crack.

Evidence from field sampling regarding chloride transport in the vicinity of cracked concrete indicates that this effect is much stronger close to water level, probably due to the amount of water held in the crack.

Efforts to compare actual penetration profiles to model results were qualitative at best, but tended to support the general trends observed, suggesting that the model is consistent with observations.

ACKNOWLEDGMENTS

REFERENCES

1. Li, L. and Sagüés, A.A., Corrosion, 2001, **57**, (1), 19-28
2. A. V. Saetta, R. V. Scotta, and R. V. Vitaliani, *ACI Materials Journal*, 1993, **90** (5), 441.
3. C. J. Pereira and L. L. Hegedus, Eighth International Symposium on Chemical Reaction Engineering, Institution of Chemical Engineers Symposium Series No. 87, 1984, 427.
4. P. S. Mangat and K. Gurusamy, *Cement and Concrete Research*, 1987, **17** (4), 640.
5. L. O. Nilsson, M. Massat and L. Tang, SP 145-24., American Concrete Institute, Detroit, 1994, 469.
6. Torres-Acosta A.A., Sagüés A.A., "Concrete Cover Cracking with Localized Corrosion of Reinforcing Steel", In Proc. of the Fifth CANMET/ACI Int. Conf. On Durability of Concrete, ACI SP 192, 1997: 363-378

7. Kranc S.C., Sagüés A.A., "Computation of Corrosion Distribution of Reinforcing Steel in Cracked Concrete" US Department of Transportation, Federal Highway Administration, CD-ROM Publication No. FHWA-SA-99-014, Washington, DC, 1998.
8. A. Atkinson and A. K. Nickerson, *Journal of Materials Science*,1984, **19**, 3068.
9. "Corrosion Forecasting for 75-Year Durability Design of Reinforced Concrete", State Job 99700-3515-020, WPI 0510805, Final Report to Florida Department of Transportation, A. Sagüés and S.C. Kranc, P.I.'s, December, 2001.

$$\frac{\partial C}{\partial n} = 0$$

$$\frac{\partial C}{\partial n} = 0 \qquad \frac{\partial C}{\partial t} + D\nabla^2 C = 0 \qquad \frac{\partial C}{\partial n} = 0$$

d

CRACK

C=CONSTANT

W

CORE

R
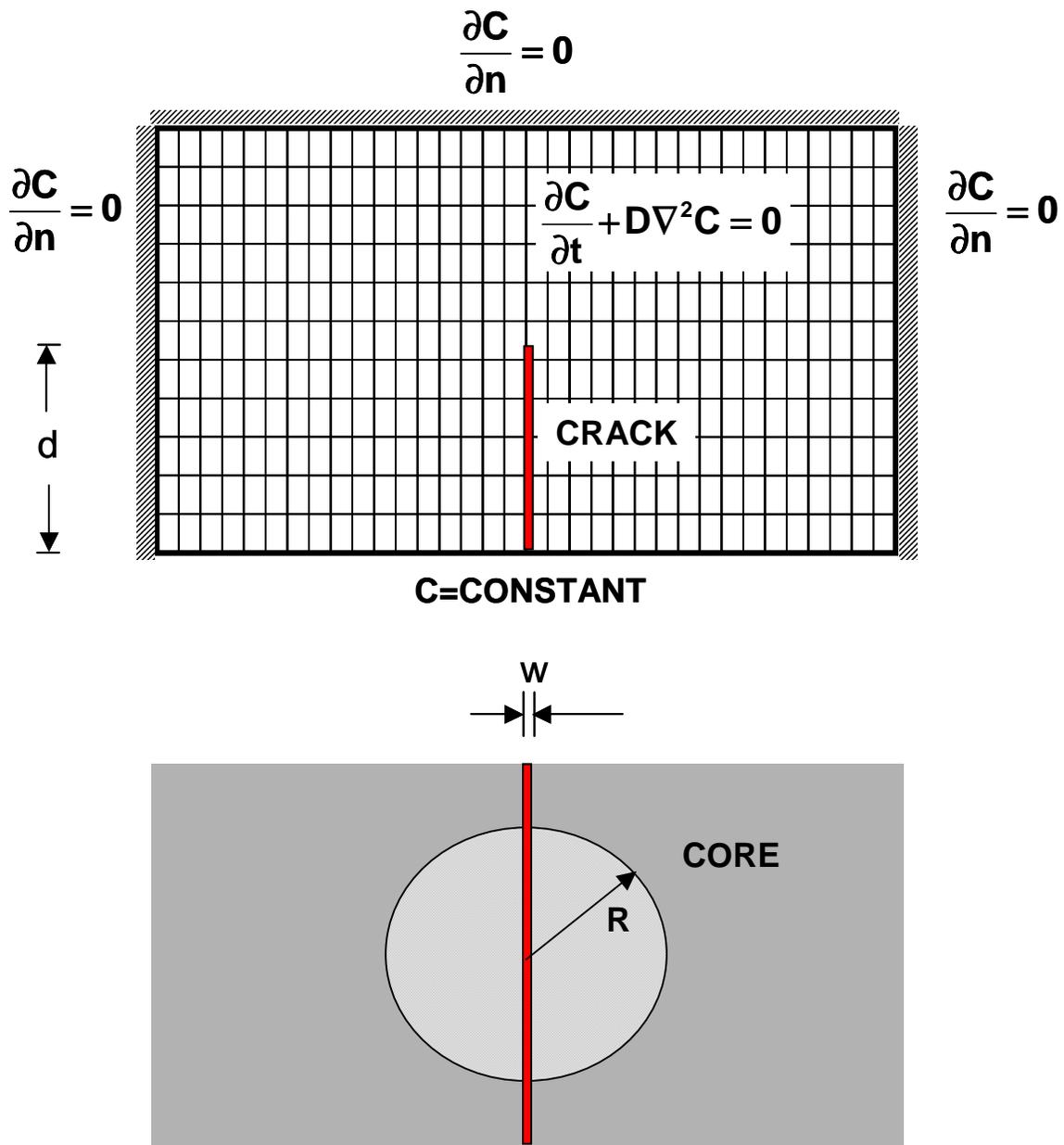
 Figure 1: Crack geometry: a) plan view of computational domain, b) frontal view of crack showing core extraction centered on crack
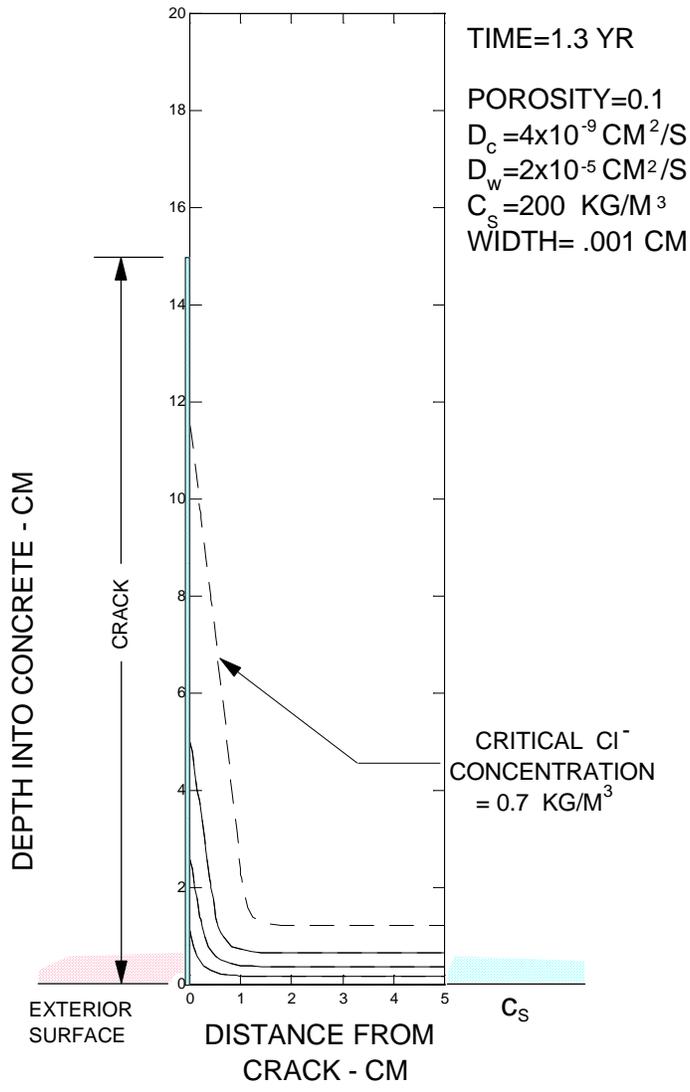
Figure 2. Concentration isocontours in the vicinity of the crack (for domain shown in Figure 1a). Conditions and time. Note critical concentration isocontour. Case C (Table 1) illustrated. Contours spaced at intervals of 5 kg/m^3.

145
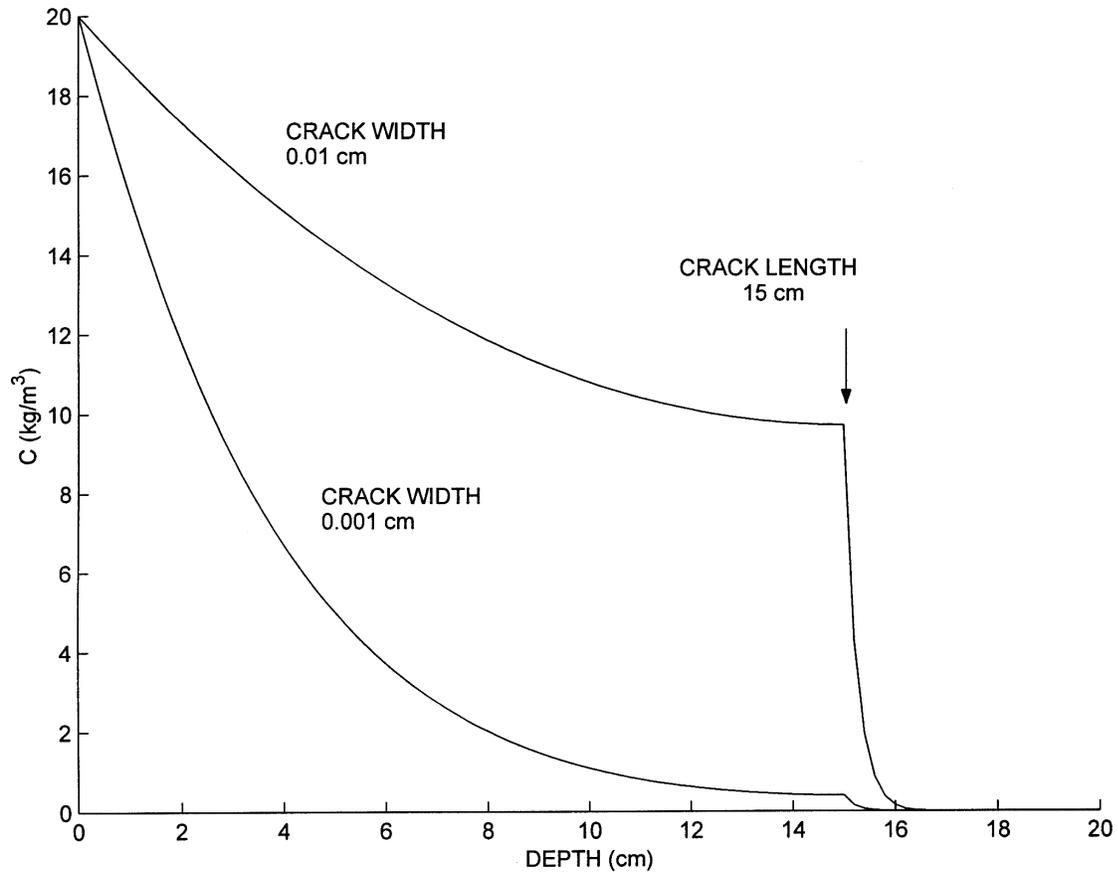
Figure 3: Profiles of concentration in concrete along the side of crack showing effect of diffusion coefficient in concrete and width of crack (cf. Table 1).
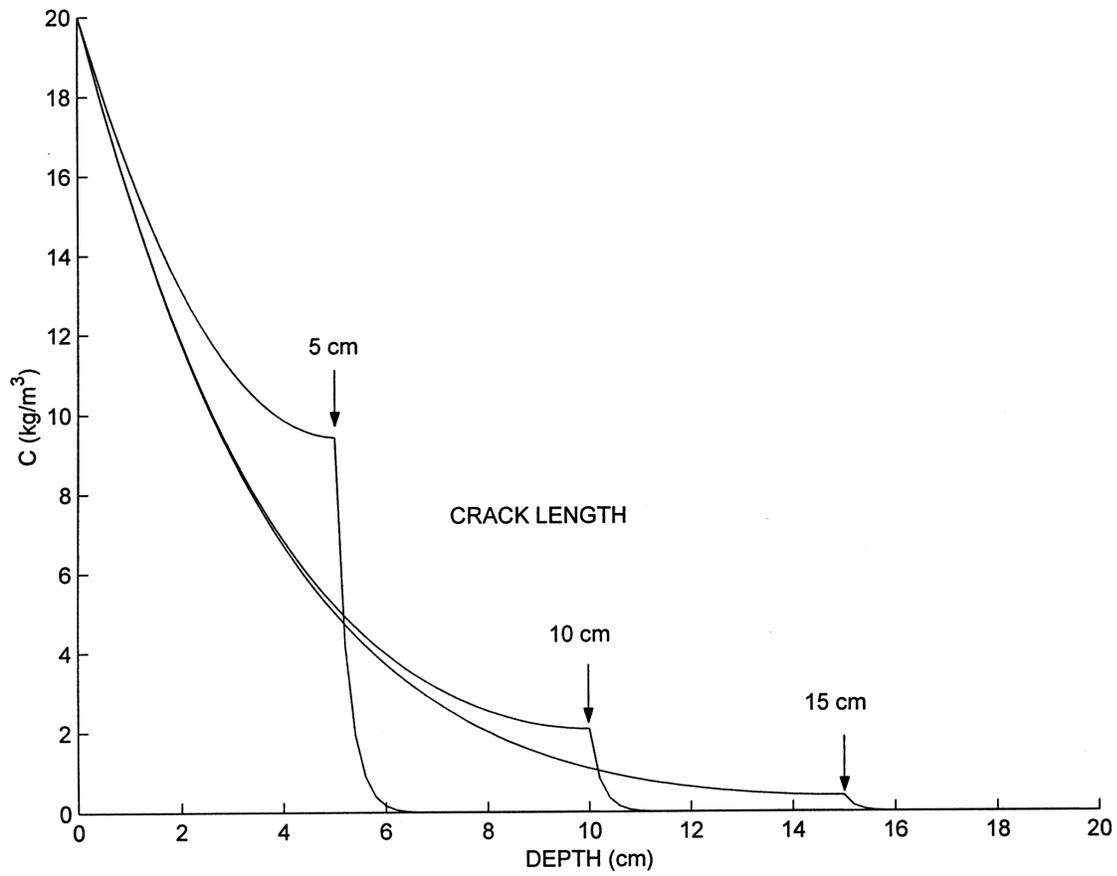
Figure 4: Profiles of concentration in concrete along the side of crack showing effect of diffusion coefficient depth of crack.
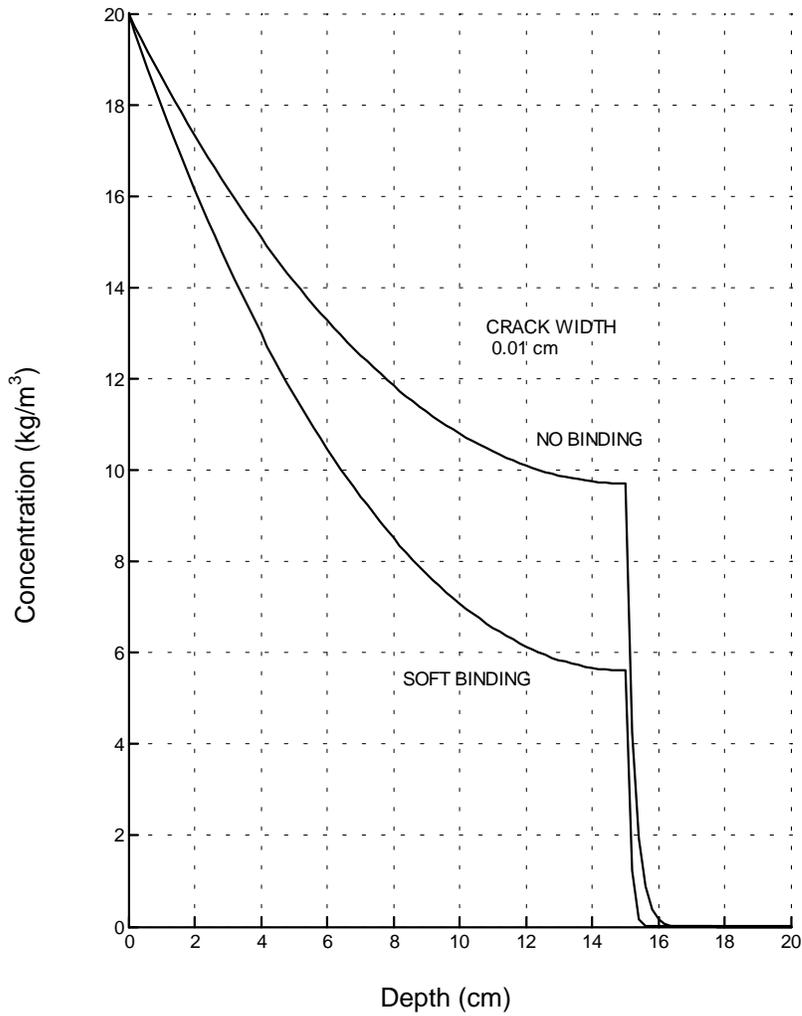
Figure 5: Profiles of concentration in concrete along the side of crack showing effect of soft binding (Case D, Table 1).
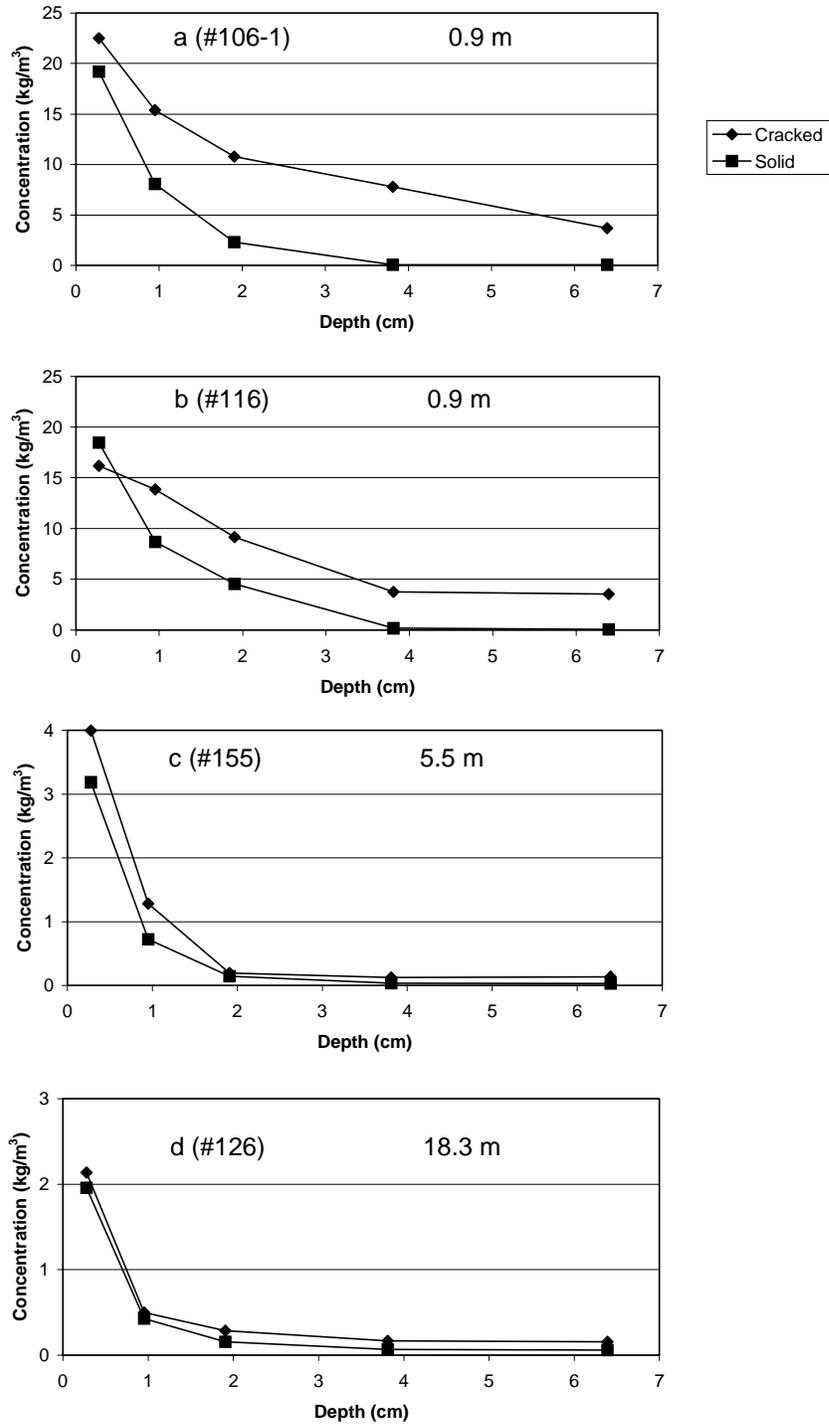
Figure 6a-d: Four core pairs from field, illustrating the importance of cracks at lower elevations, compared to relatively modest chloride penetration at higher elevations. Pier # and elevation above high tide as indicated [9]
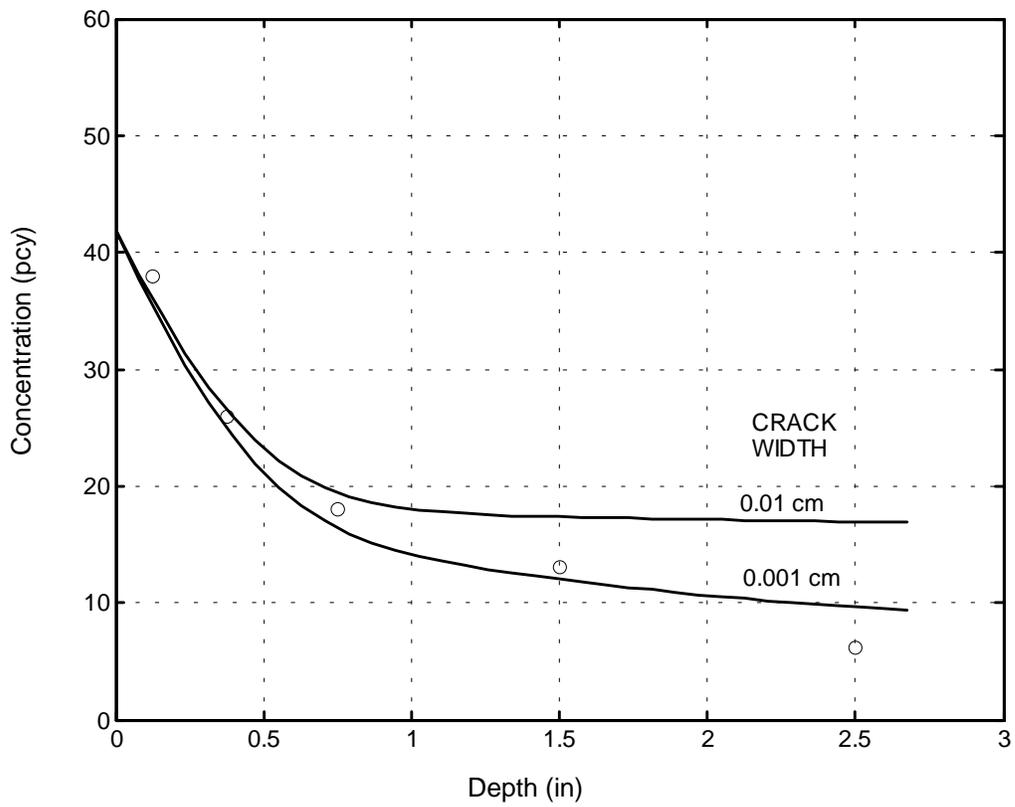
Figure 7: Comparison of field core data to slice analysis. Data samples from extracted Core #9 compared to integrated model profiles for average parameters (cf text), crack widths of 0.01 and 0.001 cm, crack depth 10 cm.
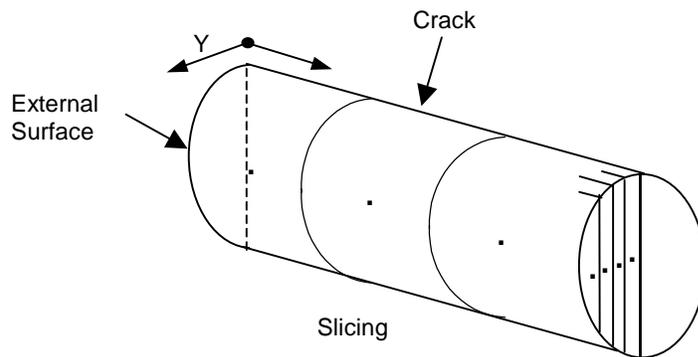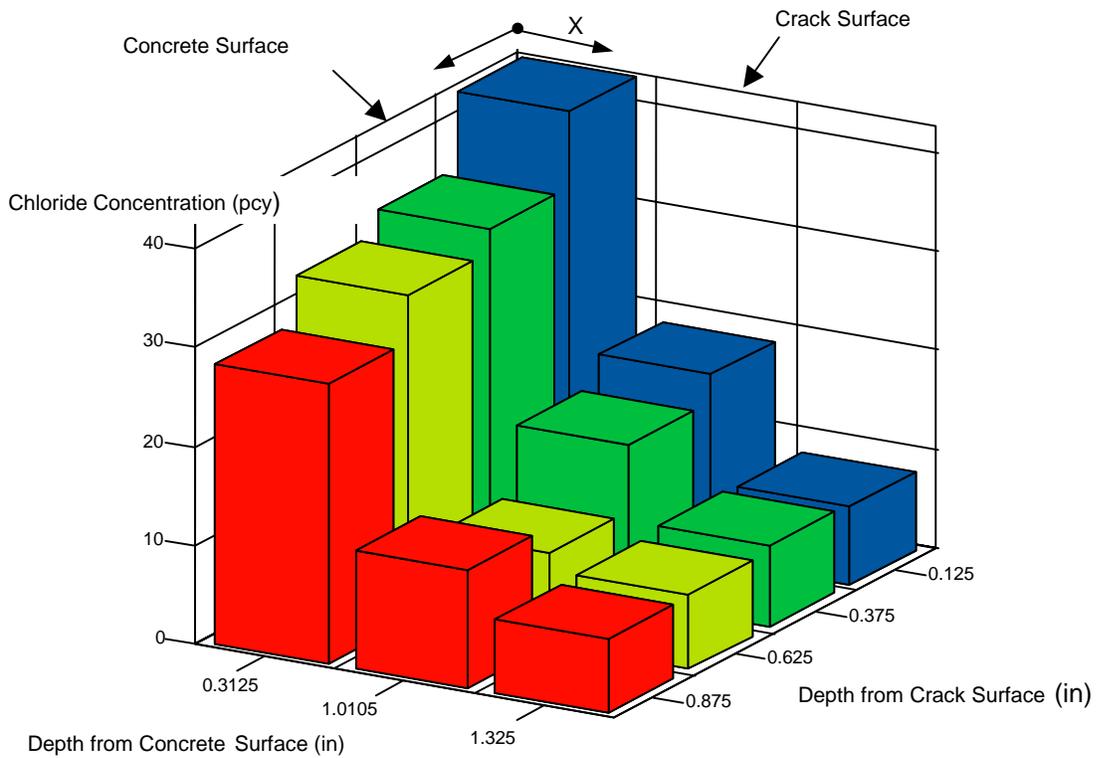
Figure 8. Two-dimensional chloride analysis of core No.543 (3 ft elevation above high tide) [9] showing preferential transport along the crack and lateral diffusion into the concrete on the side of the crack.

APPENDIX 6 - Computation of corrosion distribution of reinforcing steel in cracked concrete

This Appendix is presented as a self-standing paper. A version of this Appendix was published as a paper in ICCRRCS'1998, US Department of Transportation, Federal Highway Administration, CD-ROM Publication No. FHWA-SA-99-014, Washington, DC, 1998.

Title: Computation of corrosion distribution of reinforcing steel in
                cracked concrete

Authors: S.C. Kranc and A.A. Sagüés

ABSTRACT

Cracks in concrete may cause early localized chloride ingress and the initiation of rebar corrosion. Local corrosion can be aggravated by macrocell coupling with nearby rebar in sound concrete. Computations based on a detailed finite difference model incorporating polarization characteristics of the steel and oxygen transport through the concrete have been utilized to assess the extent of corrosion possible in cracked concrete. Butler-Volmer kinetics are assumed to describe the polarization at the steel concrete interface. This investigation presents both qualitative and quantitative information concerning the distribution of corrosion in typical reinforced concrete arrangements, as a function of system parameters that include concrete resistivity, concrete cover, crack dimensions, and steel condition. The model predicts local corrosion rates at every point of the steel assembly. Applications of the modeling results to field studies to aid in the prediction of durability are discussed.

Keywords: Corrosion computation, concrete, crack, modeling, macrocell.

INTRODUCTION

Cracks that develop early in the life of a reinforced concrete structural element can facilitate the development of active corrosion [1,2,3]. The scope of this discussion will be limited to the case of structural cracks perpendicular to the reinforcing steel bars, likely to promote highly localized corrosion. Cracks that develop later in the life of the structure caused by the products of corrosion are also of interest but will not be treated here.

In marine service, the presence of a critical concentration of chloride ions is necessary for depassivation of the steel reinforcing to occur. Early cracks in vertical pilings or columns located in the region of the splash zone are of particular concern because the surface concentration of chloride ions is high and the crack may open a direct path to the rebar. The transport of oxygen may also be enhanced. Actual transport of both chloride ions and oxygen in the crack is complicated by the fact that the crack may not be filled with water but rather involve a partially filled, bridged system,

capable of quickly transporting both chlorides (in the liquid phase) and oxygen (gas phase).

The following sequence of events is envisioned: A short time after the crack appears, the space inside is at least partially filled with water.   Even if this water is not initially saline, it soon becomes so due to marine exposure. As the chloride concentration at the steel surface reaches a critical concentration, depassivation occurs and a period of active corrosion begins at a small region where the crack meets the steel. A new distribution of electrical potential, current flow, and oxygen concentration evolves inside the concrete to support this localized active corrosion, and results in the formation of a corrosion macrocell. If the concrete is oxygen rich initially, a relatively high rate of corrosion is possible, and some time elapses before a steady state is reached with regard to potential and oxygen concentration. That steady state also will reflect the enhanced transport of oxygen to the corroding region on the steel rebar. During the ensuing period of corrosion propagation, the steel is weakened by loss of section, but the region of active corrosion may not grow substantially into the surrounding steel since some degree of local cathodic prevention may occur.   The concrete cover may develop additional cracking later, as the products of corrosion swell at the steel-concrete interface.

Corrosion localization poses an important question as to which deterioration process may first limit the service life of a structure.   Active corrosion in an uncracked structural element can be relatively uniform and corrosion-induced concrete cracks and spalls are the expected form of early structural deterioration. It is of considerable interest to know whether, in the case of preexisting cracks, localized corrosion could instead cause early damage by local acute loss of rebar cross section and consequent mechanical failure. This can be achieved by examination of the factors responsible for localized corrosion under these circumstances.

The purpose of this paper is to present a computational model for the corrosion macrocell that develops as a result of local activation after chloride intrusion through a crack in the concrete cover. Semiquantitative comparisons are made between the results of this investigation and existing experimental results [1]. The effort is restricted to computing the distribution of corrosion. The effect of the crack on chloride intrusion and the later development of corrosion-induced damage will be addressed elsewhere.

MODEL DEVELOPMENT

To formulate a computational model, the following scenario is adopted. The concrete is initially cast crack free and with a negligible concentration of chloride ions. The reinforcing steel is in a uniform, passive state, with a small anodic current balanced by consumption of oxygen at the steel. The oxygen concentration throughout the concrete is nearly equal to the concentration at the surface, since little consumption actually occurs. The concrete is then placed in marine service and chloride ions begin a slow transport from the outer surface of the concrete. Early in the life of the component structural cracks form and extend to the rebar depth. After a relatively short time the

chloride concentration increases to critical levels near the crack-rebar intersection and active corrosion soon begins there. The present discussion, is limited to the period of time after local corrosion initiation has occurred.

The computation of corrosion propagation for reinforced concrete with known areas of depassivation has been discussed elsewhere [4-6]. Briefly, in the concrete, the governing equations for the diffusion of oxygen and the electrical potential in the concrete are

$$\nabla D(\nabla C) = 0 \qquad (1)$$

$$\nabla \sigma(\nabla E) = 0 \qquad (2)$$

where D and C are the oxygen diffusivity and concentration, respectively, and σ and E are the electric conductivity of the concrete and E the electric potential.

At the reinforcing steel-concrete interface, boundary conditions are dictated by ongoing electrochemical reactions. Butler-Volmer [4-6] kinetics are assumed for oxygen reduction in the passive region and in the active region both anodic and cathodic reactions are presumed to occur.   The assumed anodic reaction is iron dissolution to ferrous ions. Reverse reactions are neglected, as is the evolution of hydrogen. The metal dissolution and oxygen consumption reactions produce currents at the concrete-rebar interface that can be described by:

$$i_a = i_{0a}\, e^{(E_{0a}-E)/\beta_a} \qquad (3)$$

$$i_c = i_{0c}\, \frac{C}{C_0}\, e^{(E-E_{0c})/\beta_c} \qquad (4)$$

for the cathodic and anodic reactions (denoted with subscripts c and a, respectively). These equations are formulated in terms of local current densities and are functions of the exchange current density, i_0, the Tafel slope, β, and the equilibrium potential E_0. E is the difference of potential between the electrolyte directly in contact with the metal and the metal (see note on sign convention in Table I). The metal itself is considered as an equipotential surface by virtue of its high electric conductivity.

Applying Ohm's law at the surface (with appropriate sign convention):

$$\frac{\partial E}{\partial n} = \frac{1}{\sigma}\sum i \qquad (5)$$

where n is the normal to the surface considered. Likewise, the equivalent current density due to the consumption of oxygen is given by Fick's first law by:

154

$$\frac{\partial C}{\partial n} = \frac{i_c}{4FD} \qquad\qquad (6)$$

The factor 4 appears as the number of electrons transferred in the oxygen reduction reaction (O_2 + $2H_2O$ +4e $\rightarrow$ $4OH^-$) and F is Faraday's constant.

To formulate a solution to the governing equations, conventional finite difference modeling has been applied. The boundary conditions at the steel-concrete interface are nonlinear and implicit, requiring an iterative solution at each computational step. The procedure is detailed in Reference [7].

The method outlined above has been applied to calculate the initial corrosion state of the concrete element (passive steel, uncracked concrete), as well as the final quasi-equilibrium state which results after some part of the bar becomes active and sufficient time has elapsed for the oxygen distribution profile to develop everywhere in the concrete. A similar procedure has been used to model the evolution of the potential and concentration of oxygen with time. In this case, the equation for the oxygen profile was written to include time-dependent terms and solved by a forward difference scheme in time.

RESULTS

For the purpose of the present discussion, a small laboratory-scale prismatic specimen similar to that used by Raupach [1] was chosen for modeling.

The modeled configuration is shown in Figure 1. The test rebar was simulated in the calculations as having a square cross section, 1.2 cm (0.47 in) on a side, and running continuously for the entire length of the specimen. Cover dimension was 1.5 cm (0.59 in). The model dimensions were 15 cm (5.91 in) wide by 69.6-cm (27.4 in) long by 9.6 cm (3.78 in) thick with a small active region 1.8 cm (0.71 in) long, assumed here to extend circumferentially around the rebar. The computations were performed under the assumption of insulation to the flow of oxygen on all sides except the top. The parameter values used in calculations are given in Table 1. The values of the electrochemical parameters are representative of conditions experienced during corrosion of steel in concrete [6]. The concrete properties [8] were chosen to represent a "dry" condition with high effective oxygen diffusivity and high concrete resistivity, $\rho=\sigma^{-1}$, (Condition 1, D=10^{-3} cm^2/sec, $\rho=10^5$ Ω-cm), an intermediate condition (Condition 2, D=10^{-4} cm^2/sec, $\rho=10^4$ Ω-cm) and a "moist" condition with low oxygen diffusivity and low resistivity (Condition 3, D=10^{-5} cm^2/sec, $\rho=10^3$ Ω-cm). Note: 2×10^{-7} cm^2/sec = 1 in^2/year.

Several cases have been modeled as outlined below. The prism was assumed to have been initially uncracked, in a steady state with all the steel surface in the passive

condition. Crack formation and chloride ingress were assumed to have taken place suddenly, causing immediate activation of the small central region.

Case A) The system (with intermediate concrete Condition 2) is in the state corresponding to the moment immediately after activation of the small anodic region. The concentration of oxygen in the bulk of the concrete is still that of the previous totally passive initial steady state. Thus, as corrosion begins, the concentration of oxygen is still relatively high everywhere. Oxygen transport resulting from the crack itself is ignored. The computed instantaneous corrosion current from the active region is 3.6×10^{-4} A, for a corrosion current density of 39 µA/cm^2 average on the active region surface.

TABLE 1: PARAMETERS USED IN COMPUTATIONS

CONCENTRATION OF O_2 AT WALL: 3×10^{-7} moles/cm^3

REACTION PARAMETERS	i_0 amp/cm^2	E_0 mV	β mV
IRON DISSOLUTION	1.0×10^{-13}	840	60
OXYGEN REDUCTION	1.0×10^{-8}	-260	120

Notes:

1. All potentials are in the Saturated Calomel Electrode scale, but referred to the metal. Thus, with this convention, the oxidation reaction rate increases as the potential becomes less positive. The sign convention is reflected in the equilibrium potential ranking shown in the table for the various reactions.

2. Reverse reactions (iron reduction, etc.) are considered negligible at the potentials of interest.

3. The effective concentration of O_2 is expressed in moles of O_2 per cm^3 of pore water in the concrete. The values of D selected for computation reflect that choice of concentration units. Other units for the concentration of O_2 (for example, moles per cm^3 of concrete) can be used by appropriately adjusting the value of the effective diffusion coefficient.

Case B) This case models the time-dependent response of the system (also for concrete Condition 2), beginning from the state described in (A), whereby the oxygen concentration and potential relax toward a new terminal steady state. The oxygen transport along the crack is again ignored. The corrosion current decreases and approaches a terminal value as shown in Figure 2 over a period of a few hours, which is on the order of the characteristic time t = (1.5cm)^2/D $\approx 2 \times 10^4$ sec for diffusion of oxygen through the concrete cover. Residual relaxation of the oxygen concentration continues to occur over a much longer time frame as the oxygen concentration profile

far from the corroding spot settles into the terminal configuration. Comparable reductions of corrosion intensity with time have been reported in experimental studies [1].

Cases C1, C2, and C3) Case C2 corresponds to the terminal state resulting from the process described in Case B, also ignoring transport of oxygen from the crack. The corresponding cases for concrete Conditions 1 and 3 were computed in Cases C1 and C3, respectively. The corrosion currents from the active region in cases C1, C2, and C3 are shown in Figure 3 as a function of concrete resistivity and diffusivity. The corrosion current varies only slightly as the concrete condition changes from "moist" to "dry." The calculations assumed constant size of the active region and constant polarization parameters. Under those conditions, corrosion severity would be expected to decrease when electrolytic coupling of the anodic (active) and cathodic (passive) rebar regions become poorer as a result of increasing concrete resistivity. Conversely, corrosion severity would increase as oxygen availability became better in dryer concrete. The overall trend indicates that the effect of decreased coupling was approximately balanced by that of increasing oxygen diffusivity.

A macrocell current density $i_m = i_a - i_c$ along the rebar can be defined as the difference between the local anodic and passive current densities. Figure 4 shows i_m as a function of distance along the rebar for Cases C1-C3.   Integrating the macrocell current density over the surface of a given rebar segment gives the macrocell current for that segment. Figure 5 shows the ratio of the macrocell current of the active steel segment to the corrosion current of the same segment for Cases C1-C3. While the corrosion current is nearly the same in all three cases, the macrocell curent ranges from being nearly equal to the corrosion current ("moist" condition) to about 1/10 of it ("dry" condition). This decrease of macrocell effect is also observable in Figure 4, which reveals as well the shorter throwing power of the galvanic couple as the concrete resistivity increases [9].

Cases D1, D2, and D3) The computations described in C1-C3 were repeated, assuming this time that the crack dramatically enhances the transport of oxygen, keeping the concentration in the crack plane always equal to that of the outside concrete surface.   The computed corrosion currents of the active zone are shown in Figure 3, showing an increase over Cases C1-C3 due to oxygen enrichment in the region surrounding the corroding spot. The increase was less pronounced for the "drier" concrete conditions since oxygen availability in those cases (by bulk diffusion of oxygen) was already good. Figure 5 shows that the ratio of macrocell to corrosion current was not significantly altered by the assumption of enhanced oxygen transport at the crack. It should be noted, however, that many potentially important processes not considered in the computations may progress in the crack itself, for example transport of corrosion products away from the active region.

The dimensions of the system were chosen to permit semiquantitative comparison of the computed behavior with experimental results reported by Raupach [1]. That investigator used a concrete specimen 70 cm (27.6 in) long that was subjected to three point loading to induce cracking. The specimen was 10 cm (3.94 in) thick and 15 cm (5.91 in) wide with rebar cover a parameter of the experiment. All of the outer surfaces of the concrete were insulated from the transport of oxygen and moisture except the top. A segmented, 1.4-cm (0.55 in) diameter rebar was located at the top and a corresponding continuous rebar was located at the bottom. The crack extended to a 2-cm (0.79 in) section of bar which was then depassivated by wetting with a chloride salt solution. The rest of the rebar on either side consisted of separated but interconnected segments 7.5 cm (2.95 in) long. After an interval of time, the macrocell strength was determined by measuring the net electronic current from each sector of the rebar. The macrocell current distributions reported in Figure 4 and also those for the D series of computations were integrated over portions of the bar length to approximately match the experimental segment arrangement. Comparison of the computed and experimental macrocell currents is shown in Table 2.

As seen in Table 2, reasonable agreement was obtained between the experimental values and the computations for conditions near the center of the ranges assumed. This agreement is not an absolute model validation since the choice of other important parameters such as the polarization constants has not been tested. Nevertheless, the comparison shows that the model reproduces the main macrocell current distribution trend and that it may be a useful tool to examine the comparative effect of system variables.

The calculations with and without enhanced oxygen availability ("C" vs "D" cases) at the crack showed that oxygen transport through the crack itself may aggravate corrosion, but to a limited extent. This finding suggests that attempts at remediation by crack impregnation are not likely to dramatically reduce the corrosion rate by limiting oxygen access (crack impregnation may nevertheless hinder future chloride ingress and have a positive effect if corrosion has not yet started). The effect of oxygen transport when the active zone is larger should be nevertheless investigated in more detail since under those conditions bulk oxygen transport may be less important.

TABLE 2. COMPARISON OF COMPUTED AND EXPERIMENTAL[*] MACROCELL CURRENTS

Segment** (start -end distance from bar center)	Experi-mental*** (μA)	Computed (μA)					
		C1	C2	C3	D1	D2	D3
Central	200	34	206	237	34	208	451
3-10.5 cm	45	11	54	40	11	56	80
11.5-19 cm	30	3.4	27	39	3.4	27	74
20-27.5 cm	20	2.3	17	38	2.3	21	71

*From Ref. [1], concrete with 300 kg/m^3 (508 pcy) OPC, w/c=0.6, stored at 20°C, 80% R.H., age 29 days.
** Central segment was $\approx$ 2cm (0.79 in) wide.
***Average of segments to left and right of center.

The most important effects of the crack presence early in the life of the structure appear to be the development of localized corrosion, and its enhancement by macrocell coupling. The calculations and the previous experimental evidence indicate that corrosion localization in the cm range at the crack-rebar intersection may lead to significantly high corrosion rates. Faradaic conversion of the active segment currents into metal loss shows that, if the corrosion rates remained at the levels corresponding to cases C2 or D2, the active rebar segment would lose much of its cross section in a few years.   Under those conditions, early cracking could raise the possibility of failure by mechanical overload in a relatively short time. The potential for similar occurrences with combinations of concrete properties and cover dimensions representative of marine bridge substructure conditions is being examined by application of the model to ongoing investigations.

CONCLUSIONS

A computational model has been formulated to assess the strength of the macrocell associated with steel corrosion near cracks in reinforced concrete. Initially the corrosion

rate is relatively high due to oxygen levels in the concrete. In time the corrosion process achieves a relatively steady state condition.

Semiquantitative comparison was made to existing experimental data. Although the model configuration was not identical to the experimental specimen and some physical parameters were estimated, the experimental corrosion strength and macrocell distribution were compatible with the computations. It appears reasonable to apply this method to assessing the importance of early cracks in structural elements in service.

The calculations showed that oxygen transport through the crack itself may aggravate corrosion, but to a limited extent. This finding suggests that attempts at remmediation by crack impregnation are not likely to dramatically reduce the corrosion rate by limiting oxygen access (this conclusion might be different if the corroding area were larger).

ACKNOWLEDGMENTS

REFERENCES

1.   M. Raupach, Construction and Building Materials, Vol. 10, p. 329, 1996.

2.   N.M. Wilkins and P.F. Lawrence, "The corrosion of steel reinforcements in concrete immersed in seawater," p.119 in In Corrosion of Reinforcement in Concrete Construction, A.P. Crane Ed., Ellis Horwood Publishers, Chichester, 1983.

3.   Y. Ohno, S. Praparntanatorn, and K. Suzuki, "Influence of Cracking and Water Cement ratio on Macrocell Corrosion of Steel in Concrete," p.24 in in Corrosion of Reinforcement in Concrete Construction, C.L. Page, P.B. Bamforth and J.W. Figg, Eds., The Royal Society of Chemistry, Cambridge, 1996.

4.   S.C. Kranc, and A.A. Sagüés, "Computation of Corrosion Macrocell Current Distribution and Electrochemical Impedance of Reinforcing Steel in Concrete," in Computer Modeling in Corrosion, ASTM STP 1154, R.S. Munn, Ed., American Society for Testing and Materials, Philadelphia, PA p.95, 1992.

5.   S. C. Kranc and A.A. Sagüés, Calculation of Extended Counter Electrode Polarization Effects on the Electrochemical Impedance Response of Steel in Concrete," p. 365 in Electrochemical Impedance: Interpretation and Analysis,

ASTM STP 1188, D.C. Silverman, J.R. Scully and M.W. Kendig, Eds., American Society for Testing and Materials, Philadelphia, PA 1993.

6.   S.C. Kranc, and A.A. Sagüés, Corrosion, Vol.50, p.50, 1994.

7.   S.C. Kranc and A. A. Sagüés, J. Electrochem. Soc., Vol 144, p. 2643, 1997.

8.   K. Tuutti, "Corrosion of Steel in Concrete" (ISSN 0346-6906), Swedish Cement and Concrete Research Institute, Stockholm, 1982.

9.   A. A. Sagüés, S.C. Kranc, and F. Presuel-Moreno, "Advanced Computational Model for Sacrificial Cathodic Protection of Partially Submerged Reinforced Concrete Marine Footers," p.1, in   Repair and Rehabilitation of Reinforced Concrete Structures: The State of the Art, W.P. Silva-Araya, O. T. de Rincon, and L. Pumarada O'Neill, Eds., American Society of Civil Engineers, Reston, VA, 1998.
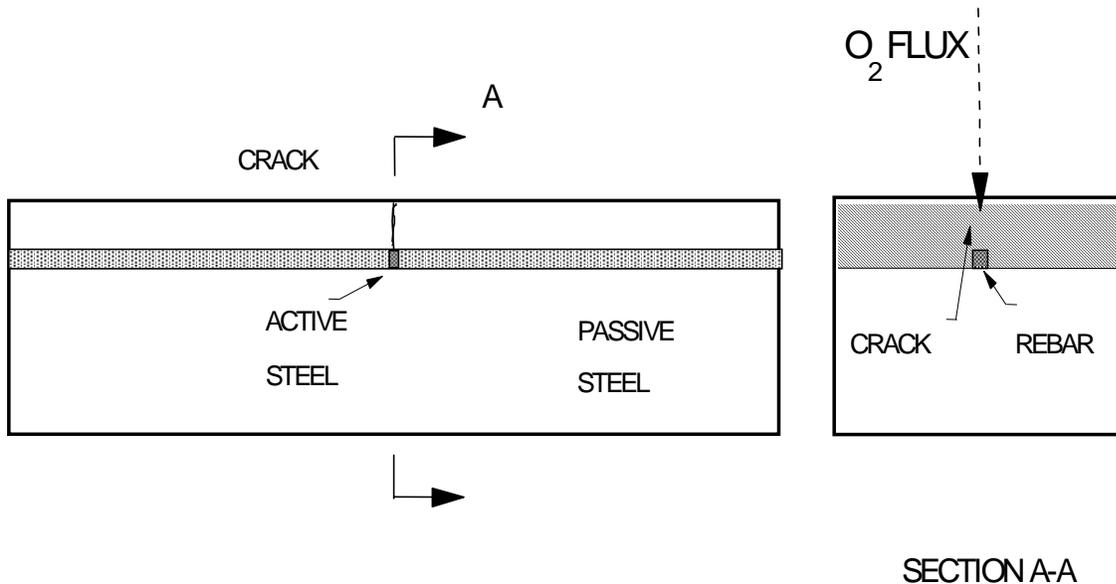
Figure 1: Configurations for model computation. Crack extends from top surface to underside of rebar as shown in Section A-A.
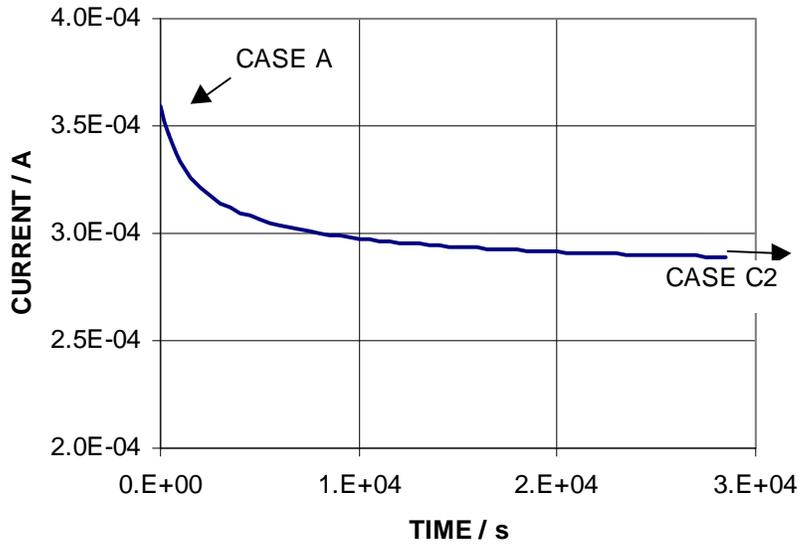
Figure 2: Initial evolution of corrosion macrocell with time. Note initial state, corresponding to Case A.
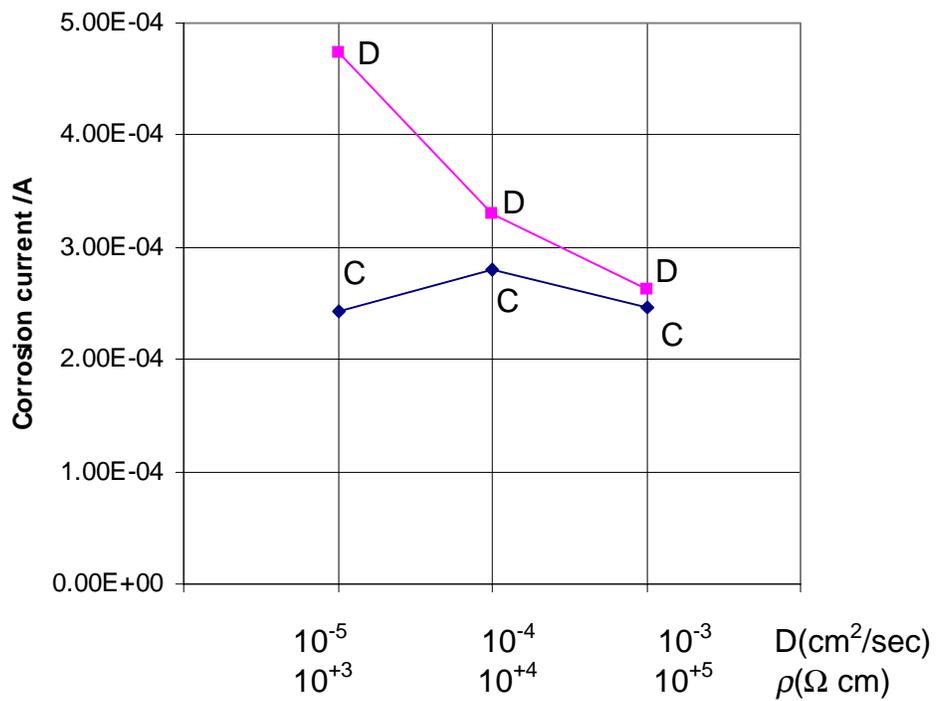
Figure 3: Corrosion current of the central active segment for cases C1-C3 and D1-D3 as function of concrete properties.
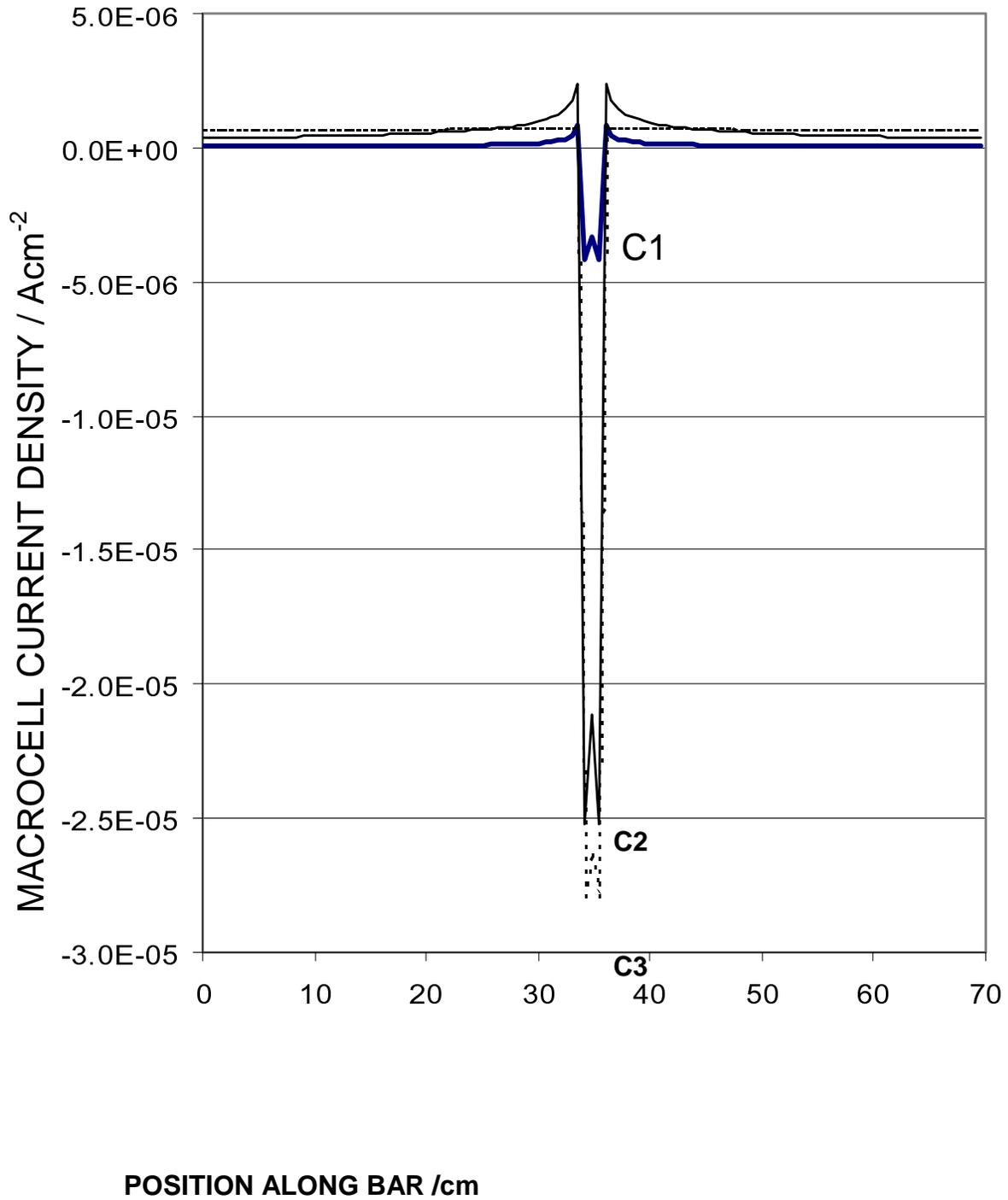
Figure 4: Macrocell current density along the bar length for cases C1-C3. Negative values mean net anodic current density.
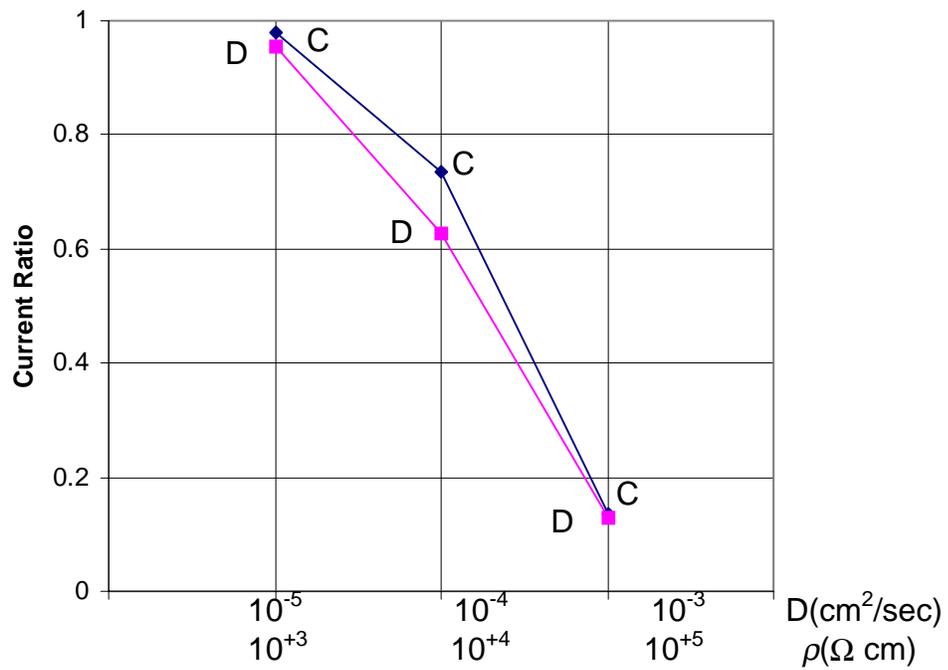
Figure 5: Ratio of macrocell current to corrosion current for the central active segment as function of concrete properties for cases C1-C3 and D1-D3.

APPENDIX 7. Model for a quantitative corrosion damage function for reinforced concrete marine substructure.

Title: Model for a quantitative corrosion damage function for reinforced concrete marine substructure.

Authors: A. A. Sagüés, S.C. Kranc

ABSTRACT

A method of generating a quantitative corrosion damage function given the concrete properties, the configuration of the substructure and basic assumptions about corrosion mechanisms is presented. The output of the model is the amount of damage requiring repair at different elevations in the substructure as a function of time. The model is illustrated for a partially submerged marine substructure column. The damage function is developed from three sequential computational model modules concerning chloride ion transport, corrosion distribution, and evaluation of surface damage. The quantitative model output is illustrated for the different stages of deterioration of the system and for corrosion protection alternatives.

INTRODUCTION AND APPROACH

The corrosion limited service life of reinforced concrete structures has been conceptualized as a two-step deterioration model (Tuutti[1]). In that model the service life is divided into a corrosion initiation stage (chloride intrusion in progress but steel not yet activated) and a corrosion propagation stage (starting when chloride concentration at steel surface reaches the threshold value C_T) during which actual corrosion damage occurs. The useful service life of the structural element is reached when corrosion damage exceeds an acceptable limit. The objective of this paper is to outline a method of generating a quantitative corrosion damage function that considers both the initiation and propagation stages, for a system that includes multiple individual elements.

The method is illustrated for a marine reinforced concrete structure, in which surface chloride content, concrete resistivity and oxygen diffusivity vary as a function of elevation with respect to the waterline. In addition, the model considers the expected variation of C_T with steel potential [2].

The entire system is initially considered to be in the passive state, and the open circuit potential is not a strong function of elevation. Chloride ions begin to penetrate to different extent at various elevations, depending on the surface chloride content. The evolution of chloride concentration as a function of potential and time is calculated by means of a *chloride transport module* that assumes diffusional chloride transport. Eventually, C_T is first reached at an elevation with fast chloride accumulation and steel depassivates locally. That causes a local potential change, and formation of a corrosion macrocell which depresses potential at the active spot and in the passive steel nearby. The redistribution of potentials and resulting corrosion rates are calculated using a *corrosion distribution module* based on previously developed computation methodology [3]. Since C_T is potential dependent, steel depassivation is not likely to happen next at spots immediately adjacent to the region of potential depression, but rather at other places with the appropriate combination of sufficiently high potential and chloride contamination. Every time an additional spot becomes active the potential distribution becomes readjusted and so does the C_T distribution. As each spot enters the active corrosion condition, the corrosion distribution module calculates the local corrosion rate, which is integrated as a function of time and converted into local corrosion penetration by means of the *surface damage evaluation module*. This module also compares the local penetration with a value M_{crit} assumed to result in concrete cover spalling for the combination of steel bar (rebar) diameter and concrete cover used at that location of the system [4,5]. When M_{crit} is reached at a given element of the system, the element is declared damaged and its projected area on the external concrete surface counted as damaged area. The sum of damaged area for the entire system as a function of time is defined as the *damage function* of the system.

EXAMPLE AND DISCUSSION

Figure 1 shows the system chosen for illustration, a partially submerged marine substructure column which is similar to the one described in Ref. 3 with the addition of an assumed surface chloride concentration (C_S) profile. The column is radially symmetric and it is divided into 101 vertical nodes and 36 radial nodes. The dimensions and assumed parameter values (which are generally representative of typical values encountered in field applications) are shown in Table 1. C_T is assumed to follow a dependence with potential given by $C_T = C_{T0} 10^{**}(E_i - E_{T0})/\alpha$, which is on the order of the dependence of pitting potential with chloride concentration threshold used in cathodic prevention investigations [2]. The values of the parameters for C_T are given in Table 1. M_{crit} was taken to be 0.01 cm, in the range of reported values [4,5]. Chloride diffusivity was for simplicity assumed to be elevation-independent. The corrosion distribution was computed as shown in Reference 3, with the addition of an assumed value i_p for the passive steel corrosion current density. Figure 2 shows the computed local potentials (for ring-shaped sections of reinforcement treated as a pervious metal sheet as detailed in Ref. 2) as function of elevation for different ages of the column. At time 0 years the potential is nearly uniform and in the passive range for all elevations. At time 21.4 years the first depassivation takes place, just above the water line where the

surface chloride concentration was highest. The potential in adjacent nodes is also affected. By time 32.3 years several other ring regions have become depassivated, but the cathodically "prevented" intermediate regions remain passive. At time 33 years the submerged region becomes active. By time 63.4 years a mature corrosion pattern has developed. Figure 3 shows the correponding corrosion rates. It should be noted that the submerged portion, although active since year 32.3, always corrodes very slowly because the assumed value for oxygen diffusivity below water (water saturated concrete) is much smaller than for the regions above water [1,6]. Figure 3 (top) shows the computed corrosion charge per unit area (integration of corrosion rate with time) for each steel element that becomes active. While nearly straight, each plot is actually a curve reflecting the integration of varying corrosion rates with time. The horizontal dashed line is the Faradaic equivalent of M_{crit}=0.01 cm. Thus for example, the first element to become active (at 21.4 years) reaches M_{crit} at about 25 years and is declared spalled at that moment. The next two elements to spall do so at approximately year 30.5 and year 31 respectively. The damage function for the system, expressed as the total count of spalled elements (each corresponding to about 0.39 m^2 of external column surface) is shown in the bottom graph of Figure 3.

Given the unit cost per m^2 of a given repair method, the damage function in the form shown in Figure 3 is directly convertible into accumulated repair cost needs. The predicted damage function can therefore be a powerful means of assessing cost effectiveness of design and rehabilitation alternatives. The ability to simulate various corrosion protection alternatives is shown in Figure 4. These are examples of predicted damage functions for a case with poorer concrete properties (Case B, same as in Table 1 but with $\rho_{H/L}$ = 2 10^3 / 10^4 ohm-cm; $D_{H/L}$ = 10^{-4} / 10^{-3} cm^2/sec; D_{Cl} =2 10^{-7} cm^2/sec), and case B but with a submerged bulk anode (operating voltage assumed to be -1 V CSE) applied from year 0, or a surface anode of the sprayed zinc type [7] (operating voltage -0.5 V CSE at the concrete surface, also applied since year 0), or the use of an admixed corrosion inhibitor that elevates the value of C_{T0} by a factor of 10 with respect to the value in Table 1. The relative gain effected by each alternative can be easily evaluated by comparing the damage functions; absolute cost comparisons can be made by multiplying by the corresponding cost factors of each option.

ACKNOWLEDGMENT

TABLE 1

Model Parameters

Steel Cover	c =	10.5 cm		
Column diameter	w=	105 cm		
Column Length	L=	1200 cm		
Concrete Resistivity	ρ_H=	10^5 ohm-cm		
	ρ_L=	$2\ 10^4$ ohm-cm		
Oxygen Diffusivity	D_H=	10^{-3} cm²/sec		
	D_L=	10^{-5} cm²/sec		
Chloride Diffusivity	D_{Cl}=	$2\ 10^{-8}$ cm²/sec		
O₂ Surface Concentration	C_{O2}=	$2.5\ 10^{-7}$ mol/cm³ (in pore water)		
Cl⁻ Surface Concentration	C_{SH}=	15 Kg/m³		
	C_{SW}=	0 Kg/m³		
	C_{SL}=	9 Kg/m³		
Chloride Threshold Parameters	C_{T0}=	0.71 Kg/m³		
	E_{T0}=	-128 mV		
	α =	400 mV		
Polarization Parameters	E_0 (-mV CSE)	i_0(A/cm²)	Tafel Slope (mV)	
Iron Dissolution	780	$1.875\ 10^{-8}$	60	
Oxygen Reduction	-160	$6.25\ \ 10^{-10}$	160	
Steel Passive Current Density	$i_p = 0.058\ 10^{-6}$ A/cm²			

Note: See Ref. 3 for further definitions and conventions used.

BIBLIOGRAPHY

K. Tuutti, "Corrosion of Steel in Concrete" (ISSN 0346-6906), Swedish Cement and Concrete Research Institute, Stockholm, 1982.

L. Bertolini, F. Bolzoni, T. Pastore and P. Pedeferri, "New Experiences on Cathodic Prevention of Reinforced Concrete Structures", pp. 390-398 in Corrosion of Reinforcement in Concrete Construction", C. Page, P. Bamforth and J. Figg, Eds., Society for Chemical Industry, Special Publication No. 183, London, 1996.

S.C. Kranc and A.A. Sagüés,"Computation of Reinforcing Steel Corrosion Distribution in Concrete Marine Bridge Substructures", Corrosion, Vol. 50, p.50, 1994.

C. Andrade, C. Alonso, J. Rodriguez and M. Garcia, "Cover Cracking and Amount of Rebar Corrosion: Importance of the Current Applied Accelerated Tests", pp. 263-273 in Concrete Repair, Rehabilitation and Protection, R. Dihr and M. Jones, Eds, E&FN Spon, London, 1996.

A. Torres-Acosta and A. Sagüés, A Concrete Cover Cracking and Corrosion Expansion of Embedded Reinforcing Steel@, *These Proceedings*.

O. Gjorv, O. Vennesland and A. El-Busaidy, Materials Performance, Vol.25, No.12, p.39 (1986).

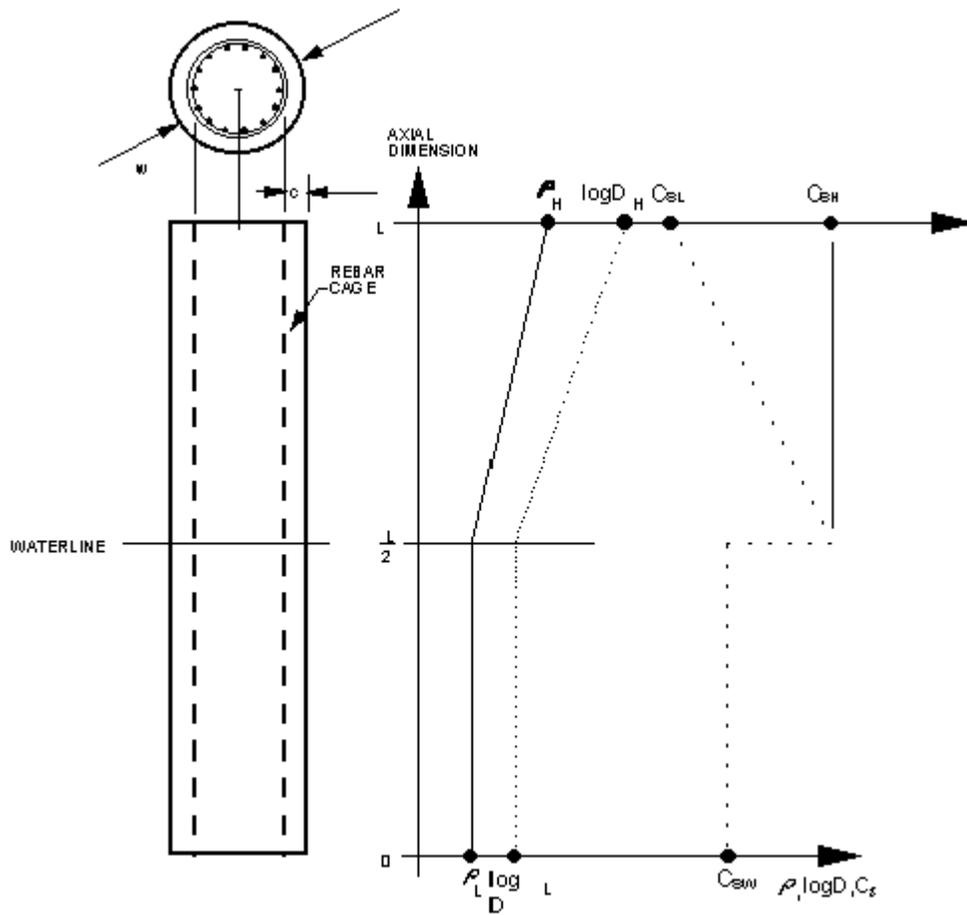Sagüés, A. and Powers, R., Corrosion, Vol. 52. p.508, 1996.
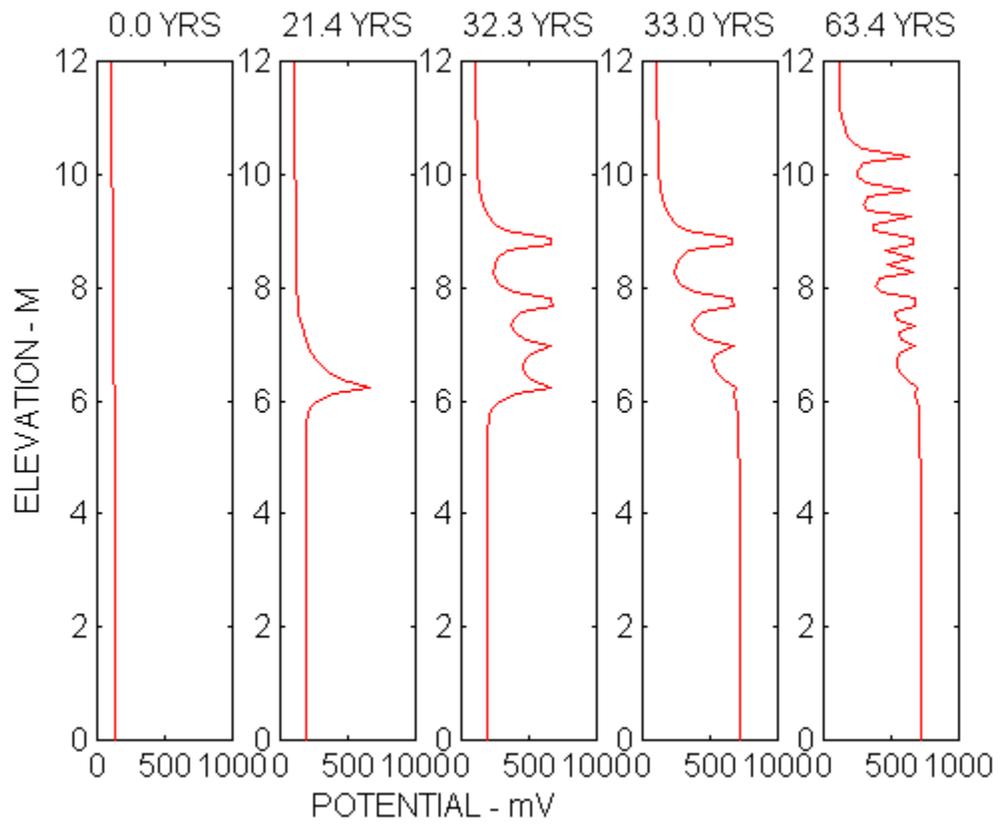
Figure 1: Configuration of the system modeled.

Figure 2: Corrosion potential as a function of elevation at various times.
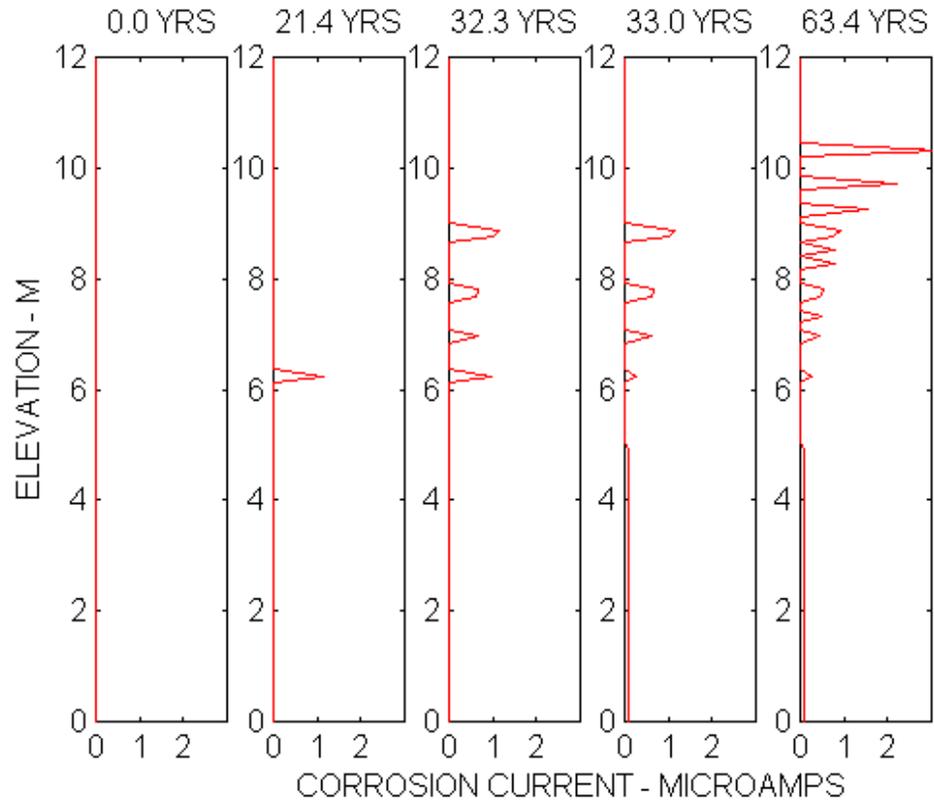
Figure 3: Corrosion current as a function of elevation at various times. Element area = 0.39
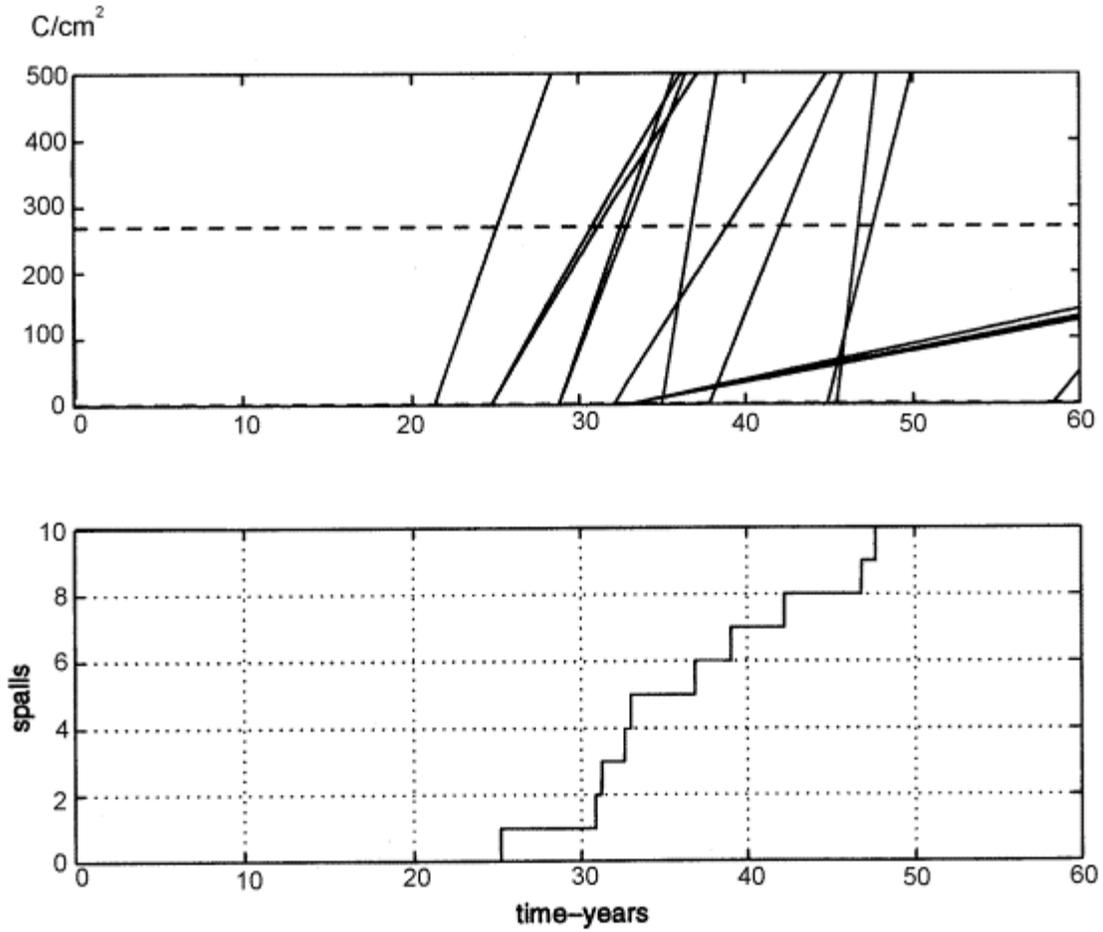
Figure 4: Top: Cumulative corrosion charge of the various activated elements as function of time. Bottom: Damage function. Each element has area = 0.39 m^2.
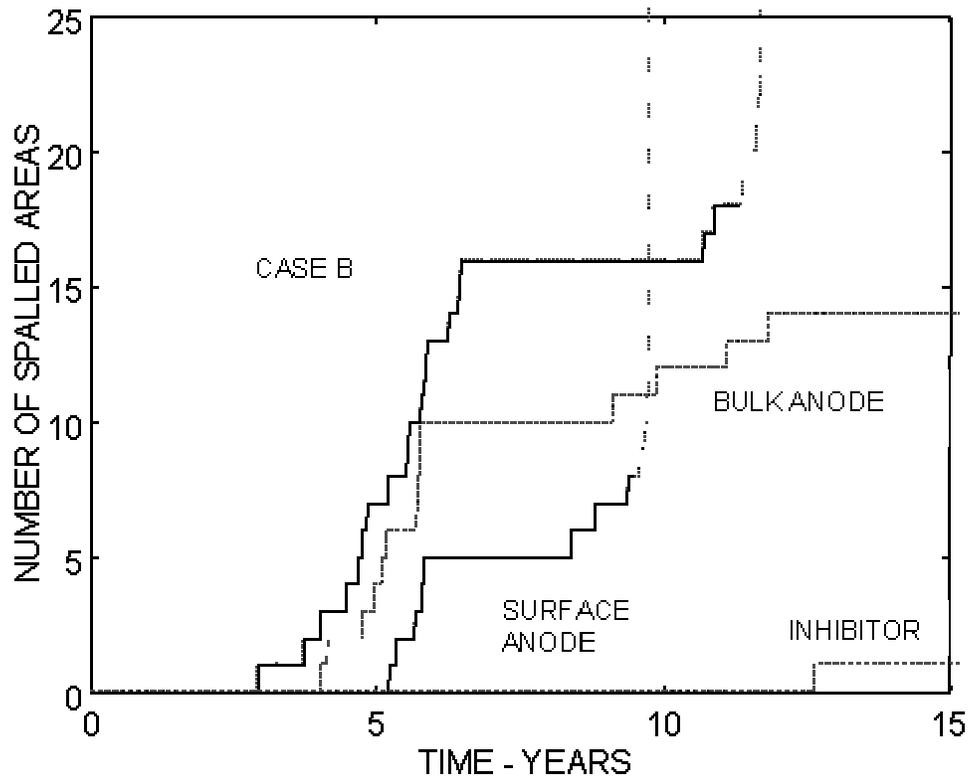
 Figure 5: Example of damage functions for case B and corrosion mitigation alternatives.

CONVERSION FACTORS, US CUSTOMARY TO METRIC UNITS

Multiply	by	to obtain
inch	25.4	mm
foot	0.3048	meter
square inches	645	square mm
cubic yard	0.765	cubic meter
pound/cubic yard	0.593	kg/cubic meter
$inch^2$/year	$2.046\ 10^{-7}$	cm^2/sec
gallon/cubic yard	4.95	liter/cubic meter
standard cubic feet/hour	466.67	ml/minute
ounces	28.35	gram
pound	0.454	kilogram
pound (lb)	4.448	newtons
kip (1000 lb)	4.448	kilo Newton (kN)
pound/in^2	0.0069	MPa
kip/in^2	6.895	MPa
ft-kip	1.356	kN-m
in-kip	0.113	kN-m